technische universität
dortmund

Dissertation zur Erlangung des
Doktorgrades der Naturwissenschaften

Nonequilibrium spin phenomena in quantum dots

induced by periodic optical excitation

vorgelegt von

Philipp Schering
geboren in Coesfeld

Theoretische Physik I
Fakultät Physik
Technische Universität Dortmund

2021

Erstgutachter:	Prof. Dr. Götz S. Uhrig
Zweitgutachter:	Prof. Dr. Frithjof B. Anders
Drittgutachter:	Prof. Dr. Mikhail M. Glazov
Vorsitzender der Prüfungskommission:	Prof. Dr. Dr. Wolfgang Rhode
Abgabedatum:	14. Juli 2021
Datum der mündlichen Prüfung:	1. Oktober 2021

Abstract

The coherent control of a charge carrier spin that is localized in a semiconductor quantum dot and the generation of long-lived states for information storage are of particular interest for quantum information processing. This spin interacts predominantly with the surrounding nuclear spins in the quantum dot, which can be described by the central spin model. The periodic application of circularly polarized laser pulses induces nonequilibrium spin dynamics in the quantum dot, giving rise to various phenomena that can be observed in experiments. In this thesis, models and semiclassical approaches are developed to simulate the driven spin dynamics in this system under experimental conditions. For the case where a transverse magnetic field is applied, it is found that the part of the spin mode locking effect stemming from nuclei-induced frequency focusing depends nonmonotonically on the strength of the magnetic field, with strong similarities to experimental observations. The complex behavior is related to various nuclear magnetic resonances with respect to the repetition rate of the laser pulses, which can be exploited for novel kind of nuclear magnetic resonance spectroscopy of the emerging nonequilibrium steady states. For the case where a longitudinal magnetic field is applied, the influence of the pump pulse power on the spin inertia and on the polarization recovery effect is analyzed. With the help of the developed model, the related experiments can be understood and described quantitatively. In this context, a novel effect termed resonant spin amplification in Faraday geometry is predicted, which enables the direct measurement of the longitudinal g factor of the resident charge carriers. Model calculations are used to find the optimal conditions for its detection and ways to improve its visibility are pointed out. The comparison with recent experiments that demonstrate the realization of the effect shows a remarkable agreement.

Kurzfassung

Die kohärente Kontrolle eines Ladungsträgerspins, der in einem Halbleiterquantenpunkt lokalisiert ist, sowie die Erzeugung langlebiger Zustände zur Informationsspeicherung sind von besonderem Interesse für die Quanteninformationsverarbeitung. Solch ein Spin wechselwirkt hauptsächlich mit den ihn umgebenden Kernspins im Quantenpunkt, was durch das Zentralspinmodell beschrieben werden kann. Durch periodische Anregung mit zirkular polarisierten Laserpulsen lässt sich die Spindynamik in Quantenpunkten in ein Nichtgleichgewicht treiben, wodurch verschiedene Phänomene auftreten können, die sich in Experimenten beobachten lassen. In dieser Arbeit werden theoretische Modelle und semiklassische Methoden entwickelt, um die getriebene Spindynamik unter experimentellen Bedingungen zu simulieren. Im Falle eines angelegten transversalen Magnetfelds zeigt sich, dass der Teil des „Spin Mode Locking" Effekts (Synchronisation von Spin-Moden), welcher aufgrund einer durch die Kernspins induzierten Frequenzfokussierung entsteht, eine nicht-monotone Abhängigkeit von der Stärke des Magnetfelds aufweist, mit starken Parallelen zu experimentellen Beobachtungen. Verantwortlich für das komplexe Verhalten sind verschiedene Kernspinresonanzen bezogen auf die Wiederholungsrate der Laserpulse. Hieraus ergibt sich eine neue Art von Kernspinresonanzspektroskopie, durch welche die langlebigen Nichtgleichgewichtszustände untersucht werden können. Im Falle eines angelegten longitudinalen Magnetfelds wird der Einfluss der Pulsleistung auf den „Spin Inertia" (Spinträgheit) und den „Polarization Recovery" (Wiederherstellung der Spinpolarisation) Effekt untersucht. Die zugehörigen Experimente lassen sich durch das entwickelte Modell quantitativ verstehen und beschreiben. In diesem Zusammenhang wird ein neuer Effekt vorhergesagt, welcher als „Resonant Spin Amplification in Faraday Geometry" (Resonante Spinverstärkung in Faraday Geometrie) bezeichnet wird und die direkte Bestimmung des longitudinalen g-Faktors der Ladungsträger ermöglicht. Optimale Bedingungen für dessen Beobachtung und Möglichkeiten zu Verbesserung seiner Sichtbarkeit werden aufgezeigt. Der Vergleich mit kürzlich durchgeführten Experimenten, welche die Existenz des Effekts bestätigen, zeigt eine hervorragende Übereinstimmung.

List of publications

Major parts of the thesis are reused or adapted from the author's contributions to the following publications:

- B. Fauseweh, P. Schering, J. Hüdepohl, and G. S. Uhrig
  Efficient algorithms for the dynamics of large and infinite classical central spin models
  Phys. Rev. B **96**, 054415 (2017)

- P. Schering, B. Fauseweh, J. Hüdepohl, and G. S. Uhrig
  Nuclear frequency focusing in periodically pulsed semiconductor quantum dots described by infinite classical central spin models
  Phys. Rev. B **98**, 024305 (2018)

- I. Kleinjohann, E. Evers, P. Schering, A. Greilich, G. S. Uhrig, M. Bayer, and F. B. Anders
  Magnetic field dependence of the electron spin revival amplitude in periodically pulsed quantum dots
  Phys. Rev. B **98**, 155318 (2018)

- P. Schering, G. S. Uhrig, and D. S. Smirnov
  Spin inertia and polarization recovery in quantum dots: Role of pumping strength and resonant spin amplification
  Phys. Rev. Research **1**, 033189 (2019)

- P. Schering, P. W. Scherer, and G. S. Uhrig
  Interplay of spin mode locking and nuclei-induced frequency focusing in quantum dots
  Phys. Rev. B **102**, 115301 (2020)

List of publications

- P. Schering and G. S. Uhrig
  Nuclear magnetic resonance spectroscopy of nonequilibrium steady states in quantum dots
  EPL (Europhys. Lett.) **133**, 57003 (2021)

- P. Schering, E. Evers, V. Nedelea, D. S. Smirnov, E. A. Zhukov, D. R. Yakovlev, M. Bayer, G. S. Uhrig, and A. Greilich
  Resonant spin amplification in Faraday geometry
  Phys. Rev. B **103**, L201301 (2021)

Further publications with contributions from the author:

- U. Seifert, P. Bleicker, P. Schering, A. Faribault, and G. S. Uhrig
  Persisting correlations of a central spin coupled to large spin baths
  Phys. Rev. B **94**, 094308 (2016)

- R. Röhrig, P. Schering, L. B. Gravert, B. Fauseweh, and G. S. Uhrig
  Quantum mechanical treatment of large spin baths
  Phys. Rev. B **97**, 165431 (2018)

- P. Schering, P. W. Scherer, and G. S. Uhrig
  "Simulation of nonequilibrium spin dynamics in quantum dots subjected to periodic laser pulses", in *High Performance Computing in Science and Engineering '20, Transactions of the High Performance Computing Center, Stuttgart (HLRS) 2020*, edited by W. E. Nagel, D. H. Kröner, and M. M. Resch (Springer International Publishing, in press)

Acronyms

Notation	Description
CSM	central spin model
DNP	dynamic nuclear polarization
DTWA	discrete truncated Wigner approximation
EM	extended model
ERC	even resonance condition
FWHM	full width at half maximum
NESS	nonequilibrium steady state
NIFF	nuclei-induced frequency focusing
NMR	nuclear magnetic resonance
NRC	nuclear resonance condition
ODE	ordinary differential equation
ORC	odd resonance condition
PRC	polarization recovery curve
PSC	phase synchronization condition
QD	quantum dot
RSA	resonant spin amplification
SD approach	Spectral Density approach
SML	spin mode locking
TPA	trion probability approach
TWA	truncated Wigner approximation

Contents

I

Introduction

Chapter 1

Motivation and outline

Over the past decades, quantum information processing has emerged to be one of the most active and promising fields in physics, and in the past two decades, the very first quantum computers were built. The guiding idea is to exploit quantum mechanical features such as superposition and entanglement to develop algorithms that can solve computational problems much more efficiently than classical computers [1]. Popular examples developed in the 90s are the Shor algorithm [2, 3], allowing one to factorize large numbers in polynomial time, and the Grover algorithm [4], which enables a faster search in unstructured databases. Another idea proposed by Feynman [5] is the simulation of quantum systems using quantum computers [6]. Nowadays, quantum information processing has come a long way and potentially, quantum supremacy has been demonstrated recently for dedicated problems [7, 8]. Even though it has been argued that the Sycamore processor with 53 qubits used in Ref. [7] does not actually reach quantum supremacy because of a non-optimal implementation of the classical algorithm [9], it is only a matter of time until it is accomplished without dispute because the number of qubits increases year after year. The Sycamore processor utilizes so-called transmon qubits based on superconducting circuits [10]. Generally speaking, a qubit is an effective quantum mechanical two-level system. Several realizations of a qubit are conceivable, all with their own advantages and disadvantages [11], and it is not yet clear which hardware implementation will prevail.

But what are the physical requirements for the implementation of a fault-tolerant quantum computer? In a seminal work by DiVincenzo [12], five criteria are proposed. In a more recent work by Ladd *et al.* [11], they are rephrased into three more general criteria, which are based on the assumption that the third DiVincenzo criterion is fulfilled. This criterion states that the coherence time, often denoted

as T_2, must be large compared to the time of a single logical operation to be able to perform complex computations, i.e., decoherence effects need to be minimized. The remaining DiVincenzo criteria rephrased by Ladd *et al.* [11] are:

- "*Scalability:* The computer must operate in a Hilbert space whose dimensions can grow exponentially without an exponential cost in resources (such as time, space or energy)." [11]
- "*Universal logic:* The large Hilbert space must be accessible using a finite set of control operations; the resources for this set must also not grow exponentially." [11]
- "*Correctability:* It must be possible to extract the entropy of the computer to maintain the computer's quantum state." [11]

Implementations of quantum computers based on spins of charge carriers in semiconductor quantum dots (QDs) [13, 14] are an alternative to implementations based on superconducting circuits [11]. In QDs, charge carriers can be bound to a localized potential with discrete energy levels, similar to an electron bound to the nucleus of an atom and hence, QDs are often referred to as artificial atoms [15–17]. Electrostatically defined QDs are primarily controlled electrically and operate at very low temperatures $< 1\,\mathrm{K}$ [18]. Self-assembled QDs, based on a random growth process, operate at cryogenic temperatures of $\sim 4\,\mathrm{K}$ and are typically controlled by optical methods [19].

Individual charge carriers in QDs can be generated, manipulated, and coherently controlled [20–38]. Furthermore, it is possible to decouple them from the environment responsible for decoherence, e.g., by applying suitable schemes of control pulses [34, 39]. In terms of scalability, there is the advantage of the vast experience of the semiconductor industry and integrated solutions with existing semiconductor technologies are conceivable [14, 40].

Spins of charge carriers in quantum dots as stationary qubits offer spin coherence times in the range of microseconds [18, 19, 41], which is orders of magnitude below the values of other solid-state competitors such as electrons bound to dopants bound or nitrogen-vacancy centers in diamond [11]. At the low temperatures at which QDs are operated, the main interaction of a localized charge carrier spin is the hyperfine interaction with the nuclei of the lattice, leading to fast decoherence [18, 19, 42]. While it is possible to decrease the influence of the detrimental nuclear spin bath

by polarizing it [43, 44], the degree of polarization must be $> 99.9\%$ to have a sufficiently strong impact on the coherence time [18, 42], which is yet to be accomplished. Another possibility is the application of dynamical decoupling schemes to overcome the problem of decoherence caused by a noisy environment. For instance, Bluhm *et al.* [34] applied a multiple-pulse Carr-Purcell-Meiboom-Gill echo sequence [39, 45] and achieved an increase of the coherence time by two orders of magnitude to more than $200\,\mu$s. Similarly, dynamical decoupling was applied successfully to prolong the coherence time of hole spins localized in InGaAs QDs [46, 47]. More advanced pulse sequences can lead to further improvements [48–52]. The development of such dynamical decoupling schemes is a separate field of research [53–63].

Studying the evolution of the nuclear spin bath is possible by means of a coherent population trapping technique that is sensitive to the nuclear spin bath [64–66]. In recent years, there has been a shift of interest towards nuclear spins in QDs thanks to their long lifetimes of seconds up to hours (depending on the applied magnetic field) [25, 42, 44, 67–69]. The idea is to exploit the nuclear spin system in QDs as a long-lived quantum resource, which can be used as a quantum memory for the quantum information originally stored in the spins of charge carriers [67, 70–73]. This extremely challenging task was accomplished recently by Gangloff *et al.* [70] with a nuclear spin bath consisting of $10^4 - 10^5$ nuclei. The accomplishment can be considered as "the missing piece of the puzzle for a semiconductor nanostructure QI [quantum information] platform" [74].

1.1 Research objectives

Already a decade earlier than the recent work of Gangloff *et al.* [70], it has been identified that the hyperfine interaction of localized electron spins with the complex nuclear spin system needs not necessarily be destructive. Greilich *et al.* [25] studied QD ensembles subjected to a transverse magnetic field and demonstrated that the nuclear spin system can be manipulated indirectly via the hyperfine interaction such that the broad distribution of precession frequencies are focused onto very few modes describing spin dynamics commensurable with the laser repetition rate. Tailoring the applied laser pulse protocol can even lead to the formation of single-mode precessions of the full ensemble of charge carrier spins [75, 76]. Related to

this fascinating phenomenon, there are several open questions raised in Sec. 2.4.1. Addressing these issues and expanding the general understanding of this effect is a particular focus of this thesis. It requires the development of sophisticated theoretical models and approaches to study the intertwined electron-nuclear spin system under nonequilibrium conditions caused by the periodic application of laser pulses for extremely long times.

In the context of quantum information [1, 11, 14, 40] and spintronics [77, 78], it is a fundamental requirement to have a detailed understanding of the underlying physical systems for many applications, e.g., to coherently control them [20–37, 40, 41]. In the last part of the thesis, the focus lies on the simulation of experimental setups that enable the characterization of the spin system in QDs.

1.2 Outline

The thesis is divided into three parts. The introductory Part I provides the motivation and foundation for the research results presented in Parts II and III.

Starting in Chap. 2, the reader is introduced to self-assembled semiconductor QDs, to a mechanism that provides a way of polarizing localized spins in singly-charged QDs, and to the pump-probe spectroscopy used to monitor the spin dynamics in experiments. The various spin phenomena that are analyzed in this thesis and related open questions are introduced afterwards.

In Chap. 3, the fundamental model to describe the spin dynamics in singly-charged QDs, the central spin model, is introduced. After briefly discussing the numerous theoretical approaches to this model, the semiclassical approach to the spin dynamics applied in this thesis is introduced. Based on an approximation valid for short times, important characteristics of the short-time dynamics are discussed.

In view of demanding numerical simulations required to study the spin dynamics for the experimentally relevant long timescales and large system sizes, efficient algorithms to the semiclassical approach are developed in Chap. 4.

In the following chapters, the research focuses on experimental setups in which singly-charged QDs are subjected to trains of periodic laser pulses inducing spin polarization. The difference between Part II and III is the direction of the applied

magnetic field. In Chaps. 5–7, a transverse magnetic field is used (Part II), while a longitudinal field is applied in Chaps. 8 and 9 (Part III). The chapters are written in a mostly self-containing way because they represent related but yet separate research projects. Thus, it is not necessarily required to read the full thesis if one is interested in a particular topic, but reading at least Chaps. 2 and 3 is strongly recommended to gain a general understanding of the underlying physics and of the terminology used.

The most efficient algorithm to the semiclassical approach developed in Chap. 4 is put to use in Chap. 5, marking the beginning of Part II. We study the nonequilibrium spin dynamics arising from two generic pulses that are applied periodically to the system in the presence of a transverse magnetic field. The role of the Zeeman effect for the nuclear spins in the QDs is analyzed and the results for the two different pulses are compared.

Based on the insight gained in Chap. 5, a sophisticated model is established in Chap. 6 to describe two interrelated effects appearing in the related experiments: spin mode locking and nuclei-induced frequency focusing. The interplay of these two effects, which determines the emerging nonequilibrium steady states, is investigated.

Further improvements to the model are developed in Chap. 7 by accounting for the isotope composition of the QDs. The results highlight the importance of nuclear magnetic resonances for the arising nonequilibrium spin physics.

In Part III, an experimental setup is studied in which a longitudinal magnetic field is applied to the QDs. To this end, existing models are generalized in Chap. 8. In particular, the role of the pump pulse strength on the emerging spin phenomena is explored. At the end of the chapter, a novel effect termed resonant spin amplification in Faraday geometry is predicted.

Recent experiments confirm the existence of the effect. They are analyzed in Chap. 9, showing a remarkable agreement with model calculations and its predictions. Furthermore, possible ways to enhance the visibility of resonant spin amplification in Faraday geometry are proposed.

Chapter 10 concludes the thesis by summarizing the major developments and results. In an outlook, promising routes for future research are pointed out.

Chapter 2

Experimental background

In this chapter, semiconductor quantum dots are briefly introduced with a particular focus on self-assembled ones. Afterwards, it is discussed how spin polarization can be induced in singly-charged QDs by optical means. At last, an overview of the spin phenomena in singly-charged QDs relevant for this thesis is given and open questions are pointed out.

2.1 Semiconductor quantum dots

Quantum dots are nanometer-sized objects that consist of several thousand atoms of a semiconductor compound. There is a large variety of methods to synthesize QDs, e.g., colloidal chemistry, molecular beam epitaxy, or metal-organic chemical vapor deposition [19, 42]. In so-called gate-defined QDs, lithographic QDs are formed in a two-dimensional electron gas hosted by, e.g., a GaAs/AlGaAs heterostructure [18, 42]. Here, we focus on self-assembled InGaAs QDs grown by the Stranski-Krastanow growth method [79] during molecular beam epitaxy [80, 81]. Monolayers of InAs are deposited on a substrate of GaAs (called the barrier). Even though the lattice constant for InAs is 7% smaller than for GaAs, the InAs layer (called the wetting layer) adapts to the lattice structure of the GaAs barrier. Inevitably, this results in strain when depositing additional layers of InAs. After a critical thickness of about 1.5 monolayers of InAs is reached [81], the strain is partially relaxed as a consequence of the formation of little 'islands', which are referred to as quantum dots [19, 38]. This process happens spontaneously and hence, at irregular positions. This is the reason why such QDs are called 'self-assembled'. They have a typical diameter of $20 - 80\,\mathrm{nm}$ and a height of $2 - 10\,\mathrm{nm}$, i.e., they are fairly flat [19, 38, 42, 82]. The QD sample is prepared for optical spectroscopy

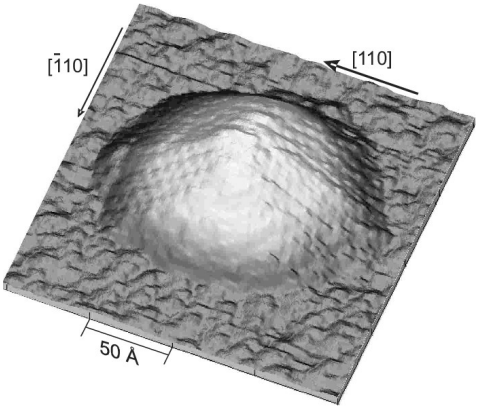

Figure 2.1: Image of an uncapped InAs QD grown on a GaAs barrier, which is made visible by scanning tunneling microscopy. Reprinted from Ref. [83], ©2008 American Institute of Physics, with the permission of AIP Publishing.

by covering it again with the barrier material (GaAs), called the capping layer. An example of a small InAs QD grown on a GaAs barrier (without capping layer) is shown in Fig. 2.1 [83].

In realistic samples of self-assembled InGaAs QDs, there is a significant fraction of Ga in the QDs; we refer to them as $In_xGa_{1-x}As$ QDs whenever the ratio of In and Ga becomes important. The Ga doping is the consequence of the interdiffusion between the QDs and the barriers, resulting from the process of thermal annealing for which the sample is heated to $\sim 900\,°C$ [84–88]. The benefits of this process are that it homogenizes the ensemble of QDs and reduces lattice defects. Furthermore, it allows for tuning the relevant optical transition energies [89, 90].

A controlled n doping can be obtained by an additional δ-doping layer of, e.g., Si, which is grown a few nanometer below the QD layer [23, 91–94]. This process allows one to control the density of the charge carriers, e.g., to obtain QDs that are on average singly charged by electrons. A p doping can be achieved by exploiting residual carbon impurities typical for GaAs-based materials [95], providing a p doping even if the sample is nominally undoped [96–98].

The structure of QDs provides a three-dimensional confinement of the charge carriers (electrons or holes, depending on the doping), i.e., they are *localized*. The energy levels of such charge carriers are discrete, similar to the states of an electron bound to the nucleus of an atom [15–17, 99–102]. Combined with the strong localization, it lead to the motivation to use the spin states of the charge carriers as qubits [11, 13]. The localization is also responsible for the hyperfine interaction being the dominant interaction in QDs. For n-doped QDs, the localized electron is effectively

coupled to $10^4 - 10^6$ nuclear spins [19, 103–107]. The relevant interactions in QDs are discussed in Sec. 3.1.

2.2 Optical spin orientation in singly-charged quantum dots

In view of the optical manipulation of the spin states of localized charge carriers in QDs, we discuss the relevant mechanisms. Strict selection rules determine the electric dipole interaction of an electromagnetic wave with carriers in a semiconductor [108]. For more details, see the text book [109] and the review article [19], on which the following discussion is based. We focus on GaAs and InAs, which are direct semiconductors. At the Γ point, the band structure can be treated in the effective mass approximation. Neglecting the spin splitting, there is a two-fold degenerate, isotropic conduction band above the band gap. The valence bands consist of several sub-bands as a consequence of the spin-orbit interaction: light- and heavy-hole bands (both anisotropic, but different effective masses), and an isotropic split-off band. All three sub-bands are two-fold degenerate in spin.

2.2.1 Optical selection rules

In the following, the lateral dimensions of the QDs are considered to be much larger than their height as it is the case for self-assembled QDs. The growth axis $z \parallel [001]$ serves as quantization axis for the spin states. In zinc blende based semiconductors, e.g., GaAs or InAs, energy and angular momentum are conserved for transitions between the valence and the conduction band. Since the periodic part of the Bloch function of the conduction states is s like, a conduction electron carries a spin with z projection $S^z = \pm 1/2$ ($\hbar$ set to unity). The p-like valence states are determined by the spin-orbit interaction. For the states with total angular momentum $J = 3/2$, one distinguishes between the heavy-hole bands with z projection $J^z = \pm 3/2$ and the light-hole bands with $J^z = \pm 1/2$. At the Γ point, the light- and heavy-hole bands in InGaAs are typically separated by several tens of meV, with the light-hole band being lower in energy. The split-off band with total angular momentum $J = 1/2$ is even further down in energy and hence, it can be omitted in the following discussion.

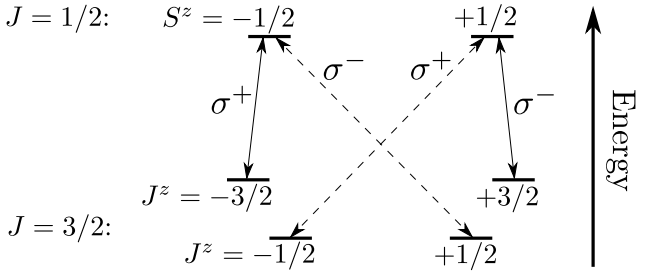

Figure 2.2: Optical selection rules for the interband transitions between valence- and conduction-band electrons in direct semiconductors. The split-off band is omitted. The conduction band is two-fold degenerate with $S^z = \pm 1/2$. The valence electrons states are related to the heavy-hole band with $J^z = \pm 3/2$ and light-hole band with $J^z = \pm 1/2$, respectively. Figure inspired by Ref. [19].

The absorption of a photon can change the angular momentum of an electron by ± 1 for a photon with helicity $\sigma^{\pm}$. The resulting optical selection rules between the valence and conduction states are visualized in Fig. 2.2. The absorption and emission of a photon share the same selection rules. Consider a σ^+ photon of suitable energy absorbed by an electron in the heavy-hole band with $J^z = -3/2$. The electron is excited to the conduction band with $S^z = -1/2$. The absorption of a σ^- photon results in a similar transition, but with opposite sign. Transitions to the conduction band starting from the light-hole states with $J^z = \pm 1/2$ are also possible by absorption of $\sigma^{\mp}$ photons, but they are not of importance in the following discussion because they are separated in energy from the heavy-hole states.

In a neutral QD with an empty conduction band prior to the photon absorption, a bound electron-hole pair (exciton) with integer angular momentum can be excited optically as a consequence of the attractive coulomb interaction between the electron promoted to the conduction band and the remaining hole in the valence band; see, e.g., Refs. [82, 110] for more details. In n-doped singly-charged QDs, three-particle complexes called trions (also referred to as charged excitons) can be formed [82, 110]. For instance, if there is a resident electron in the conduction band with $S^z = +1/2$, a singlet negatively-charged trion T^- (also referred to as X^-) can be formed when a valence-band electron with $J^z = -3/2$ is promoted to the conduction band with $S^z = -1/2$ by absorption of a σ^+ photon. Then, the two electrons in the conduction band form a spin singlet and a heavy-hole with unpaired spin ($J^z = +3/2$) is left behind. Similarly, in p-doped QDs, singlet positively-charged trions T^+ (also referred to as X^+) can be excited, which consists of two heavy-holes

in a spin singlet and an unpaired electron spin with $S^z = \pm 1/2$.

These photoexcited quasiparticles (trions) have a certain lifetime until the electron and hole recombine, i.e., the quasiparticle decays back to the ground state. The recombination is predominantly radiative in direct-band semiconductors such as GaAs or InAs. In singly-charged QDs, the trion recombination time is of the order of a few hundred picoseconds [82]. In this thesis, InGaAs QDs with a recombination time of $\tau_0 \approx 400\,\mathrm{ps}$ [23, 111] are considered.

2.2.2 Microscopic two-level model for the optical excitation of trions

Inducing a finite spin polarization of the localized charge carriers in singly-charged QDs can be achieved via the excitation of intermediate trion states [23, 112–115]. In the following, we consider an ensemble of QDs singly-charged by electrons (n doped) and introduce the two-level model developed in Ref. [113] to describe the spin initialization process in this system microscopically. Here, the lateral dimensions of the QDs are considered to be flat (as for self-assembled QDs) so that the growth axis $z \parallel [001]$ serves as quantization axis for the spin states. The case of three-dimensional, spherical nanocrystals grown of III-V semiconductor compounds is discussed in Ref. [116].

The QDs are excited by a circularly polarized laser pulse with helicity $\sigma^{\pm}$, exciting singlet negatively-charged trion states that consist of two electrons in a spin singlet and a heavy hole with unpaired spin.[1] For instance, the ground state described by a resident electron with spin z projection $+1/2$ can be promoted to a negatively-charged singlet trion T^- with spin z projection $+3/2$ through the absorption of a σ^+ photon of suitable energy. If the spin z projection of the ground state is $-1/2$, a σ^- photon is required to excite a T^- trion with spin z projection $-3/2$. The photon energy shall be close to the trion transition energy (about $1.3 - 1.4\,\mathrm{eV}$ in InGaAs QDs [19, 23, 94, 95, 117]) so that the excitation of light-hole spin states can be neglected. Furthermore, it is assumed that the energy level splitting induced by an external magnetic field as a consequence of the Zeeman effect is small in comparison to the spectral width of the pulse, i.e., the splitting can be neglected

[1] The model is also applicable to QDs singly charged by heavy holes (p doped). But since the selection rules to excite positively-charged trions are different, the pulse helicity needs to be inverted.

as well. Then, the relevant states can be described by a four-component wave function

$$\mathbf{\Psi} = (\psi_{1/2},\, \psi_{-1/2},\, \psi_{3/2},\, \psi_{-3/2})^{\top}, \tag{2.1}$$

where the subscripts '$\pm 1/2$' refer to the resident electron spin states and '$\pm 3/2$' to the photoexcited trion states. The duration of the laser pulse τ_p shall be long compared to the oscillation period of the carrier frequency ω_pu of the electromagnetic wave, but short compared to the electron spin dynamics in the QD so that they can be neglected. Typically, trains of optical pulses are applied to the QDs with repetition time T_R. In contrast to Ref. [113], we do not assume that the trion recombination time τ_0 is much smaller than T_R because this assumption does not hold for the experiments analyzed in Chap. 9 with $T_\mathrm{R} = 1\,\mathrm{ns}$ and $\tau_0 = 400\,\mathrm{ps}$ [94].[2]

A circularly polarized pulse of a given helicity connects only two spin states as described above; see also Fig. 2.2. Hence, it is sufficient to treat the system as a two-level model. The corresponding transformation of the wave functions for the spin states induced by the optical pulse can be written as [113]

$$\mathrm{i}\,\frac{\partial}{\partial t}\psi_{\pm 3/2} = \omega_\mathrm{T}\,\psi_{\pm 3/2} + V_\pm(t)\,\psi_{\pm 1/2}\,, \tag{2.2a}$$

$$\mathrm{i}\,\frac{\partial}{\partial t}\psi_{\pm 1/2} = V_\pm^*(t)\,\psi_{\pm 3/2}\,. \tag{2.2b}$$

Here, ω_T is the trion transition frequency and $V_\pm(t) = V_{0,\pm}\,\mathrm{e}^{-\mathrm{i}\omega_\mathrm{pu}t}$ describes the interaction of the circularly polarized light with frequency ω_pu with the QDs. Its precise definition is not of importance here, but $V_{0,\pm}$ depends on an effective dipole moment for the respective transition (see Ref. [113] for details).

To solve the system of differential equations, it is convenient to switch to a rotated frame by applying the ansatz $\widetilde{\psi}_{\pm 3/2} = \psi_{\pm 3/2}\,\mathrm{e}^{\mathrm{i}\omega_\mathrm{T}t}$. It results in the equations

$$\mathrm{i}\,\frac{\partial}{\partial t}\widetilde{\psi}_{\pm 3/2} = \widetilde{V}_\pm(t)\,\psi_{\pm 1/2}\,, \tag{2.3a}$$

$$\mathrm{i}\,\frac{\partial}{\partial t}\psi_{\pm 1/2} = \widetilde{V}_\pm^*(t)\,\widetilde{\psi}_{\pm 3/2}\,, \tag{2.3b}$$

[2] The following generalized relations for the spin initialization were derived by the author together with D. S. Smirnov for Ref. [94].

with $\widetilde{V}_{\pm}(t) = V_{\pm}(t)\,\mathrm{e}^{\mathrm{i}\omega_{\mathrm{T}}t}$. Since we consider circularly polarized pulses with helicity $\sigma^{\pm}$ represented by $\mathcal{P} = \pm 1$, we can define $V(t) \coloneqq V_{\mathcal{P}}(t)$, whereas $V_{-\mathcal{P}}(t) = 0$. Hence, two of the four wave functions are unaffected by the light,

$$\psi_{-1/2\mathcal{P}}(+\infty) = \psi_{-1/2\mathcal{P}}(-\infty)\,, \tag{2.4a}$$
$$\psi_{-1/2\mathcal{P}}(+\infty) = \psi_{-3/2\mathcal{P}}(-\infty)\,. \tag{2.4b}$$

It follows from Eq. (2.3) that the solutions of the remaining two wave functions are complex conjugated. The solutions have the general form

$$\psi_{+1/2\mathcal{P}}(+\infty) = Q\,\mathrm{e}^{\mathrm{i}\Phi}\,\psi_{1/2\mathcal{P}}(-\infty) + Q'\,\mathrm{e}^{-\mathrm{i}\Phi'}\,\widetilde{\psi}_{3/2\mathcal{P}}(-\infty)\,, \tag{2.5a}$$
$$\widetilde{\psi}_{+3/2\mathcal{P}}(+\infty) = Q\,\mathrm{e}^{-\mathrm{i}\Phi}\,\widetilde{\psi}_{3/2\mathcal{P}}(-\infty) + Q'\,\mathrm{e}^{\mathrm{i}\Phi'}\,\psi_{1/2\mathcal{P}}(-\infty)\,, \tag{2.5b}$$

where Q, Q', Φ, and Φ' are real, phenomenological parameters. Since the transformation must be unitary, it follows $Q^2 + Q'^2 = 1$ because of particle conservation.

The occupancy numbers of the ground (superscript 'G') and trion (superscript 'T') states can be calculated according to

$$n^{\mathrm{G}} = |\psi_{-1/2}|^2 + |\psi_{+1/2}|^2\,, \tag{2.6a}$$
$$n^{\mathrm{T}} = |\psi_{-3/2}|^2 + |\psi_{+3/2}|^2\,, \tag{2.6b}$$

satisfying $n^{\mathrm{G}} + n^{\mathrm{T}} = 1$. Physically, this means that the system is either in the ground or in the excited state. The components of the resident charge carrier spin $\boldsymbol{S}$, which we express as quantum mechanical averages of the spin operators, are given by

$$S^x = \mathrm{Re}\left(\psi_{-1/2}\psi^*_{+1/2}\right), \tag{2.7a}$$
$$S^y = \mathrm{Im}\left(\psi_{-1/2}\psi^*_{+1/2}\right), \tag{2.7b}$$
$$S^z = \frac{1}{2}\left(|\psi_{+1/2}|^2 - |\psi_{-1/2}|^2\right). \tag{2.7c}$$

The two relevant trion states represent an effective two-level system that can be modeled by a pseudospin 1/2 denoted as $\boldsymbol{J}$. We also express its components by

quantum mechanical averages of the spin operators so that they are given by

$$J^x = \mathrm{Re}\left(\psi_{-3/2}\psi^*_{+3/2}\right), \tag{2.8a}$$
$$J^y = \mathrm{Im}\left(\psi_{-3/2}\psi^*_{+3/2}\right), \tag{2.8b}$$
$$J^z = \frac{1}{2}\left(|\psi_{+3/2}|^2 - |\psi_{-3/2}|^2\right). \tag{2.8c}$$

In the following, it is assumed that there is no optical coherence between the ground and trion states before the arrival of the pulse. Mathematically, this assumption is expressed by the replacement of the products of the form $\psi^*_{\pm 3/2}(-\infty)\psi_{\pm 1/2}(-\infty)$ with zeros. In this case, it follows from Eqs. (2.5) that the spin components (subscript 'b', $t = -\infty$) and after (subscript 'a', $t = +\infty$) the pulse are related by

$$S^x_\mathrm{a} = Q\cos(\Phi)S^x_\mathrm{b} + \mathcal{P}Q\sin(\Phi)S^y_\mathrm{b}, \tag{2.9a}$$
$$S^y_\mathrm{a} = Q\cos(\Phi)S^y_\mathrm{b} - \mathcal{P}Q\sin(\Phi)S^x_\mathrm{b}, \tag{2.9b}$$
$$S^z_\mathrm{a} = -\mathcal{P}\frac{1-Q^2}{4}\left(n^\mathrm{G}_\mathrm{b} - n^\mathrm{T}_\mathrm{b}\right) + \frac{1+Q^2}{2}S^z_\mathrm{b} + \frac{1-Q^2}{2}J^z_\mathrm{b}, \tag{2.9c}$$

for the electron spin, and similarly for the trion pseudospin by

$$J^x_\mathrm{a} = Q\cos(\Phi)J^x_\mathrm{b} - \mathcal{P}Q\sin(\Phi)J^y_\mathrm{b}, \tag{2.10a}$$
$$J^y_\mathrm{a} = Q\cos(\Phi)J^y_\mathrm{b} + \mathcal{P}Q\sin(\Phi)J^x_\mathrm{b}, \tag{2.10b}$$
$$J^z_\mathrm{a} = \mathcal{P}\frac{1-Q^2}{4}\left(n^\mathrm{G}_\mathrm{b} - n^\mathrm{T}_\mathrm{b}\right) + \frac{Q^2+1}{2}J^z_\mathrm{b} + \frac{1-Q^2}{2}S^z_\mathrm{b}. \tag{2.10c}$$

These relations depend on the occupation numbers of the ground and trion state, which are obviously also affected by the pulse. Their values before and after the pulse are related by

$$n^\mathrm{G}_\mathrm{a} = \frac{1+Q^2}{2}n^\mathrm{G}_\mathrm{b} + \frac{1-Q^2}{2}n^\mathrm{T}_\mathrm{b} - \mathcal{P}\left(1-Q^2\right)\left(S^z_\mathrm{b} - J^z_\mathrm{b}\right), \tag{2.11a}$$
$$n^\mathrm{T}_\mathrm{a} = \frac{1+Q^2}{2}n^\mathrm{T}_\mathrm{b} + \frac{1-Q^2}{2}n^\mathrm{G}_\mathrm{b} + \mathcal{P}\left(1-Q^2\right)\left(S^z_\mathrm{b} - J^z_\mathrm{b}\right). \tag{2.11b}$$

Here, $0 \leq Q^2 \leq 1$ describes the probability for the pulse *not* to excite a trion, i.e., Q is a measure for the spin initialization efficiency. The occupation numbers before the pulse determine how many trions are excited and thus, the degree of the induced spin polarization. The most efficient case is obtained for $Q = 0$: The

transverse components are erased, whereas a finite spin polarization is induced along the z axis, i.e., after the pulse the electron spin is completely oriented along this axis. The phase $-\pi \leq \Phi \leq \pi$ describes a spin rotation induced by detuned pulses. Qualitatively, it can be understood as an effective magnetic field pointing along the direction of light propagation that acts on the spins during the presence of the pulse. This dynamic Zeeman effect results from the optical Stark effect in the field of the circularly polarized light, which induces a splitting of the spin states with z projections $\pm 1/2$, similar to a real longitudinal magnetic field [115, 118]. Note that the phase Φ only plays a role for $Q \neq 0$. For completeness, we recall that the helicity of the circularly polarized light is represented by $\mathcal{P} = \pm 1$.

The pulse parameters Q and Φ depend on the pulse shape and the detuning of the photon energy from the trion transition. The application to ensembles of QDs in which the transition energy is inhomogeneously broadened is discussed in Chap. 9. In this case, the pulses are inevitably detuned. In terms of applications, pulses with a controlled detuning can be used, e.g., to implement spin rotations for coherent spin control [20, 29–32, 41, 119, 120].

The recombination dynamics of the occupancy numbers after the pulse can be described by the simple exponential law

$$n^{\mathrm{G}}(t) = n_{\mathrm{a}}^{\mathrm{G}} + n_{\mathrm{a}}^{\mathrm{T}} \left[1 - \exp\left(-\frac{t}{\tau_0}\right)\right], \tag{2.12a}$$

$$n^{\mathrm{T}}(t) = n_{\mathrm{a}}^{\mathrm{T}} \exp\left(-\frac{t}{\tau_0}\right), \tag{2.12b}$$

with τ_0 being the aforementioned trion recombination time. This description ensures the particle conservation $n^{\mathrm{G}}(t) + n^{\mathrm{T}}(t) = n_{\mathrm{a}}^{\mathrm{G}} + n_{\mathrm{a}}^{\mathrm{T}} = 1$ for all times t. The exponential recombination dynamics described by Eq. (2.12) can be derived using a Lindblad approach [121] incorporating a photonic bath into which the transition energy dissipates during the radiative recombination [122, 123].

Typical initial conditions are $\boldsymbol{S}_{\mathrm{b}} = 0$, $\boldsymbol{J}_{\mathrm{b}} = 0$, $n_{\mathrm{b}}^{\mathrm{G}} = 1$, and $n_{\mathrm{b}}^{\mathrm{T}} = 0$. They represent a system that is in a disordered ground state, which is the experimental situation with temperatures of $\sim 4 - 6\,\mathrm{K}$ [24, 25, 117] considering the relevant interactions in a QD (discussed in Sec. 3.1).

Note that even though Eqs. (2.9), (2.10), and (2.11) are derived using pure spin states, they are also valid for mixed states as long as the pulse duration is much

shorter than the electron and hole spin precession in a magnetic field and also much shorter than their spin relaxation times [113]. Furthermore, there may be no optical coherence between the ground and trion states before the arrival of the pulse, i.e., it must decay much faster than the pulse repetition time T_R. If the assumptions are not fulfilled, the density matrix formalism must be employed. But for the experiments that are analyzed in this thesis, the formalism described here is sufficient.

For illustration purposes, it is instructive to discuss the most efficient case with $Q = 0$ starting from these initial conditions. Application of a single pulse yields $S_\mathrm{a}^z = -\mathcal{P}/4$ and $J_\mathrm{a}^z = \mathcal{P}/4$ (all other components are zero since $Q = 0$), i.e., the spin z projections of the ground and excited states have opposite signs. On the occupancy level, we simply have $n_\mathrm{a}^\mathrm{G} = n_\mathrm{a}^\mathrm{T} = 1/2$. The physical interpretation is that for an disordered ground state, only half of the states can be promoted to the excited state by a pulse of a given helicity, in accordance with the optical selection rules.

The pulse relations derived in Ref. [113] are easily retained by inserting $n_\mathrm{b}^\mathrm{G} = 1$, $n_\mathrm{b}^\mathrm{T} = 0$, and $\boldsymbol{J}_\mathrm{b} = 0$. This simplification would be valid for $\tau_0 \ll T_\mathrm{R}$, e.g., for the commonly used pulse repetition time $T_\mathrm{R} = 13.2\,\mathrm{ns}$ [23–25, 93, 117]. In this case, the pulse relations reduce to [113–115]

$$S_\mathrm{a}^z = -\mathcal{P}\frac{1-Q^2}{4} + \frac{1+Q^2}{2} S_\mathrm{b}^z\,, \tag{2.13a}$$

$$S_\mathrm{a}^x = Q\cos(\Phi) S_\mathrm{b}^x + \mathcal{P}Q\sin(\Phi) S_\mathrm{b}^y\,, \tag{2.13b}$$

$$S_\mathrm{a}^y = Q\cos(\Phi) S_\mathrm{b}^y - \mathcal{P}Q\sin(\Phi) S_\mathrm{b}^x\,, \tag{2.13c}$$

$$J_\mathrm{a}^z = S_\mathrm{b}^z - S_\mathrm{a}^z\,, \tag{2.13d}$$

$$J_\mathrm{a}^x = J_\mathrm{a}^y = 0\,, \tag{2.13e}$$

which is slightly easier to interpret. It is worth to mention that these relations can be also derived by starting from the density matrix and then calculating the expectation values of the spin operators; see Ref. [123] for details.

In the case of resonant pulses ($\omega_\mathrm{pu} = \omega_\mathrm{T}$), the relations can be simplified even further and one obtains $\Phi = 0$ and $Q = \cos(\Theta/2)$, i.e., no in-plane rotation of the

spin components takes place. Here, Θ is an effective pulse area defined as [113]

$$\Theta := 2\int_{-\infty}^{\infty} f(t)\,\mathrm{d}t\,, \tag{2.14}$$

with $f(t)$ being the smooth envelope of the electromagnetic pulse, which can have, e.g., a Gaussian, hyperbolic secant, or a rectangular shape. The spin polarization induced by a single pulse depends periodically on the pulse area Θ, which is typical for two-level systems as a consequence of the Rabi effect [113]. If the pulses are strong enough, they can not only excite the system from the ground to the excited state but also de-excite the excited state back to the ground state. Pulses with $\Theta = (k+1)\pi$, $k \in \mathbb{N}$, are most efficient in inducing a spin polarization along the z axis. Indeed, measurements on ensembles of QDs show a periodic dependence of the induced spin polarization on the pulse area [23].

Up to this point, we have not discussed the spin dynamics taking place after application of the pulse. Let us assume for the moment that there is no interaction between the spins in the QD. In this hypothetical case, the time evolution of the average spin polarization would be solely determined by the radiative recombination of the trion, i.e., it simply decays into the ground state. As a result of the optical selection rules [112, 114, 124], the corresponding dynamics is simply described by

$$\frac{\mathrm{d}}{\mathrm{d}t}\boldsymbol{S} = \frac{J^z}{\tau_0}\boldsymbol{e}_z\,, \tag{2.15a}$$

$$\frac{\mathrm{d}}{\mathrm{d}t}\boldsymbol{J} = -\frac{\boldsymbol{J}}{\tau_0}\,, \tag{2.15b}$$

where only the z projection of the trion pseudospin contributes to the spin polarization of the ground state during the recombination. This follows from the optical selection rules for the optical transitions between the bands Γ_6 and Γ_8 in GaAs-based semiconductors [114, 124]. Thus, since we consider no further interactions for now, only the z projections of the spins play a role. Their solution is analogous to Eq. (2.12) and has the form

$$S^z(t) = S^z_\mathrm{a} + J^z_\mathrm{a}\left[1 - \exp\left(-\frac{t}{\tau_0}\right)\right], \tag{2.16a}$$

$$J^z(t) = J^z_\mathrm{a}\exp\left(-\frac{t}{\tau_0}\right), \tag{2.16b}$$

where $\boldsymbol{e}_z$ is the unit vector along the z axis. Clearly, in the limit $t \to \infty$ we have $S^z(t \to \infty) = S^z_\mathrm{a} + J^z_\mathrm{a}$ and $J^z(t \to \infty) = 0$, i.e., the long-time spin polarization of the ground state depends on the initial polarization induced by the pulse. Assuming the aforementioned disordered initial state and applying Eqs. (2.9c) and (2.10c), we simply have $S^z_\mathrm{a} = -\mathcal{P}(1-Q^2)/4$ and $J^z_\mathrm{a} = \mathcal{P}(1-Q^2)/4$ and thus, no polarization persists because $S^z(t \to \infty) = 0$ follows.

This consideration illustrates that further spin dynamics must take place such that a part of the induced spin polarization in the ground state persists for times $t \gg \tau_0$. An easy way to achieve this is the application of a transverse magnetic field [112] as will be discussed in Chap. 6. Internal interactions of the spins in the QD also lead to an imperfect recombination, but typically to a much smaller degree [93, 125, 126]. The resulting mechanisms are very important in the context of the spin inertia and polarization recovery effects, which are discussed in Sec. 2.4 and Chap. 8.

2.3 Time-resolved pump-probe spectroscopy

Time-resolved pump-probe spectroscopy is a powerful experimental tool to investigate the dynamics of charge carrier spins in semiconductor nanostructures [77, 127, 128]. As discussed in Sec. 2.2, spin polarization in QDs can be induced by circularly polarized laser pulses. Such pulses are referred to as pump pulses. In addition, with a time delay Δt ranging from pico- up to microseconds in modern setups [129], so-called probe pulses are applied. They are linearly polarized and have a small power not to disturb the system. The delay can be tuned with a mechanical delay line. In the experiments of interest, the pulses with a typical duration of the order of picoseconds are applied periodically with repetition time T_R; common values are $T_\mathrm{R} = 13.2\,\mathrm{ns}$ [23–25, 93, 117] or $T_\mathrm{R} = 1\,\mathrm{ns}$ [76, 94, 130]. To reduce the signal-to-noise ratio, the measurements are integrated in time, i.e., averaged over repeated measurements.

Figure 2.3 shows a graphical illustration of the pump-probe technique. As a consequence of the spin Faraday effect, the polarization plane of the probe pulse transmitted through the semiconductor nanostructure (e.g., an ensemble of QDs) is rotated by a certain angle [113–115]. The rotation of the probe polarization plane is referred to as Faraday rotation; its measurement yields a signal proportional to the projection of the spin polarization on the direction of light propagation (typically

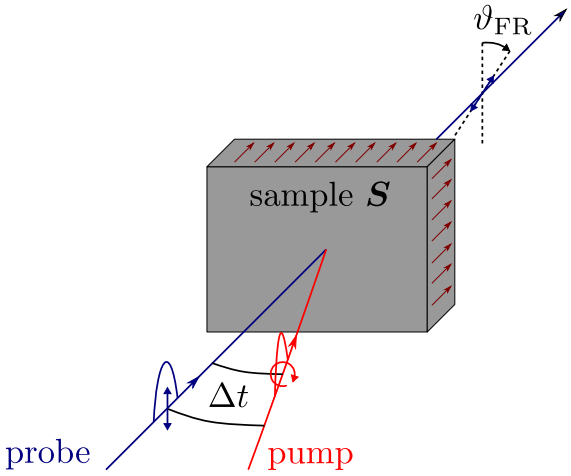

Figure 2.3: Illustration of the pump-probe technique: The circularly polarized pump pulse induces a spin polarization $\boldsymbol{S}$ in the sample. The linearly polarized probe pulse is applied to the sample with time delay Δt. After transmitting through the sample, the polarization plane of the probe pulse is rotated by the Faraday rotation angle ϑ_{FR}, yielding the projection of the spin polarization on the direction of light propagation. Figure inspired by Ref. [131].

the z projection) at a certain point in time $t = \Delta t$. Variation of the time delay Δt gives access to the time evolution of the spin polarization. A similar accessible quantity also yielding a signal proportional to the spin polarization is the Faraday ellipticity [113–115]. In experiments where the reflected instead of the transmitted probe beam is studied, the Kerr rotation is measured. The pump and probe light can be degenerate or detuned in photon energy, allowing for probing the spin dynamics of different subsets of an inhomogeneous sample. The signal is integrated in time to obtain an adequate signal-to-noise ratio, i.e., long trains of the pump-probe protocol need to be applied.

Exemplary Faraday rotation traces measured by Greilich *et al.* [23] for an n-doped InGaAs QD ensemble are shown in Fig. 2.4(a). In this experiment, an external magnetic field is applied parallel to the axis of the pump pulse incidence (Voigt geometry). The traces reveal periodic oscillations of the spin polarization representing the Larmor precession about the external magnetic field with a decaying amplitude caused by dephasing. At small time delays, additional beats are visible stemming from the heavy hole in the trion with a radiative lifetime of about 400 ps or from electrons of neutral QD excitons.[3] Furthermore, Greilich *et al.* analyzed the measured traces by fitting a function $\propto \exp(-t/T_2^*)\cos(\Omega t)$. The extracted Larmor frequencies Ω are plotted in Fig. 2.4(b) as a function of the magnetic field; its linear dependency gives access to the transverse g factor of the electrons [Fig. 2.4(d)]. It is

[3]The transverse heavy-hole g factor was later measured to be much smaller than the value extracted from the beats [132]. Hence, the beats are most likely related to the spin precession of excitons excited in neutral QDs.

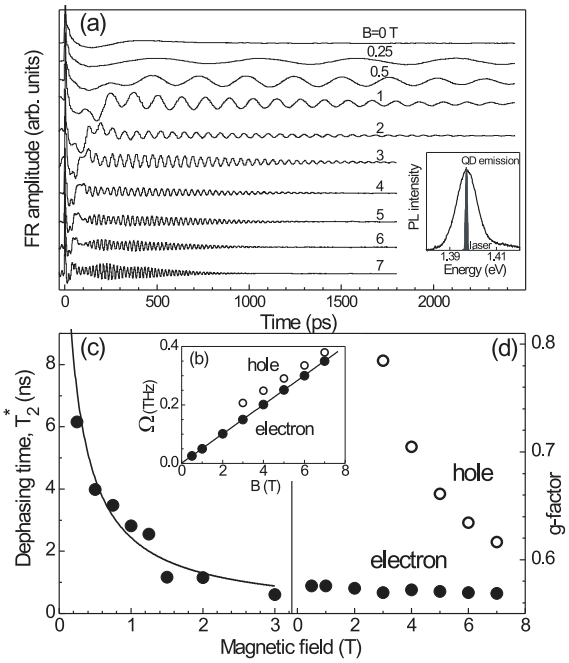

Figure 2.4: (a) Faraday rotation traces measured for an n-doped InGaAs QD ensemble in Voigt geometry for various strengths of the external magnetic field B. The inset shows the photoluminescence (PL) spectrum of the QD sample along with the spectrum of the laser. **(b)** Extracted Larmor frequencies Ω showing a linear dependence on the magnetic field. **(c)** Dephasing time T_2^* and **(d)** transverse g factor as a function of the magnetic field. Reprinted with permission from Ref. [23], ©2006 American Physical Society.

also evident from Fig. 2.4(a) that the spin polarization vanishes significantly faster for larger magnetic fields. Figure 2.4(c) shows the extracted values of $T_2^* \propto B^{-1}$, representing dephasing times that mainly result from the inhomogeneous character of the QD ensemble with slightly varying electronic g factor from QD to QD. The two main mechanisms responsible for spin dephasing in QDs are discussed in Sec. 3.3.4.

2.4 Spin phenomena in singly-charged quantum dots

Various spin phenomena can be studied in singly-charged QDs by means of the pump-probe spectroscopy. The effects particularly important for this thesis are spin mode locking in combination with nuclei-induced frequency, polarization recovery, and the spin inertia effect. In the following, these phenomena are briefly introduced while showcasing recent experimental results. Open questions with respect to these results are pointed out.

2.4.1 Spin mode locking and nuclei-induced frequency focusing

First, let us discuss two interrelated effects that can occur when a strong transverse magnetic field (Voigt geometry) is applied to singly-charged QDs while exciting them periodically by circularly polarized laser pulses to induce a spin polarization via the excitation of trion states. Typically, the pulses are applied with a repetition time of $T_\mathrm{R} = 13.2\,\mathrm{ns}$ and the pulse protocol has a duration of up to minutes. The experiments that we intend to describe were performed on n-doped InGaAs QD ensembles [24, 25, 117]. There are also other experiments performed on p-doped samples [95, 133, 134], but we do not focus on them here. As mentioned in Sec. 2.3, a spin polarization induced in this way quickly dephases on the timescale of nanoseconds as can be seen in Fig. 2.4(a) [23], so the polarization probed immediately before the next pump pulse is expected to be zero. The *spin mode locking* (SML) effect describes the phenomenon that there can be a revival signal before the arrival of the next pump pulse [24]. Representative Faraday ellipticity traces showing this behavior can be seen in Fig. 2.5(a) [117]. The phenomenon is related to the optical selection rules governing the trion excitation in conjunction with the Larmor precession of the localized electron spins. Combined, a selection of precession modes with a distance $\propto T_\mathrm{R}^{-1}$ favoring commensurable dynamics between two pulses takes place [24, 135]. The consequence is the appearance of a revival signal with its maximum at the next pulse incidence thanks to constructive interference. The amplitude of the revival depends on many factors as will be discussed below and it can be much larger than in the examples shown in Fig. 2.5(a); see, e.g., Refs. [23, 25, 95].

Another effect related to the synchronization of precession modes is resonant spin amplification (RSA) [77, 133, 135–137], which describes the resonant buildup of the spin polarization if certain conditions are met. It can also occur as a consequence of the periodic application of pump pulses in the presence of a transverse magnetic field, similarly to SML. We do not discuss its details at this point; a brief discussion can be found in Sec. 8.3.5. But it is worth to know that the two effects, SML and RSA, occur in different regimes determined by the repetition time of the pump pulses and the dephasing time of the spin polarization. Qualitatively speaking, the SML effect can take place if the spin polarization dephases before the next pump pulse arrives, whereas RSA occurs if there is a finite spin polarization at the incidence of the pump. The different regimes are discussed in detail in Refs. [133, 135]. In Part II of the thesis where nonequilibrium spin phenomena in the presence

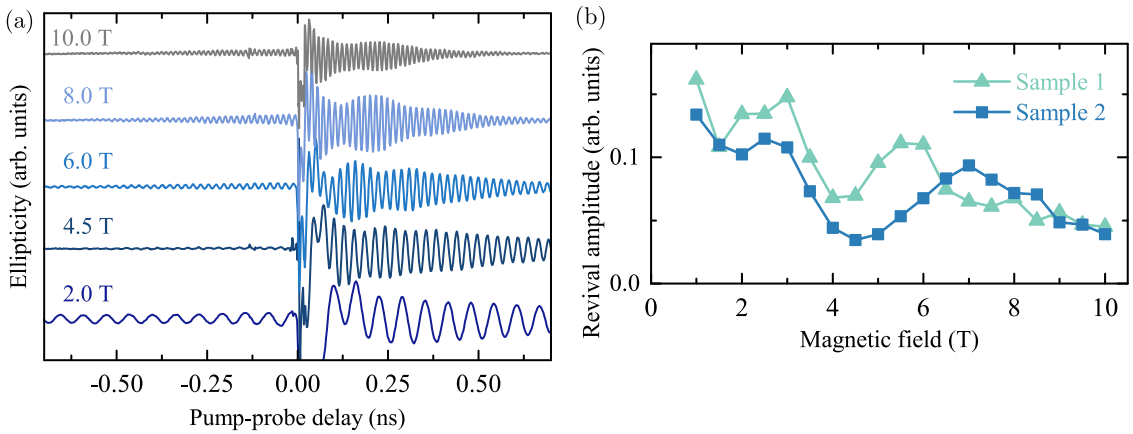

Figure 2.5: (a) Faraday ellipticity traces showing spin mode locking in combination with nuclei-induced frequency focusing for various strengths of the applied transverse magnetic field. **(b)** Extracted revival amplitudes as a function of the magnetic field for two different samples of *n*-doped InGaAs QDs. The lines are a guidance to the eye. The experiments were performed at a temperature of 4.7 K. The dependence of the revival amplitude on the magnetic field is strongly nonmonotonic. Both figures are reprinted with permission from Ref. [117], ©2018 American Physical Society.

of a transverse magnetic field are studied, only the SML regime is considered.

Another effect known as *nuclei-induced frequency focusing* (NIFF) can change the SML behavior significantly. The hyperfine interaction of the localized electron spins with the surrounding bath of nuclear spins in the QD is the dominant interaction as will be discussed in Sec. 3.1. Hence, an electron spin not only sees the external magnetic field but also an effective magnetic field because of its interaction with the nuclei. This effective magnetic field is known as the *Overhauser field*. Then, in a classical picture, their Larmor precession takes place about the superposition of both fields. Fascinatingly, the periodic application of pump pulses can induce a selection of certain polarizations in the Overhauser field that favor commensurable dynamics [25]. This effect is referred to as *nuclear focusing* and it is the origin of NIFF. It is enabled by the hyperfine interaction between the electron and the nuclear spin bath. The electron spins with a precession frequency being a multiple of the laser repetition rate are not (or barely) affected by the pump pulses due to the optical selection rules and hence, neither the nuclei see an abrupt change in their dynamics. But in QDs with unsynchronized electron spin dynamics, the nuclei are indirectly affected by the pulse as a consequence of the hyperfine interaction. This electron-nuclear spin system evolves in time until a nonequilibrium steady

state (NESS) favoring commensurable dynamics is reached.

Exploiting nuclear focusing by applying tailored pulse protocols can result in a single-mode spin precession of a huge number of electron spins in the QD ensemble [75, 76]. This particular asset allows one to overcome dephasing constraints induced by the varying electronic g factor from QD to QD and by the hyperfine interaction with the nuclei. A huge benefit in this context is the macroscopic lifetime of the nuclear polarization of seconds up to several hours [25, 42, 67–69]. Further control of the selected nuclear polarizations can be achieved by applying a second pump beam [25], which may also have a different repetition time [76].

Nuclear focusing is a nonequilibrium phenomenon and its interplay with SML is highly nontrivial. In essence, the interaction of the electron spins with the nuclei needs to be taken into account and the spin initialization process also needs to be described appropriately. The tremendous task of a thorough theoretical description becomes evident considering that the train of pulses is applied for up to minutes in the experiments [25] and the shortest timescale of the spin dynamics is the electronic Larmor period of $\sim 10\,\mathrm{ps}$ in a magnetic field of 10 T. Therefore, up to 13 orders of magnitude in time need to be treated theoretically. Several experimental and theoretical studies have been conducted since the pioneering experiments of Greilich *et al.* [24, 25]. Theoretical approaches range from quantum mechanical [25, 117, 138–143] to (semi)classical [122, 131, 135, 139, 144, 145]. Quantum mechanical approaches are limited to small numbers of nuclear spins because of the exponentially growing Hilbert space, must employ certain approximations, or resort to a perturbative treatment. The numerous experimental investigations [24, 26, 76, 95, 98, 117, 120, 122, 130, 133, 134, 146–150] highlight the complexity of the phenomenon. There are also interesting studies in which electron spins are driven by continuous-wave laser excitation to lock nuclear spins into certain polarizations [151–155], but we consider only the pulsed laser excitation in this thesis.

One of the main open questions addressed in this thesis is the magnetic field dependence of the revival amplitude resulting from the interplay of SML and NIFF, for which experiments reveal a complex nonmonotonic dependence [95, 117, 122], e.g., the dependence shown in Fig. 2.5(b) [117]. Throughout Chaps. 5–7, a sophisticated model is developed to investigate the interplay of SML and NIFF and to understand

the magnetic field dependence better. We will see that nuclear magnetic resonances with respect to the laser repetition rate play an important role in this context.

2.4.2 Polarization recovery

The application of a magnetic field to the QDs along the direction of the pump pulse incidence (Faraday geometry) leads to a stabilization of the spin polarization along the magnetic field, which would otherwise be destroyed by the hyperfine interaction of the charge carrier spin with the nuclei on the timescale of nanoseconds. Effectively, the spin lifetime increases. This effect is referred to as *polarization recovery* [98, 125, 126]. In the simplest isotropic model, the spin polarization without application of a magnetic field is three times smaller than for large fields [88, 104, 115]. This simple case is discussed in Sec. 3.3.

The corresponding polarization recovery curve (PRC), i.e., the dependence of the spin polarization on the strength of the longitudinal magnetic field, is usually symmetric around zero field. The typical shape the PRC is V-like [88], e.g., like the one shown in the top-left panel of Fig. 2.6 [93]. However, it was demonstrated by Zhukov *et al.* [93] in a pump-probe experiment that the PRC can also be M-like for p-doped InGaAs QDs (top-right panel).

The different shapes are related to the different spin initialization processes in n- and p-doped QDs. Generally, the spin orientation mechanism described in Sec. 2.2 is valid for both types. But if there was no further interaction after the trion excitation, the trion would simply decay into the ground state so that no spin polarization persists. Applying a strong transverse magnetic field is probably the most efficient strategy for spin initialization because the fast Larmor precession during the trion recombination leads to a sizable spin polarization in the ground state afterwards [112]. This mechanism does not work in the case of a longitudinal field because a spin pointing along a magnetic field does not precess. But other interactions also lead to a finite spin generation rate [93, 125]. Typically, the spin polarization induced in this way is rather small because it strongly depends on the balance between the radiative trion recombination and the nonradiative trion decay.

For n-doped QDs where negatively-charged trions are excited, the nonradiative trion decay is mostly unrelated to the hyperfine interaction because this interaction is generally weak for heavy holes (discussed in Sec. 3.1) [19, 93, 97, 115, 156–158].

In this case, the spin generation rate barely depends on the magnetic field. For p-doped QDs, however, the trion consists of two heavy holes in a spin singlet together with an unpaired electron spin. Since the hyperfine interaction for electrons is much stronger than for heavy holes, it yields an important but magnetic field dependent contribution to the spin generation. The magnetic field dependence is related to the same mechanism that leads to the increase of the spin lifetime of the charge carriers for larger fields: the electron spin and the nuclear spins decouple. Hence, the spin generation rate decreases in p-doped samples for larger fields.

The different mechanisms for n- and p-doped QDs are visualized in Fig. 2.7 [93]. The black curve visualizes the increase of the spin lifetime of the ground state caused by the application of the longitudinal magnetic field. In both cases, this dependence is

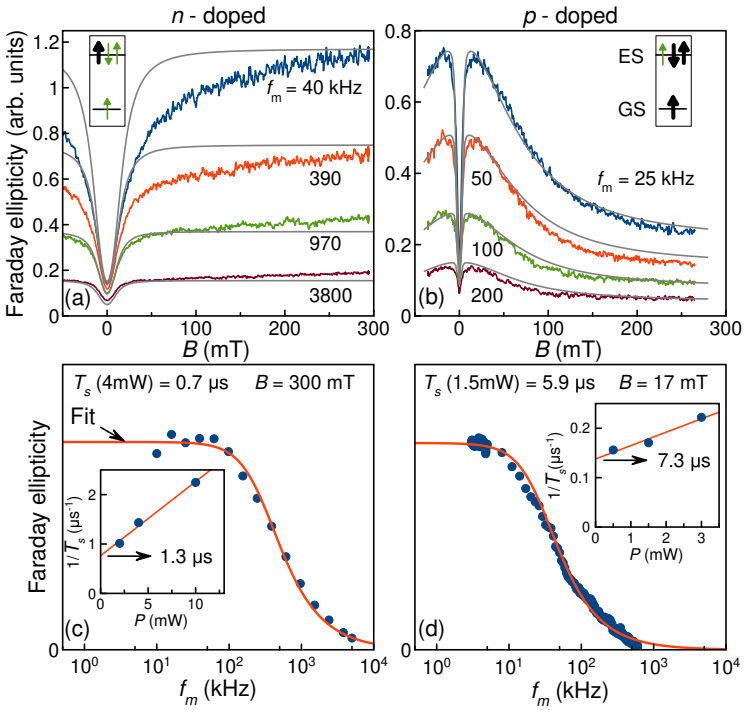

Figure 2.6: Upper row: Polarization recovery curves measured for (a) n-doped and (b) p-doped InGaAs QDs. The gray solid lines represent model calculations. In the pump-probe experiments, the helicity of the pump pulses is modulated with frequency f_m between σ^+ and σ^-. Bottom row: Spin inertia measurements giving access to the effective spin relaxation times of the resident charge carriers in the (c) n-doped and (d) p-doped QDs. The insets show a linear extrapolation to zero pump power to extract the intrinsic spin relaxation time. Reprinted with permission from Ref. [93], ©2018 American Physical Society.

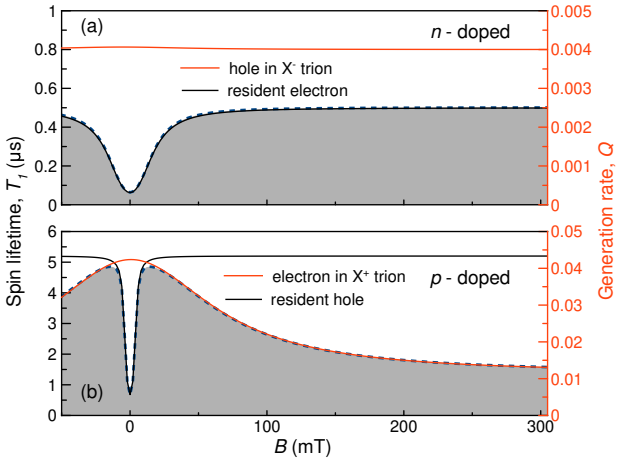

Figure 2.7: Schematic dependence of the spin lifetime (black) and spin generation rate (orange) on the magnetic field for (a) *n*-doped and (b) *p*-doped QDs. The resulting spin polarization (dashed blue) is essentially proportional to the product of spin lifetime and generation rate. Reprinted with permission from Ref. [93], ©2018 American Physical Society.

V-like. The spin generation rate (orange) follows the dependence described above for the respective doping. The resulting spin polarization is essentially proportional to the product of spin lifetime and generation rate, which is displayed by the dashed-blue curves (also highlighted by the gray-shaded area under this curve).

Measurements of PRCs can be used to determine a variety of parameters characterizing the spin dynamics in the QDs [93, 126]. Especially the combination with the spin inertia effect, which is introduced in the following section, is very powerful. We revisit this kind of experiment in Chap. 8 and extend the existing theory [125], which is valid in the limit of weak pump pulses, to account for an arbitrary pumping efficiency. For instance, the model calculations shown in the top-left panel of Fig. 2.6 for the *n*-doped case do not reproduce the width of the zero-field minimum of the PRCs well for small modulation frequencies [93]. Our theoretical framework is extended and put to use in Chap. 9. The improved understanding related to spin saturation effects, which turn out to influence the PRC shape, allows for an even better characterization of QD samples by means of polarization recovery measurements.

2.4.3 Spin inertia

Measuring long spin relaxation times of charge carriers in QDs is rather hard. A convenient method is the measurement of the so-called *spin inertia effect* [93, 125, 159]. In this kind of experiment, a longitudinal magnetic field is applied so that the measurement of the spin inertia gives access to the longitudinal spin relaxation time

(of the order of microseconds) of the resident charge carriers. The QDs are subjected to a long train of circularly polarized laser pulses with repetition time T_R, periodically exciting trion states to induce spin polarization. The central aspect is that the helicity of the pulses is modulated between σ^+ and σ^- with frequency f_m. This modulation scheme is illustrated in Fig. 2.8(a) [125]. The linearly polarized probe pulses share the same repetition time and are usually applied slightly (about 50 ps) before the arrival of the pump. The probed signal is modulated with the same frequency as the pump beam, otherwise the integrated signal would simply yield zero.

The spin inertia effect manifests itself in the dependence of the spin polarization on the modulation frequency. When this frequency is larger than the spin relaxation rate of the resident charge carriers, the spin polarization decreases; see the bottom row of Fig. 2.6 for exemplary measurements on n- and p-doped InGaAs QDs [93]. This behavior, which is visualized in Fig. 2.8(b) [125], led to terming this effect *spin inertia* because it can be understood as an inertia of the spin polarization that prevents it from following a switching of the pump helicity arbitrarily quickly. For instance, if the modulation frequency is larger than in Fig. 2.8(b), fewer pulses are applied before the helicity is inverted and hence, the spin polarization builds up

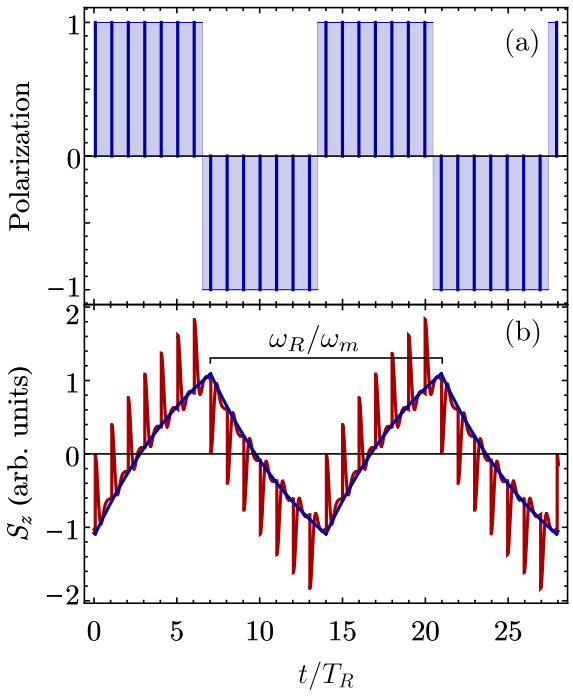

Figure 2.8: Behavior of typical spin dynamics without application of a magnetic field [panel (b)] as a consequence of switching the pump helicity (polarization) [panel (a)] with frequency $\omega_\mathrm{m} = 2\pi f_\mathrm{m}$. The vertical lines in (a) depict the arrival of the pump pulses applied with repetition rate $\omega_\mathrm{R} = 2\pi/T_\mathrm{R}$. The dark-blue line in (b) highlights the dependence of the spin polarization S^z if it is probed just before each pump pulse as in the experiments. Adapted with permission from Ref. [125], ©2018 American Physical Society.

less. Vice versa, if the modulation frequency is smaller, the spin polarization builds up more.

In Chap. 8, the influence of the pumping strength on the effective spin relaxation time is analyzed and it is shown that the extrapolation to zero pump power as in the insets of the bottom row of Fig. 2.6 [93] yields the intrinsic spin relaxation time of the resident charge carriers. In Chap. 9, the spin inertia effect is exploited to reduce the average degree of spin polarization, which turns out to be beneficial for the detection of a novel effect called resonant spin amplification in Faraday geometry, which is predicted in Chap. 8.

Chapter 3

Model for a localized spin in a quantum dot

The theoretical description of the spin phenomena introduced in Sec. 2.4 requires the calculation of the spin dynamics in singly-charged III-V semiconductor QDs. Here, we focus mainly on n-doped QDs with a single electron in the conduction band. The localization of charge carriers in QDs leads to several features which determine their spin dynamics. First, the spin-orbit interaction is suppressed, whereas the hyperfine interaction is enhanced and generally, long spin coherence and relaxation times of the order of nanoseconds are observed without application of an external magnetic field [18, 19]. Furthermore, there is the possibility to address spins of single charge carriers, e.g., by optical means as discussed in Sec. 2.2. On long timescales and especially under nonequilibrium conditions, e.g., because of the periodic application of pump pulses, the combined dynamics of electronic and nuclear spins becomes important [115]. This intertwined electron-nuclear spin system is the main subject studied in Part II of the thesis.

The reduced Planck constant $\hbar$ is set to unity in theoretical considerations henceforth. For convenience, $\hbar$ is included in the equations whenever the conversion to SI units is important, e.g., to connect with experiments.

3.1 Interactions in quantum dots

The spin-orbit interaction is responsible for several spin relaxation mechanisms in bulk semiconductors or quantum wells [108, 109]. In QDs, however, the confinement of the charge carriers leads to a strong suppression of these effects because of the

absence of translational motion [115, 160, 161]. Hence, spin relaxation mechanisms induced by the spin-orbit interaction play no role.

3.1.1 Hyperfine interaction

The strong localization of charge carriers in QDs has the consequence that the dominant interaction of an electron in an s-type conduction band is the hyperfine interaction with the nuclear spins of the host lattice [19, 104–106, 115, 162, 163]. The hyperfine interaction describes the coupling of a nuclear magnetic moment $\hat{\boldsymbol{\mu}}_\mathrm{n} = \gamma_\mathrm{n}\hat{\boldsymbol{I}}$ to the magnetic moment of an electron. Here, γ_n is the gyromagnetic ratio of the nucleus with spin $\hat{\boldsymbol{I}}$. Fermi [164] derived the hyperfine interaction between an electron and a nucleus from relativistic arguments. Similar derivations can be found, e.g., in Refs. [115, 165]. For an s-band electron, i.e., without any orbital contribution to its magnetic moment, only the Fermi-contact hyperfine interaction is relevant. It is described by the Hamiltonian [115, 164–167]

$$\hat{\mathcal{H}}_\mathrm{contact-hf} = -\frac{\mu_0}{4\pi}\frac{8\pi}{3}\gamma_\mathrm{s}\gamma_\mathrm{n}|\varphi(\boldsymbol{r})|^2\hat{\boldsymbol{S}}\cdot\hat{\boldsymbol{I}}\,, \tag{3.1}$$

where $\hat{\boldsymbol{S}}$ represents the electron spin with spin $S = 1/2$, $\varphi(\boldsymbol{r})$ is the electronic wave function at the position $\boldsymbol{r}$ of the nucleus with spin $\hat{\boldsymbol{I}}$, $\gamma_\mathrm{s} \approx -2\mu_\mathrm{B}\hbar^{-1}$ is the gyromagnetic ratio of a free electron, μ_B is the Bohr magneton, and μ_0 is the vacuum permeability. Importantly, the interaction strength of the contact hyperfine interaction is proportional to the probability density $|\varphi(\boldsymbol{r})|^2$ of the electron at the position of the nucleus. The Hamiltonian (3.1) induces a small shift in the nuclear magnetic resonance frequency, called the Knight shift [168]. This shift is induced by the interaction with the magnetic moment of the electron, which can be interpreted as an effective magnetic field (the Knight field) at the position of the nucleus.

For electrons in an s-type band, the probability density of the electron at the position of the nucleus is finite and hence, the Fermi-contact hyperfine interaction is nonzero. But for holes in a p-type band, the probability density is zero at the position of the nucleus so that there is no contribution from the Fermi-contact interaction. Instead, the hyperfine interaction of a nuclear spin with a hole is of

dipole nature. The relevant Hamiltonian is [115, 157, 165, 167]

$$\hat{\mathcal{H}}_{\mathrm{dd}} = -\frac{\mu_0}{4\pi}\gamma_{\mathrm{s}}\gamma_{\mathrm{n}}\hat{\boldsymbol{I}}\cdot\left(\frac{\hat{\boldsymbol{L}}}{r^3} - \frac{\hat{\boldsymbol{S}}}{r^3} + 3\frac{\hat{\boldsymbol{r}}(\hat{\boldsymbol{S}}\cdot\hat{\boldsymbol{r}})}{r^5}\right), \tag{3.2}$$

where $\hat{\boldsymbol{L}} = \hat{\boldsymbol{r}} \times \hat{\boldsymbol{p}}$ is the angular momentum operator of the charge carrier. The first term describes the orbital part of the interaction, which is important if the charge carrier is in a p-type band, and the last two terms represent the dipole-dipole interaction. But for electrons in an s-type band, the contribution from the Hamiltonian (3.2) to the hyperfine interaction is much weaker than the Fermi-contact term (3.1).

In the envelope function approximation, the electronic wave function in a nondegenerate ground-state orbital can be written as $\varphi(\boldsymbol{r}) = \sqrt{v_0}\Psi(\boldsymbol{r})u(\boldsymbol{r})$, where $u(\boldsymbol{r})$ is the lattice-periodic $\boldsymbol{k} = 0$ Bloch amplitude, $\Psi(\boldsymbol{r})$ is the slowly varying ground-state envelope function, and v_0 is the atomic volume. We normalize the Bloch amplitude over a unit cell Ω according to

$$\int_{\Omega} |u(\boldsymbol{r})|^2 \,\mathrm{d}\boldsymbol{r} = n_{\mathrm{a}}\,, \tag{3.3}$$

where n_{a} is the number of atoms in the unit cell ($n_{\mathrm{a}} = 2$ in III-V semiconductors with zinc blende crystal structure) [167]. This normalization is convenient because the resulting effective coupling constant is independent of n_{a}. We define this constant according to [167]

$$A \coloneqq A_{\mathrm{hf}} v_0 |\Psi(\boldsymbol{r}_{\mathrm{n}})|^2 \tag{3.4}$$

with

$$A_{\mathrm{hf}} \coloneqq -\frac{\mu_0}{4\pi}\frac{8\pi}{3}\gamma_{\mathrm{s}}\gamma_{\mathrm{n}}|u(\boldsymbol{r}_{\mathrm{n}})|^2 \tag{3.5}$$

and represent the Hamiltonian (3.1) as the simple Heisenberg-like interaction

$$\hat{\mathcal{H}}_{\mathrm{contact-hf}} = A\hat{\boldsymbol{S}}\cdot\hat{\boldsymbol{I}}\,. \tag{3.6}$$

Typically, A_{hf} is of the order of 100 μeV, while A depends on the localization volume of the electron and is of the order of $0.1 - 1\,\mu$eV [104, 107]. The values relevant in InGaAs QDs are given in Table 3.1.

Table 3.1: Nuclear spins I [169], gyromagnetic ratios γ_n [167], hyperfine coupling strengths A_hf [167], natural abundances (NA) [170], and relative abundances (RA) of the different isotopes in $\mathrm{In}_x\mathrm{Ga}_{1-x}\mathrm{As}$ QDs. The RA follows from the NA and the zinc blende crystal structure.

Isotope	I	γ_n ($\mathrm{rad\,s^{-1}\,T^{-1}}$)	A_hf (μeV)	NA	RA
^{69}Ga	3/2	6.43×10^7	74	0.601	$0.5 \times 0.601 \times (1-x)$
^{71}Ga	3/2	8.18×10^7	96	0.399	$0.5 \times 0.399 \times (1-x)$
^{75}As	3/2	4.60×10^7	86	1	0.5
^{113}In	9/2	5.88×10^7	110	0.043	$0.043 \times 0.5x$
^{115}In	9/2	5.90×10^7	110	0.957	$0.957 \times 0.5x$

3.1.2 Central spin model

Extending the Hamiltonian (3.6) to the situation in QDs where N nuclear spins interact with the electron spin gives rise to the so-called *central spin model* (CSM)

$$\hat{\mathcal{H}}_\mathrm{CSM} = \sum_{k=1}^{N} A_k \hat{\boldsymbol{S}} \cdot \hat{\boldsymbol{I}}_k \,. \tag{3.7}$$

Its star-like topology is illustrated in Fig. 3.1. The central electron spin sees the effective magnetic field

$$\hat{\boldsymbol{B}}_\mathrm{ov} \coloneqq \sum_{k=1}^{N} A_k \hat{\boldsymbol{I}}_k \,, \tag{3.8}$$

which is commonly referred to as the *Overhauser field* [171] and represents the sum of all nuclear spins $\hat{\boldsymbol{I}}_k$ weighted by their hyperfine coupling A_k. This model, first introduced by Gaudin as a case of an integrable model solvable by means of the Bethe ansatz [172–177], is the fundamental model applied in this thesis to study the spin dynamics of localized electrons in III-V semiconductor QDs.

An electron spin has the spin quantum number $S = 1/2$, while the spin of the nuclei depends on the isotope composition of the QD. Often, $I = 1/2$ is chosen in a quantum mechanical treatment for simplicity. For InGaAs QDs, the nuclear spin is $I = 3/2$ for Ga and As, and $I = 9/2$ for In (see Table 3.1).

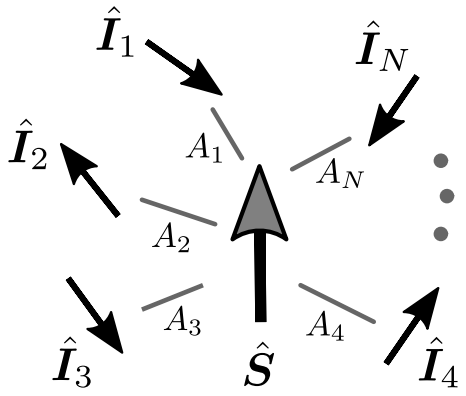

Figure 3.1: Illustration of the central spin model: The central spin $\hat{\boldsymbol{S}}$ couples to N bath spins $\hat{\boldsymbol{I}}_k$ with coupling constants A_k in a star-like topology.

As a consequence of the electronic envelope wave function, the strength of hyperfine interaction depends strongly on the distance between the electron spin and the nuclei so that the individual couplings A_k in a QD differ significantly. According to Eq. (3.4), A_k is proportional to the probability density of the electronic envelope wave function $\Psi(\boldsymbol{r}_k)$ at the position $\boldsymbol{r}_k$ of the nuclear spin $\hat{\boldsymbol{I}}_k$,

$$A_k = A_{\mathrm{hf}} v_0 |\Psi(\boldsymbol{r}_k)|^2 \,, \tag{3.9}$$

where v_0 is the atomic volume and A_{hf} is a material-dependent constant defined in Eq. (3.5). As discussed before, the electron is in an s-type conduction band, i.e., in its orbital ground state. Commonly, its envelope wave function is approximated to be isotropic and of the form [106, 178]

$$\Psi(\boldsymbol{r}_k) = \Psi(0) \exp\left[-\frac{1}{2}\left(\frac{r_k}{l_0}\right)^m\right] . \tag{3.10}$$

For $m = 2$, it is a Gaussian with characteristic radius l_0 as it follows if the electron is assumed to be trapped in a harmonic potential. For $m = 1$, the envelope wave function corresponds to a hydrogen-like s state with characteristic radius $2l_0$. We restrict ourselves to the Gaussian case with $m = 2$.

Next, we intend to parameterize the couplings A_k as a function of its index k and instead of the position $\boldsymbol{r}_k$. Note that the index k not only denotes the number of the nuclei at position $\boldsymbol{r}_k$ but also the total number of nuclei within the radius r_k if the nuclei are numbered such that $r_{k+1} > r_k$. For approximately two-dimensional (flat)

QDs, we can exploit the quadratic scaling $k \propto r_k^2$ in 2D.[1] Furthermore, it is clear from Eq. (3.10) that the interaction with many of the nuclei is exponentially weak, i.e., for a QD with N nuclear spins, not all of them contribute significantly to the Overhauser field. We define N_{eff} as the number of nuclear spins within the radius $\sqrt{2}l_0$, i.e., N_{eff} denotes the effective number of nuclear spins coupled to the electron spin.[2] Thus, we have $k = N_{\text{eff}}$ at $r_k = \sqrt{2}l_0$ and consequently, the relation

$$\left(\frac{r_k}{\sqrt{2}l_0}\right)^2 = \frac{k}{N_{\text{eff}}} \tag{3.11}$$

holds [178]. Inserting Eq. (3.11) into (3.10) to parameterize the couplings (3.9) yields

$$A_k = C \exp\left(-\frac{2k}{N_{\text{eff}}}\right) . \tag{3.12}$$

This parameterization is applied in major parts of the thesis. It is also considered in various other studies, e.g., in Refs. [123, 141, 142, 177–182]. Since the effective number of nuclei interacting with the electron spin in a QD ranges from 10^4 to 10^6 (smaller QDs correspond to smaller values of N_{eff} because of the stronger localization of the electron) [19, 103–107], it is not practical to treat the CSM (3.7) for a realistic bath size. Instead, it is convenient to normalize the couplings A_k with respect to the characteristic energy scale

$$A_{\text{Q}} \coloneqq \sqrt{\sum_{k=1}^{N} A_k^2} \tag{3.13}$$

given by the square root of the sum of squares of the couplings [104, 183]. In Sec. 3.3.4, we will see that the inverse of this energy scale defines the dephasing time of the electron spin caused by its interaction with the nuclear spin bath. Using this normalization, the number of effectively coupled nuclei N_{eff} can then be varied independent of A_{Q} (or of related quantities), which is beneficial to establish scaling arguments up to realistic bath sizes. Expressing the parameterization (3.12) in

[1] The scaling would be cubic in 3D and linear in 1D.

[2] Using the radius $\sqrt{2}l_0$ instead of l_0 as in Ref. [178] allows for an alternative definition of the number of effectively coupled nuclear spins via the ratio $N_{\text{eff}} \coloneqq (\sum_k A_k)^2 / \sum_k A_k^2$ in the limit $N \to \infty$, $N_{\text{eff}} \gg 1$. This definition is introduced in Sec. 4.1.

units of A_Q, we have

$$C = \sqrt{\frac{\exp(4/N_\mathrm{eff}) - 1}{1 - \exp(-4N/N_\mathrm{eff})}} A_\mathrm{Q} \,. \tag{3.14}$$

In the thermodynamic limit, i.e., in the limit of an infinite number of bath spins N, this expression reduces to

$$\lim_{N\to\infty} C = \sqrt{\exp\left(\frac{4}{N_\mathrm{eff}}\right) - 1} A_\mathrm{Q} \,. \tag{3.15}$$

If we further assume the situation $N_\mathrm{eff} \gg 1$, which is realistic in QDs, an expansion for large N_eff yields

$$C = \frac{2}{\sqrt{N_\mathrm{eff}}} A_\mathrm{Q} + \mathcal{O}\left(N_\mathrm{eff}^{-3/2}\right) \,. \tag{3.16}$$

This relation implies $A_k \propto A_\mathrm{Q}/\sqrt{N_\mathrm{eff}}$, i.e., the rate of change of the nuclear spins caused by the hyperfine interaction is slower by a factor $\mathcal{O}(1/\sqrt{N_\mathrm{eff}})$ compared to the characteristic energy scale A_Q describing the interaction of the electron spin with the Overhauser field. The physical interpretation is straightforward: a stronger localization of the electron in the QD implies that less nuclei are effectively coupled to the electron spin. Hence, the probability density of the electron at the site of a particular nucleus increases and in turn, also the individual interaction strength with this nucleus. For a QD with $N_\mathrm{eff} \approx 10^4 - 10^6$ effectively coupled nuclear spins, the individual couplings A_k are of the order of $0.1 - 1\,\mu$eV because of the scaling with $1/\sqrt{N_\mathrm{eff}}$ [104, 107]. Since A_Q^{-1} is of the order of nanoseconds, the nuclear spin dynamics takes place on a timescale of the order of 100 to 1000 ns [104]. Furthermore, since the individual couplings are so small, the typical scenario under experimental conditions with temperatures of $\sim 4\,$K is an initially disordered state represented by a density matrix $\hat{\rho} \propto \hat{\mathbb{1}}$, which corresponds to the infinite temperature limit.

3.1.3 Application of a magnetic field

In the experiments introduced in Sec. 2.4, an external magnetic field is applied to the QD either in a transverse or longitudinal configuration relative to the z axis

serving as quantization axis. Generally, the Zeeman effect for the electron spin is described by the Hamiltonian

$$\hat{\mathcal{H}}_{\mathrm{eZ}} = \gamma_{\mathrm{e}} B_{\mathrm{ext}} \boldsymbol{n}_B \cdot \hat{\boldsymbol{S}}, \tag{3.17}$$

where $\boldsymbol{n}_B$ represents the direction of the magnetic field, $\gamma_e = g_{\mathrm{e}}\mu_{\mathrm{B}}\hbar^{-1}$ denotes the electronic gyromagnetic ratio, and g_{e} is the electronic g factor in the QD (not the g factor of a free electron). A typical value for the electronic g factor in InGaAs QDs is $g_{\mathrm{e}} \approx -0.6$ and it only has a small anisotropy [23, 93, 132].

The Hamiltonian (3.17) is also valid for heavy holes, but their g factor is strongly anisotropic and can also depend on the in-plane orientation of the QD sample [96, 132]. For the transverse g factor, $|g_{\mathrm{h}}^{\perp}| = 0.05 - 0.15$ [96, 132] is a typical value. In contrast, the longitudinal g factor $g_{\mathrm{h}}^{\parallel} = -0.45$ [93, 132] has a value similar to the electronic g factor.

For the nuclear spins, the Zeeman Hamiltonian is analogously given by

$$\hat{\mathcal{H}}_{\mathrm{nZ}} = \sum_{k=1}^{N} \gamma_{\mathrm{n},k} B_{\mathrm{ext}} \boldsymbol{n}_B \cdot \hat{\boldsymbol{I}}_k \,. \tag{3.18}$$

Note that the gyromagnetic ratios $\gamma_{\mathrm{n},k}$ differ for the various isotopes in a QD, but generally, they are three orders of magnitude smaller than γ_{e} because of the larger nucleus mass relative to the electron mass [19, 167]. For this reason, it is often possible to neglect the nuclear Zeeman effect, but it can also play a crucial role when the long-time behavior is important as we will see in Part II.

An overview of relevant parameters (spin, gyromagnetic ratio, hyperfine coupling strength, relative abundance) for the different isotopes in $\mathrm{In}_x\mathrm{Ga}_{1-x}\mathrm{As}$ QDs is given in Table 3.1.

3.1.4 Anisotropic central spin model

The hyperfine interaction of a hole spin $\hat{\boldsymbol{J}}$ in a QD of is much weaker than for an electron spin because it is caused by the dipole-dipole interaction. The Fermi-contact term vanishes as a consequence of the p-type character of the valence band. Yet, the problem can be recast to an anisotropic CSM in which the anisotropy degree depends on the mixing of heavy and light hole states induced by the shape

and strain of the QD [156, 157]. The Hamiltonian of the anisotropic CSM has the form [156, 157, 184]

$$\hat{\mathcal{H}}_{\mathrm{CSM,anisotropic}} = \sum_{k=1}^{N} \widetilde{A}_k \left[\hat{J}^z \hat{I}_k^z + \frac{1}{\lambda} \left(\hat{J}^x \hat{I}_k^x + \hat{J}^y \hat{I}_k^y \right) \right] , \tag{3.19}$$

where λ describes the degree of anisotropy and $\lambda \to \infty$ for heavy holes and $\lambda = 1/2$ for light holes. Because of the aforementioned heavy-light hole mixing, a typical value for primarily heavy holes in InGaAs QDs is $\lambda \approx 5 - 10$ [93, 97]. The isotropic CSM (3.7) for localized electron spins is recovered for $\lambda = 1$. The coupling constants $\widetilde{A}_k$ are much smaller than the A_k appearing in the isotropic CSM. Because of the weaker interaction, the coherence time for hole spins is about one order of magnitude larger than for electron spins [19]. Calculations of the hyperfine interaction tensors for electrons and holes in GaAs and Si based on density functional theory combined with $\boldsymbol{k} \cdot \boldsymbol{p}$ theory are presented in Ref. [158].

Taking the anisotropic hyperfine interaction of hole spins into account is crucial for the description of the polarization recovery effect in p-doped QDs (Chap. 8); see also Sec. 2.4.2. In n-doped QDs, the anisotropic hyperfine interaction of the unpaired heavy-hole spin in negatively-charged trions T^- plays only a minor and often negligible role (Chaps. 6–9).

3.1.5 Further interactions

Since each nucleus with nonzero spin carries a magnetic moment, they also interact with each other via the dipole-dipole interaction. The Hamiltonian describing this interaction between two nuclear spins $\hat{\boldsymbol{I}}$ and $\hat{\boldsymbol{I}}'$ has the form [165]

$$\hat{\mathcal{H}}_{\mathrm{dd-nuclei}} = \frac{\mu_0}{4\pi} \gamma_{\mathrm{n}} \gamma_{\mathrm{n}'} \left(\frac{\hat{\boldsymbol{I}} \cdot \hat{\boldsymbol{I}}'}{r^3} - 3 \frac{\left(\hat{\boldsymbol{I}} \cdot \hat{\boldsymbol{r}} \right) \left(\hat{\boldsymbol{I}}' \cdot \hat{\boldsymbol{r}} \right)}{r^5} \right) , \tag{3.20}$$

where γ_{n} and $\gamma_{\mathrm{n}'}$ are the respective gyromagnetic ratios and $\boldsymbol{r}$ is the distance vector between the two nuclei. The dynamics induced by this interaction is usually negligible because it takes place on a timescale of the order of $100\,\mu$s [104]. The dipole-dipole interaction between the nuclear spins provides, however, a mechanism for nuclear spin diffusion and thermalization. Since the Hamiltonian (3.20)

does not conserve the total spin of the nuclei, it can cause slow nuclear spin relaxation [115].

The formation of self-assembled InGaAs QDs is caused by the partial relaxation of strain stemming from the different lattice constants of the InAs wetting layer and the GaAs barrier (see Sec. 2.1). The remaining strain in the formed QDs results in the formation of electric field gradients, giving rise to a quadrupolar interaction for nuclei with spin $I > 1/2$. This interaction is described by the Hamiltonian [115]

$$\hat{\mathcal{H}}_{\mathrm{q}} = \sum_{\alpha,\beta\in\{x,y,z\}} \frac{\partial^2 V}{\partial r^\alpha \partial r^\beta} \frac{|e|Q}{6I(2I-1)} \left[\frac{3}{2}\left(\hat{I}^\alpha \hat{I}^\beta + \hat{I}^\beta \hat{I}^\alpha\right) - I\,(I+1)\right], \tag{3.21}$$

where V is the potential of the electric field, e is the elementary charge, and Q is a constant describing the quadrupole moment. The quadrupolar interaction provides another relaxation mechanism for the electron spin on the timescale of about $1\,\mu$s [185]. We neglect this interaction despite dealing with nuclear spins with $I = 3/2$ (Ga, As) and $I = 9/2$ (In); its influence is the subject of other research [97, 143, 185–190].

3.2 Theoretical approaches to the central spin model

Numerous approaches have been developed to study the central spin model. This overview is not comprehensive, but it is supposed to highlight the difficulties of the theoretical treatment of this model. Already from a purely theoretical perspective, solving the CSM is an interesting task, but it is mainly studied in the context of decoherence of the central spin induced by the interaction with a spin bath. Although an analytic solution for this integrable model can be derived using the Bethe ansatz [172–177, 179], the dynamics in the CSM comprising a large spin bath still poses a challenging issue even today. The exact solution for an inhomogeneous parametrization of the hyperfine couplings can only be computed for fairly small systems of up to 48 bath spins since the exact eigenstates must be sampled, e.g., by Monte Carlo methods [177, 179, 180, 182].

A common approximation is the so-called *box model* in which all couplings A_k are chosen to be equal [104, 115, 122, 138–140, 163, 181, 191–195]. Essentially, the envelope wave function $\Psi(\boldsymbol{r}_k)$ in Eq. (3.9) is assumed to be a constant with a certain

cutoff radius. This approximation neglects, however, an additional decoherence mechanism stemming from the nonuniform distribution of the hyperfine couplings, but it is often sufficient to describe effects qualitatively while being much easier to handle. The approach can be improved in terms of a graded box model for which $\Psi(\boldsymbol{r}_k)$ is approximated by a sequence of step functions [196].

Many complementary theoretical techniques have been developed to analyze the CSM for large bath sizes and long times. Besides the already mentioned Bethe ansatz, exact diagonalization [106, 117, 189, 190, 197], Chebyshev expansion techniques [184, 198, 199], or a direct evolution of the density matrix via the Liouvillean using a perturbative treatment [141, 142] can be applied to study small systems of up to 20 bath spins. These approaches can treat the spin dynamics up to long times. Larger bath sizes up to about 1000 spins can be treated using the time-dependent density matrix renormalization group, but this method is restricted to intermediate times up to about $40A_{\mathrm{Q}}^{-1}$ [181–183, 200]. The limit of infinite times to study persisting correlations of the central spin can be addressed by mathematically rigorous lower bounds [180, 201]. Techniques based on rate equations or on non-Markovian master equations can be employed to access large bath sizes, but they require a sufficiently strong external field to be well justified [105, 138, 163, 178, 202–206]. This is also the case for approaches based on equations of motion [207, 208]. Cluster expansion techniques are another type of approaches, but they are restricted by the maximum cluster size, limiting the maximum time up to which the results are reliable [209–216].

In the limit of large spin baths, the CSM Hamiltonian (3.7) can be mapped to a four-dimensional impurity that couples to a noninteracting bosonic bath [182]. Remarkably, even in the limit of an infinite bath the CSM does not become completely classical. While this approach is promising, its practical application in the current form is limited because of extensive memory requirements [217], i.e., a better implementation or methodical improvements are called for.

Recently, a promising quantum mechanical method has been proposed by Lindoy and Manolopoulos [218]. They demonstrated that their method yields accurate results for large bath sizes up to $N = 999$ and long timescales up to $100A_{\mathrm{Q}}^{-1}$ by comparison with other established methods such as time-dependent density matrix renormalization group, Bethe ansatz, and also semiclassical approaches. The approach does not suffer from the statistical errors occurring when using a Monte

Carlo sampling for the exact eigenstates of the CSM obtained from the Bethe ansatz as in Refs. [177, 179]. Furthermore, there is no growth of a truncation error as in the approach based on time-dependent density matrix renormalization group applied in Refs. [181–183, 200]. The main idea is to construct a sequence of simpler Hamiltonians that converges to the original CSM Hamiltonian the more sub-Hamiltonians are included. In a way, this approach is similar to the graded box model used by Petrov *et al.* [196], but the required modification of the distribution of hyperfine couplings is performed in a more sophisticated way. The approach has been applied to study, e.g., radical pair recombination reactions, also demonstrating that semiclassical approaches [219, 220] to the CSM work remarkably well [221].

Treating the CSM in a semiclassical or classical manner is a commonly used and powerful approach to study its real-time dynamics. Various kinds of such approaches have been proposed and applied over the years. In one approach, the bath consisting of a large number of nuclei is replaced by an effective time-dependent field [104, 183, 200, 222, 223]. When the slow dynamics of the nuclear spins play no role, the Overhauser field may be approximated as frozen in time, which simplifies the theoretical treatment significantly (Sec. 3.3.4). Subsequently, random fluctuations of the bath resulting from its interaction with the central spin can be included [104]. When the spin bath is assumed to behave like a stochastic field, the fluctuations of the central spin can be studied by solving Bloch-Langevin equations [200, 224]. However, such an approach is insufficient to describe effects such as nuclear focusing or dynamic nuclear polarization [19, 42, 115, 225] because no backaction from the central spin on the bath spins is included [200]. Another drawback is that the bath fluctuations need to be known a priori. It was also argued that the saddle-point approximation of the spin-coherent path integral representation describes the dynamics of the central spin well because quantum fluctuations become less important if the number of bath spins is large [226]. Similarly, the spin-coherent states P representation of the density matrix combined with time-dependent mean-field theory essentially amounts to solving classical equations of motion, showing very good agreement with the exact quantum mechanical solutions [227, 228].

The comparison of data stemming from quantum mechanical approaches utilizing time-dependent density matrix renormalization group, Chebychev expansion, or Bethe ansatz with classical simulations that are ensemble-averaged over normal distributions also shows very good agreement [182, 200, 229]. Details on this semi-

classical approach introduced by Stanek *et al.* [200] are given in Sec. 3.3. It is supported by the analytical argument that according to the central limit theorem, the Overhauser field stemming from a very large number of fluctuating nuclear spins behaves like a classical variable [183, 200, 229]. Furthermore, the classical and quantum mechanical version of the CSM have the same conserved quantities [173, 200, 226].

The big advantage of (semi)classical approaches is that they can handle the large number of nuclear spins present in QDs while also allowing for calculating real-time dynamics up to very long times. These are exactly the requirements to study the effects SML and NIFF under experimental conditions where trains of periodic pulses are applied to the QDs for extremely long times. For this reason, we resort to the approach promoted by Stanek *et al.* [200], which is introduced in the following.

3.3 Semiclassical approach

Treating the Overhauser field in QDs as a classical variable is well justified because of the huge number of nuclear spins that are effectively coupled to the central spin [183, 200, 229]. But for the single central spin with $S = 1/2$, this argument does not hold because it is a quantum mechanical object whose backaction on the nuclear spins is not classical. In the following, we introduce the *truncated Wigner approximation* (TWA) [230] as the theoretical foundation of our semiclassical approach and apply it to the CSM. In this approximation, the central spin is not treated purely classically. Instead, quantum fluctuations enter through random initial conditions of the classical equations of motion to be solved.

3.3.1 Truncated Wigner approximation

The TWA is a semiclassical approach based on the Wigner-Weyl quantization of the phase space; see Ref. [230] for a review. A compact discussion of its application to spin systems can be found in Refs. [231, 232]. In this phase-space representation, the classical limit in which quantum fluctuations vanish and the structure of quantum corrections can be naturally recovered [230]. In our case, the classical limit corresponds to the classical spin limit where spins are treated as rotating three-dimensional vectors. In the framework of the TWA, classical equations of motion

must be solved with initial conditions sampled from appropriate probability distributions through which leading order quantum fluctuations enter. The equations of motion themselves are not affected, i.e., they are purely classical.

The Wigner-Weyl transform describes a mapping of the Hilbert space of a quantum mechanical system to its corresponding phase space. This mapping can be accomplished by introducing so-called phase-point operators $\hat{A}$ expressed in terms of the classical phase-space variables $\boldsymbol{p}$ and $\boldsymbol{q}$ via [230, 232–234]

$$\langle \boldsymbol{q}' | \hat{A}(\boldsymbol{p}, \boldsymbol{q}) | \boldsymbol{q}'' \rangle = \frac{1}{(2\pi)^D} \, \delta \left(\boldsymbol{q} - \frac{\boldsymbol{q}' + \boldsymbol{q}''}{2} \right) \mathrm{e}^{\mathrm{i}\boldsymbol{p}\cdot(\boldsymbol{q}' - \boldsymbol{q}'')} \,, \tag{3.22}$$

where D is the dimension of the phase space and $\delta(x)$ is the Dirac delta function. The phase-point operators defined in this way relate the quantum mechanical density matrix $\hat{\rho}$ to a quasiprobability distribution, which is known as the Wigner function [230, 232, 233, 235]

$$W(\boldsymbol{p}, \boldsymbol{q}) = \mathrm{Tr} \left[\hat{\rho} \, \hat{A}(\boldsymbol{p}, \boldsymbol{q}) \right] . \tag{3.23}$$

Generally, this quasiprobability distribution is normalized for any proper density matrix, but it can be nonpositive. The Wigner function is the so-called Weyl symbol of the density matrix. The Weyl symbol

$$\mathcal{O}_{\mathrm{W}}(\boldsymbol{p}, \boldsymbol{q}) = \mathrm{Tr} \left[\hat{O}(\boldsymbol{p}, \boldsymbol{q}) \, \hat{A}(\boldsymbol{p}, \boldsymbol{q}) \right] \tag{3.24}$$

maps any operator $\hat{O}(\boldsymbol{p}, \boldsymbol{q})$ to a function over the classical phase space. In this representation, the time evolution of its expectation value can be calculated according to [230, 232]

$$\langle \hat{O} \rangle(t) = \iint \mathcal{O}_{\mathrm{W}}(\boldsymbol{p}, \boldsymbol{q}) \, W(\boldsymbol{p}, \boldsymbol{q}, t) \, \mathrm{d}\boldsymbol{p} \, \mathrm{d}\boldsymbol{q} \,, \tag{3.25}$$

i.e., the Weyl symbol is averaged over the phase space weighted by the Wigner function. But typically, it is not possible to compute the time evolution exactly from this expression. A common approximation is the TWA. In this semiclassical approach, quantum fluctuations are accounted for in leading order [230]. In the following, we work in the Heisenberg picture where the Wigner function is fixed to its initial value $W(\boldsymbol{p}_0, \boldsymbol{q}_0)$. The Weyl symbol is time-dependent and follows a classical trajectory within the framework of the TWA. Concretely, the approximation

is given by [230, 232]

$$\langle \hat{O} \rangle(t) \approx \iint \mathcal{O}_{\mathrm{W}} \left(\boldsymbol{p}_{\mathrm{cl}}(t), \boldsymbol{q}_{\mathrm{cl}}(t) \right) W(\boldsymbol{p}_0, \boldsymbol{q}_0) \, \mathrm{d}\boldsymbol{p}_0 \, \mathrm{d}\boldsymbol{q}_0 \,, \tag{3.26}$$

where the time dependence of $\boldsymbol{p}_{\mathrm{cl}}(t)$ and $\boldsymbol{q}_{\mathrm{cl}}(t)$ is determined by Hamilton's equations starting from the initial conditions $\{\boldsymbol{p}_0, \boldsymbol{q}_0\}$.

The TWA can be generalized to spin systems [230, 231] by means of the spin-coherent state representation [236, 237]. In this representation, the spin operators are expressed as bosons using the Schwinger representation [238]. Spin operators satisfy the canonical commutation relations

$$\left[\hat{S}^{\alpha}, \hat{S}^{\beta} \right] = \mathrm{i} \sum_{\gamma} \varepsilon_{\alpha\beta\gamma} \hat{S}_{\gamma} \,, \tag{3.27}$$

$\alpha, \beta, \gamma \in \{x, y, z\}$, with the Levi-Civita symbol $\varepsilon_{\alpha\beta\gamma}$. The commutation relations are inherited when the spin operators are represented by two bosons according to [230, 231, 238]

$$\hat{S}^{\alpha} = \frac{1}{2} \sum_{i,j \in \{1,2\}} \hat{a}_i^{\dagger} \, \sigma_{ij}^{\alpha} \, \hat{a}_j \,, \tag{3.28}$$

where the σ^{α} are the Pauli matrices and $\hat{a}_i$, $\hat{a}_i^{\dagger}$ are the bosonic annihilation and creation operators. Any operator $\hat{O}$ that can be expressed as a function of the boson operators $\hat{a}$ and $\hat{a}^{\dagger}$ can be mapped to a function over the classical phase space of canonical variables $\boldsymbol{\alpha}$ and $\boldsymbol{\alpha}^*$, which are vectors of complex numbers. Analogous to Eq. (3.26), the TWA in this representation has the form [231]

$$\langle \hat{O} \rangle(t) \approx \iint \mathcal{O}_{\mathrm{W}} \left(\boldsymbol{\alpha}_{\mathrm{cl}}(t), \boldsymbol{\alpha}_{\mathrm{cl}}^*(t) \right) W(\boldsymbol{\alpha}_0, \boldsymbol{\alpha}_0^*) \, \mathrm{d}\boldsymbol{\alpha}_0 \, \mathrm{d}\boldsymbol{\alpha}_0^* \,. \tag{3.29}$$

Again, leading order quantum corrections appear only through the initial conditions determined by the Wigner function W, which is conserved along the classical trajectories of the Weyl symbol $\mathcal{O}_{\mathrm{W}}$. The trajectories follow from solving Hamilton's equations for the canonical variables [231],

$$\mathrm{i} \frac{\mathrm{d}}{\mathrm{d}t} \alpha_{\mathrm{cl},k} = \frac{\partial \mathcal{H}_{\mathrm{cl}}}{\partial \alpha_{\mathrm{cl},k}^*} \,, \tag{3.30}$$

where $\mathcal{H}_{\mathrm{cl}}$ is the classical Hamiltonian function. In fact, these equations are Gross-

Pitaevskii equations [230]. The factor i stems from using the coherent state Poisson brackets, which is the classical analogue of the commutator [230, 231]. Resorting to Eq. (3.28) to represent the spin operators by bosons, the classical equations of motion for the spin components result to be [231]

$$\frac{\mathrm{d}}{\mathrm{d}t} S_{\mathrm{cl}}^{\alpha} = \sum_{\beta,\gamma} \varepsilon_{\alpha\beta\gamma} \frac{\partial \mathcal{H}_{\mathrm{cl}}}{\partial S_{\mathrm{cl}}^{\beta}} S_{\mathrm{cl}}^{\gamma} \,. \tag{3.31}$$

The big advantage of this approximation is the linear scaling in the degrees of freedom in comparison to the exponentially increasing Hilbert space in the quantum mechanical treatment of systems consisting of N spins.

The dynamics stemming from the TWA is exact for an Hamiltonian bilinear in boson operators and hence, the TWA is also exact for systems linear in spin operators [230]. The expansion parameter for spin systems is $1/S$, i.e., the TWA works better for systems with large spin [230]. The classical limit in which quantum fluctuations vanish corresponds to $S \gg 1$.

Typically, the Wigner function describing the initial conditions is approximated by a Gaussian-like distribution whose variance resembles Heisenberg's uncertainty principle. This choice does not reduce the accuracy of the approximation because the difference between the exact Wigner function and the appropriately chosen normal distribution is of the same order in $1/S$ as the corrections to the dynamics stemming from the TWA (3.29) [231]. In fact, Davidson and Polkovnikov [231] found that this Gaussian TWA consistently yields better results than the TWA using the exact Wigner function. This has the advantage that normal distributions are much easier to handle because they are always positive. In contrast, the exact Wigner function can involve negative probabilities.

It is possible to generalize the TWA to any $SU(N)$ group of operators, leading to the appearance of hidden variables that represent local spin-spin correlations [231]. Other approaches resort to a discrete phase space [232, 239]. Including higher-order quantum corrections is also possible in terms of stochastic quantum jumps [230], but they are generally hard to handle.

3.3.2 Application to the central spin model

In the following, the Gaussian TWA is applied to the Hamiltonian relevant for the spin dynamics in QDs. We consider the classical Hamiltonian $\hat{\mathcal{H}}_{\mathrm{QD}} \to \mathcal{H}_{\mathrm{QD}}$ with

$$\hat{\mathcal{H}}_{\mathrm{QD}} \coloneqq \hat{\mathcal{H}}_{\mathrm{CSM}} + \hat{\mathcal{H}}_{\mathrm{eZ}} + \hat{\mathcal{H}}_{\mathrm{nZ}} \,. \tag{3.32}$$

The Hamiltonians $\hat{\mathcal{H}}_{\mathrm{CSM}}$, $\hat{\mathcal{H}}_{\mathrm{eZ}}$, and $\hat{\mathcal{H}}_{\mathrm{nZ}}$ are given by Eqs. (3.7), (3.17), and (3.18), respectively. The Hamiltonian $\hat{\mathcal{H}}_{\mathrm{QD}}$ the main model studied in this thesis and includes the hyperfine interaction of the central electron spin with the surrounding nuclear spins and also the Zeeman terms for both the electron and nuclear spins.

The equations of motion for the classical spins $\boldsymbol{S}$ and $\boldsymbol{I}_k$ within can be derived using Eq. (3.31). A straightforward calculation (see Appendix A) yields

$$\frac{\mathrm{d}}{\mathrm{d}t}\boldsymbol{S} = \left(\sum_{k=1}^{N} A_k \boldsymbol{I}_k + \gamma_{\mathrm{e}} B_{\mathrm{ext}} \boldsymbol{n}_B\right) \times \boldsymbol{S} \,, \tag{3.33a}$$

$$\frac{\mathrm{d}}{\mathrm{d}t}\boldsymbol{I}_k = (A_k \boldsymbol{S} + \gamma_{\mathrm{n},k} B_{\mathrm{ext}} \boldsymbol{n}_B\ ) \times \boldsymbol{I}_k \,, \qquad k \in \{1, 2, \ldots, N\} \,. \tag{3.33b}$$

These equations are essentially Bloch equations that describe precessions about time-dependent, effective magnetic fields. The time dependence results from the interrelated dynamics of the central spin $\boldsymbol{S}$ and the N bath spins $\boldsymbol{I}_k$. The same equations can be derived using time-dependent mean-field theory [240], but it does not naturally incorporate an ensemble average over a distribution of initial conditions for the classical trajectories as in the TWA. This ensemble average, however, is essential for the semiclassical approach to work appropriately [200].

As discussed earlier, the spin system is initially disordered under typical experimental conditions. Hence, we approximate the Wigner function W in Eq. (3.29) by a multivariate normal distribution with mean value zero. The quantum mechanical second moments of the spin operators are

$$\left\langle \hat{S}^{\alpha} \hat{S}^{\beta} \right\rangle = \frac{1}{4} \delta_{\alpha\beta} \,, \tag{3.34a}$$

$$\left\langle \hat{I}_j^{\alpha} \hat{I}_k^{\beta} \right\rangle = \frac{I_k(I_k+1)}{3} \delta_{\alpha\beta}\, \delta_{jk} \,, \tag{3.34b}$$

$$\left\langle \hat{S}^{\alpha} \hat{I}_k^{\beta} \right\rangle = 0 \,, \tag{3.34c}$$

$\alpha, \beta \in \{x, y, z\}$, for the central spin $\hat{\boldsymbol{S}}$ with spin $S = 1/2$ and the bath spins $\hat{\boldsymbol{I}}_k$ with spin I_k. They represent the second-order quantum fluctuations that we intend to approximate by normal distributions. To reproduce the second moments (3.34) in the semiclassical picture, we use the variances

$$\mathrm{Var}\left[S^\alpha\right] = \frac{1}{4} \tag{3.35}$$

for the components of the initial central spin and

$$\mathrm{Var}\left[I_k^\alpha\right] = \frac{I_k(I_k+1)}{3} \tag{3.36}$$

for the components of each bath spin. In practice, the integration over this distribution in Eq. (3.29) is approximated by a Monte-Carlo sampling over M configurations while the classical trajectories are obtained by solving the equations of motion (3.33) numerically. For instance, the time-evolution of the central spin $\boldsymbol{S}$ is calculated according to

$$\overline{\boldsymbol{S}(t)} = \frac{1}{M}\sum_{m=1}^{M} \boldsymbol{S}_m(t)\,, \tag{3.37}$$

where the overline is used to denote the ensemble average over the M classical trajectories $\boldsymbol{S}_m(t)$.

The semiclassical approach is compared with full quantum mechanical simulations utilizing time-dependent density matrix renormalization group, Chebychev expansion, and Bethe ansatz in Refs. [182, 200, 229]. The comparison shows very good agreement with and without application of a magnetic field and becomes even better for larger spin baths. A very similar approach is developed in Ref. [226] based on the path integral formalism. It is applied in Ref. [122] to simulate the spin dynamics in a QD subjected to periodic laser pulses and in Ref. [190] to calculate fourth-order spin correlation functions for an extended version of the CSM. In these works, the initial conditions of the spins are sampled from the Bloch sphere, which is a valid alternative provided the spin length is treated appropriately. Other related semiclassical approaches are applied in Refs. [219, 220] to study radical pair recombination reactions, also showing very good agreement with quantum mechanical calculations [221].

But why does the semiclassical treatment work so well for the CSM? First, the Over-

hauser field behaves like a classical variable in the limit of a large number of bath spins N as a consequence of the central limit theorem [183, 200, 229]. Second, the classical and the quantum mechanical version of the CSM share the same conserved quantities [173, 200, 226]. Nevertheless, the approximation is rather crude for the single central spin with $S = 1/2$, which is far from the classical limit, but yet, the approach works surprisingly well. In Chaps. 5 and 6, we will see that when studying the dynamics of the Overhauser field, it is extremely important that the initial conditions of the central spin are sampled from an appropriate distribution.

The required averaging over initial conditions has another advantage. Typically, it is difficult to distinguish the present semiclassical approach from the calculation of ensemble averages required to describe experiments on QDs. For instance, the ensemble average required to describe a homogeneous ensemble of QDs is identical to the average appearing in the semiclassical approach. Furthermore, it mimics the influence of quantum fluctuations of the Overhauser field in repeated measurements of the spin dynamics (required to improve the signal-to-noise ratio) for homogeneous ensembles and also for single QDs. Hence, these circumstances [104, 115] are automatically described by the semiclassical approach.

3.3.3 Numerical treatment and implementation

Solving the system of ordinary differential equations (ODE) given in Eq. (3.33) (or similar ODEs introduced later) is straightforward by applying standard Runge-Kutta methods. We use the Dormand-Prince method [241] as ODE solver, which is an adaptive fifth-order Runge-Kutta algorithm. Six function evaluations are used to calculate fourth- and fifth-order solutions; their difference is used to estimate the error for the adaptive stepsize control. A particular advantage of this method is the 'First Same as Last' principle: the method uses six function evaluations despite having seven steps. This is achieved by reusing the last stage for the subsequent integration step. An implementation is provided by ODEINT [242], which is part of the BOOST C++ library. Another implementation is provided in Ref. [243]. Both implementations are used for different parts of this thesis. The latter turned out to be a bit more efficient.

The random numbers required for the sampling of the initial conditions can be obtained from the Mersenne-Twister pseudo random number generator [244], which

is provided by the C++ standard library RANDOM. The library also provides convenient routines to directly sample from normal distributions.

The required ensemble average over M trajectories constitutes a big challenge if several orders of magnitude in time need to be simulated. But since the trajectories are independent, a parallelization of the code using MPI (Message Passing Interface) [245] is very powerful, scaling very well up to $M/2 - M$ CPU cores for $M = \mathcal{O}(10^4)$. The relative error following from the statistical nature of the approach scales like $1/\sqrt{M}$ [200, 229]. Depending on the desired accuracy of the results, the typical ensemble size ranges from $M \approx 10^4$ to 10^6.

In view of large scale simulations, special care needs to be taken to ensure that the vectorization capabilities of modern CPUs are utilized as much as possible using the available SIMD (single instruction, multiple data) instructions such as AVX, AVX2, or even AVX-512. To utilize these instructions efficiently, the system size needs to be large, but not too large with respect to the L1 cache of the CPU. The ODE system (3.33) has the dimension $3(N+1)$, where $N \gg 1$ is the number of bath spins. Later in Chaps. 6–9, we have to deal with similar ODE systems, but they are of the small dimension 6 or 9 so that in a naive implementation, the vectorization capabilities of the CPU are barely utilized. But since the calculation of an ensemble average is still required, one can group the numerous ODEs together and solve them simultaneously. This procedure enables the efficient vectorization of the code; the cache usage can be optimized by tuning the number of independent ODEs grouped together. More details on the performance of the simulations conducted for this thesis are given in Ref. [246].

Rotating frame

A particular obstacle is the treatment of the fast Larmor precession of the electron spin in strong external magnetic fields, which needs to be resolved numerically. This problem occurs especially when applying a strong transverse magnetic field with $B_{\text{ext}}\boldsymbol{n}_B = B_{\text{ext}}\boldsymbol{e}_x$, where $\boldsymbol{e}_x$ is the unit vector along the x axis. In this case, the runtime scales approximately linearly with B_{ext} for large magnetic fields. A more efficient way to treat this dynamics consists of switching to a rotated frame by applying the rotation ansatz $\boldsymbol{S}(t) = \underline{\underline{D}}(t)\boldsymbol{Z}(t)$ to Eq. (3.33a). The proper choice

for the rotation matrix is

$$\underline{\underline{D}}(t) = \begin{pmatrix} 1 & 0 & 0 \\ 0 & \cos(ht) & \sin(ht) \\ 0 & -\sin(ht) & \cos(ht) \end{pmatrix}, \tag{3.38}$$

which describes the Larmor precession with frequency $h = \gamma_\mathrm{e} B_\mathrm{ext}$. The slow dynamics induced by the interaction with the nuclear spins is included in $\boldsymbol{Z}(t)$. Inserting the ansatz into Eq. (3.33a) yields

$$\frac{\mathrm{d}}{\mathrm{d}t}\boldsymbol{S} = \left(\frac{\mathrm{d}}{\mathrm{d}t}\underline{\underline{D}}\right)\boldsymbol{Z} \times \boldsymbol{S} + \underline{\underline{D}}\frac{\mathrm{d}}{\mathrm{d}t}\boldsymbol{Z}\,, \tag{3.39}$$

with

$$\left(\frac{\mathrm{d}}{\mathrm{d}t}\underline{\underline{D}}\right)\boldsymbol{Z} = \boldsymbol{h} \times \boldsymbol{S} \tag{3.40}$$

and $\boldsymbol{h} = h\boldsymbol{e}_x$. Thus, the term describing the Larmor precession about the external magnetic field vanishes in the rotated frame and we have

$$\frac{\mathrm{d}}{\mathrm{d}t}\boldsymbol{Z} = \underline{\underline{D}}^{-1}\left(\boldsymbol{B}_\mathrm{ov} \times \boldsymbol{S}\right) = \left(\underline{\underline{D}}^{-1}\boldsymbol{B}_\mathrm{ov}\right) \times \boldsymbol{Z} \tag{3.41}$$

with

$$\underline{\underline{D}}^{-1}(t) = \begin{pmatrix} 1 & 0 & 0 \\ 0 & \cos(ht) & -\sin(ht) \\ 0 & \sin(ht) & \cos(ht) \end{pmatrix}. \tag{3.42}$$

The consequence is that no term linear in h appears in the ODE to be solved. Instead, the new prefactors $\cos(ht)$ and $\sin(ht)$ appear, which are $\mathcal{O}(1)$ instead of $\mathcal{O}(h)$. It is not a priori clear whether this approach is more efficient than the straightforward numerical integration of the ODE system (3.33a) because sine and cosine functions need to be evaluated. This is numerically much more expensive than calculating, e.g., a simple multiplication or addition of two variables. It turns out that for a typical ODE dimension of $\mathcal{O}(200)$, the rotating frame approach is about three times faster than the naive implementation for large magnetic fields. But oscillations with frequency h are also present in the nuclear spin bath because of its interaction with the central spin, and they still need to be resolved numerically.

Hence, the runtime still scales approximately linearly with the strength of the applied magnetic field.

A much more efficient but approximate approach is developed and applied in Chap. 7. There, the fast and slow degrees of freedom are treated separately for all dynamical variables. The terms governing the fast Larmor precession are treated analytically, while the terms governing the slow dynamics are expanded in the large magnetic field while neglecting corrections of the order $\mathcal{O}(h^{-2})$.

3.3.4 Frozen Overhauser field approximation

An instructive approximation valid for short times is the frozen Overhauser field approximation [104]. It is based on the observation that the dynamics of the bath spins resulting from the hyperfine interaction is slower by a factor of $1/\sqrt{N_{\text{eff}}}$ in comparison to the central spin dynamics in the random Overhauser field. The Larmor precession of the nuclear spins is also three orders of magnitude slower than for the electron spin, i.e., it can be neglected on short timescales. The approximation consists of simply neglecting any dynamics of the nuclear spins, i.e., the Overhauser field is assumed to be frozen in time so that only Eq. (3.33a) remains to be solved. Its general solution has the form [104, 115]

$$\begin{aligned}\boldsymbol{S}(t) = [\boldsymbol{S}(0)\cdot\boldsymbol{n}_{\text{eff}}]\,\boldsymbol{n}_{\text{eff}} + [\boldsymbol{S}(0) - (\boldsymbol{S}(0)\cdot\boldsymbol{n}_{\text{eff}})\,\boldsymbol{n}_{\text{eff}}]\cos(\Omega_{\text{eff}}t) \\ + \boldsymbol{S}(0)\times\boldsymbol{n}_{\text{eff}}\sin(\Omega_{\text{eff}}t)\,,\end{aligned} \tag{3.43}$$

where $\boldsymbol{n}_{\text{eff}} = (\boldsymbol{B}_{\text{ov}}+\gamma_{\text{e}}B_{\text{ext}}\boldsymbol{n}_B)/|\boldsymbol{B}_{\text{ov}}+\gamma_{\text{e}}B_{\text{ext}}\boldsymbol{n}_B|$ denotes the direction of the effective magnetic field $\boldsymbol{\Omega}_{\text{eff}} = \boldsymbol{B}_{\text{ov}} + \gamma_{\text{e}}B_{\text{ext}}\boldsymbol{n}_B$, which is the sum of the Overhauser field and the external magnetic field.

Zero magnetic field

First, we consider the case without external magnetic field, i.e., $B_{\text{ext}} = 0$, and apply the Gaussian TWA (3.29) where the Wigner function is approximated by the

isotropic multivariate normal distribution[3]

$$p(\boldsymbol{B}_{\mathrm{ov}}) = \frac{1}{\left(\sqrt{\pi}\omega_{\mathrm{n}}\right)^3} \exp\left(-\frac{\boldsymbol{B}_{\mathrm{ov}}^2}{\omega_{\mathrm{n}}^2}\right) . \tag{3.44}$$

Its variance in all spatial directions $\alpha \in \{x, y, z\}$ is given by

$$\mathrm{Var}\left[B_{\mathrm{ov}}^{\alpha}\right] := \frac{\omega_{\mathrm{n}}^2}{2} = \sum_{k=1}^{N} A_k^2 \,\mathrm{Var}\left[I_k^{\alpha}\right] = \frac{I(I+1)}{3} A_{\mathrm{Q}}^2 \,. \tag{3.45}$$

Here, we assume that all bath spins have the same spin I. The frequency ω_{n} is the characteristic frequency of the central spin precession about the Overhauser field. Since we identify the bath spins as the nuclear spins in QDs, we choose the label 'n'. The average over a probability distribution for initial conditions of the central spin is neglected and instead, a deterministic initial condition $\boldsymbol{S}(0)$ is considered.[4] Finally, the integration of Eq. (3.43) weighted by the distribution (3.44) yields [104, 115, 183]

$$\overline{\boldsymbol{S}(t)} = \int \boldsymbol{S}(t, \boldsymbol{B}_{\mathrm{ov}})\, p(\boldsymbol{B}_{\mathrm{ov}})\, \mathrm{d}\boldsymbol{B}_{\mathrm{ov}} \tag{3.46a}$$

$$= \frac{\boldsymbol{S}(0)}{3}\left[1 + \left(2 - t^2\omega_{\mathrm{n}}^2\right) \exp\left(-\frac{t^2\omega_{\mathrm{n}}^2}{4}\right)\right] . \tag{3.46b}$$

The overline is used to denote the ensemble average, which replaces the quantum-mechanical average $\langle \hat{\boldsymbol{S}}(t) \rangle$. The dependence is plotted in Fig. 3.2 for the case where the central spin is initially polarized in z direction. The polarization first decreases significantly to almost zero and increases again afterwards to a constant value. The decay is solely determined by the low-energy scale $\omega_{\mathrm{n}} \propto A_{\mathrm{Q}}$. Clearly, the long-time limit is $\overline{\boldsymbol{S}(t \to \infty)} = \boldsymbol{S}(0)/3$, i.e., one third of the initial central spin polarization remains. The influence of the nuclear spin dynamics, which induces a slow long-time decay on the timescale $\mathcal{O}(\omega_{\mathrm{n}}^{-1}/\sqrt{N_{\mathrm{eff}}})$, is analyzed in detail in Chap 4.

[3] In Chaps. 8 and 9, the Overhauser field is denoted as $\boldsymbol{\Omega}_{\mathrm{n}}$ (instead of $\boldsymbol{B}_{\mathrm{ov}}$) to be consistent with the related literature.

[4] The average over a distribution of initial conditions for the central spin becomes important when taking the nuclear spin dynamics into account.

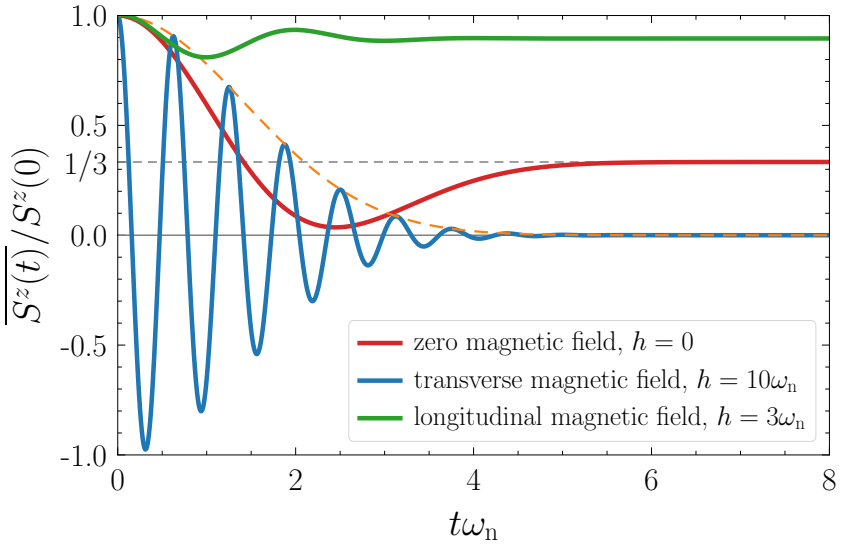

Figure 3.2: Central spin dynamics in the frozen Overhauser field approximation: Without magnetic field [red, Eq. (3.46b)], the spin polarization initially decays to almost zero and then increases to a plateau at 1/3 of the initial polarization. Applying a strong transverse magnetic field $h \gg \omega_\mathrm{n}$ [blue, Eq. (3.49)] leads to a complete dephasing of the initial spin polarization (orange-dashed envelope) while oscillating with frequency h. In contrast, applying a longitudinal magnetic field [green, Eq. (3.47)] stabilizes the spin polarization and dampens the amplitude of the oscillations. In all three examples, the initial spin polarization is chosen to point along the z axis, i.e., $\boldsymbol{S}(0) = S^z(0)\boldsymbol{e}_z$.

Longitudinal magnetic field

We now turn to the case of a longitudinal magnetic field with $B_\mathrm{ext}\boldsymbol{n}_B = B_\mathrm{ext}\boldsymbol{e}_z$ and $\boldsymbol{S}(0) = S^z(0)\boldsymbol{e}_z$. The averaging procedure is the same, but the solution is more complicated [115, 185],

$$\overline{S^z(t)} = S^z(0)\left(1 - \frac{\omega_\mathrm{n}^2}{h^2}\left[1 - \cos(ht)\exp\left(-\frac{t^2\omega_\mathrm{n}^2}{4}\right)\right] + \frac{\omega_\mathrm{n}^3}{h^3}D\left(\frac{h}{\omega_\mathrm{n}}\right) - \frac{\sqrt{\pi}\omega_\mathrm{n}}{2h}\exp\left(-\frac{h^2}{\omega_\mathrm{n}^2}\right)\mathrm{Re}\left\{\mathrm{erfi}\left[\omega_\mathrm{n}\left(\frac{1}{h} - \mathrm{i}\frac{t}{2}\right)\right]\right\}\right), \tag{3.47}$$

with the Dawson function $D(x) = \exp(-x^2)\int_0^x \exp(y^2)\,\mathrm{d}y$, the imaginary error function $\mathrm{erfi}(x) = (2/\sqrt{\pi})\exp(x^2)D(x)$, and $h = \gamma_\mathrm{e}B_\mathrm{ext}$. The time evolution is plotted in Fig. (3.2) for $h = 3\omega_\mathrm{n}$, showing a periodic but dampened oscillation because of the precession about the effective magnetic field, which is the sum of the Overhauser field and the external magnetic field. Compared to the case without

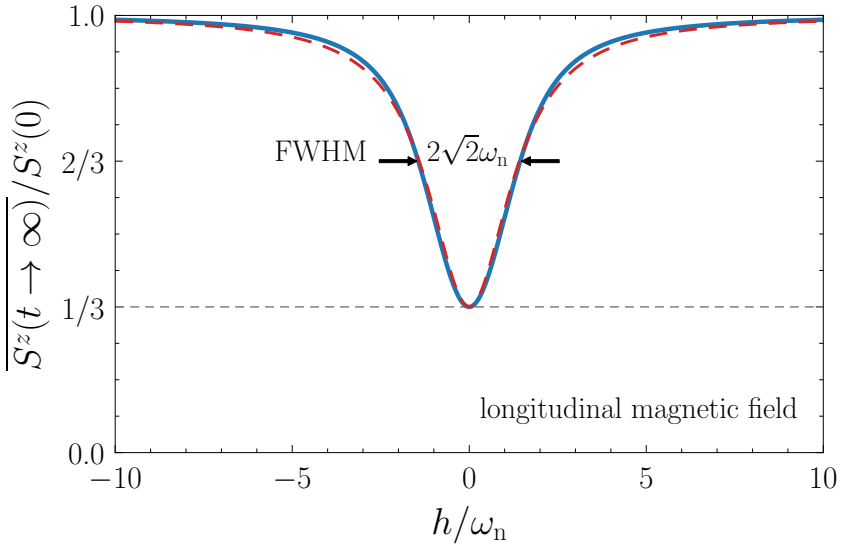

Figure 3.3: Dependence of the long-time spin polarization on the longitudinal magnetic field h, calculated using Eq. (3.48a) (blue, solid) and Eq. (3.48b) (red, dashed). The full width at half maximum (FWHM) given by $2\sqrt{2}\omega_\mathrm{n}$ is indicated. The initial spin polarization is chosen to point along the z axis, i.e., $\boldsymbol{S}(0) = S^z(0)\boldsymbol{e}_z$.

magnetic field, the nondecaying fraction of the spin polarization increases. In the long-time limit $t \gg \omega_\mathrm{n}^{-1}$, it follows for the nondecaying fraction [88, 115]

$$\frac{\overline{S^z(t\to\infty)}}{S^z(0)} = 1 - \frac{\omega_\mathrm{n}^2}{h^2} + \frac{\omega_\mathrm{n}^3}{h^3}\, D(h/\omega_\mathrm{n}) \tag{3.48a}$$

$$\approx 1 - \frac{2}{3}\frac{1}{1+h^2/(2\omega_\mathrm{n}^2)}\,. \tag{3.48b}$$

This dependence, which is shown in Fig. 3.3, describes the suppression of the nuclei-induced spin relaxation, resulting from the application of the longitudinal magnetic field h. The central spin polarization is stabilized along the direction of this field. The full width at half maximum (FWHM) of the Lorentzian dip is $2\sqrt{2}\omega_\mathrm{n}$ [88]. The dependence represents the V-like shape of polarization recovery curves characteristic for n-doped QDs (see Sec. 2.4.2). More general forms appearing in pump-probe experiments are studied in Chaps. 8 and 9.[5]

[5] In Chaps. 8 and 9, the Larmor frequency is denoted as Ω_L (instead of h) to be in line with the related literature.

Transverse magnetic field

In contrast to a longitudinal magnetic field, the application of a transverse field $B_{\mathrm{ext}}\boldsymbol{n}_B \perp \boldsymbol{S}(0)$ results in a dephasing of the central spin caused, which is caused by its interaction with the random Overhauser field. We again assume that the initial spin polarization $\boldsymbol{S}(0) = S^z(0)\boldsymbol{e}_z$ points along the z axis. For strong magnetic fields with $h \gg \omega_{\mathrm{n}}$, the time evolution of the central spin is described by [104, 115, 183]

$$\overline{S^z(t)} = S^z(0)\cos(ht)\exp\left[-\left(\frac{t}{T_{\mathrm{n}}^*}\right)^2\right]. \tag{3.49}$$

The z component of the spin polarization oscillates with the Larmor frequency h while dephasing takes place on the timescale[6]

$$T_{\mathrm{n}}^* := \frac{2}{\omega_{\mathrm{n}}} = \sqrt{\frac{6}{I(I+1)}}A_{\mathrm{Q}}^{-1} \tag{3.50}$$

because of the interaction with the random Overhauser field. The decay is Gaussian and for $t \gg T_{\mathrm{n}}^*$, no average spin polarization remains. The time evolution described by Eq. (3.49) is visualized in Fig. 3.2 for $h = 10\omega_{\mathrm{n}}$. In QDs, this dephasing time is of the order of nanoseconds, depending on the number of effectively coupled nuclear spins [19, 104].

So far, we considered only the dephasing caused by the random Overhauser field. In ensembles of self-assembled QDs in which the randomly grown QDs differ slightly, there is an additional inhomogeneity that needs to be considered. The electronic g factor g_{e} differs slightly from QD to QD [23, 24]. This g factor spread is responsible for an additional dephasing mechanism and can be modeled by the Gaussian distribution

$$p(g_{\mathrm{e}}) = \frac{1}{\sqrt{2\pi}\Delta g_{\mathrm{e}}}\exp\left[-\frac{1}{2}\left(\frac{g_{\mathrm{e}} - \overline{g_{\mathrm{e}}}}{\Delta g_{\mathrm{e}}}\right)^2\right] \tag{3.51}$$

with variance $(\Delta g_{\mathrm{e}})^2$ and mean value $\overline{g_{\mathrm{e}}}$. To calculate the influence of the g factor spread on the spin dynamics, Eq. (3.49) weighted by its distribution must be integrated over the electronic g factor. The result is the simple replacement $T_{\mathrm{n}}^* \to T_2^*$

[6] Depending on the context, the energy and time is normalized to either ω_{n}, A_{Q}, or T_{n}^*. The conversion between these quantities is given by Eq. (3.50).

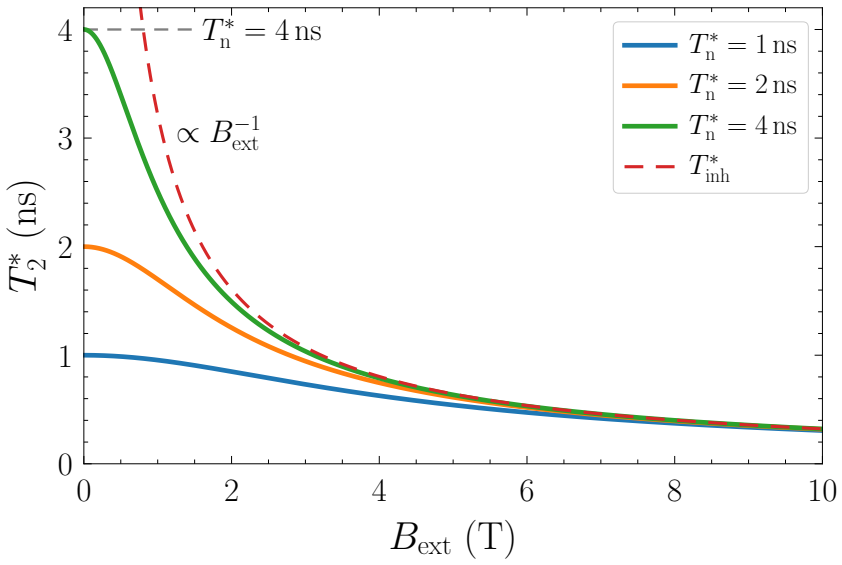

Figure 3.4: Dependence of the total dephasing time T_2^* on the magnetic field strength B_{ext} calculated from Eq. (3.52b) for various typical dephasing times T_{n}^* stemming from the interaction with the random nuclear spin bath. The red dashed curve depicts the B_{ext}^{-1} following from Eq. (3.53). Parameters: $g_{\mathrm{e}} = 0.555$, $\Delta g_{\mathrm{e}} = 0.005$.

in Eq. (3.49), where the total dephasing time T_2^* is given by

$$(T_2^*)^{-2} := (T_{\mathrm{n}}^*)^{-2} + (T_{\mathrm{inh}}^*)^{-2} \tag{3.52a}$$

$$\Rightarrow T_2^* = \frac{T_{\mathrm{n}}^* T_{\mathrm{inh}}^*}{\sqrt{(T_{\mathrm{n}}^*)^2 + (T_{\mathrm{inh}}^*)^2}}\,. \tag{3.52b}$$

The inhomogeneous dephasing time

$$T_{\mathrm{inh}}^* := \frac{\sqrt{2}}{\Delta g_{\mathrm{e}} \mu_{\mathrm{B}} \hbar^{-1} B_{\mathrm{ext}}}\,, \tag{3.53}$$

results from the spread Δg_{e} of the electronic g factor and is magnetic field dependent. The consequence is a B_{ext}^{-1} dependence of the dephasing time T_2^* in QD ensembles for large magnetic fields as observed in experiments; see Fig. 2.4(c) [23, 24]. The dependence $T_2^*(B_{\mathrm{ext}})$ given by Eq. (3.52b) is visualized in Fig. 3.4 for various typical values of T_{n}^* (of the order of nanoseconds) using $\overline{g_{\mathrm{e}}} = 0.555$ [25] and $\Delta g_{\mathrm{e}} = 0.005$ [24, 123]. For $B_{\mathrm{ext}} \to 0$, the total dephasing time T_2^* is limited by T_{n}^*, while for large B_{ext}, T_2^* is approximately equal to T_{inh}. Slight deviations from this dependence found in pump-probe experiments performed on inhomogeneous

ensembles of QDs can be explained [123] by taking into account the linear dependence of the electronic g factor on the trion transition energy, which also follows a distribution [24, 113].

Chapter 4

Efficient algorithms for large and infinite semiclassical central spin models

Even the semiclassical approach to the central spin model introduced in the previous chapter represents a tremendous computational challenge when considering the $10^4 - 10^6$ effectively coupled nuclear spins in a QD [19, 103–107] up to the extremely long times relevant in experiments. In this chapter, efficient algorithms are established that enable us to meet this challenge successfully. With the help of these algorithms, timescales can be explored that previously were inaccessible for very large bath sizes. In this way, we establish that the long-time behavior of the system is governed by a low-energy scale different from the energy scale A_Q. This low-energy scale is proportional to square root of the inverse number of effectively coupled bath spins, i.e., proportional to $A_\mathrm{Q}/\sqrt{N_\mathrm{eff}}$.

The chapter is set up as follows.[1] First, the model to be analyzed is specified in Sec. 4.1. In Sec. 4.2, three approaches to its semiclassical simulation are introduced of which two work very well. The results are shown and compared in Sec. 4.3. A particular focus lies on the long-time behavior and its scaling with the number of effectively coupled bath spins. Finally, conclusions are drawn in Sec. 4.4.

[1] This chapter is based on the author's publication [247], ©2017 American Physical Society, which originated from J. Hüdepohl's master's thesis [248] supervised by G. S. Uhrig and B. Fauseweh. The author's contribution was an improvement of the Spectral Density approach over its original version [248], its application to different parametrizations of the hyperfine couplings, its convergence analysis, a study of the long-time spin dynamics, creation of all figures including the calculation of all data, and partial writing of the manuscript.

4.1 Semiclassical central spin model

We consider the classical version of the CSM (3.7),

$$\mathcal{H}_{\mathrm{CSM}} = \sum_{k=1}^{N} A_k \boldsymbol{S} \cdot \boldsymbol{I}_k \,, \tag{4.1}$$

in which a central spin $\boldsymbol{S}$ (spin 1/2) is coupled to N bath spins $\boldsymbol{I}_k$ with coupling constants A_k. The classical spins $\boldsymbol{S}$ and $\boldsymbol{I}_k$ are represented as three-dimensional vectors. The sum of all bath spins weighted by their couplings forms the Overhauser field

$$\boldsymbol{B}_{\mathrm{ov}} = \sum_{k=1}^{N} A_k \boldsymbol{I}_k \,. \tag{4.2}$$

We will see that the classical treatment only requires very limited information about the bath spins as their spin I essentially determines the length of the corresponding classical vector. For simplicity, we choose $I = 1/2$ for all bath spins in the calculations.

In a QD singly-charged by an electron, the coupling constants are determined by the Fermi-contact hyperfine interaction strength, which is proportional to the probability density of the electron at the position of a nuclear spin. For a Gaussian wave function in two dimensions, the result is an exponential parametrization of the couplings (see Sec. 3.1.2 for details)

$$A_k = C \exp(-k\gamma) \,, \qquad k \in \{1, \ldots, N\} \,. \tag{4.3}$$

Here, C is an energy constant and the parameter $\gamma > 0$ is related to the number of effectively coupled spins as we will see below. Note that N is effectively infinite in QDs. In our calculations, we use the energy A_{Q} defined by

$$A_{\mathrm{Q}}^2 \coloneqq \sum_{k=1}^{N} A_k^2 \tag{4.4}$$

as the natural energy unit. In the limit of an infinite spin bath $N \to \infty$, it follows

$$C = \sqrt{\frac{1-\exp(-2\gamma)}{\exp(-2\gamma)}} A_{\mathrm{Q}} \tag{4.5a}$$

$$= \sqrt{2\gamma} A_{\mathrm{Q}} + \mathcal{O}(\gamma^{3/2}) \,, \tag{4.5b}$$

where the second relation holds for small values of $\gamma \gg 1$.

What is the significance of the parameter γ? Besides A_{Q}, we introduce the sum of all couplings

$$A_{\mathrm{S}} \coloneqq \sum_{k=1}^{N} A_k \tag{4.6}$$

to clarify this question. Let us consider the simplest parametrization for comparison, namely a uniform one where all $A_k = C$, implying $A_{\mathrm{S}} = CN$ and $A_{\mathrm{Q}}^2 = C^2 N$ so that the ratio $A_{\mathrm{S}}^2/A_{\mathrm{Q}}^2 = N$ yields the number of bath spins. For the parametrization (4.3) in the limit $N \to \infty$, we have

$$A_{\mathrm{S}} = \sum_{k=1}^{\infty} C \exp(-k\gamma) = C \frac{\exp(-\gamma)}{1-\exp(-\gamma)} \,, \tag{4.7a}$$

$$A_{\mathrm{Q}}^2 = \sum_{k=1}^{\infty} C^2 \exp(-2k\gamma) = C^2 \frac{\exp(-2\gamma)}{1-\exp(-2\gamma)} \,. \tag{4.7b}$$

Note that for large baths for which $N\gamma \gg 1$ holds, there is only an exponentially small difference between large finite N and $N \to \infty$. From Eq. (4.7) we deduce

$$N_{\mathrm{eff}} \coloneqq \frac{A_{\mathrm{S}}^2}{A_{\mathrm{Q}}^2} = \frac{1-\exp(-2\gamma)}{[1-\exp(-\gamma)]^2} \tag{4.8a}$$

$$= \frac{2}{\gamma} + \mathcal{O}(\gamma) \,, \tag{4.8b}$$

where the last relation holds again for small values of γ. Hence, the *effective* number of bath spins is not infinity even in the limit $N \to \infty$, but proportional to the inverse of $\gamma = 2/N_{\mathrm{eff}}$. This implies $\gamma \approx 10^{-4} - 10^{-6}$ for generic QDs with $N_{\mathrm{eff}} \approx 10^4 - 10^6$. In contrast, for large values of γ the dynamics of the central spin is determined by a small number of bath spins and can be determined using a fully quantum mechanical description [117, 141, 189].

In this chapter, we study the autocorrelation function of the central spin

$$S^{zz}(t) \coloneqq \left\langle \hat{S}^z(t)\hat{S}^z(0) \right\rangle \tag{4.9}$$

for small values of γ, i.e., large spin baths. Note that the autocorrelation $S^{zz}(t)$ is fully equivalent to the time evolution of the expectation values of $\hat{S}^z(t)/2$ evaluated for an initial $|\uparrow\rangle$ central spin with spin $S = 1/2$ as we study here. We focus on the case where the system is initially completely disordered, corresponding to infinite temperature or equivalently to the fact that its density matrix is proportional to the identity,

$$\hat{\rho} = \frac{1}{Z}\,\hat{\mathbb{1}}\,, \tag{4.10}$$

where Z is the dimension of the total Hilbert space normalizing the density matrix. As discussed at the end of Sec. 3.1.2, this is a common scenario in experiments performed on QDs at temperatures of $\sim 4 - 6\,\mathrm{K}$.

We apply the semiclassical approach to the CSM by applying the TWA as discussed in Sec. 3.3. The classical equations of motion (3.33) to be solved for M random configurations of the initial conditions are given in Sec. 3.3.2. Here, we consider only the case without magnetic field, for which the equation of motion for the central spin $\boldsymbol{S}$ is given by

$$\frac{\mathrm{d}}{\mathrm{d}t}\boldsymbol{S} = \boldsymbol{B}_{\mathrm{ov}} \times \boldsymbol{S} \tag{4.11}$$

with the Overhauser field $\boldsymbol{B}_{\mathrm{ov}} = \sum_{k=1}^{N} A_k \boldsymbol{I}_k$, and for the N nuclear spins $\boldsymbol{I}_k$ we have

$$\frac{\mathrm{d}}{\mathrm{d}t}\boldsymbol{I}_k = A_k \boldsymbol{S} \times \boldsymbol{I}_k\,, \qquad k \in \{1, 2, \ldots, N\}\,. \tag{4.12}$$

The initial conditions of the vector components are drawn randomly from a normal distribution with mean value zero and variance determined such that it coincides with the quantum mechanical expectation values for the spin operators given by Eq. (3.34). Thus, for a single spin component of the central spin the variance is given by $1/4$ and by $I(I+1)/3$ for the bath spins. Obviously, for bath spins with $I = 1/2$, all variances are given by $1/4$.

In practice, an ensemble average over an appropriate large number of configurations

of the random fields needs to be calculated. The calculation of 10^6 independent trajectories is required to reduce the relative statistical error below 10^{-3} [200]. This, however, limits the number of bath spins that can be treated in the semiclassical simulation within reasonable times to about 10^3. In the following sections, we introduce algorithms that reduce the number of equations of motion to a manageable size of about $100 - 200$ equations, even in the limit of an infinite bath size $N \to \infty$.

4.2 Expansion of the Overhauser field

In this section, optimized algorithms are derived that allow us to calculate the dynamics of the central spin by means of the semiclassical approach much more efficiently. We start with the Hierarchy approach, which uses a hierarchy of Overhauser fields to describe the dynamics. Then, the significantly improved Lanczos approach is developed, which uses orthogonal polynomials of the Overhauser fields to overcome problems with the long-time behavior in the Hierarchy approach. Finally, the Spectral Density approach is introduced, which extends the Lanczos approach and leads to uniform convergence of the results in time.

4.2.1 Hierarchy approach

For an exact solution of the classical equations of motion (4.11) and (4.12), $3(N+1)$ coupled differential equations need to be solved. In order to reduce the number of equations significantly, we aim at using the Overhauser field as dynamical variable instead of the individual bath spins. To this end, we introduce the hierarchy of Overhauser fields

$$\boldsymbol{B}_n \coloneqq \sum_{k=1}^{N} A_k^n \, \boldsymbol{I}_k \,. \tag{4.13}$$

Clearly, $\boldsymbol{B}_1$ is the original Overhauser field $\boldsymbol{B}_{\mathrm{ov}}$. The dynamics of the hierarchy is given by the easily derived equation of motion

$$\frac{\mathrm{d}}{\mathrm{d}t}\boldsymbol{B}_n = \boldsymbol{S} \times \boldsymbol{B}_{n+1} \,, \tag{4.14}$$

which is exact if the full hierarchy $n \in \{1, 2, \ldots, N\}$ is considered. A possible truncation, however, cuts the hierarchy according to $n \in \{1, 2, \ldots, N_{\mathrm{tr}}\}$ with $N_{\mathrm{tr}} < N$. This neglects the higher Overhauser fields and treats the last one $\mathrm{B}_{N_{\mathrm{tr}}}$ as constant.

While the individual vectors $\boldsymbol{I}_k$ are uncorrelated, normally distributed random fields, the hierarchy of Overhauser fields $\boldsymbol{B}_n$ is correlated obeying

$$\left\langle \hat{B}_n^\alpha \hat{B}_m^\beta \right\rangle = \frac{I(I+1)}{3}\, \delta_{\alpha\beta} \sum_{k=1}^{N} A_k^{n+m}\,. \tag{4.15}$$

This symmetric correlation matrix can be mapped to uncorrelated diagonal fields by applying an orthogonal transformation. In this way, the initial conditions of the correlated components B_n^α can be determined from uncorrelated variables drawn randomly from a normal distribution [248].

In the numerical simulations, see Sec. 4.3, it becomes evident that the Hierarchy approach does not converge well. This can be traced back to the fact that for fixed $\boldsymbol{S}$, the set of linear differential equations (4.12) can be diagonalized yielding purely imaginary eigenvalues, which implies oscillatory solutions. They represent the precession of angular momenta as it has to be. But the truncated system of linear differential equations (4.14) cannot be diagonalized so that instead of oscillatory solutions, we find a polynomial behavior that approximates the precessions only poorly.

4.2.2 Lanczos approach

The Lanczos approach is based on the observation that in the Hierarchy approach, higher powers of A_k appear in the equations of motion. We introduce uncorrelated fields with polynomials p_n of A_k as prefactors,

$$\boldsymbol{P}_n \coloneqq \sum_{k=1}^{N} p_n(A_k)\, \boldsymbol{I}_k\,, \tag{4.16}$$

where the subscript n denotes the degree of the polynomial. In order to have uncorrelated fields, it is required that the polynomials are orthogonal with respect

to the scalar product

$$(p_n|p_m) \coloneqq \sum_{k=1}^{N} p_n(A_k)\, p_m(A_k) = \delta_{nm}\,. \tag{4.17}$$

Then, the correlation matrix is also diagonal,

$$\left\langle \hat{P}_n^{\alpha} \hat{P}_m^{\beta} \right\rangle = \frac{I(I+1)}{3} A_{\mathrm{Q}}^2\, \delta_{\alpha\beta}\, \delta_{nm}\,, \tag{4.18}$$

which is very advantageous but not yet the key point for introducing these generalized Overhauser fields.

We construct the polynomials in the usual way by iterated multiplication of the argument, i.e., by the Lanczos algorithm [249]. The starting point is $p_0(x) \coloneqq 0$, $p_1(x) \coloneqq x$, which is a bit unusual compared to standard orthogonal polynomials starting at $p_1(x) = 1$. The advantage is that $\boldsymbol{P}_1 = \boldsymbol{B}_{\mathrm{ov}}$ follows immediately from this choice. For the iteration, it is assumed that the recursion

$$x\, p_m(x) = \beta_m\, p_{m+1}(x) + \alpha_m\, p_m(x) + \beta_{m-1}\, p_{m-1}(x) \tag{4.19}$$

for orthonormalized p_m holds up to $m = n - 1$. The real coefficients α_m, $\beta_m \geq 0$ result from the Lanczos iterative determination of the orthogonal polynomials. The next step of the induction iterates $\widetilde{p}_{n+1} \coloneqq x p_n$, where the tilde indicates that this polynomial is not yet the next orthonormalized one. The overlaps with the already defined polynomials are

$$(\widetilde{p}_{n+1}|p_{n-1}) = (x p_n|p_{n-1}) = \beta_{n-1}\,, \tag{4.20a}$$

$$(\widetilde{p}_{n+1}|p_n) = (x p_n|p_n) = \alpha_n\,. \tag{4.20b}$$

Furthermore, we compute and define

$$\beta_n \coloneqq \sqrt{\left|\widetilde{p}_{n+1} - \alpha_n\, p_n - \beta_{n-1}\, p_{n-1}\right|^2}\,, \tag{4.21a}$$

$$p_{n+1}(x) \coloneqq \frac{1}{\beta_n} \left(\widetilde{p}_{n+1} - \alpha_n\, p_n - \beta_{n-1}\, p_{n-1}\right)\,. \tag{4.21b}$$

A straightforward calculation confirms that p_{n+1} defined in this way obeys the Eq. (4.19) for $m = n$ and is orthonormalized with respect to all previously defined polynomials. We stress that the above construction does not require a finite spin

bath. As long as the scalar product in Eq. (4.17) is well-defined, i.e., converges, the Lanczos approach works.

Following this recursion, the equations of motion for the generalized fields $\boldsymbol{P}_n$ become

$$\frac{\mathrm{d}}{\mathrm{d}t}\boldsymbol{P}_n = \boldsymbol{S} \times \sum_{k=1}^{N} A_k \, p_n(A_k) \, \boldsymbol{I}_k \tag{4.22a}$$

$$= \boldsymbol{S} \times \left(\beta_n \boldsymbol{P}_{n+1} + \alpha_n \boldsymbol{P}_n + \beta_{n-1} \boldsymbol{P}_{n-1}\right) . \tag{4.22b}$$

The central spin $\boldsymbol{S}$ still obeys Eq. (4.11) and the Overhauser field $\boldsymbol{B}_{\mathrm{ov}}$ is equal to $\boldsymbol{P}_1$ because of the choice $p_1(A_k) = A_k$.

If truncated at finite $N_{\mathrm{tr}} < N$, the equations of motion (4.22) are similar to the ones of the Hierarchy approach, but they have two important advantages. The first is that the initial values for the components of the polynomial fields $\boldsymbol{P}_n$ are *uncorrelated* normally distributed variables with variance $I(I+1)A_{\mathrm{Q}}^2/3$ and mean value zero. The second advantage, which is crucial, is that the set of linear differential equations (4.22b) is diagonalizable for fixed central spin. The result are imaginary eigenvalues representing the expected precessions in the dynamics.

4.2.3 Spectral Density approach

The Lanczos approach provides differential equations of the form

$$\frac{\mathrm{d}}{\mathrm{d}t}\boldsymbol{P}_n = \boldsymbol{S} \times \sum_{k=1}^{N_{\mathrm{tr}}} \left(\underline{\underline{T}}\right)_{nk} \boldsymbol{P}_k \, , \tag{4.23}$$

where the $\left(\underline{\underline{T}}\right)_{nk}$ are the matrix elements of the tridiagonal matrix

$$\underline{\underline{T}} = \begin{pmatrix} \alpha_1 & \beta_1 & 0 & 0 & \cdots & 0 \\ \beta_1 & \alpha_2 & \beta_2 & 0 & \cdots & 0 \\ 0 & \beta_2 & \alpha_3 & \beta_3 & \ddots & \vdots \\ 0 & 0 & \beta_3 & \alpha_4 & \ddots & 0 \\ \vdots & \vdots & \ddots & \ddots & \ddots & \beta_{N_{\mathrm{tr}}-1} \\ 0 & 0 & \cdots & 0 & \beta_{N_{\mathrm{tr}}-1} & \alpha_{N_{\mathrm{tr}}} \end{pmatrix} . \tag{4.24}$$

The matrix $\underline{\underline{T}}$ is symmetric and real so that it can be diagonalized with real eigenvalues ε_α and eigenvectors $\boldsymbol{U}_\alpha \in \mathbb{R}^L$, $\alpha \in \{1, 2, \ldots, N_{\mathrm{tr}}\}$. Then, we can define the diagonal dynamical vectors

$$\boldsymbol{Q}_\alpha(t) \coloneqq \sum_{m=1}^{N_{\mathrm{tr}}} (\boldsymbol{U}_\alpha)_m \, \boldsymbol{P}_m(t) \,. \tag{4.25}$$

Their dynamics is determined by the equations of motion

$$\frac{\mathrm{d}}{\mathrm{d}t}\boldsymbol{Q}_\alpha = \varepsilon_\alpha \boldsymbol{S} \times \boldsymbol{Q}_\alpha \,, \tag{4.26}$$

which is even simpler than in the Lanczos approach thanks to the diagonalization. The equation of motion (4.11) of the central spin is still determined by the Overhauser field $\boldsymbol{B}_{\mathrm{ov}}$, which equals the first polynomial field

$$\boldsymbol{P}_1(t) = \sum_{\alpha=1}^{N_{\mathrm{tr}}} (\boldsymbol{U}_\alpha)_1 \, \boldsymbol{Q}_\alpha(t) \,, \tag{4.27}$$

where we assume that all elements $(\boldsymbol{U}_\alpha)_1$ are non-negative for later use. If not, the vectors $\boldsymbol{Q}_\alpha$ can be scaled appropriately. So far, this approach is equivalent to the Lanczos approach, except that it is expressed in a diagonal basis. The Spectral Density approach goes some steps further, realizing a suitable continuum limit.

First, we know from mathematics that orthogonal polynomials $q_n(x)$ require a scalar product that is defined by a weight function $w(x) \geq 0$ [250],

$$(f|g) \coloneqq \int w(x) \, f(x) \, g(x) \, \mathrm{d}x \,, \tag{4.28a}$$

$$(q_m|q_n) = \int w(x) \, q_m(x) \, q_n(x) \, \mathrm{d}x = \delta_{mn} \,. \tag{4.28b}$$

The only difference between the p_n and the standard definition is that the p_n start with $p_1(x) = x$ instead of $q_1(x) = 1$. Thus, we simply define

$$q_n(x) \coloneqq \frac{p_n(x)}{x} \,. \tag{4.29}$$

Furthermore, we recall that the weight function can be retrieved from the $1, 1$ matrix

element of the retarded resolvent of $\underline{\underline{T}}$ by

$$w(x) = -\frac{1}{\pi} \operatorname{Im} \left[\lim_{\delta \to 0+} \left(\frac{1}{x + \mathrm{i}\delta - \underline{\underline{T}}} \right)_{1,1} \right] . \tag{4.30}$$

Expressed in the diagonal basis, this equation implies

$$w(x) = \sum_{\alpha=1}^{N_{\mathrm{tr}}} |(\boldsymbol{U}_\alpha)_1|^2 \; \delta(x - \varepsilon_\alpha) \, . \tag{4.31}$$

Next, we calculate the weight function. Since the orthonormality (4.17) must be preserved in Eq. (4.28b), we deduce

$$\begin{aligned} (p_m | p_n) &= \sum_{k=1}^{N} p_m(A_k) \, p_n(A_k) && \text{(4.32a)} \\ &= \sum_{k=1}^{N} A_k^2 \, q_m(A_k) \, q_n(A_k) && \text{(4.32b)} \\ &= (q_m | q_n) \, . && \text{(4.32c)} \end{aligned}$$

Comparing Eq. (4.32b) with (4.28b) reveals

$$w(x) \coloneqq \sum_{k=1}^{N} x^2 \, \delta(x - A_k). \tag{4.33}$$

The integral over $w(x)$ simply yields A_{Q}^2.

Naturally, the weight function for any finite spin bath consists of a finite number of δ peaks. In view of the extremely large number of bath spins in QDs, it is reasonable to establish a suitable continuum limit. This can be realized by approximating the discrete sum by an integral. To this end, we start from a general parametrization of the couplings given by

$$A_k = D \, f(\gamma k) \, , \tag{4.34}$$

where $f(x)$ for $x \in [0, x_0]$ is a monotonic decreasing function that starts at $f(0) = 1$ and vanishes at $f(x_0) = 0$. If $\gamma \ll 1$, we can replace the sum in Eq. (4.33) by

an integral,

$$w(x) = \sum_{k=1}^{N} x^2\, \delta(x - Df(\gamma k)) \tag{4.35a}$$

$$\approx \int_0^{x_0} \frac{x^2}{\gamma}\, \delta(x - Df(y))\, \mathrm{d}y \tag{4.35b}$$

$$= \frac{x^2}{\gamma D |f'(y)|}\, \theta(x(D-x))\Big|_{x=Df(y)}\,, \tag{4.35c}$$

where $\theta(x)$ is the Heaviside step function and $f'(x)$ denotes the first derivative of the function $f(x)$. This is the general result. For the exponential parametrization (4.3) the weight function $w(x)$ is easily computed yielding

$$w(x) = \frac{x}{\gamma}\, \theta(x(\sqrt{2\gamma}A_\mathrm{Q} - x))\,. \tag{4.36}$$

This particularly simple spectral density, which is linear with slope $1/\gamma$ on the interval $[0, \sqrt{2\gamma}A_\mathrm{Q}]$, is illustrated in Fig. 4.1. Further continuous weight functions are derived in Sec. 4.2.4.

We point out that thanks to the simplicity of the linear weight function, the tridi-

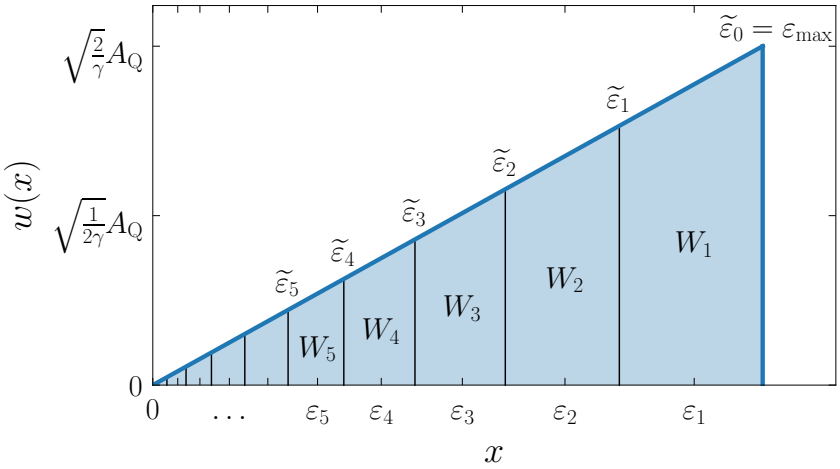

Figure 4.1: Illustration of the spectral density $w(x)$ given by Eq. (4.36), which results from the exponential parametrization (4.3) in the limit of small γ. In addition, the interval boundaries $\widetilde{\varepsilon}_k$, the corresponding weights W_k, and the chosen energies ε_k are highlighted as they result in the Spectral Density approach from the procedure explained around Eq. (4.40) for $N_\mathrm{tr} = 10$, $\lambda = 0.85$.

agonal coefficients $\{\alpha_n, \beta_n\}$ as they enter in Eq. (4.24) can be provided analytically for the limit $N \to \infty$, $\gamma \ll 1$. From the known continued fraction representation for the Jacobi polynomials [251], we deduce

$$\alpha_n = \frac{4n^2}{4n^2-1}\sqrt{\frac{\gamma}{2}}\,, \tag{4.37a}$$

$$\beta_n = \frac{\sqrt{n(n+1)}}{2n+1}\sqrt{\frac{\gamma}{2}}. \tag{4.37b}$$

This allows us to carry out calculations based on the Lanczos approach directly in the continuum limit. For large enough N_{tr}, the result obtained in this way is numerically exact and serves as a benchmark for the Spectral Density approach. For illustration, the first three generalized Overhauser fields following from these recursion coefficients are

$$\boldsymbol{P}_1 = \sqrt{\gamma}\sum_{k=1}^{N}\overline{A}_k\boldsymbol{I}_k\,, \tag{4.38a}$$

$$\boldsymbol{P}_2 = \sqrt{\gamma}\sum_{k=1}^{N}\left(3\overline{A}_k - \sqrt{8}\right)\overline{A}_k\boldsymbol{I}_k\,, \tag{4.38b}$$

$$\boldsymbol{P}_3 = \sqrt{\gamma}\sum_{k=1}^{N}\sqrt{3}(5\overline{A}_k^2 - 6\sqrt{2}\overline{A}_k + 3)\overline{A}_k\boldsymbol{I}_k\,, \tag{4.38c}$$

where $\overline{A}_k \coloneqq A_k/\sqrt{\gamma}$.

The Spectral Density approach aims at a most efficient representation of the continuous spectral density $w(x)$ by a small number of dynamic variables. Hence, we choose the well-established exponential discretization of the energies in order to capture the long-time behavior efficiently. First, the energy range $[0, \sqrt{2\gamma}A_{\mathrm{Q}}]$ for which the spectral density is finite is divided into N_{tr} intervals $\mathcal{I}_k \coloneqq [\widetilde{\varepsilon}_{k+1}, \widetilde{\varepsilon}_k]$ with

$$\widetilde{\varepsilon}_k = \lambda^k\,\frac{\varepsilon_{\max}(N_{\mathrm{tr}}-k)}{N_{\mathrm{tr}}}\,, \qquad k \in \{0,1,\ldots,N_{\mathrm{tr}}\}\,, \tag{4.39}$$

where $N_{\mathrm{tr}}+1$ is the number of grid points $\widetilde{\varepsilon}_k$ and $\varepsilon_{\max}$ is the maximum value for which $w(x)$ is finite, i.e., $\varepsilon_{\max} = \sqrt{2\gamma}A_{\mathrm{Q}}$ for the spectral density given by Eq. (4.36). This discretization scheme is visualized in Fig. 4.1. The factor $\lambda < 1$ ensures an exponentially finer discretization for smaller energies to capture the long-time

dynamics efficiently. This factor is chosen according to

$$\lambda = \left(\frac{N_{\mathrm{tr}}}{\varepsilon_{\max} t_{\max}}\right)^{\frac{1}{N_{\mathrm{tr}}-1}} . \tag{4.40}$$

The guiding idea of the above expression is to identify a maximum time $t_{\max}$ up to which the time evolution needs to be calculated. Then, the modes with sufficiently low energies are kept such that they precess at most a fraction of a complete revolution, i.e., we set $\widetilde{\varepsilon}_{N_{\mathrm{tr}}-1} t_{\max} = 1$. This condition fixes λ such that it is given by Eq. (4.40). In rare cases where Eq. (4.40) would yield a value $\lambda > 1$, we set $\lambda = 1$, refraining from an exponential zoom towards large energies because the linear discretization is already sufficient.

Finally, the discretization energies ε_k are chosen such that they are the average over $w(x)$ between $\widetilde{\varepsilon}_k$ and $\widetilde{\varepsilon}_{k-1}$,

$$\varepsilon_k \coloneqq \int_{\widetilde{\varepsilon}_k}^{\widetilde{\varepsilon}_{k-1}} x\, w(x)\, \mathrm{d}x \Bigg/ \int_{\widetilde{\varepsilon}_k}^{\widetilde{\varepsilon}_{k-1}} w(x)\, \mathrm{d}x\,, \qquad k \in \{1, 2, \ldots, N_{\mathrm{tr}}\}\,. \tag{4.41}$$

This choice guarantees that the weight and the first moment for each of the intervals and hence, also for the total weight function, is correctly represented by the discretization. The finite set of differential equations is now given by

$$\frac{\mathrm{d}}{\mathrm{d}t}\boldsymbol{Q}_k = \varepsilon_k \boldsymbol{S} \times \boldsymbol{Q}_k\,, \qquad k \in \{1, 2, \ldots, N_{\mathrm{tr}}\}\,. \tag{4.42}$$

Equation (4.11) for the central spin is still valid and thanks to Eqs. (4.27) and (4.31), the Overhauser field can be expressed as

$$\boldsymbol{B}_{\mathrm{ov}} = \boldsymbol{P}_1 = \sum_{k=1}^{N_{\mathrm{tr}}} \sqrt{W_k}\boldsymbol{Q}_k\,, \tag{4.43}$$

where W_k denotes the weight in the interval $\mathcal{I}_k$, which is given by the integral

$$W_k = \int_{\widetilde{\varepsilon}_k}^{\widetilde{\varepsilon}_{k-1}} w(x)\, \mathrm{d}x. \tag{4.44}$$

Thus, the only free parameter left is the number of intervals N_{tr}. It must be chosen large enough to reach reliable results as we will see in Sec. 4.3.3.

The auxiliary fields $\boldsymbol{Q}_k$ represent the sums of the bath spins whose couplings lie

within the interval $\mathcal{I}_k$. According to the central limit theorem, each initial component of the vectors $\boldsymbol{Q}_k$ can be drawn from a normal distribution because they represent large linear sums of the bath spins, and they are uncorrelated for different k. Thus, the $3N_{\mathrm{tr}}$ components Q_k^α, $\alpha \in \{x, y, z\}$, can be initialized according to a normal distribution around zero with variance

$$\mathrm{Var}\left[Q_k^\alpha\right] = \frac{I(I+1)}{3}\,. \tag{4.45}$$

The influence of the sum over all bath spins whose couplings lie within the interval $\mathcal{I}_k$ is accounted for by weighting the auxiliary fields $\boldsymbol{Q}_k$ with $\sqrt{W_k}$ when calculating the Overhauser field from Eq. (4.43) because the SD approach is constructed such that $\sum_{k=1}^{N_{\mathrm{tr}}} \sqrt{W_k}^2 = A_{\mathrm{Q}}^2$ holds.

It is worth to mention that the exponential discretization advocated above can also be used to efficiently approximate the discrete weight function defined in Eq. (4.33) for finite bath sizes [248]. But we emphasize that the continuum limit yields excellent results in view of the large number of bath spins in QDs. Moreover, it has the conceptually advantageous features (i) to reduce the number of parameters (N drops out) and (ii) to allow for scaling arguments as we will see in Sec. 4.3.4.

4.2.4 Weight functions

In the previous section, the linear weight function (4.36) was derived for the exponential parametrization (4.3) of the couplings. This finding is supplemented in the following for three alternative, generic Gaussian parametrizations.

One-dimensional Gaussian parametrization

We consider the Gaussian parametrization of the couplings

$$A_k = C\exp(-\alpha^2 k^2) \tag{4.46}$$

with $k \in \{1, 2, 3, \dots\}$, i.e., in dimension $d = 1$. For small values of α, it is justified to approximate the sums over all couplings by integrals. For A_{Q}^2, we calculate

$$A_{\mathrm{Q}}^2 = \sum_k A_k^2 = \frac{C^2}{\alpha} \int_0^\infty \exp(-2y^2)\,\mathrm{d}y = \frac{C^2\sqrt{2\pi}}{4\alpha}\,, \tag{4.47}$$

and analogously for A_{S}, we obtain

$$A_{\mathrm{S}} = \sum_k A_k = \frac{C}{\alpha} \int_0^\infty \exp(-y^2)\,\mathrm{d}y = \frac{C\sqrt{\pi}}{2\alpha}\,. \tag{4.48}$$

Then, the effective number of bath spins $N_{\mathrm{eff}} = A_{\mathrm{S}}^2/A_{\mathrm{Q}}^2$ is given by

$$N_{\mathrm{eff}} = \sqrt{\frac{\pi}{2}}\frac{1}{\alpha} \tag{4.49}$$

and setting $\alpha = \sqrt{\frac{\pi}{8}}\gamma$ implies $\gamma = 2/N_{\mathrm{eff}}$ as before. We opt for this choice of α for a better comparability between the different parametrizations. The energy

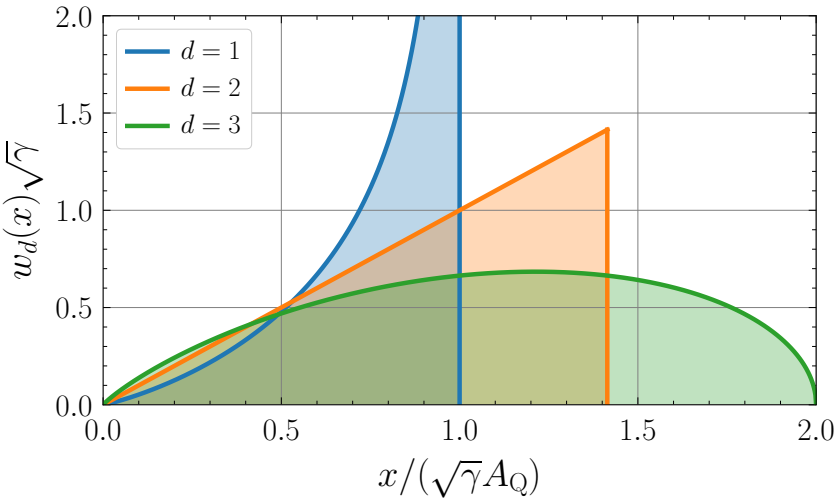

Figure 4.2: Comparison of the three weight functions $w_d(x)$ resulting from a Gaussian parameterization of the hyperfine couplings in d dimensions. The different weight functions are given by Eqs. (4.51), (4.57), and (4.63). The linear weight function resulting from the two-dimensional Gaussian parameterization is equal to that of a one-dimensional exponential parameterization as discussed in the main text. This fact underlines the relevance of the linear weight function for the description of QDs.

constant C in units of A_{Q} results to

$$C = \sqrt{\gamma} A_{\mathrm{Q}} \tag{4.50}$$

and finally, the weight function for the Gaussian parameterization in one dimension is given by

$$w_1(x) = \frac{x^2}{\alpha} \int_0^\infty \delta(x - C\exp(-y^2))\,\mathrm{d}y \tag{4.51a}$$

$$= \sqrt{\frac{2}{\pi}} \frac{x}{\gamma} \frac{1}{\ln(C/x)}\,\theta(x(C-x)). \tag{4.51b}$$

In Fig. 4.2, this weight function is compared to the other weight functions derived below for the same value of γ, i.e., for the same number of effectively coupled bath spins.

Two-dimensional Gaussian parametrization

Next, we consider the parametrization of the couplings

$$A_r = C\exp(-\alpha^2 r^2)\,, \tag{4.52}$$

where $r \in \mathbb{Z}^2$ is a two-dimensional vector. For small values of α, it is again justified to approximate the sums over all couplings by integrals. For A_{Q}^2, we calculate

$$A_{\mathrm{Q}}^2 = \sum_r A_r^2 = \frac{2\pi C^2}{\alpha} \int_0^\infty y\exp(-2y^2)\,\mathrm{d}y = \frac{\pi C^2}{2\alpha} \tag{4.53}$$

and for A_{S}, we find

$$A_{\mathrm{S}} = \sum_r A_r = \frac{2\pi C}{\alpha} \int_0^\infty y\exp(-y^2)\,\mathrm{d}y = \frac{\pi C}{\alpha}\,. \tag{4.54}$$

Hence, the number of effectively coupled bath spins $N_{\mathrm{eff}} = A_{\mathrm{S}}^2/A_{\mathrm{Q}}^2$ results to

$$N_{\mathrm{eff}} = \frac{2\pi}{\alpha}\,. \tag{4.55}$$

Setting $\alpha = \pi\gamma$ implies $\gamma = 2/N_{\text{eff}}$ as before for a better comparability with the other generic weight functions. For the energy constant C, we obtain

$$C = \sqrt{2\gamma} A_{\text{Q}} \tag{4.56}$$

so that the weight function for the Gaussian parameterization in two dimensions is given by

$$w_2(x) = \frac{2\pi x^2}{\alpha} \int_0^\infty y\, \delta(x - C\exp(-y^2))\, \mathrm{d}y \tag{4.57a}$$

$$= \frac{x}{\gamma}\, \theta(x(C-x))\,. \tag{4.57b}$$

Clearly, the Gaussian parametrization of the couplings in two dimensions yields precisely the same weight function as the exponential parametrization (4.3) in one dimension. This has to be the case because the one-dimensional exponential parameterization follows from the scaling $k \propto r_k^2$ valid in two dimensions, where k labels the bath spins $\boldsymbol{I}_k$ with distance $r_k < r_{k+1}$ from the central spin (see Sec. 3.1.2). It is the weight function that we apply to study the spin dynamics in QDs. In Fig. 4.2, the linear weight function $w_2(x)$ given by Eq. (4.57) is compared to the other generic ones.

Three-dimensional Gaussian parametrization

Finally, we consider the parametrization of the couplings

$$A_r = C\exp(-\alpha^2 r^2)\,, \tag{4.58}$$

where $r \in \mathbb{Z}^3$ is a three-dimensional vector. For small values of α, it is again justified to approximate the sums over all couplings by integrals. For A_{Q}^2 and A_{S}, we calculate

$$A_{\text{Q}}^2 = \sum_r A_r^2 = \frac{4\pi C^2}{\alpha} \int_0^\infty y^2 \exp(-2y^2)\, \mathrm{d}y = \frac{C^2}{\alpha} \left(\frac{\pi}{2}\right)^{3/2}\,, \tag{4.59}$$

$$A_{\text{S}} = \sum_r A_r = \frac{4\pi C}{\alpha} \int_0^\infty y^2 \exp(-y^2)\, \mathrm{d}y = \frac{\pi^{3/2} C}{\alpha}\,, \tag{4.60}$$

so that the number of effectively coupled bath spins $N_{\text{eff}} = A_{\text{S}}^2/A_{\text{Q}}^2$ results to

$$N_{\text{eff}} = \frac{(2\pi)^{3/2}}{\alpha}\,. \tag{4.61}$$

Setting $\alpha = (2\pi)^{3/2}\gamma/2$ implies $\gamma = 2/N_{\text{eff}}$ as before for a better comparability with the other generic weight functions. The energy constant C results to

$$C = 2\sqrt{\gamma}A_{\text{Q}}\,. \tag{4.62}$$

and the weight function for a Gaussian parameterization in three dimensions is given by

$$w_3(x) = \frac{4\pi x^2}{\alpha}\int_0^\infty y^2\,\delta(x - C\exp(-y^2))\,\mathrm{d}y \tag{4.63a}$$

$$= \sqrt{\frac{2}{\pi}}\frac{x}{\gamma}\sqrt{\ln\left(\frac{C}{x}\right)}\,\theta(x(C-x))\,. \tag{4.63b}$$

This weight function is compared to the other generic ones in Fig. 4.2. The differences are not very large since they result only from square roots of logarithmic factors. The influence of the dimensionality on the long-time dynamics is studied in Sec. 4.3.4.

4.3 Results

In Sec. 4.2, three different algorithms that aim at enhancing the performance of the semiclassical simulation of spin dynamics in the CSM are proposed: the Hierarchy approach (Sec. 4.2.1), the Lanczos approach (Sec. 4.2.2), and the Spectral Density approach (Sec. 4.2.3). The enhancement of the performance is crucial to study the long-time behavior for large spin baths. While in the full semiclassical simulation the dimension of the ODE system is proportional to N, the dimension in the proposed algorithms scales with $N_{\text{tr}} \leq N$. The total dimension of the ODE system is given by $3(N_{\text{tr}}+1)$ in all three algorithms. In this section, we analyze how the truncation parameter N_{tr} must be chosen to obtain reliable results. Additionally, we study the dependence of the long-time behavior on the parameter γ, which is proportional to the inverse effective number of bath spins. In this way, we retrieve the long-time scale of the slow spin dynamics [163, 178], which is essentially given

by the inverse of the maximum individual coupling $1/A_1 = 1/(\sqrt{2\gamma}A_Q)$. It is a particular strength of the advocated Spectral Density approach that the dynamics on this long timescale is accessible.

4.3.1 Comparison of all approaches

All numerical data shown has been averaged over $M = 10^6$ random initial configurations (unless stated otherwise), which are sampled from the appropriate normal distributions for all spin components to approximate the quantum mechanical spin dynamics by means of the Gaussian TWA. For simplicity, all spins are considered as spin 1/2.

The time evolution of the central spin autocorrelation $S^{zz}(t)$ is shown in Fig. 4.3. The result obtained from the full semiclassical simulation for $N = 1000$ bath spins at $\gamma = 10^{-2}$ is shown in black. This result serves as our benchmark for the three algorithms. But first, let us briefly discuss the characteristics of the autocorrelation $S^{zz}(t)$. Since the central spin represents a spin with $S = 1/2$, the autocorrelation

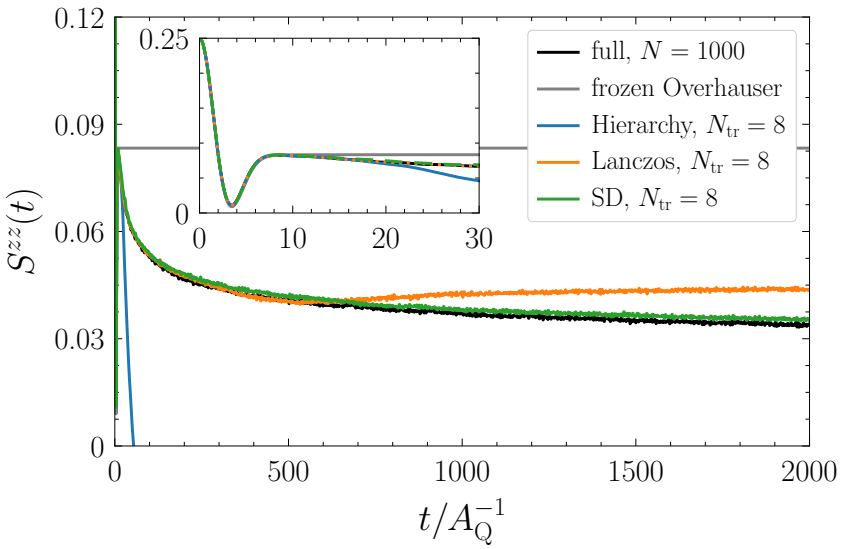

Figure 4.3: Comparison of the central spin autocorrelation S^{zz} calculated by means of the Hierarchy, the Lanczos, and the Spectral Density (SD) approach for fixed truncation parameter $N_{tr} = 8$ with the result of the full semiclassical simulation for $N = 1000$ bath spins (except for the SD approach, which employs the continuum limit $N \to \infty$) and $\gamma = 10^{-2}$. The short-time behavior is shown in the inset. The solution resulting from the frozen Overhauser field approximation (Sec. 3.3.4) is included for comparison.

simply starts at $S^{zz}(0) = 1/4$. The initial decay and subsequent revival to $S^{zz}(0)/3$, which can be seen in the inset, is almost identical to the solution resulting from the frozen Overhauser field approximation in Sec. 3.3.4 (included in gray). Minimal differences stem from the finite bath size considered in the full semiclassical simulation and from its statistical nature. But in contrast to this solution, an additional slow long-time decay of the autocorrelation caused by the dynamics of the nuclear spins occurs in the semiclassical simulation. This long-time decay is studied in detail in Sec. 4.3.4.

The Hierarchy, Lanczos and Spectral Density (SD) approach for fixed truncation parameter $N_{\mathrm{tr}} = 8$ are compared with the numerically exact solution of the full semiclassical simulation in Fig. 4.3. All algorithms capture the short-time dynamics shown in the inset very well up to $t \approx 16 A_{\mathrm{Q}}^{-1}$. But the Hierarchy approach shows a strong deviation already at $t \approx 20 A_{\mathrm{Q}}^{-1}$. Its results improve when N_{tr} is increased and they become exact for $N_{\mathrm{tr}} = N$, but the convergence is slow. Hence, we conclude that this algorithm is not efficient and do not discuss it further. We have anticipated this conclusion already in Sec. 4.2.1. The general mathematical structure of the Hierarchy approach is not appropriate to capture the long-time dynamics since it leads to polynomial instead of oscillatory solutions because of the impossibility to diagonalize the truncated linear differential equations (4.14).

In contrast, both the Lanczos and the SD approach capture the exact solution up to remarkably long times in spite of the fairly small truncation parameter. The Lanczos approach starts to deviate at about $t \approx 700 A_{\mathrm{Q}}^{-1}$, while the SD approach is close to the exact solution for all displayed times. A deeper understanding of how the results of the Lanczos and the SD approach depend on the truncation parameter N_{tr} is developed in the following.

4.3.2 Lanczos approach

Figure 4.4(a) shows the dependence of the results for the Lanczos approach on the truncation parameter N_{tr}. It is obvious that after a specific time, the solution starts to deviate from the exact result and displays an artificial plateau region. Up to this specific time the solution is very accurate. In order to know beforehand until which time the results are reliable, we introduce the time $t_{\max}$ at which the relative deviation exceeds a certain relative threshold ξ, for instance $\xi = 0.1$. The

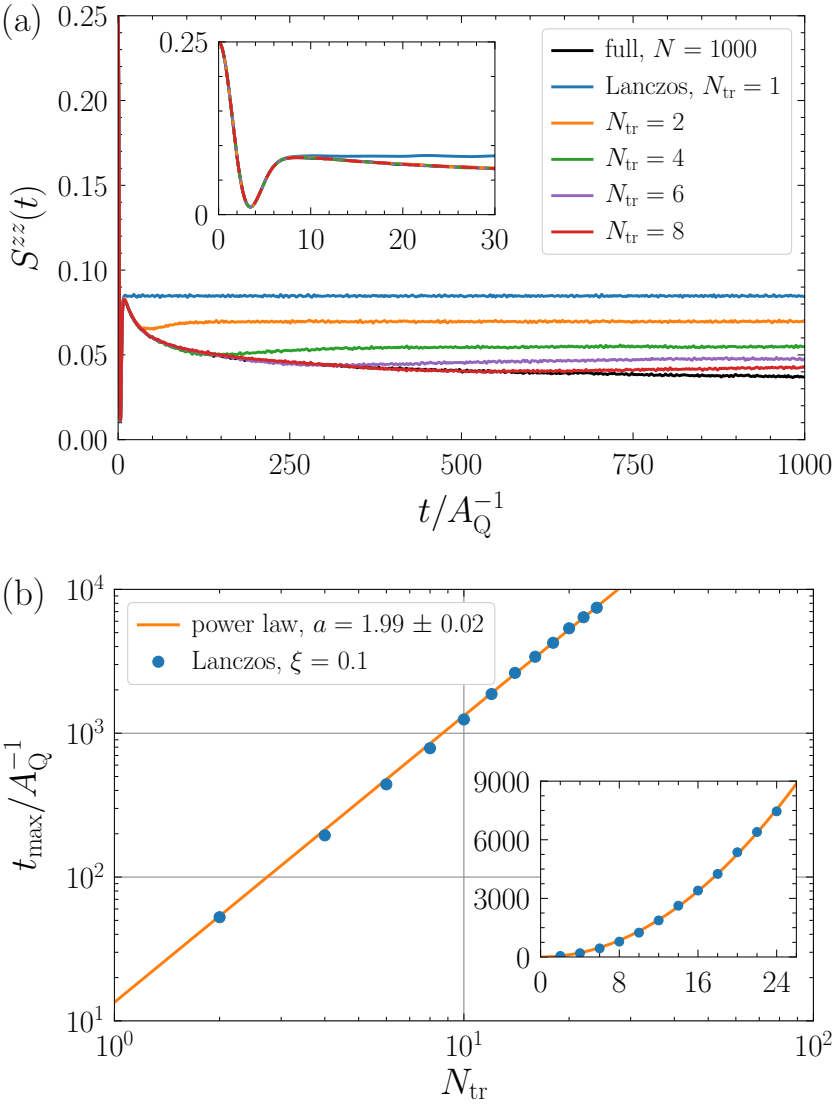

Figure 4.4: (a) Results of the Lanczos approach for various truncation parameters N_{tr} compared to solution of the full semiclassical simulation for $N = 1000$ bath spins at $\gamma = 10^{-2}$. The inset shows the short-time behavior. **(b)** Scaling of the time t_{max} up to which the Lanczos approach is reliable (relative deviation threshold $\xi = 0.1$) with the truncation parameter N_{tr} . Fitting a power law $t_{\mathrm{max}} \propto N_{\mathrm{tr}}^{a}$ yields the exponent $a = 1.99 \pm 0.02$.

dependence of $t_{\max}$ on N_{tr} is studied in Fig. 4.4(b). A power law fit $t_{\max} \propto N_{\mathrm{tr}}^{a}$ in the double-logarithmic plot clearly reveals that the scaling is quadratic, i.e., $t_{\max} \propto N_{\mathrm{tr}}^{2}$. Therefore, by increasing the truncation parameter N_{tr} much longer times can be simulated using the Lanczos approach while still having a significant advantage in performance over the full semiclassical simulation. We stress that increasing N_{tr} does not lead to a deterioration of the description of the short-time dynamics; see the inset of Fig. 4.4(a).

4.3.3 Spectral Density approach

In contrast to the Lanczos approach, the SD approach shows a completely different behavior when increasing the truncation parameter N_{tr} (which is actually a discretization parameter here); see Fig. 4.5(a). Similar to the Lanczos approach, the SD approach works better for larger N_{tr} and the short-time behavior is correctly described independent of N_{tr}. But the convergence is roughly uniform, i.e., for N_{tr} deviations with a similar magnitude occur for intermediate and large times. We consider this to be an important advantage because we are interested in a reliable description for very long times. The reason for this behavior lies in the particular construction of the SD approach. The energies included in the description of the bath are designed to capture all the relevant dynamics in the time interval under study; see Eqs. (4.39) and (4.40). The crucial advantage is that this construction captures the dynamics on all timescales efficiently.

In order to assess the accuracy of the SD approach quantitatively, we plot in Fig. 4.5(b) the root-mean-square deviation Δ_S between the SD result and a highly accurate Lanczos calculation ($N_{\mathrm{tr}} = 32$) in the time interval $t/A_{\mathrm{Q}}^{-1} \in [0, 10^4]$ as a function of the truncation parameter $N_{\mathrm{tr}} \geq 4$. Clearly, a rapid convergence is visible. It can be fitted by the function

$$\Delta_S(N_{\mathrm{tr}}) = \frac{A}{N_{\mathrm{tr}}^{B}} + C\,, \tag{4.64}$$

yielding $A = 0.21 \pm 0.01$, $B = 2.44 \pm 0.04$, and $C = (2.9 \pm 0.2) \times 10^{-4}$ for the fit parameters. The fit reveals that the average convergence is better than quadratic in the inverse number of tracked dynamic vectors. The constant offset C occurs naturally since a statistical error remains for all N_{tr} because of the ensemble av-

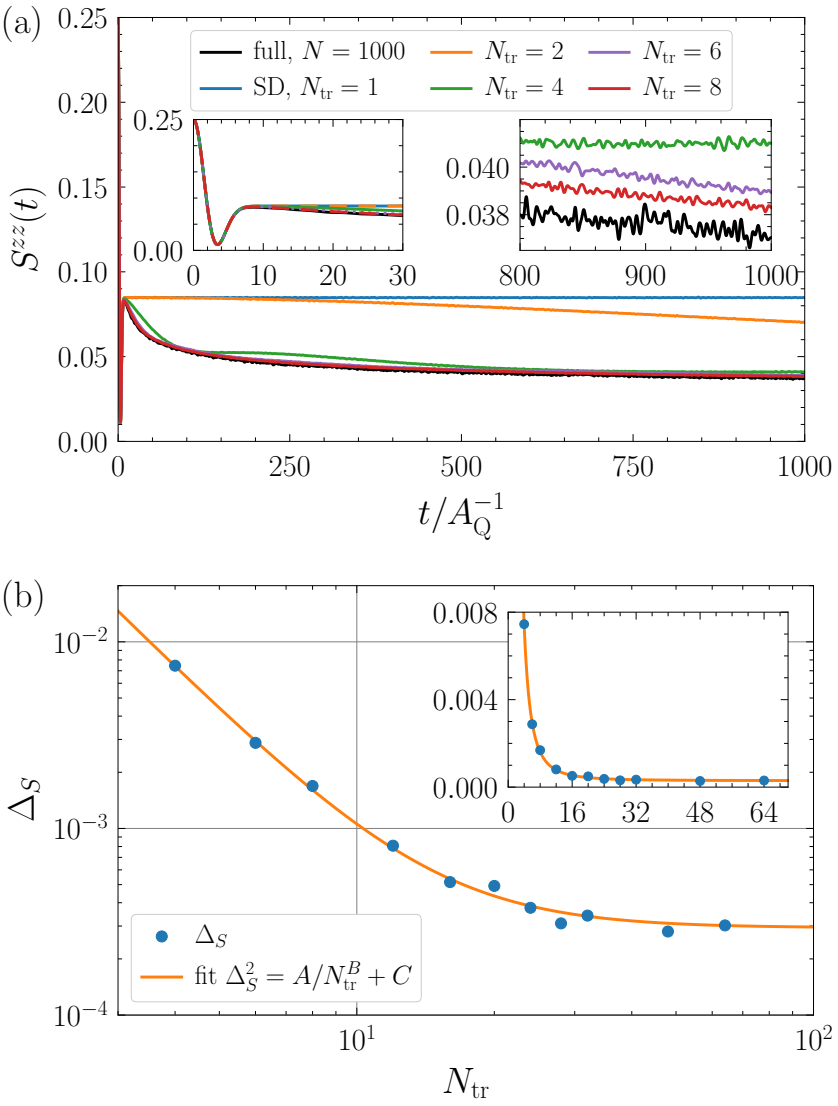

Figure 4.5: (a) Comparison of the results from the SD approach and the full semiclassical simulation for various truncation parameters N_{tr} at $\gamma = 10^{-2}$. The full simulation is performed for $N = 1000$ bath spins; the SD approach employs the continuum limit $N \to \infty$. The left inset shows the short-time behavior. The fluctuations visible in the right inset result from the averaging over $M = 10^6$ random initial configurations. **(b)** Root-mean-square deviation Δ_S in the time interval $t/A_{\mathrm{Q}}^{-1} \in [0, 10^4]$ between the SD result and a highly accurate Lanczos calculation ($N_{\mathrm{tr}} = 32$) in the continuum limit at $\gamma = 10^{-2}$. Here, the ensemble averages for the SD and Lanczos results are calculated over $M = 10^7$ configurations. The orange solid line depicts the fit of type (4.64) calculated for $N_{\mathrm{tr}} \geq 4$.

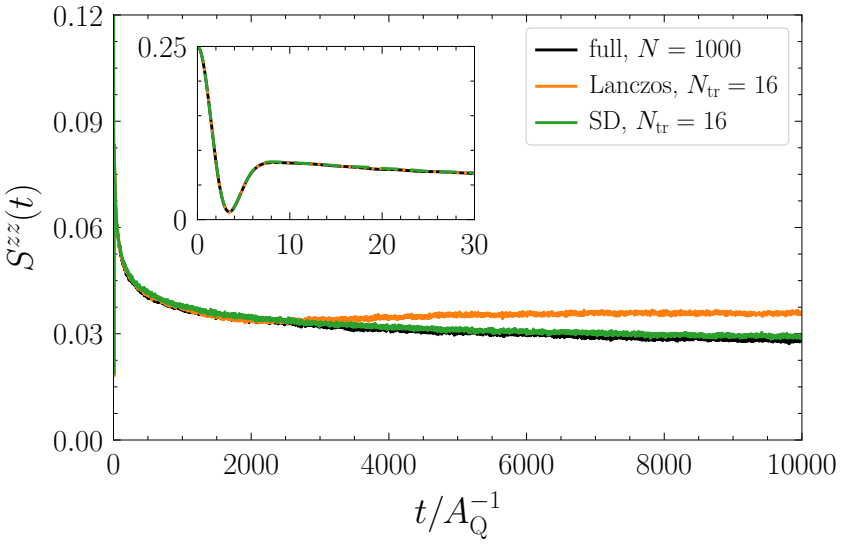

Figure 4.6: Comparison of the results from the Lanczos and SD approach for $N_{\mathrm{tr}} = 16$ to the full semiclassical simulation for very long times up to $t = 10^4 A_{\mathrm{Q}}^{-1}$ at $\gamma = 10^{-2}$. The Lanczos and the full calculations are performed for $N = 1000$ bath spins; the SD approach employs the continuum limit $N \to \infty$. The inset shows the short-time behavior.

erage over $M = 10^7$ random initial configurations. This statistical error scales like $1/\sqrt{M}$ [200].

The advantageous feature of the SD approach is summarized in Fig. 4.6, clearly demonstrating that the SD approach captures the dynamics of the central spin model more efficiently than the Lanczos approach for very long times if the same value of N_{tr} is chosen. We stress that the Lanczos approach has the advantage to yield very precise data when simulating shorter times, but such times are not a computational challenge. Both approaches can deal with infinitely large spin baths $N \to \infty$ while the number of effectively coupled bath spins $N_{\mathrm{eff}} = 2/\gamma$ remains finite.

4.3.4 Long-time behavior

Above, we have illustrated that the SD approach is especially suited to describe the dynamics at very long times accurately. For this reason, we apply this algorithm for the following analysis and use $N_{\mathrm{tr}} = 32$ in the following calculations. The calculations are carried out for infinitely large spin baths $N \to \infty$, i.e., in the continuum limit.

Let us investigate the influence of the parameter γ, which represents the inverse number of effectively coupled bath spins via $\gamma = 2/N_{\text{eff}}$. Figure 4.7(a) shows a set of representative results for various values of γ up to times $t = 10^4 A_{\text{Q}}^{-1}$. In all cases, the short-time behavior is very similar to the result obtained from the frozen Overhauser field approximation (included in Fig. 4.3). On the long-time scale, a

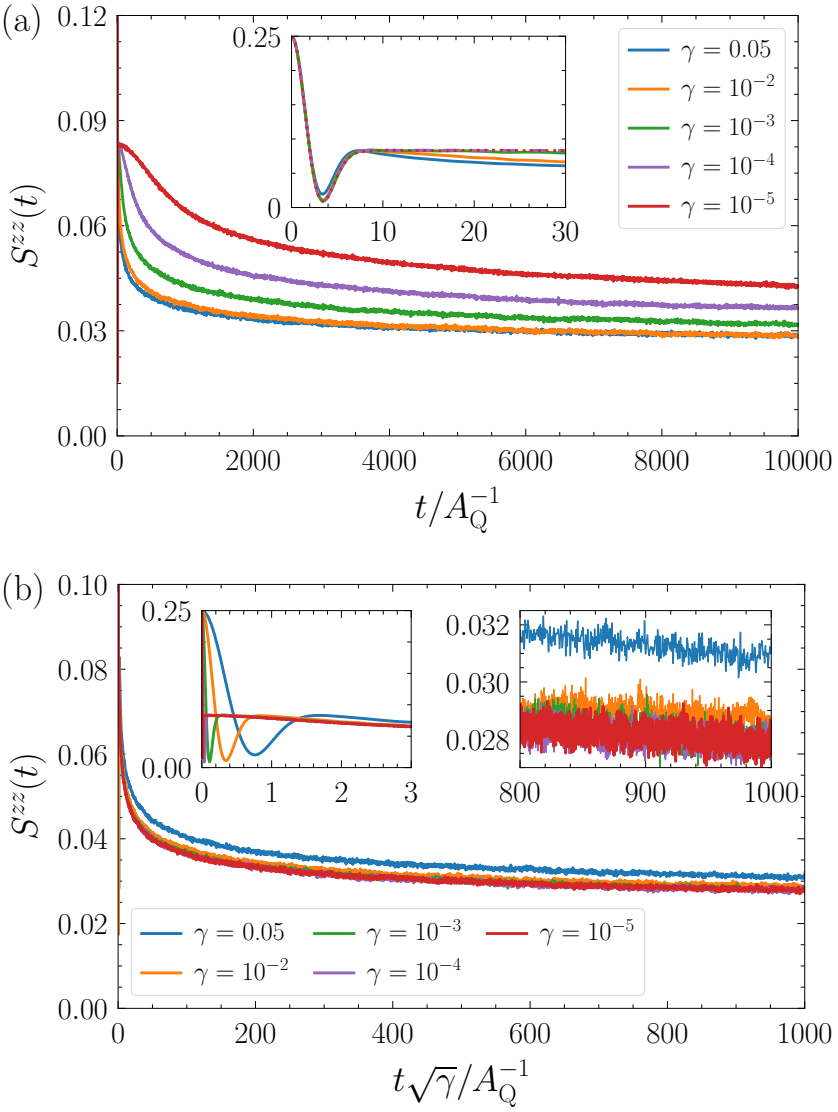

Figure 4.7: (a) Central spin autocorrelation $S^{zz}(t)$ for various values of γ up to very long times calculated using the SD approach. The calculations are performed for $N \to \infty$ bath spins with a truncation parameter $N_{\text{tr}} = 32$. **(b)** Scaled results from Fig. 4.7(a) showing an excellent data collapse as long as the short-time dynamics and the long-time dynamics are separated clearly, i.e., for $\sqrt{\gamma} \ll 1$.

slow decay of the autocorrelation takes place. While the curves are qualitatively very similar, smaller values of γ imply a slower long-time decay. We stress that the short-time dynamics (see the inset) is not altered by changing γ because it is determined by the energy scale A_Q. Hence, all curves coincide in the inset up to about $t \approx 8A_\mathrm{Q}^{-1}$, and this is also the reason why the frozen Overhauser field approximation works well for short times. Only the result for $\gamma = 0.05$ deviates slightly. We attribute this to the fact that for $\gamma = 0.05$, the continuum limit, i.e., the step from Eq. (4.35a) to (4.35b) justified for $\gamma \ll 1$, does not capture the discrete bath perfectly.

Turning back to the long-time dynamics, the question arises whether the dynamics for different values of γ can be mapped to a single curve. This would imply that the contained information is essentially the same. Practically, a good data collapse would help future theoretical simulations so that only moderate values of γ (instead of very small ones) need to be studied. A larger value of γ implies a faster long-time decay, i.e., the long-time limit is easier to reach numerically. Studying Fig. 4.1 and the analytic result for the weight function given in Eq. (4.36), it is obvious that the maximum energy occurring in the weight function $w(x)$ sets a second energy scale. This energy scale is $\sqrt{\gamma}A_\mathrm{Q}$. The first energy scale is A_Q as discussed above for the inset of Fig. 4.7(a). Hence, it is natural to assume that the long-time dynamics is determined by the second, much smaller energy scale $\sqrt{\gamma}A_\mathrm{Q}$. To corroborate this hypothesis, we plot the data from Fig. 4.7(a) with a scaled time argument in Fig. 4.7(b). Indeed, an impressive data collapse is achieved. In particular for small values of γ, the scaling with $\sqrt{\gamma}$ works perfectly. For larger values of γ, e.g., $\gamma = 0.05$, the two energy scales A_Q and $\sqrt{\gamma}A_\mathrm{Q}$ are not clearly separated so that the scaling is not fully quantitative. Obviously, the short-time dynamics does not match anymore after scaling the time with the factor $\sqrt{\gamma}$; see the inset of Fig. 4.7(b). It results from the fact that the corresponding short-time scale is solely determined by A_Q^{-1}.

Another question is how the correlations of the central spin decay. For the quantum mechanical model with a finite bath, we know from rigorous lower bounds [180, 201] that the correlations are persistent, i.e., no complete decay occurs. Even for infinite baths, the correlations persist if the couplings are distributed such that their distribution can be described as a probability distribution $p(A)$ with finite moments [201]. Note that this is not the case for the exponential parametrization (4.3) and for the Gaussian parametrizations of the couplings considered in Sec. 4.2.4. The reason is

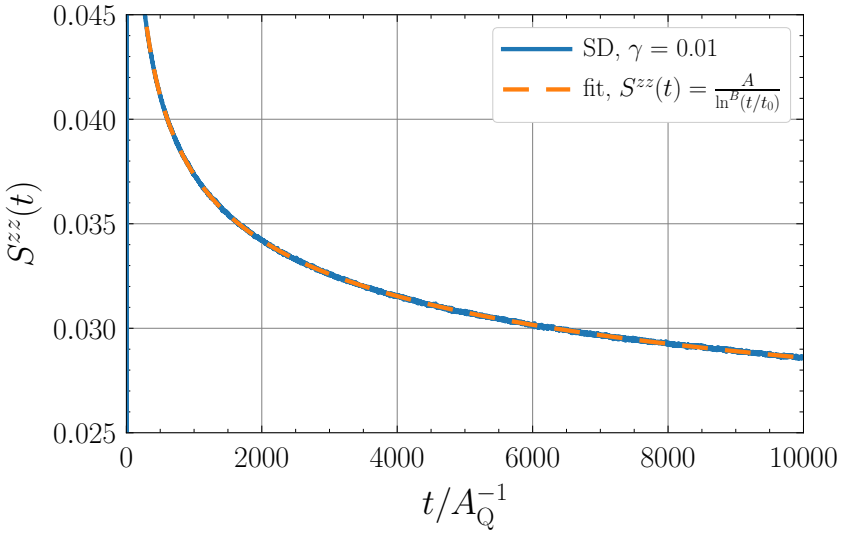

Figure 4.8: Analysis of the long-time behavior of the autocorrelation, averaged over $M = 10^8$ trajectories, by a logarithmic fit (4.65). The fit parameters are $A = 0.303 \pm 0.001$, $B = 1.024 \pm 0.001$, and $t_0 = (0.442 \pm 0.003) A_{\mathrm{Q}}^{-1}$.

that these parametrizations imply that there is an infinite number of very weakly coupled spins so that no normalization of a probability distribution $p(A)$ is possible. We recall that the lower bounds as discussed in Refs. [180, 201] result from the existence of conserved quantities such as the total angular momentum and the total energy. These quantities are conserved also for the classical Hamiltonian 4.1 and the choices of couplings we are considering here. Hence, it is not astonishing that the correlations persist very long. They are protected by conservation laws and thus, they decay very slowly as can be seen in Fig. 4.7.

The question arises how the slow decay can be described quantitatively. Various studies propose a slow logarithmic decay [223, 226, 227]. Hence, we fit the simulated data for $\gamma = 10^{-2}$ according to

$$S^{zz}(t) = \frac{A}{\ln^B(t/t_0)} \,. \tag{4.65}$$

The simulation and the fit of the long-time behavior are compared in Fig. 4.8. The fit is obtained in the interval $t/A_{\mathrm{Q}}^{-1} \in [3 \times 10^2, 10^4]$ and works very well, supporting the results of previous research [223, 226, 227]. The obtained fit parameters are $A = 0.303 \pm 0.001$, $B = 1.024 \pm 0.001$, and $t_0 = (0.442 \pm 0.003) A_{\mathrm{Q}}^{-1}$. The fit is of comparable quality if we fixed $B = 1$. Hence, the existence of a logarithmic factor

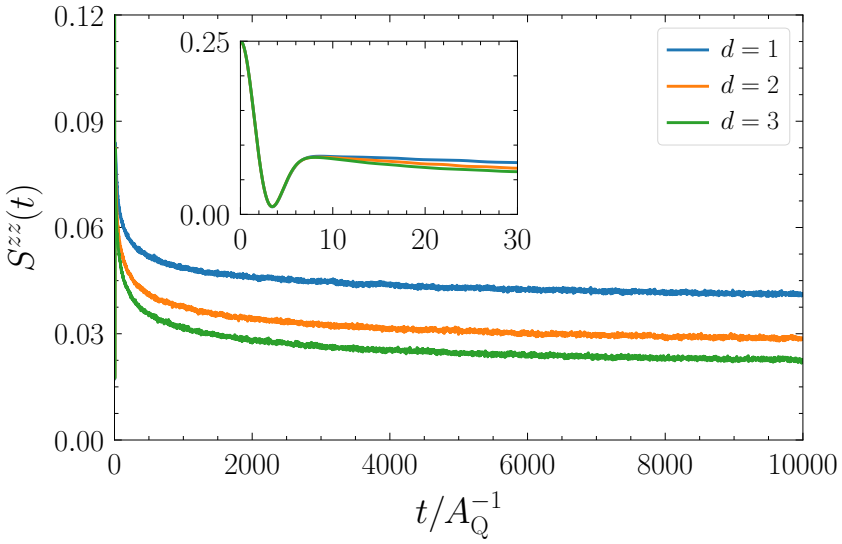

Figure 4.9: Comparison of the central spin autocorrelation for three generic weight functions $w_d(x)$ relevant in dimension $d = 1$, $d = 2$, and $d = 3$ for $\gamma = 10^{-2}$. The weight functions are given in Eqs. (4.51), (4.57), and (4.63), respectively. Note that the $d = 2$ Gaussian case is identical to the linear weight function $w(x)$ given by Eq. (4.36).

is certain, but further details such as logarithmic corrections found in Ref. [180] cannot be determined reliably. Since the dynamics can be scaled quantitatively with $\sqrt{\gamma}$ if γ is sufficiently small, there is no need to show or analyze data for other values of γ.

Finally, let us address the influence of the weight function. We do not study wildly different weight functions but stay with the plausible choices of Sec. 4.2.4. As discussed in Sec. 3.1.2, the strength of the Fermi-contact hyperfine interaction is proportional to the probability density of the electron at the position of the nuclear spins in the QD. Assuming to first approximation a parabolic trapping potential as it results from any Taylor expansion, Gaussian wave functions are the most plausible assumption (see Sec. 3.1.2). Previously in Sec. 4.2.4, we computed the three corresponding weight functions $w_d(x)$ in dimension $d = 1$, 2, and 3. The $d = 2$ case is covered by the linear weight function that we have used so far.

In Fig. 4.9, we compare the resulting central spin autocorrelation for the same value of $\gamma = 10^{-2}$, which implies the same number of effectively coupled bath spins. The results indicate that the influence of the dimension is only of moderate importance. The behavior is identical on short times $t \lesssim 8A_{\mathrm{Q}}^{-1}$ as it has to be because the distribution of the couplings is not of importance on this timescale solely determined

by A_{Q}^{-1}. The feature of a very slowly, logarithmically decaying autocorrelation is found in all dimensions. The same is true for the scaling of the long-time dynamics with $\sqrt{\gamma}$. The difference is that the slow long-time decay is initially faster in larger dimensions.

4.4 Chapter conclusion

We considered the central spin model as the relevant description of two-level systems coupled to large spin baths. While the quantum model is the ultimate aim in order to describe experimental results, it has been shown that semiclassical simulations comprising appropriate ensemble averages over normally distributed initial conditions provide very good approximations to the quantum mechanical solution [182, 200, 226, 227]. Thus, this chapter aimed at establishing efficient approaches to deal with this semiclassical approach to the CSM. Two demanding requirements had to be met: very large numbers of bath spins and very long times.

Instead of addressing single spins, we introduced generalized higher Overhauser fields to develop a much more efficient approach than the full semiclassical simulation. A first attempt, the Hierarchy approach, failed because of an inappropriate mathematical structure. But the Lanczos and the SD approach turned out to be extremely powerful because only a limited number of dynamical vectors needs to be tracked. The number of these vectors, denoted as N_{tr}, is the control parameter determining the accuracy of both approaches.

The Lanczos approach, which displays a nonuniform convergence, works excellently up to a certain threshold in time t_{max}. This time can be pushed higher and higher by increasing N_{tr}; the scaling is $t_{\mathrm{max}} \propto N_{\mathrm{tr}}^2$. The Lanczos approach is particularly suited if high-precision data is required for not too long times.

The SD approach is adjusted to a preset time interval. Within this interval, it displays a uniform and better than quadratic convergence at very moderate computational cost. Moreover, it is based on the appealing concept of a continuum limit that amounts to setting the *total* number of bath spins to infinity while the number of effectively coupled bath spins N_{eff} within the localization volume of the central spin is kept as the relevant parameter. In order to establish an appropriate

continuum limit, we introduced weight functions and determined them for generic cases.

Employing the powerful SD approach, we identified the energy scale that is responsible for the long-time dynamics. This low-energy scale is given by $A_{\mathrm{Q}}/\sqrt{N_{\mathrm{eff}}}$, where A_{Q} is the root of the square sum of all couplings. The energy A_{Q} is known to determine the short-time behavior [104, 183]; see also Sec. 3.3.4. The low-energy scale $A_{\mathrm{Q}}/\sqrt{N_{\mathrm{eff}}}$ also appeared in previous investigations [163, 178]. But we emphasize that the SD approach can produce reliable real-time data up to these very long timescales for infinite baths with very large numbers of effectively couples bath spins. This allowed us to show by explicit and systematically controlled calculations that a scaling of the long-time tails of the autocorrelation with the low-energy scale yields a convincing data collapse.

Physically, the low-energy scale $A_{\mathrm{Q}}/\sqrt{N_{\mathrm{eff}}}$ is obviously a representative value of the individual couplings of the bath spins. This observation is highly plausible because the individual bath spin $\boldsymbol{I}_k$ can react to the behavior of the central spin only by the rate A_k. As long as the bath itself remains static, the autocorrelation of the central spin does not decay but remains constant at one third of its initial value (Sec. 3.3.4). Hence, further decay of the autocorrelation will be slow and can only happen at the rate at which the bath spins precess. For QDs with $N_{\mathrm{eff}} = 10^4 - 10^6$ effectively coupled nuclear spins and A_{Q}^{-1} being of the order of nanoseconds, the long-time scale is of the order of 10^2 to 10^3 ns [19, 104].

Finally, we studied the influence of the dimensionality of the electronic wave function by computing the different weight functions $w_d(x)$. The resulting dynamics, however, indicates only a moderate dependence on the dimension d. This observation also implies that the details of the couplings in a QD do not matter much. The key parameters are the high-energy and the low-energy scale, which dominate the short-time and the long-time behavior, respectively.

The established approaches and the above observations provide a reliable algorithmic and conceptual foundation for many further investigations. The approach is straightforwardly extended to finite external magnetic fields acting on the central spin or on the bath spins. In particular, it can be applied to study QDs subjected to trains of pulses in conjunction with a transverse external magnetic field, where the effect of nuclei-induced frequency focusing takes place on extremely long

timescales [25]. This is the subject of the following three chapters, constituting Part II of the thesis.

II

Nonequilibrium spin phenomena in a transverse magnetic field

Chapter 5

Nuclei-induced frequency focusing in infinite semiclassical central spin models

Singly-charged QDs subjected to periodic laser pulses in a transverse magnetic field can show the fascinating phenomenon of spin mode locking (SML) [24] as a consequence of nuclei-induced frequency focusing (NIFF) [25]. An overview over these two effects is given in Sec. 2.4.1. When a strong transverse magnetic field is applied to the QDs, the localized electron spins can be manipulated to respond coherently through the application of long trains of periodic laser pulses, where the pulses applied with repetition time T_{R} induce a synchronization of the precession frequency of the electron spin with the repetition rate of the pulses. The synchronization can be achieved through a focusing of the nuclear spin bath onto certain polarizations: The Overhauser field, i.e., the effective magnetic field applied by the nuclear spins on the electron spin via the hyperfine interaction, is driven indirectly until commensurability of the electronic precession frequency and the pulse repetition rate is reached.

In this chapter, we apply the efficient semiclassical Spectral Density approach developed in Sec. 4.2.3 to study this effect. The approach enables us to study the experimentally relevant bath sizes and long pulse sequences for the experimental situation in which the spin dynamics in the QDs approaches a nonequilibrium steady state. A very useful observation in this context is that the intrinsic timescale of the spin bath scales like the square root of the number N_{eff} of effectively coupled bath spins, i.e., $t_{\mathrm{nuclei}} \propto \sqrt{N_{\mathrm{eff}}} A_{\mathrm{Q}}^{-1}$. Thus, one can perform calculations for smaller baths and scale them up to the orders of magnitude relevant under experimental conditions. Whether such a scaling still holds in the system with external magnetic field while being subjected to periodic pulses is one of the open issues in the field.

The objective of this chapter is to make use of the methodological progress developed in the previous chapter to consider the effect of periodic pulses on the CSM. We do not aim at a quantitative simulation of the experimental scenario yet; this is the subject of Chaps. 6 and 7. In order to keep the simulations simple and efficient, we study two kinds of pulses: a classical and a semiclassical pulse. Both pulses orient the central spin along the z axis, independent of the direction it had before the pulse. Thus, the alignment induced by the pulse is perpendicular to the applied external magnetic field, which is oriented along the x axis (Voigt geometry). The semiclassical pulse also accounts for the quantum mechanical uncertainty. The pulse relations derived in Sec. 2.2.2 are considered in the following chapters.

The chapter is set up as follows.[1] In Sec. 5.1, the model to be studied is specified and the two different pulse models are introduced. In Sec. 5.2, representative results are provided for the CSM subjected to periodic pulses without coupling of the bath spins to the external magnetic field, i.e., the nuclear Zeeman effect is neglected. Clear evidence for NIFF is found. The scaling behavior with respect to the size of the spin bath and to the applied magnetic field is studied. In Sec. 5.3, the influence of the additional Larmor precession of the nuclear spins about the external magnetic field, which turned out to be relevant for the nonequilibrium dynamics [117, 122, 142], is investigated. Finally, the most promising model is applied to an experimental scenario in Sec. 5.4.[2] A conclusion is given in Sec. 5.5.

5.1 Model and simulation

In the following, the ingredients for the semiclassical simulation of the CSM by means of the Spectral Density approach are summarized. The theoretical foundation for this approach is the TWA introduced in Sec. 3.3.

[1] This chapter is based on the author's publication [252], ©2018 American Physical Society. J. Hüdepohl performed early calculations on this topic for his master's thesis [248] supervised by G. S. Uhrig and B. Fauseweh. The author continued this work by studying different pulse models and including the nuclear Zeeman effect. Further contributions were the calculation of all data, creation of all figures, and writing the major parts of the manuscript.

[2] This section is based on the author's contribution to Ref. [117] (Sec. VI therein), ©2018 American Physical Society.

5.1.1 Semiclassical central spin model with transverse magnetic field

The classical Hamiltonian of the CSM with magnetic field to be considered is given by

$$\mathcal{H}_{\mathrm{QD}} = \sum_{k=1}^{N} A_k \boldsymbol{S} \cdot \boldsymbol{I}_k - hS^x - h_{\mathrm{n}} \sum_{k=1}^{N} I_k^x \,, \tag{5.1}$$

where the classical three-dimensional vector $\boldsymbol{S}$ represents the central electron spin and the vectors $\boldsymbol{I}_k$ represent the N nuclear spins forming a spin bath. The hyperfine couplings A_k represent the coupling between the electron spin and the nuclear spins. The external magnetic field $h = \gamma_{\mathrm{e}} B_{\mathrm{ext}} = g_{\mathrm{e}} \mu_{\mathrm{B}} \hbar^{-1} B_{\mathrm{ext}}$ is applied in Voigt geometry, i.e., along the x axis. A generic electronic g factor is $g_{\mathrm{e}} = 0.555$ [25].[3] The last term in Eq. (5.1) is the nuclear Zeeman term with $h_{\mathrm{n}} = \gamma_{\mathrm{n}} B_{\mathrm{ext}}$, where $\gamma_{\mathrm{n}} = \gamma_{\mathrm{e}}/800$ is approximately an average value for the gyromagnetic ratio of the nuclear spins in GaAs or InGaAs QDs [117, 122, 142, 167]. This factor takes into account that the nuclear magnetic moment is three orders smaller than the electronic one.

The hyperfine couplings A_k are proportional to the probability density of the localized electron at the position of the kth nucleus. As discussed in detail in Secs. 3.1.2 and 4.1, a plausible choice for the parameterization of the couplings in self-assembled QDs is

$$A_k = C \exp(-k\gamma) \,, \qquad k \in \{1, 2, \ldots, N\} \,. \tag{5.2}$$

Here, C is an energy constant and $\gamma \ll 1$ is a small parameter given by $\gamma = 2/N_{\mathrm{eff}}$, with N_{eff} being the number of effectively coupled bath spins. Note that the total number of bath spins N is essentially infinite because all spins in the QD are coupled to the central spin, but most of them extremely weakly. The number N_{eff} quantifies the number of bath spins that are *effectively* coupled to the central spin; see Sec. 3.1.2 and 4.1 for details. A realistic value for γ in QDs with $N_{\mathrm{eff}} = 10^4 - 10^6$ effectively coupled nuclear spins [19, 103–107] is $\gamma = 10^{-4} - 10^{-6}$.

[3] Note that we consider the coupling to the external magnetic field with negative sign in this chapter. This is different from the other parts of the thesis, but the replacement $B_{\mathrm{ext}} \to -B_{\mathrm{ext}}$ easily recovers the coupling with a positive sign. Similarly, the electronic g factor in InGaAs QDs is actually negative [132]. But for the physics to be investigated, the sign with which the magnetic field couples to the spins is not of particular importance because of symmetry reasons: the Overhauser field is represented as a random classical field centered around zero polarization. The sign becomes important whenever the direction of a certain polarization needs to be uniquely identified.

The energy constant C in Eq. (5.2) is specified via the square root of the sum of the squared couplings

$$A_{\mathrm{Q}} = \sqrt{\sum_{k=1}^{N} A_k^2} \tag{5.3}$$

because this energy scale determines the dynamics of the central spin for short times. The corresponding timescale A_{Q}^{-1} is of the order of nanoseconds [19, 104]. For small values of γ in the limit $N \to \infty$ of an infinite bath size, $C = \sqrt{2\gamma} A_{\mathrm{Q}}$ results in leading order in γ; see Eq. (4.5).

The Overhauser field $\boldsymbol{B}_{\mathrm{ov}}$ is the sum of all bath spins weighted by their coupling constant,

$$\boldsymbol{B}_{\mathrm{ov}} = \sum_{k=1}^{N} A_k \boldsymbol{I}_k \,. \tag{5.4}$$

Since we assume that the initial bath is completely disordered, we describe it by randomly chosen initial conditions with mean value zero. The variances of the Overhauser field components $\boldsymbol{B}_{\mathrm{ov}}^{\alpha}$, $\alpha \in \{x, y, z\}$ shall mimic their quantum mechanical counterpart, i.e.,

$$\mathrm{Var}\left[B_{\mathrm{ov}}^{\alpha}\right] = \frac{5}{4} A_{\mathrm{Q}}^2, \tag{5.5}$$

where the factor $5/4$ follows from the observation that all nuclear spins in GaAs QDs have $I = 3/2$ if no indium needs to be considered [167, 169]. This simplification is lifted in Chap. 7.

5.1.2 Setup of the simulation

The equations of motion resulting from the classical Hamiltonian (5.1) are the well-known differential equations describing precessions

$$\frac{\mathrm{d}}{\mathrm{d}t}\boldsymbol{S} = (\boldsymbol{B}_{\mathrm{ov}} - h\boldsymbol{e}_x) \times \boldsymbol{S} \,, \tag{5.6a}$$

$$\frac{\mathrm{d}}{\mathrm{d}t}\boldsymbol{I}_k = (A_k \boldsymbol{S} - h_{\mathrm{n}}\boldsymbol{e}_x) \times \boldsymbol{I}_k \,, \qquad k \in \{1, 2, \ldots, N\} \,, \tag{5.6b}$$

where $\boldsymbol{e}_x$ is the unit vector along the x axis. While these equations can be solved numerically by standard algorithms such as Runge-Kutta methods of various orders, the direct simulation of $10^4 - 10^6$ equations, let alone of an infinite number of them, is not an option. For this reason, we resort to the very efficient Spectral

Density approach developed in Sec. 4.2.3, where the ensemble of bath spins parameterized according to Eq. (5.2) in the continuum limit $N \to \infty$ is represented by the linear spectral density given by Eq. (4.36).

In the following, the Spectral Density approach is briefly recapitulated. In this approach, the equations of motion (5.6b) for the N bath spins $\boldsymbol{I}_k$ are replaced by the N_{tr} equations of motion

$$\frac{\mathrm{d}}{\mathrm{d}t}\boldsymbol{Q}_k = (\varepsilon_k \boldsymbol{S} - h_{\mathrm{n}}\boldsymbol{e}_x) \times \boldsymbol{Q}_k \tag{5.7}$$

for the auxiliary fields $\boldsymbol{Q}_k$, which represent linear sums of bath spins. In this representation, the Overhauser field is given by

$$\boldsymbol{B}_{\mathrm{ov}} = \sum_{k=1}^{N_{\mathrm{tr}}} \sqrt{W_k}\boldsymbol{Q}_k \,. \tag{5.8}$$

The energies ε_k and weights W_k follow from the discretization of the spectral density (4.36), which is explained around Eq. (4.40). A visualization of the discretization procedure is given in Fig. 4.1. The key advantage is that the dimension $3(N_{\mathrm{tr}}+1)$ of the ODE is only $\mathcal{O}(10^2)$ instead of $\mathcal{O}(10^4 - 10^6)$. This substantial reduction is achieved thanks to the uniform convergence of the Spectral Density approach with the truncation parameter N_{tr}. In the time interval for which the discretization of the weight function is optimized, the accuracy is essentially the same for all times. The deviations show a better than quadratic decrease when increasing N_{tr}.

We use the semiclassical simulation based on the Gaussian TWA as approximation of the quantum mechanical problem (Sec. 3.3). In this semiclassical approach, the solutions calculated from the classical equations of motion must be averaged over M random initial configurations to determine the autocorrelation function

$$S^{zz}(t) \coloneqq \overline{S^z(t)S^z(0)} \tag{5.9}$$

as approximation of the quantum mechanical autocorrelation function $\langle \hat{S}^z(t)\hat{S}^z(0)\rangle$. The averaging over the classical trajectories is denoted by the overline in Eq. (5.9). Each spin component of each bath spin and of the central spin is chosen according to normal distributions centered around zero and with variance $1/4$ for the central electron spin ($S = 1/2$) and with variance $5/4$ for the bath spins ($I = 3/2$). Since

the auxiliary fields $\boldsymbol{Q}_k$ represent linear sums of many bath spins, their components are also normally distributed. Furthermore, different fields are uncorrelated. Hence, we have to ensure that

$$\overline{Q_j^\alpha Q_k^\beta} = \frac{5}{4}\,\delta_{jk}\,\delta_{\alpha\beta} \tag{5.10}$$

holds at $t = 0$, which is easily realized by initializing the $3N_{\mathrm{tr}}$ components Q_k^α according to normal distributions with variance $5/4$ and mean value zero. The same variance for all Q_k^α can be chosen because we consider a single species of nuclear spins with $I = 3/2$ for simplicity. The influence of the different numbers of bath spins contributing to the auxiliary fields $\boldsymbol{Q}_k$ is accounted for by the weights W_k, which enter in the calculation of the Overhauser field as given by Eq. (5.8).

5.1.3 Pulse models

Next, we turn to the pulses acting on the central spin. In real experiments, the optical pulses of circularly polarized light with well-defined frequency excite trions of only one spin orientation (see Sec. 2.2). The trions decay fast on the timescale of 400 ps [23, 111], leaving behind a partially polarized spin if a transverse magnetic field is applied [23, 112–114, 117, 122, 135, 141]. In this chapter, we neglect this time and mimic the whole pulse by an instantaneous orientation of the central spin along the z axis.

As a first description of the pulse, we consider pulse model I given by the relation

$$\boldsymbol{S}_{\mathrm{a}} = \begin{pmatrix} 0 \\ 0 \\ |\boldsymbol{S}_{\mathrm{b}}| \end{pmatrix}, \tag{5.11}$$

which orients the full central spin vector $\boldsymbol{S}$ onto the z axis while preserving its length, i.e., the vector is simply rotated. Note that the pulse is always applied separately to each of the M configurations, not to the averaged quantity $\overline{\boldsymbol{S}}$ (this is also true for all other pulses considered in the thesis). The subscripts denote the central spin vector before ('b') and after ('a') the pulse. This pulse is idealized in the sense that it does not respect Heisenberg's uncertainty relation for the central spin. It is very close to the classical pulse studied by Petrov and Yakovlev [139], which simply sets $\boldsymbol{S}_{\mathrm{a}} = \boldsymbol{e}_z/2$. In our case, the initial components $\boldsymbol{S}(0)$ are random as a

consequence of the application of the Gaussian TWA, i.e., the vector length is fixed at $t = 0$ such that it reproduces on average the quantum mechanical expectation values $\langle \hat{\boldsymbol{S}}^2 \rangle = S(S+1) = 3/4$ and $\langle (\hat{S}^\alpha)^2 \rangle = 1/4$ for a spin with $S = 1/2$.

Pulse model II is set up to mimic the quantum mechanical aspects better. The guiding idea is that *each* application of a pulse represents a quantum mechanical measurement with the definite outcome of a spin $|\uparrow\rangle$ state. In the framework of the Gaussian TWA, this case can be modeled by the following Wigner function that describes the central spin components after a pulse,

$$W(S_\mathrm{a}^x, S_\mathrm{a}^y, S_\mathrm{a}^z) \approx \frac{2}{\pi} \exp\left(-\frac{(S_\mathrm{a}^x)^2 + (S_\mathrm{a}^y)^2}{4} \right) \delta\left(S_\mathrm{a}^z - \frac{1}{2} \right), \tag{5.12}$$

where $\delta(S^z - 1/2)$ is the Dirac delta function that ensures the definite outcome $S_\mathrm{a}^z = 1/2$ [230, 237]. Because of the quantum mechanical uncertainty, the outcome is random for the transverse components in accordance with the quantum mechanical expectation values $\langle (\hat{S}^\alpha)^2 \rangle = 1/4$. Translating this choice of the Wigner function to a concrete pulse model requires that the components of the central spin after a pulse are given by

$$\boldsymbol{S}_\mathrm{a} = \begin{pmatrix} X \\ Y \\ \frac{1}{2} \end{pmatrix}, \tag{5.13}$$

where X and Y are chosen for each pulse at random from a normal distribution around zero with variance $1/4$. This implies vanishing expectation values of X and Y while ensuring that the quantum mechanical expectation values for the spin length $\langle \hat{\boldsymbol{S}}^2 \rangle = S(S+1) = 3/4$ and $\langle (\hat{S}^\alpha)^2 \rangle = 1/4$ are reproduced on average after each pulse. Since the pulse model II is based on the TWA, it be considered as semiclassical.

Alternatively, X and Y could be chosen uniformly distributed on a circle with radius $X^2 + Y^2 = (1/2)^2$, which would be a third pulse model. However, we tested that the difference to pulse model II is hardly noticeable and hence, we restrict ourselves to pulse model II in addition to pulse model I. We expect that pulse model I is more efficient in generating NIFF, but pulse model II should be more realistic in terms of mimicking the quantum mechanical system.

5.2 Results without nuclear Zeeman effect

We start the numerical analysis by neglecting the nuclear Zeeman term in the Hamiltonian (5.1), i.e., we set $h_\mathrm{n} = 0$. The influence of this term is studied later in Sec. 5.3 by comparing the results of this section with simulations in which the nuclear Zeeman effect is included.

Typical experiments are performed at external magnetic fields of 0.5 to 10 T [24, 25, 95, 117, 122]. In our units, 1 T corresponds approximately to $h = 40A_\mathrm{Q}$. The pulses in the experiments are usually applied with a repetition time of $T_\mathrm{R} = 13.2\,\mathrm{ns}$. In the simulations, we use $T_\mathrm{R} = 5\pi A_\mathrm{Q}^{-1}$, which is roughly in the experimentally relevant range if A_Q^{-1} is of the order of 1 ns [19, 104]. The repetition time is chosen as a multiple of πA_Q^{-1} to make effects stemming from commensurability easier to discern. A concrete conversion to SI units takes place in Sec. 5.4.

The results presented in this chapter stemming from semiclassical simulations are averaged over $M = 10^5$ trajectories starting from random initial configurations if not stated otherwise. The results for representative illustrations are averaged over $M = 10^6$ configurations. The truncation parameter is chosen to be $N_\mathrm{tr} = 44$ for simulations in which up to $n_\mathrm{p} = 10^4$ pulses are applied. For simulations with more pulses, N_tr is increased such that the discretization parameter λ defined in Eq. (4.40) remains constant. This ensures the same accuracy level independent of the number of pulses studied. Based on the analysis in Sec. 4.3.3, it turned out that $\lambda \approx 0.87$ is a good choice to obtain reliable results. Note that thanks to the exponential discretization of the weight function, the truncation parameter has to be increased only slightly for much longer simulations, e.g., $N_\mathrm{tr} = 58$ is sufficient to study ten times more pulses ($n_\mathrm{p} = 10^5$).

5.2.1 Results for pulse model I

Figure 5.1 shows the dynamics of the central spin caused by the periodic application of pulses of type I [Eq. (5.11)] in an external magnetic field of $h = 40A_\mathrm{Q}$. In the upper panel, the dynamics of the central spin after the first two pulses is shown. After the incidence of a pulse ($t/T_\mathrm{R} = 0, 1, 2, \dots$), the autocorrelation $S^{zz}(t)$ always takes the value 0.75 because initially, all three components of the central spin are sampled from a normal distribution with mean value zero and variance 1/4 that

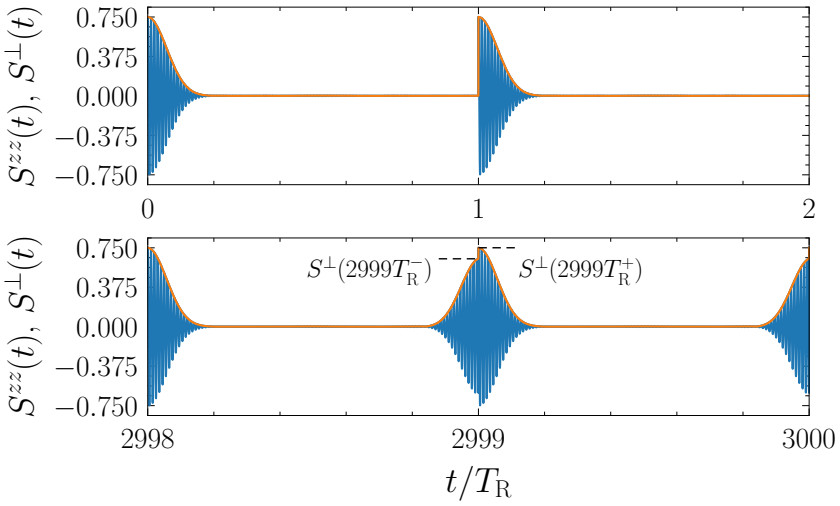

Figure 5.1: Representative result for the autocorrelation $S^{zz}(t)$ defined in Eq. (5.9) (blue) when applying trains of pulses of type I [Eq. (5.11)] at a magnetic field of $h = 40A_{\mathrm{Q}}$, pulse repetition time $T_{\mathrm{R}} = 5\pi A_{\mathrm{Q}}^{-1}$, and $\gamma = 10^{-2}$. The envelope $S^{\perp}(t)$ defined in Eq. (5.14b) is depicted in orange.

are then rotated onto the z axis by the pulse (5.11). Afterwards, the central spin precesses about the external magnetic field while dephasing on the timescale A_{Q}^{-1}, analogous to what we have seen using the frozen Overhauser field approximation in Sec. 3.3.4. The dephasing is Gaussian and can be described by Eq. (3.49). After many more pulses (3000 pulses in the case of the lower panel of Fig. 5.1), a strong revival signal is visible just before the next pulse arrives. Its origin is the effect of nuclei-induced frequency focusing, which is analyzed below.

In order not to be distracted by the fast Larmor precession, we address the envelope directly by defining

$$S^{yz}(t) \coloneqq \overline{S^{y}(t)S^{z}(0)}\,, \tag{5.14a}$$

$$S^{\perp}(t) \coloneqq \sqrt{[S^{zz}(t)]^2 + [S^{yz}(t)]^2}\,, \tag{5.14b}$$

and using $S^{zz}(t)$ defined by Eq. (5.9). The modulus $S^{\perp}(t)$ represents the envelope of a fast precession about the x axis along which the external magnetic field is oriented. In Fig. 5.1, the envelope is highlighted in orange.

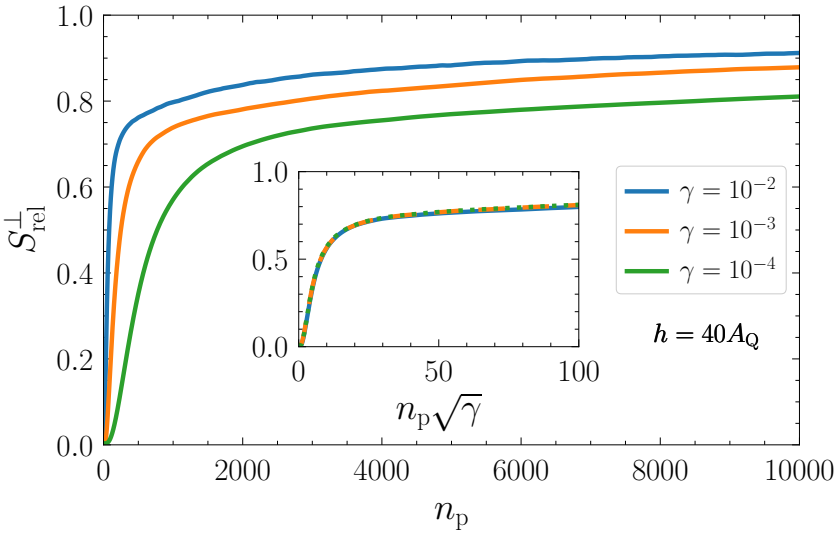

Figure 5.2: Relative revival amplitude $S^{\perp}_{\mathrm{rel}}$ as a function of the number of pulses n_{p} at a magnetic field of $h = 40A_{\mathrm{Q}}$ for various values of the inverse bath size γ using pulse model I from Eq. (5.11). Inset: Excellent data collapse when the time axis is scaled with $\sqrt{\gamma}$.

We characterize the degree of NIFF by studying the relative revival amplitude

$$S^{\perp}_{\mathrm{rel}}(n_{\mathrm{p}}) \coloneqq \frac{S^{\perp}(n_{\mathrm{p}}T_{\mathrm{R}}^{-})}{S^{\perp}(n_{\mathrm{p}}T_{\mathrm{R}}^{+})}\,, \qquad n_{\mathrm{p}} \in \mathbb{N}\,, \tag{5.15}$$

which is the quotient of the envelopes just before $(n_{\mathrm{p}}T_{\mathrm{R}}^{-})$ and after $(n_{\mathrm{p}}T_{\mathrm{R}}^{+})$ a pulse is applied; see Fig. 5.1 at $t/T_{\mathrm{R}} = 2999$. Figure 5.2 shows the buildup of the relative revival amplitude for various inverse bath sizes γ. We already know from Eq. (4.8b) that smaller values of γ correspond to a larger number N_{eff} of effectively coupled bath spins. Since each individual coupling A_k is proportional to $\sqrt{2\gamma}$, the dynamics of each bath spin is slower for smaller values of γ and accordingly, the buildup of the revival amplitude as a consequence of NIFF takes longer.

In view of demanding numerical simulations, we intend to make use of scaling arguments to reduce the required computational resources. In Sec. 4.3.4, a scaling of time with $\sqrt{\gamma}$ is established, but for $h = 0$ and without periodic application of pulses. The inset in Fig. 5.2 demonstrates that this scaling is also valid for the revival amplitude $S^{\perp}_{\mathrm{rel}}(t)$ at a finite magnetic field of $h = 40A_{\mathrm{Q}}$ and periodically applying pulses of type I. Thus, we can study the magnetic field dependence later for one particular value of $\gamma = 10^{-2}$ and scale the results accordingly if smaller

values of γ need to be investigated.

The origin of the revival signal visible in the dynamics of the central spin is a focusing within the Overhauser field distribution along the axis of the external magnetic field, i.e., along the x axis. Since the spin bath in a QD consists of nuclear spins, we refer to this behavior as nuclear focusing. The basic idea is the following: Each pulse kicks the central electron spin and in turn, its motion has a small effect on each bath spin. As long as the central spin does not precess with a frequency commensurable with the pulse repetition rate, these periodic kicks continue to influence the state of the bath spins. Only once commensurability is approached, the periodic application of pulses ceases to influence the distribution of bath spins until a nonequilibrium steady state is reached. Thus, after application of long pulse trains the expected result is a stationary distribution of the Overhauser field that is strongly peaked at polarizations that induce commensurable precessions [25, 117, 122, 139].

To investigate the nuclear focusing quantitatively, we study the probability distribution of the effective magnetic field

$$h_{\mathrm{eff}} \coloneqq |h\boldsymbol{e}_x - \boldsymbol{B}_{\mathrm{ov}}|\,, \tag{5.16}$$

which is the relevant quantity to describe the Larmor precession for each of the independent trajectories in the semiclassical approach. The upper panel in Fig. 5.3 illustrates the dynamic buildup of nuclear focusing after n_{p} pulses. The probability distribution $p(h_{\mathrm{eff}})$ starts as a Gaussian with a variance determined by the initial conditions (5.5). Then, as a consequence of the periodic pulse application, the shape of the distribution evolves towards a comblike structure made up of various peaks. The peaks appear to be perfectly centered around the values of h_{eff} that satisfy the odd resonance condition (ORC)

$$h_{\mathrm{eff}}^{\mathrm{odd}}\, T_{\mathrm{R}} = (2|k|+1)\pi\,, \qquad k \in \mathbb{Z}\,, \tag{5.17}$$

indicated by the dashed vertical lines in Fig. 5.3. This resonance condition is termed to be 'odd' because $2|k|+1$ is an odd integer. It corresponds to a half-integer number of spin revolutions of the central spin within the pulse repetition time T_{R}. The distance between these modes is obviously proportional to T_{R}^{-1}. Small sub-peaks in the middle between the main peaks are found additionally in the early

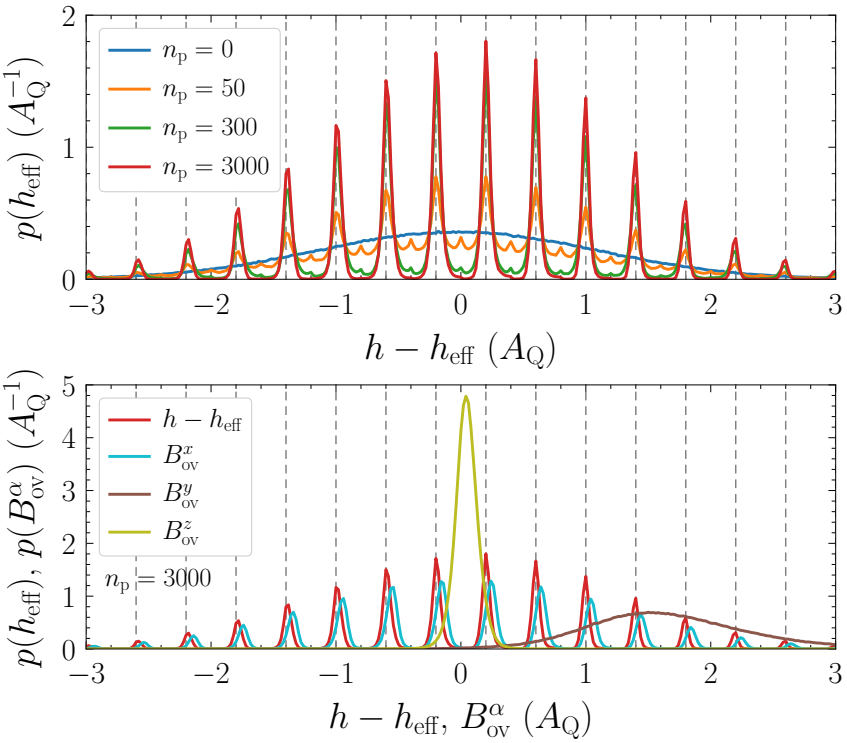

Figure 5.3: Upper panel: Probability distribution $p(h_\mathrm{eff})$ of the effective magnetic field h_eff [defined in Eq. (5.16)], shifted by $h = 40A_\mathrm{Q}$, after n_p pulses of type I at $\gamma = 10^{-2}$. The vertical dashed lines indicate the values of h_eff that satisfy the ORC (5.17). Lower panel: Same as upper panel, but after $n_\mathrm{p} = 3000$ pulses. In addition, the probability distributions of the Overhauser field components B_ov^α, $\alpha \in \{x, y, z\}$, are shown.

stages. Their positions are determined by the even resonance condition (ERC)

$$h_\mathrm{eff}^\mathrm{even}\, T_\mathrm{R} = 2\pi|k|\,, \qquad k \in \mathbb{Z}\,, \tag{5.18}$$

with $2|k|$ being an even integer, corresponding to an integer number of spin revolutions within the pulse repetition time T_R. However, these modes appear to be suppressed quite fast, i.e., after a few hundred pulses.

How do the single components of the Overhauser field B_ov^α evolve? An example is given in the lower panel of Fig. 5.3, in which the probability distributions of the components B_ov^α are shown together with the one of h_eff after $n_\mathrm{p} = 3000$ pulses. Obviously, the comblike structure of the distribution $p(h_\mathrm{eff})$ results mainly from the distribution of B_ov^x, i.e., from the component of the Overhauser field parallel to the external field. This is in accordance with the results of other stud-

ies [24, 25, 117, 122, 139]. However, the peaks found in the distribution $p(B_{\mathrm{ov}}^{x})$ are shifted slightly away from the ORC (5.17). The reason is the finite contribution from transverse components B_{ov}^{y} and B_{ov}^{z} to the effective magnetic field h_{eff}, i.e., they have an influence on the resonance conditions. The influence decreases for larger external fields.

Surprisingly, the probability distribution $p(B_{\mathrm{ov}}^{y})$ is shifted to a finite mean value $\overline{B_{\mathrm{ov}}^{y}} > 0$ while also becoming slightly narrower. For B_{ov}^{z}, a strong narrowing effect occurs so that its contribution to h_{eff} almost vanishes. The finding that the application of periodic pulses can also generate nontrivial Overhauser fields perpendicular to the external magnetic field and to the direction of the polarization of the pulses carries an interesting message also for experiments. It would be interesting to conceive experiments that can measure the components of the Overhauser field perpendicular to the external field. Here, we find that the average y component can be of the order of $|\overline{B_{\mathrm{ov}}^{y}}| \approx 100\,\mathrm{mT}$ after long pulse trains. To our knowledge, however, such effects have not yet been observed experimentally. Usually, such a polarization takes place along the axis of the external field as a consequence of dynamic nuclear polarization [42, 115, 225].

In order to study the process of nuclear focusing quantitatively, we analyze the weight of the even and odd resonances by defining the following intervals. The even resonance is characterized by all values of h_{eff} in the intervals

$$[h_{\mathrm{eff}}^{\mathrm{even}} - \pi/(2T_{\mathrm{R}}),\, h_{\mathrm{eff}}^{\mathrm{even}} + \pi/(2T_{\mathrm{R}})]\ . \tag{5.19}$$

Their normalized number with respect to the configuration size M defines the weight Σ_{even}. Analogously, the odd resonance is characterized by all values of h_{eff} in the intervals

$$\left[h_{\mathrm{eff}}^{\mathrm{odd}} - \pi/(2T_{\mathrm{R}}),\, h_{\mathrm{eff}}^{\mathrm{odd}} + \pi/(2T_{\mathrm{R}})\right]\ . \tag{5.20}$$

Obviously, the relation

$$\Sigma_{\mathrm{even}}(n_{\mathrm{p}}) + \Sigma_{\mathrm{odd}}(n_{\mathrm{p}}) = 1 \tag{5.21}$$

holds for all times and hence, it is sufficient to investigate only one of the two weights; we choose Σ_{even}. Initially, both weights have the same value of 0.5. In case of a perfect even resonance, Σ_{even} rises to unity. In case of a perfect odd resonance, it

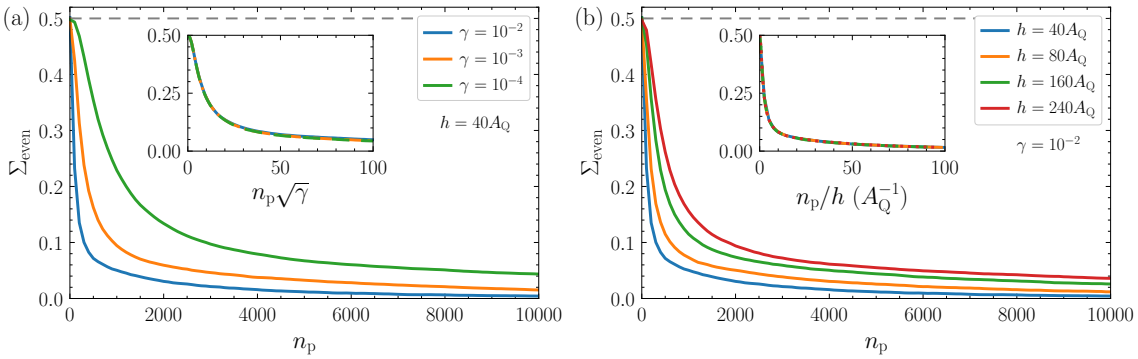

Figure 5.4: (a) Dependence of the weight Σ_{even} on the number of pulses n_{p} at $h = 40A_{\mathrm{Q}}$ for various inverse bath sizes γ using pulse model I. Inset: Excellent data collapse when scaling the number of pulses n_{p} with $\sqrt{\gamma}$. **(b)** Same as (a), but for fixed $\gamma = 10^{-2}$ and varying the external field h. Inset: Excellent data collapse when scaling the number of pulses n_{p} with $1/h$.

shrinks to zero. Figure 5.4(a) depicts Σ_{even} as a function of the number of pulses for various values of γ at $h = 40A_{\mathrm{Q}}$. Again, the scaling with $\sqrt{\gamma}$ leads to a remarkable collapse of the curves as demonstrated in the inset. Therefore, we conclude that the degree of nuclear focusing in the effective field, i.e., the convergence of Σ_{even} to zero, directly influences the relative revival amplitude $S_{\mathrm{rel}}^{\perp}$ of the central spin.

Up to now, we only studied external fields of moderate strength, i.e., $h = 40A_{\mathrm{Q}}$. The question arises as to what happens when h is increased. For now, we restrict ourselves to the range $h \in [40A_{\mathrm{Q}}, 240A_{\mathrm{Q}}]$, corresponding to fields of approximately 1 to 6 T in experiments. Figure 5.4(b) shows the time dependence of the weight Σ_{even} for various magnetic fields h. In general, the application of a larger field results in a slower buildup of nuclear focusing. We find that a scaling of time with $1/h$ leads to a perfect collapse of the curves as demonstrated in the inset of Fig. 5.4(b).

The linear scaling at high magnetic fields is at odds with the quantum mechanical analysis of Ref. [141], which indicates a quadratic scaling $\propto 1/h^2$. The quadratic scaling is also found in the classical analysis of Ref. [131] for the case that the system is not yet close to the resonance condition, but a different pulse model is used and the nuclear Zeeman effect is accounted for. Indeed, we will see in the following sections that the classical pulse (5.11) and neglecting the nuclear Zeeman effect are both responsible for the observed linear scaling behavior.

Another way to investigate the resonance behavior is to compare the phases of the

revival signal to the post-pulse signal. If there is a phase shift by π, the resonance is odd. If there is no phase shift, the resonance is even. In principle, also other phase shifts could occur. The details of this analysis are given in Appendix B. We always find a phase shift of π with deviations up to 3%, demonstrating the dominance of the odd resonance in agreement with the analysis of $\Sigma_{\text{even}} < 0.5$. Thus, this pulse model clearly favors odd resonances in agreement with what is found without nuclear Zeeman effect in a quantum mechanical analysis for small spin baths [141]. The nuclear Zeeman effect can have an important impact on the resonance condition [117, 122, 142], i.e., it can change the resonance chosen by the system. We come back to this point in Sec. 5.3 where the effect is included.

In summary, the application of periodic pulses of type I leads to efficient nuclear focusing at odd resonance. The rate of the nuclear focusing scales with $\sqrt{\gamma}$, i.e., it is inversely proportional to the square root of the effective bath size. In addition, the rate scales inversely proportional with the external magnetic field h, which is at odds with the finding of a quantum mechanical approach [141] and also with a classical approach [131] that accounts for the nuclear Zeeman effect. We attribute this discrepancy to the both the classical nature of pulse model I and to the omission of the nuclear Zeeman effect. Generally, the scalings with $\sqrt{\gamma}$ and $1/h$ generate very nice data collapses so that quantitative extrapolations are possible with a high degree of accuracy.

5.2.2 Results for pulse model II

Next, we turn to pulse model II and carry out the same analyses as for pulse model I. The motivation is twofold. First, we want to see to which extent the previous findings change if the pulse is changed. The underlying issue is whether and to which extent the findings are robust to the details of the pulse. Second, pulse model II is closer to a quantum mechanical pulse because it accounts for the uncertainty principle and hence, we are interested in its phenomenology.

Indeed, several qualitative differences are found. Overall, the tendency for the system to show nuclear focusing is much less pronounced for pulse model II than for pulse model I. This can be seen by comparing the lower panel of Fig. 5.5 to the lower panel of Fig. 5.1. In both figures, representative spin dynamics are shown after the same number of pulses for identical parameters but using the two different

pulses. The comparison of Fig. 5.6 to Fig. 5.2, which show the buildup of the relative revival amplitude $S^{\perp}_{\mathrm{rel}}$ for various values of γ at $h = 40A_{\mathrm{Q}}$, is more quantitative. The obvious difference is that the revival signal when using pulse model II does not reach amplitudes as large as when using pulse model I (note the different scales on the y axes). In addition, the data is much noisier because of the statistical component of pulse model II described by Eq. (5.13). The statistical fluctuations decrease with $1/\sqrt{M}$ for larger configuration sizes M.

The most striking feature, however, is the *nonmonotonic* dependence of the relative revival amplitude on the inverse bath size γ; see Fig. 5.6. The fastest buildup of the revival amplitude is found for $\gamma = 10^{-2}$, but for $\gamma = 10^{-4}$ it is only slower by approximately a factor of 2 while reaching a larger saturation value. Obviously, no scaling with any power of γ can lead to a collapse of the curves. Quite unexpectedly, the buildup for $\gamma = 10^{-3}$ is slower than for the other two curves and no significant revival amplitude is reached at all. The revival amplitudes for $\gamma = 3 \times 10^{-3}$ and $\gamma = 3 \times 10^{-4}$ are also rather small, but larger than for $\gamma = 10^{-3}$. Hence, we assume that there is a qualitative transition occurring at around $\gamma \approx 10^{-3}$. We come back to this point later.

We stress that the saturation values of the relative revival amplitude stay far away from the theoretical maximum of unity, i.e., the periodic pulses of type II induce only imperfect nuclear focusing. This is in contrast to the results for pulse model I where $S^{\perp}_{\mathrm{rel}}$ reaches almost unity and underlines the importance of the pulse properties.

How does the Overhauser field evolve when applying periodic pulses of type II? The evolution of a representative probability distribution $p(h_{\mathrm{eff}})$ of the effective magnetic field is depicted in the upper panel of Fig. 5.7 for $h = 40A_{\mathrm{Q}}$ and $\gamma = 10^{-2}$. The peaks in the distribution of the effective magnetic field are much broader and smaller in amplitude, i.e., the degree of nuclear focusing is much less pronounced compared to the distribution induced by the periodic application of pulse model I (see Fig. 5.3). The peaks in Fig. 5.7 are not located at values of the effective field that fulfill the ORC (5.17). Instead, the peak positions correspond to the ERC (5.18). Note that in contrast to the distribution obtained for pulse model I, the y and z components of the Overhauser field maintain their initial Gaussian shape (lower panel). Yet, the peaks found in the distribution of B^{x}_{ov} are still shifted slightly to the right of the theoretically expected resonance condition. This is not the case

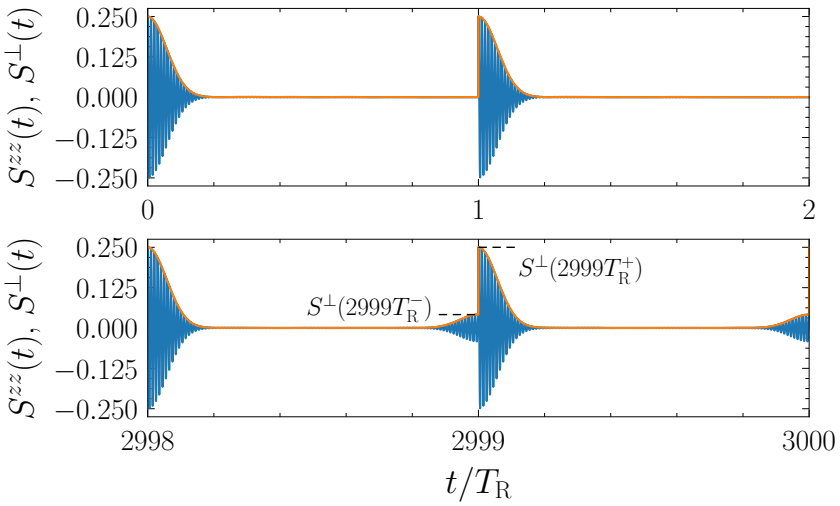

Figure 5.5: Representative result for the autocorrelation $S^{zz}(t)$ defined in Eq. (5.9) (blue) when applying trains of pulses of type II from Eq. (5.13) at a magnetic field of $h = 40A_{\mathrm{Q}}$, pulse repetition time $T_{\mathrm{R}} = 5\pi A_{\mathrm{Q}}^{-1}$, and $\gamma = 10^{-2}$. The envelope $S^{\perp}(t)$ defined in Eq. (5.14b) is depicted in orange.

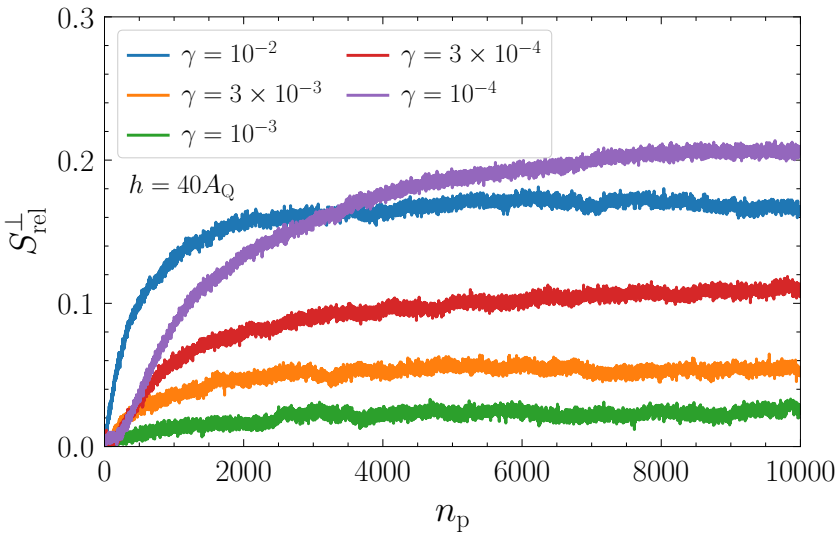

Figure 5.6: Relative revival amplitude $S^{\perp}_{\mathrm{rel}}$ as a function of the number of pulses n_{p} at $h = 40A_{\mathrm{Q}}$ for various inverse bath sizes γ using pulse model II.

for the distribution of the effective magnetic field because it also incorporates the influence of the transverse components B_{ov}^{y} and B_{ov}^{z} on the Larmor frequency. As before, the shift decreases for larger external fields.

When pulses of type II are applied long enough, the distribution of the effective magnetic field becomes quasistationary. This means that it does not change anymore if it is analyzed stroboscopically, i.e., at a given instant in time relative to the pulses, for instance just before each pulse. But the peaks in the distribution do not become arbitrarily sharp: they keep a substantial width and there is always some weight around both kinds of resonances. This qualitative behavior is confirmed quantitatively by the weight $\Sigma_{\mathrm{even}}(n_{\mathrm{p}})$ approaching neither zero nor one as we will see in the following.

Remarkably, we find a transition from even to odd resonance when studying smaller

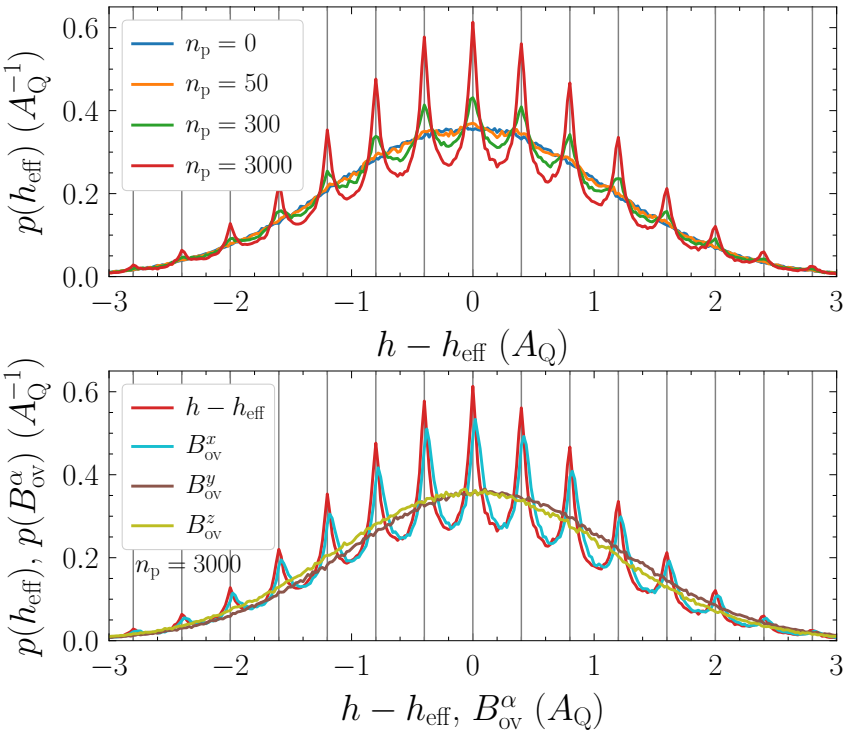

Figure 5.7: Upper panel: Probability distribution $p(h_{\mathrm{eff}})$ of the effective magnetic field, shifted by $h = 40A_{\mathrm{Q}}$, after n_{p} pulses of type II at $\gamma = 10^{-2}$. The vertical solid lines indicate the values of h_{eff} that satisfy the ERC (5.18). Lower panel: Same as upper panel, but after $n_{\mathrm{p}} = 3000$ pulses. Additionally, the probability distributions of the Overhauser field components B_{ov}^{α}, $\alpha \in \{x, y, z\}$, are shown.

values of γ. This is demonstrated in Fig. 5.8 for the weight Σ_{even} at $h = 40A_{\mathrm{Q}}$ and $80A_{\mathrm{Q}}$. Upon reducing γ, the even resonance ($\Sigma_{\mathrm{even}} > 0.5$) is replaced by the odd resonance ($\Sigma_{\mathrm{even}} < 0.5$). It is not a continuous shift of the peak positions in the Overhauser field distribution leading to this transition. Instead, the probability distribution $p(h_{\mathrm{eff}})$ of the effective magnetic field becomes featureless at the transition point between even and odd resonance, e.g., at $\gamma \approx 10^{-3}$ and $h = 40A_{\mathrm{Q}}$. No coexistence of even and odd resonances as found in the semiclassical analysis of Ref. [122] is observed.

We emphasize that Fig. 5.8 indicates that the change of the Overhauser field distribution occurs at a rate proportional to $\sqrt{\gamma}$. Even though we change γ by two orders of magnitude, the curves in Fig. 5.8 approach saturation after approximately the same number of scaled pulses $n_{\mathrm{p}}\sqrt{\gamma}$. Since Σ_{even} shows a nonmonotonic dependence on γ because of the resonance transition, the impossibility to achieve a data collapse by the scaling is obvious. Yet, the characteristic timescale remains $\sqrt{\gamma}A_{\mathrm{Q}}$ as for pulse model I.

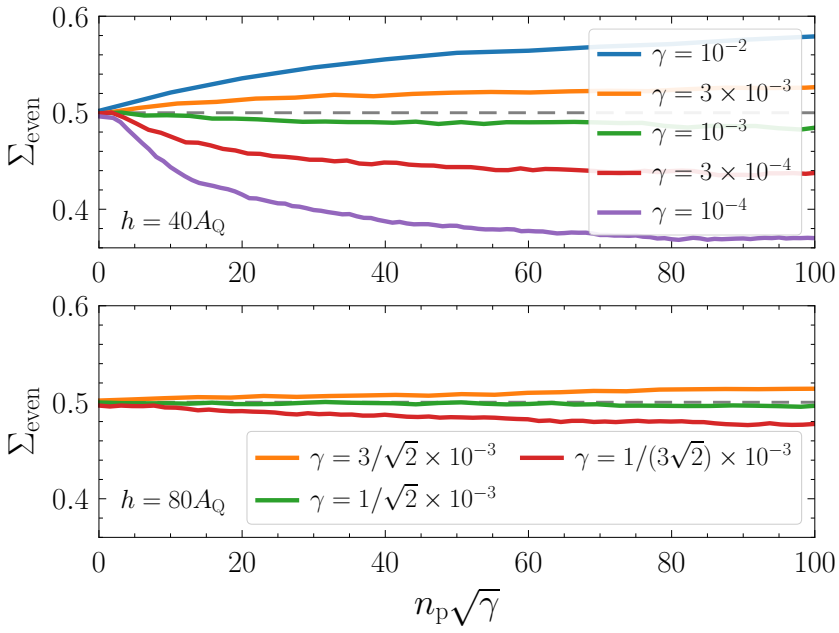

Figure 5.8: Upper panel: Dependence of the weight Σ_{even} on the scaled number of pulses $n_{\mathrm{p}}\sqrt{\gamma}$ at $h = 40A_{\mathrm{Q}}$ for various inverse bath sizes y using pulse model II. Lower panel: Same as upper panel, but for $h = 80A_{\mathrm{Q}}$ and adjusted values of γ such that $P = h\gamma^2$ remains constant.

To corroborate the existence of the transition between even and odd resonance, we investigate the phase shift $\Delta\varphi$ obtained by fitting the autocorrelation $S^{zz}(t)$ just before and just after a pulse. We analyze the combinations of h and γ used in Fig. 5.8 and some other parameter combinations. As expected, the phase shifts are directly connected to the parity of the resonance: if $\Sigma_{\text{even}} > 0.5$, no phase shift occurs, whereas it takes the value π if $\Sigma_{\text{even}} < 0.5$. More details of this analysis can be found in Appendix B.

To our knowledge, this kind of transition has not yet been observed in other, similar calculations. At present, we do not have an explanation for its occurrence because there are so many energy scales in the problem so that various combinations can become relevant. But we strive to provide a heuristic description for which parameters h and γ the transition occurs. From a wide range of numerical experiments, the working hypothesis ensues that the transition occurs for

$$P := h\gamma^2 = \text{const}\,. \tag{5.22}$$

We find that for $h = 40A_{\text{Q}}$ and $\gamma = 1.5 \times 10^{-3}$, no tendency towards even or odd resonance is apparent so that this parameter combination provides the estimate $P = 9 \times 10^{-5}A_{\text{Q}}$. From this value, we generate other possible combinations of h and γ that should correspond to parameters at the transition according to the conjecture (5.22). Figure 5.9 puts this conjecture to a test. Note that the scale on the ordinate is roughly five times smaller than in Fig. 5.8. Indeed, for large enough external fields, the conjecture (5.22) appears to hold within the statistical accuracy. We point out that this result is not very sensitive to the precise value of P. For instance, a similar plot as in Fig. 5.9 can be obtained for $P = 3.8 \times 10^{-5}A_{\text{Q}}$.

Next, the issue of scaling the dynamics with the magnetic field h arises. We cannot expect a simple power-law scaling close to the resonance transition, just as we did not find a power-law scaling with γ because of the transition. Yet, the typical rate of nuclear focusing can be investigated far away from the transition to see whether a scaling law can be identified. There are two ways to keep away from the transition. Either one stays far in the regime of even resonance, i.e., for relatively small spin baths (large values of γ) at a given magnetic field, or one stays far in the regime of odd resonance, i.e., for relatively large spin baths (small values of γ). If we take the above determined value of $P = 9 \times 10^{-5}A_{\text{Q}}$ and insert $\gamma = 10^{-5}$ into Eq. (5.22), we obtain $h = 9 \times 10^{5}A_{\text{Q}}$, which corresponds to a magnetic field larger than $2 \times 10^{4}\,\text{T}$.

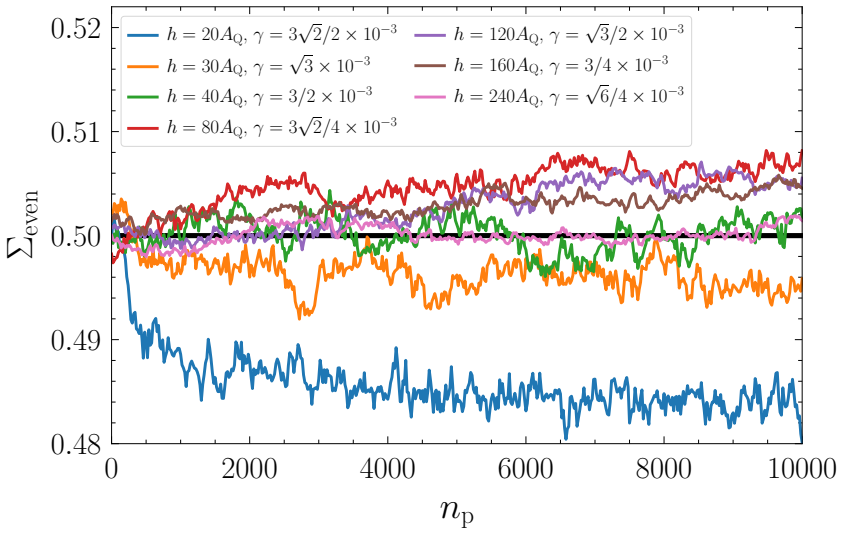

Figure 5.9: Dependence of the weight Σ_{even} on the number of pulses n_p for various pairs of magnetic field h and inverse bath size γ fulfilling $P = h\gamma^2 = 9 \times 10^{-5} A_Q$ to test the conjecture (5.22).

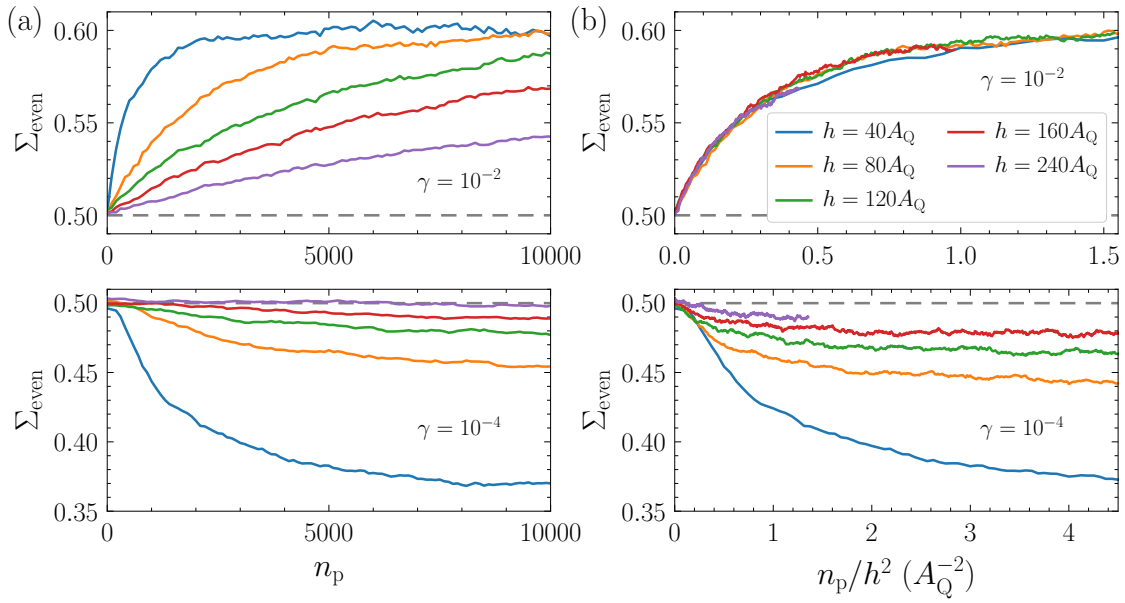

Figure 5.10: **(a)** Upper panel: Dependence of the weight Σ_{even} on the number of pulses n_p at $\gamma = 10^{-2}$ for various magnetic fields h using pulse model II. Lower panel: Same as upper panel, but for $\gamma = 10^{-4}$. **(b)** Same as (a), but the scaled number of pulses n_p/h^2 is plotted on the abscissa.

Hence, systems with bath sizes of this magnitude such as QDs are expected to be in the regime of odd resonance without nuclear Zeeman effect. Other systems with much smaller spin baths, e.g., NV centers or spins in organic molecules, can very well be in the regime of even resonance. Note that the practical importance of these implications are limited because we will see that the nuclear Zeeman effect has a significant impact on the physics.

First, we study the regime of even resonance. The upper panel of Fig. 5.10(a) displays the buildup of Σ_{even} for $\gamma = 10^{-2}$ and various external fields h. Clearly, larger fields imply a slower buildup as expected. Can we reach a data collapse by rescaling the number of pulses n_{p} by a power of h? For pulse model I, we succeeded in doing so with a linear scaling, but it does not work here. Instead, the rate of the increase of Σ_{even} scales with $1/h^2$. This is shown by the collapse of the curves in displayed in the upper panel of Fig. 5.10(b). This scaling is in agreement with the quantum mechanical [141] and the classical [131] result mentioned before.

Next, we address the regime of odd resonance occurring for very large spin baths. The lower panel of Fig. 5.10(a) displays the decrease of Σ_{even} at $\gamma = 10^{-4}$ for various external fields h. The number of pulses after which Σ_{even} approaches saturation scales approximately with $1/h^2$ as shown in the lower panel of Fig. 5.10(b). However, the saturation values differ vastly for different fields h, with larger h corresponding to a less pronounced nuclear focusing at the odd resonance.

We summarize that pulse model II without nuclear Zeeman effect displays regimes of even and odd resonance with a transition between the two depending on the precise values of the external magnetic field and of the bath size. According to the heuristic description (5.22) of the transition point, QDs are far in the regime of odd resonance. The overall rate of change of the Overhauser field is proportional to $\sqrt{\gamma}$ and inversely proportional to h^2. The latter agrees with the finding in a quantum mechanical study for small spin baths [141], underlining that pulse model II leads to a better description of the quantum mechanical problem. The data collapse obtained by application of the scaling laws is not quantitative because of the resonance transition and the resulting nonmonotonic dependence on the bath size and on the magnetic field.

5.3 Influence of the nuclear Zeeman effect

In any experiment performed on QDs, an external magnetic field acts on the electron spin as well as on the nuclear spins by the Zeeman effect. In many circumstances, the latter can safely be neglected since it is smaller by three orders of magnitude because of the larger mass of the nuclei compared to the electron mass. But in the CSM as a model for QDs, a magnetic field of about 2 T ($h = 80A_\mathrm{Q}$) is about two orders of magnitude larger than the intrinsic energy scale A_Q of the CSM. For large spin baths with $\gamma \approx 10^{-5}$, the electronic Zeeman energy is four orders of magnitude larger than the largest coupling $A_1 = \sqrt{2\gamma}A_\mathrm{Q} \approx 0.0045A_\mathrm{Q}$. But the nuclear Zeeman energy ($h_\mathrm{n} = 0.1A_\mathrm{Q}$) is one order of magnitude larger than A_1. Even for $\gamma = 10^{-2}$, both energies have the same order of magnitude. Hence, the nuclear Zeeman effect clearly needs to be considered and it is possible that it introduces qualitatively important changes to the physics. For instance, there is evidence that the even resonance can be favored over the odd resonance when the nuclear Zeeman effect is included [117, 122, 142].

The nuclear Zeeman term in the Hamiltonian (5.1) is included by using $h_\mathrm{n} = \gamma_\mathrm{n}B_\mathrm{ext}$ with $\gamma_\mathrm{n}/\gamma_\mathrm{e} = 1/800$ [117, 122, 142, 167], i.e., $h_\mathrm{n} = h/800$. First, the nonequilibrium spin physics resulting from the periodic application of pulses of type I is analyzed. Afterwards, the analysis is repeated for pulse model II.

5.3.1 Pulse model I

The buildup of the relative revival amplitude $S^{\perp}_\mathrm{rel}$ caused by the application of periodic pulses of type I at a magnetic field of $h = 40A_\mathrm{Q}$ is shown in Fig. 5.11 for various values of γ. The relative revival amplitude approaches unity for $\gamma = 10^{-2}$, whereas the curves for smaller values of γ have not yet reached saturation. A comparison to the curves in Fig. 5.2 without nuclear Zeeman effect reveals that this effect slows down the buildup of the revival signal significantly, especially for smaller values of γ.

It is obvious that the scaling with $\sqrt{\gamma}$ does not work anymore. Instead, we find a remarkable data collapse by scaling the number of pulses n_p with γ as demonstrated in the inset of Fig. 5.11. This finding is in agreement with the observation of Jäschke

et al. [122] in a semiclassical analysis for which a scaling with the inverse of the bath size is also found.

The question arises as to why the scaling changes from $\sqrt{\gamma}$ to γ after including the nuclear Zeeman effect. We attribute this qualitative change to the relative strengths of the couplings to which an individual bath spin is subjected. Without nuclear Zeeman effect, the coupling A_k is the only energy relevant for the individual bath spin. These couplings scale like $\sqrt{\gamma}$ and thus, the evolution of the central spin exerts an effect onto each bath spin at a rate proportional to $\sqrt{\gamma}A_\mathrm{Q}$. But if the nuclear Zeeman term $\propto h_\mathrm{n}$ is included, each bath spin is dominated by this term and precesses predominantly about the external magnetic field if $\gamma \ll 1$ as in QDs. Then, the coupling to the central spin, i.e., the precession about the Knight field $A_k\boldsymbol{S}$ in the classical picture, is just a perturbation on top of the coupling to the external field. This perturbation is effective only in second order A_k^2/h_n. This difference is similar to the Stark effect, which is generically second order, but first order if the perturbed system is degenerate, i.e., without internal dynamics. We conclude that with nuclear Zeeman effect, the central spin dynamics influences the bath spins only in second order.

In the following, we exploit the linear scaling in γ and perform the following calcu-

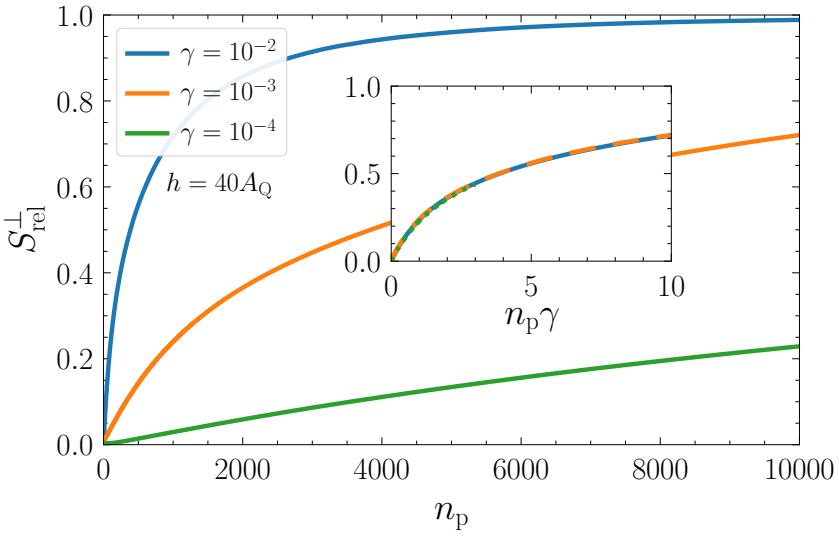

Figure 5.11: Relative revival amplitude $\boldsymbol{S}^\perp_\mathrm{rel}$ as a function of the number of pulses n_p at $h = 40A_\mathrm{Q}$ for various values of γ using pulse model I in presence of the nuclear Zeeman effect. Inset: Excellent data collapse when scaling the number of pulses n_p with γ.

lations for a relatively large value of $\gamma = 10^{-2}$ because no qualitative changes for smaller values are to be expected. We stress that for realistic values $\gamma \approx 10^{-4}-10^{-6}$, all time dependencies are slower by two to three orders of magnitude.

Let us turn to the behavior of nuclear focusing, which is responsible for the revival signal. A representative probability distribution $p(h_{\mathrm{eff}})$ of effective magnetic field is shown in the upper panel of Fig. 5.12. The peaks are located at the values of h_{eff} fulfilling the ERC (5.18), which is in contrast to the observation in Sec. 5.2.1 for the same pulse without nuclear Zeeman effect. The fact that the nuclear Zeeman effect influences the system to favor the even resonance is in line with previous research [122, 142]. Moreover, the peak shape shows a certain asymmetry. The peak width reduces when applying longer pulse trains and eventually, the nuclear focusing appears to become perfect, i.e., the peaks in the distribution of the effective

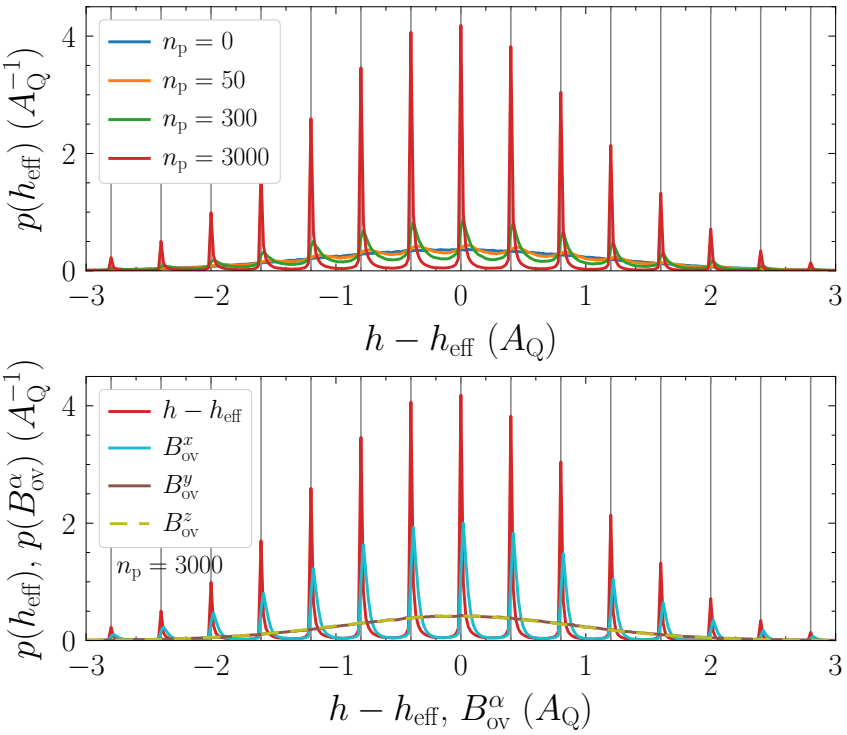

Figure 5.12: Upper panel: Probability distribution $p(h_{\mathrm{eff}})$ of the effective magnetic field, shifted by $h = 40A_{\mathrm{Q}}$, after n_{p} pulses of type I at $\gamma = 10^{-2}$ in presence of the nuclear Zeeman effect. The vertical solid lines indicate the values of h_{eff} that satisfy the even resonance condition (5.18). Lower panel: Same as upper panel, but after $n_{\mathrm{p}} = 3000$ pulses. Additionally, the distributions of the Overhauser field components B_{ov}^{α}, $\alpha \in \{x, y, z\}$, are shown.

magnetic field approach δ peaks. This behavior is strongly corroborated by the relative revival amplitude approaching unity as can be seen in Fig. 5.11.

The inclusion of the nuclear Zeeman effect leads to a drastically different behavior for the individual components of the Overhauser field. The distributions of B_{ov}^{y} and B_{ov}^{z} maintain their initial Gaussian shape and we find no average polarization $|\overline{B_{\mathrm{ov}}^{y}}| > 0$ anymore. Again, the peaks of in the distribution of B_{ov}^{x} are slightly shifted to the right of the resonance conditions because the transverse components of the Overhauser field B_{ov}^{y} and B_{ov}^{z} contribute to the effective magnetic field h_{eff}.

Further strong support for perfect nuclear focusing is provided by the study of the weight Σ_{even} of the even resonances, which is plotted in Fig. 5.13(a) as a function of the number of pulses for various values of γ at $h = 40A_{\mathrm{Q}}$. For long pulse trains, the weight approaches unity, which implies that the Overhauser field evolves towards values compatible with the ERC (5.18). In addition, scaling the number of pulses with γ [inset of Fig. 5.13(a)] leads to a perfect data collapse and corroborates this scaling also found for the revival amplitude.

Next, we turn to the variation of the magnetic field h. In Fig. 5.13(b), the increasing weight Σ_{even} is plotted for various values of h. Clearly, larger fields result in slower changes of the Overhauser field. The best collapse of the curves is obtained when scaling the number of pulses with $1/h^2$ as illustrated in the inset. We emphasize that this quadratic scaling is in contrast to what is found in Sec. 5.2.1 for pulse model I

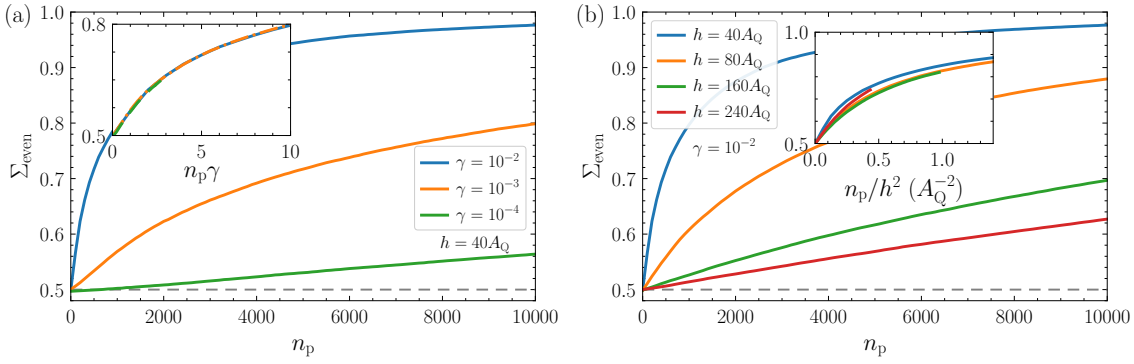

Figure 5.13: (a) Dependence of the weight Σ_{even} on the number of pulses n_{p} (inset: scaled pulses $n_{\mathrm{p}}\gamma$) at $h = 40A_{\mathrm{Q}}$ for various inverse bath sizes γ using pulse model I in presence of the nuclear Zeeman effect. **(b)** Same as (a), but for fixed $\gamma = 10^{-2}$ and various magnetic fields h. Inset: number of pulses n_{p} scaled with $1/h^2$.

without nuclear Zeeman effect. We attribute this change of scaling to the fact that the individual rate of change of each bath spin caused by the hyperfine interaction has become a second-order effect as a consequence of the additional precession of the nuclear spins about the external magnetic field. Hence, the Overhauser field becomes stiffer because of the nuclear Zeeman effect.

Since the nuclear Zeeman effect introduces an additional energy scale that depends on the strength of the external field h, it is reasonable to expect a qualitative change of the physics when increasing h from $40A_\mathrm{Q}$ to $240A_\mathrm{Q}$. A conceivable scenario would be a transition from even to odd resonance. However, we find no qualitative difference for the values of h studied in Fig. 5.13(b). Instead, the inset in Fig. 5.13(b) shows that the nuclear focusing scales well with $1/h^2$.

For completeness, we also calculate the phase shifts at the pulse boundaries. In all investigated cases, the phase shifts result to be close to zero, $\Delta\varphi \approx 0$, which is expected for a dominant even resonance.

In summary, we find very strong nuclear focusing triggered by the periodic application of pulse model I while including the nuclear Zeeman effect. The inclusion of the nuclear Zeeman effect slows the rates of nuclear focusing down considerably. The scaling with the inverse bath size γ changes from $\sqrt{\gamma}$ to γ and is quantitative, i.e., it leads to a perfect data collapse. The scaling with the magnetic field changes from $1/h$ to $1/h^2$ and is not completely perfect.

5.3.2 Pulse model II

Finally, let us study the periodic application of pulse model II in presence of the nuclear Zeeman effect. Again, we start by inspecting the buildup of the relative revival amplitude $S^{\perp}_{\mathrm{rel}}$ for various values of γ at $h = 40A_\mathrm{Q}$ in Fig. 5.14(a). Compared to the case without nuclear Zeeman effect (Fig. 5.6), the revival amplitude generally approaches larger values. But we stress that the amplitude does still not reach unity, i.e., $S^{\perp}_{\mathrm{rel}}(n_\mathrm{p} \to \infty) < 1$ as can be seen for the blue curve in Fig. 5.14(a). In this sense, the nuclei-induced frequency focusing remains imperfect.

A scaling of the number of pulses n_p with γ as applied in the inset of Fig. 5.14(a) appears to work for very small values of $\gamma \ll 10^{-2}$. But the data collapse is not as good as for pulse model I (Fig. 5.11): the revival amplitude approaches

slightly larger saturation values for smaller values of γ. The weight Σ_{even} plotted in Fig. 5.14(b) shows an analogous behavior, which was to be expected for consistency. From the weight, it is also apparent that the system favors the even resonance.

Representative results for the distributions of the effective magnetic field and for the Overhauser field components are shown in Fig. 5.15. The Overhauser field components B^y_{ov} and B^z_{ov} maintain their initial Gaussian shape. The positions of the peaks in the distribution of the effective magnetic field clearly match the ERC (5.18) and the peaks in the distribution of B^x_{ov} are again slightly shifted to the right. The degree of nuclear focusing is significantly more pronounced than for the case without nuclear Zeeman effect (Fig. 5.7), but the peaks still retain a finite width, even in the limit $n_{\text{p}} \to \infty$.

The dependence of Σ_{even} on the magnetic field h for fixed $\gamma = 10^{-2}$ and $\gamma = 10^{-3}$ is shown in Fig. 5.16(a). Again, larger values of h imply a slower nuclear focusing. In contrast to the previous results, we find no data collapse by scaling with $1/h$ or $1/h^2$. Moreover, only the even resonance is present, independent of the choice of γ and h. This finding is supported by a vanishing phase shift $\Delta\varphi \approx 0$ for all studied parameter combinations of γ and h.

Interestingly, the degree of nuclear focusing shows a minimum at a field of about $h = 160A_{\text{Q}}$ (red curve) as visible in Fig. 5.16. The minimum is clearly discernible if the number of pulses is scaled with $1/h^2$ as in Fig. 5.16(b). The scaling does not

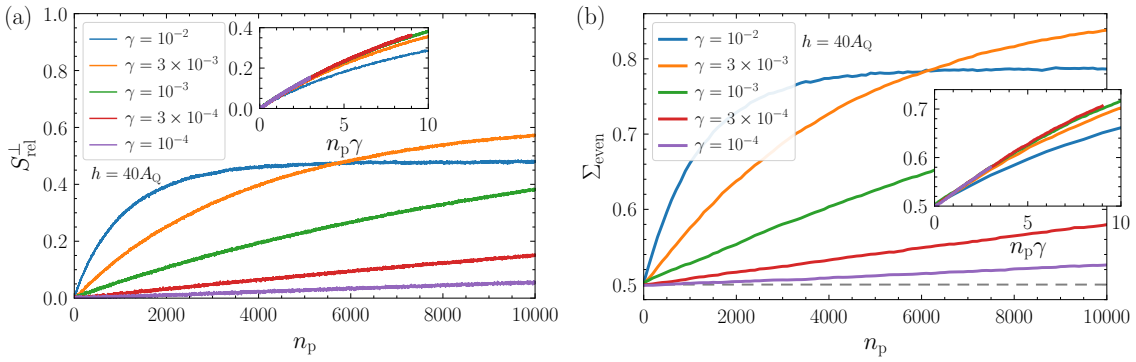

Figure 5.14: (a) Relative revival amplitude $S^{\perp}_{\text{rel}}$ as a function of the number of pulses n_{p} (inset: scaled number of pulses $n_{\text{p}}\gamma$) at $h = 40A_{\text{Q}}$ for various inverse bath sizes γ using pulse model II in presence of the nuclear Zeeman effect. **(b)** Same as (a), but displaying the weight Σ_{even} as a function of the number of pulses n_{p} (inset: scaled number of pulses $n_{\text{p}}\gamma$).

yield a perfect data collapse, but it is obvious that it captures the main influence of the magnetic field on the nuclear focusing rate, except for the nonmonotonic behavior of its degree. The minimum seems to be more pronounced for the smaller value of γ (lower panel) corresponding to a larger effective bath size.

In SI units, the magnetic field $h = 160A_\mathrm{Q}$ converts to roughly 4 T. There appears to be a connection to recent experiments where a minimum of the revival signal is found at about 3.75 T in Ref. [122] or at about 4.2 T in Ref. [117]; see also Fig. 2.5(b) taken from Ref. [117]. But under experimental conditions, the system is in a nonequilibrium steady state (NESS) as a consequence of the periodic application of pulses for up to minutes. Simulating such a NESS is extremely challenging for large values of h combined with small values of γ because of the scaling behavior found for these parameters.

In summary, significant nuclear focusing is observed for pulse model II in presence

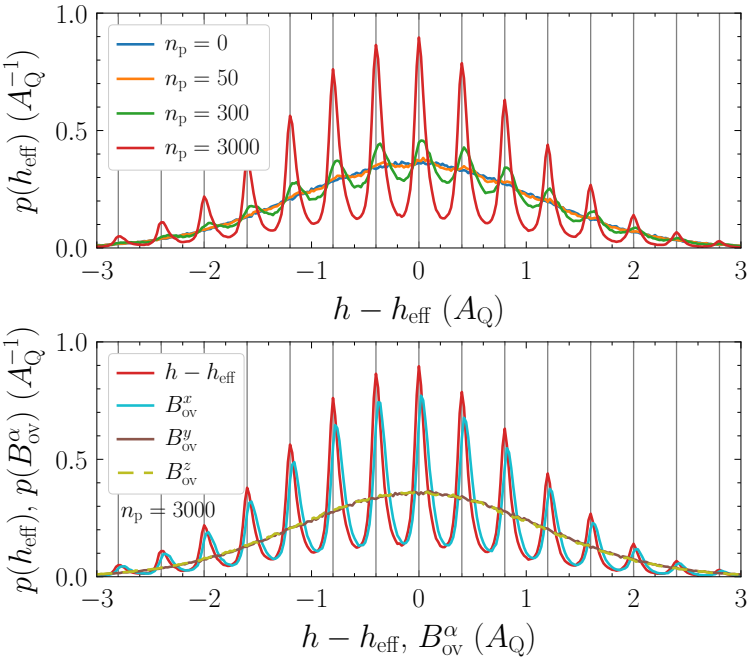

Figure 5.15: Upper panel: Probability distribution $p(h_\mathrm{eff})$ of the effective magnetic field, shifted by $h = 40A_\mathrm{Q}$, after n_p pulses of type II at $\gamma = 10^{-2}$ in presence of the nuclear Zeeman effect. The vertical dashed lines indicate the values of h_eff that satisfy the ORC (5.17). Lower panel: Same as upper panel, but after $n_\mathrm{p} = 3000$ pulses. Additionally, the probability distributions of the Overhauser field components B_ov^α, $\alpha \in \{x, y, z\}$, are shown.

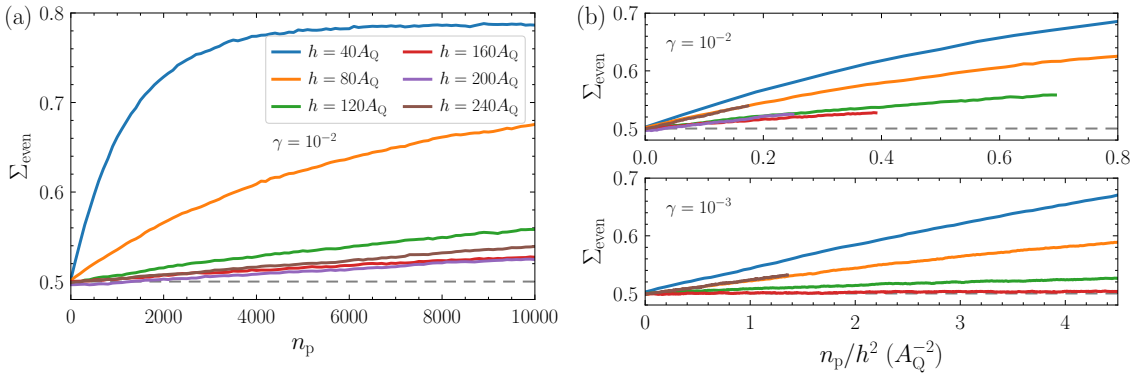

Figure 5.16: (a) Dependence of the weight Σ_{even} on the number of pulses for various magnetic fields h at $\gamma = 10^{-2}$ using pulse model II in presence of the nuclear Zeeman effect. **(b)** Same as (a), but scaling the number of pulses n_p with $1/h^2$ for $\gamma = 10^{-2}$ (upper panel) and $\gamma = 10^{-3}$ (lower panel). Taking the scale of the abscissa into account, one notes the significantly slower dynamics in the lower panel because of the linear scaling with γ.

of the nuclear Zeeman effect, but it is less pronounced than for pulse model I and generally imperfect. The inclusion of the nuclear Zeeman effect slows down the process of nuclear focusing considerably because the scaling with the inverse bath size changes from $\sqrt{\gamma}$ to γ. The scaling with the magnetic field remains at $1/h^2$, i.e., it does not change when including the nuclear Zeeman effect. Remarkably, the nuclear focusing induced by pulse model II displays nontrivial nonmonotonic features when studying the magnetic field dependence, but the even resonance prevails for all studied parameter combinations of γ and h. The nonmonotonic behavior, which is analyzed in more detail in the following, prevents a quantitative scaling with $1/h^2$.

5.4 Nonmonotonic magnetic field dependence

Let us expand on the previous analysis by studying the magnetic field dependence of the revival amplitude in the NESS regime for pulse model II in the presence of the nuclear Zeeman effect. In order to be able to compare our results to the experimental results presented in Refs. [117, 122], we must convert the applied theoretical units to physical ones. We fix $T_R = 5\pi A_Q^{-1} = 13.2\,\text{ns}$ as in the experiments so that for an electronic g factor of $g_e = 0.555$ [25], a magnetic field of $B_{\text{ext}} = 1\,\text{T}$

with corresponds to approximately $h = g_e \mu_B \hbar^{-1} B_{ext} = 41 A_Q$. At the same time, this choice implies a dephasing time of $T_n^* = \sqrt{8/5} A_Q^{-1} \approx 1.06\,\mathrm{ns}$, which follows from the conversion given by Eq. (3.50) with $I = 3/2$ for all nuclear spins. The spin polarization probed in the experiments by means of the spin Faraday effect is proportional to the spin polarization in the QDs [113, 115]. Since the periodic pulses are applied for up to minutes, the experimental situation is that the system is in a NESS with a saturated revival amplitude.

The ensemble average is calculated over $M = 10^4 - 10^5$ configurations. The precise ensemble size depends on the computational demand of a particular simulation, which scales approximately linearly with the effective bath size N_{eff} and cubically with the magnetic field h. The cubic scaling occurs as a consequence of the quadratic scaling of the number of pulses to reach the NESS combined with the fact that the Larmor frequency of the electron spin is the smallest timescale to be resolved numerically, resulting in an additional linear increase of the computation time with h.

The buildup of the relative revival amplitude $S_{rel}^{\perp}$ is shown in Fig. 5.17 for a variety of magnetic fields B_{ext} up to 5.56 T. Clearly, the applied scaling with $1/h^2$ in

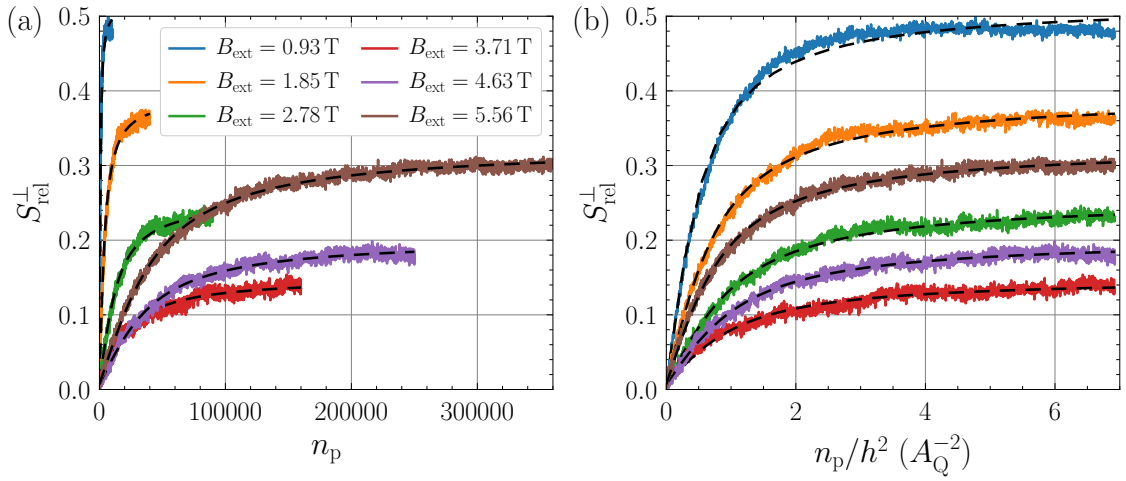

Figure 5.17: (a) Relative revival amplitude $S_{rel}^{\perp}$ as a function of the number of applied pulses n_p for various magnetic fields B_{ext} at $\gamma = 10^{-2}$ using pulse model II in the presence of the nuclear Zeeman effect. Eventually, a NESS is approached. The black dashed curves depict the fit with Eq. (5.23). **(b)** Same as (a), but with scaled number of pulses n_p/h^2. All curves reach a steady state after about $n_p/h^2 \approx 3A_Q^{-2}$.

Fig. 5.17(b) demonstrates that an approximately saturated value is reached after a very similar number of scaled pulse $n_\mathrm{p}/h^2 \approx 3A_\mathrm{Q}^{-2}$. But most importantly, the revival amplitude depends nonmonotonically on B_ext: the amplitude is large for small fields, decreases for larger fields up to about 4 T, and increases again for even larger fields.

Since the nondeterministic pulse model II induces a statistical noise in the revival amplitude, we apply the suitable fit function

$$S^\perp_\mathrm{fit}(n_\mathrm{p}) = A_\mathrm{NIFF}\frac{2}{\pi}\arctan\left(\frac{n_\mathrm{p}}{\eta}\right) + B_\mathrm{off} \tag{5.23}$$

to smoothen the data. Such fits are included in Fig. 5.17 as black dashed curves. They display a $1/n_\mathrm{p}$ convergence towards the saturation value ($n_\mathrm{p} \to \infty$) in the NESS regime given by

$$S^\perp_\mathrm{rel,NESS} \coloneqq \mathrm{sgn}(\eta)A_\mathrm{NIFF} + B_\mathrm{off}\,, \tag{5.24}$$

where $\mathrm{sgn}(\eta)$ is the sign function. The fit parameter B_off accounts for the inevitable statistical offset, whereas a finite value of A_NIFF is the result of NIFF. The rate of NIFF is characterized by the parameter η. Alternatively, an exponential saturation fit also yields a decent agreement with the numerical data, but it underestimates the real saturation value slightly because of a faster (exponential) convergence towards saturation.

The revival amplitude $S^\perp_\mathrm{rel,NESS}$ in the NESS regime as a function of the magnetic field B_ext is plotted in Fig. 5.18 for $\gamma = 10^{-2}$ ($N_\mathrm{eff} = 200$) and $\gamma = 3 \times 10^{-3}$ ($N_\mathrm{eff} \approx 667$). The error bars display the root-mean-square deviation calculated for the fit (5.23) over the last 10% data points, serving as a measure for both the fit quality and the statistical fluctuations. The nonmonotonic dependence of the revival amplitude on the magnetic field shows a pronounced minimum at around 3.9 T and a less pronounced, narrow minimum at around 7.8 T. In addition, there is a maximum close to 1 T and two maxima of similar height at around 7 T and 8.5 T. The nonmonotonic behavior is more pronounced for the larger bath (smaller γ), i.e., the maximal revival amplitude is larger and the minimal one is smaller.

The time required to approach the NESS scales linearly with γ, and quadratically in the magnetic field. For this reason, simulations for large magnetic fields and

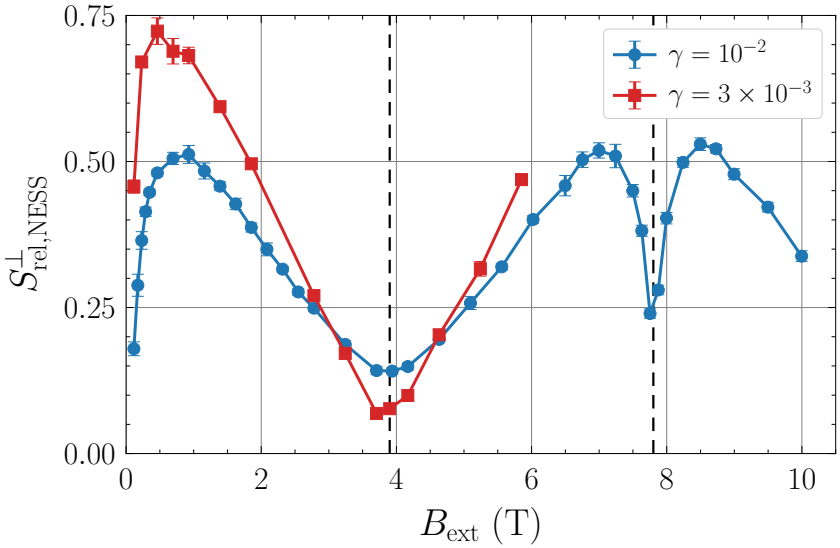

Figure 5.18: Relative revival amplitude $S^{\perp}_{\mathrm{rel,NESS}}$ in the NESS regime, determined from fits of type (5.23) using Eq. (5.24), as a function of the magnetic field B_{ext} for two different values of the inverse bath size γ using pulse model II in the presence of the nuclear Zeeman effect. The error bars display the root-mean-square deviations calculated for the fit over the last 10% data points. The two horizontal dashed lines represent the magnetic fields B_{ext} that satisfy the nuclear resonance condition (5.25) for $k = 1$ and 2.

large bath sizes are computationally very expensive so that we cannot cover the full range of magnetic fields up to 10 T for the larger spin bath with $\gamma = 3 \times 10^{-3}$ in Fig. 5.18.[4]

The first minimum at around 3.9 T is qualitatively very similar to the minimum found in experiments in the vicinity of 4 T [117, 122]; see also Fig. 2.5(b) taken from Ref. [117]. Furthermore, similar minima are found in Ref. [117] using a quantum mechanical approach for $N = 6$ bath spins, but the widths of the minima differ from our result. The differences could stem from the vastly differing bath sizes and from the difference between the quantum mechanical and the semiclassical approach. In particular, we do not account for the excitation of trion states by the pulses, which is the mechanism exploited in experiments to induce spin polarization on the quantum mechanical level as discussed in Sec. 2.2.2. This mechanism and further extensions of the semiclassical approach are the studied in Chap. 6. There, we will see that the selection rules governing the trion excitation already lead to the

[4] At a later stage, we obtained access to more powerful but limited computational resources. They were used for the more advanced simulations presented in the following chapters.

appearance of a sizable revival amplitude after very few pulses without any nuclear focusing.

But here, the revival amplitude is solely caused by NIFF, i.e., by the formation of a comblike structure in the distribution of the Overhauser field component B^x_{ov}. Figure 5.19 shows its probability distribution $p(B^x_{\mathrm{ov}})$ for the two magnetic fields $B_{\mathrm{ext}} = 0.93\,\mathrm{T}$ and $3.71\,\mathrm{T}$ in the NESS regime, i.e., the distributions do not change significantly if more pulses were applied. Both distributions show a pronounced comblike structure as the result of nuclear focusing, with peaks corresponding to the even resonance (slightly shifted because the effective magnetic field h_{eff} is the relevant quantity that determines the resonance condition). But the width and concomitantly the height of the peaks differ substantially. This is the reason for the much smaller revival amplitudes at magnetic fields in the vicinity of 3.9 T and 7.8 T. In general, a larger value of the revival amplitude corresponds to sharper peaks because sharper peaks imply an enhanced synchronization of the precession frequencies.

The positions of the two minima in Fig. 5.18 at $B_{\mathrm{ext}} \approx 3.9\,\mathrm{T}$ and $7.8\,\mathrm{T}$ are related

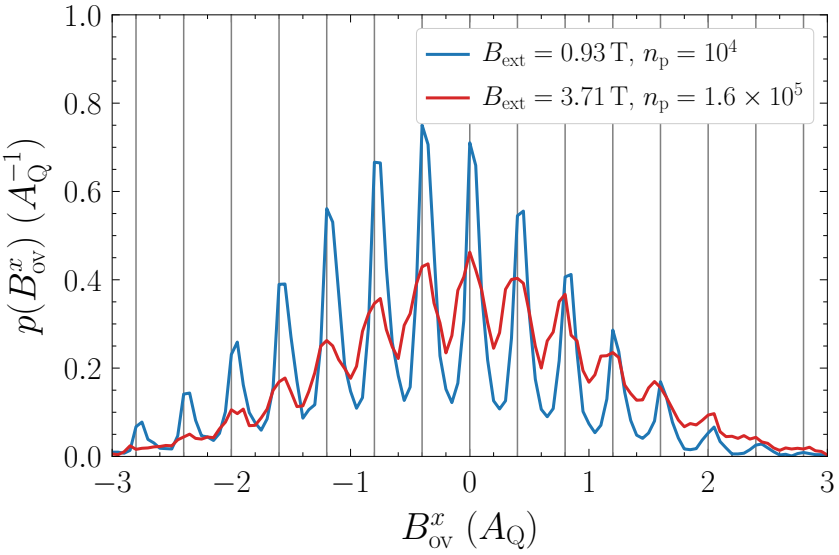

Figure 5.19: Probability distribution $p(B^x_{\mathrm{ov}})$ of the Overhauser field x component in the NESS regime reached after n_{p} pulses (denoted in the legend) for two different magnetic fields B_{ext} at $\gamma = 10^{-2}$ using pulse model II in the presence of the nuclear Zeeman effect. The vertical solid lines indicate the values of the effective magnetic field h_{eff} that fulfill the ERC (5.18), shifted by h.

to another class of resonance conditions that takes the Larmor precession of the nuclear spins into account [117, 142]. As a consequence of the nuclear Zeeman effect, they also precess about the magnetic field. The nuclear resonance condition

$$h_{\mathrm{n}} T_{\mathrm{R}} = |k|\pi\,, \qquad k \in \mathbb{Z}\,, \tag{5.25}$$

describes the number of half-turn revolutions of the nuclear spins between consecutive pulses. The small contribution from the Knight field $A_k \boldsymbol{S}$ is neglected; it could lead to tiny shifts from the nuclear resonance condition (5.25) [253]. Calculating the corresponding magnetic field B_{ext} in SI units for $k = 1$ and 2 yields the values $B_{\mathrm{ext}} \approx 3.9\,\mathrm{T}$ and $7.8\,\mathrm{T}$ ($g_{\mathrm{e}} = 0.555$ [25], $\gamma_{\mathrm{n}} = \gamma_{\mathrm{e}}/800$ [117, 122, 142, 167], and $T_{\mathrm{R}} = 13.2\,\mathrm{ns}$). They are highlighted as vertical dashed lines in Fig. 5.18 and match precisely the positions of the minima.

What is the reason in the semiclassical simulations for the nonmonotonic dependence on the magnetic field shown in Fig. 5.18? It captures the interplay of the electronic and nuclear spin precessions. An important additional clue is obtained by setting $X = Y = 0$ for each application of the pulse (5.13) or by simply applying pulse model I from Eq. 5.11, i.e., when the quantum mechanical uncertainty in the spin orientation is neglected. In this case, we find that the relative revival amplitude $S^{\perp}_{\mathrm{rel,NESS}} \to 1$ converges towards unity for all magnetic fields, corresponding to perfect nuclear focusing. Hence, it is indeed the quantum mechanical uncertainty, mimicked by the randomness of X and Y in pulse model II, which is decisive for the finite peak widths shown in Fig. 5.19. They are responsible for the imperfect nuclear focusing and the nonmonotonic behavior of the revival amplitude shown in Fig. 5.18.

An additional piece of information on how the randomness in X and Y acts against perfect nuclear focusing results from the following observation for a magnetic field around 4 T. Including only the uncertainty in the y component results in the appearance of odd resonances. In contrast, including only the uncertainty in the x component results in even resonances. Hence, they compete against each other such that the reduced nuclear focusing found when the fluctuations are included for both components can potentially be understood as an effect of destructive interference.

5.5 Chapter conclusion

Many experiments show that localized electron spins in ensembles of QDs subjected to periodic pulses in a transverse magnetic field show the phenomenon of nuclei-induced frequency focusing where the Larmor precession synchronizes to the periodicity of the pulses. Here, we simulated this setup by periodically applying pulses to the central spin model using a semiclassical approach. The algorithmic progress developed in Sec. 4.2.3 renders it possible to simulate very large spin baths that reach the experimentally relevant sizes of $10^4 - 10^6$ nuclear spins.

We studied two kinds of pulses, which both align the central spin along the z axis. Pulse model I aligns the total spin vector, whereas pulse model II contains knowledge of the quantum mechanical uncertainty so that the transverse spin components remain finite but zero on average. Both pulse models are applied to an isotropic central spin model for the cases with and without nuclear Zeeman effect.

In all cases, we found strong evidence for nuclei-induced frequency focusing. This is indicated by a strong revival signal of the central electron spin, i.e., a signal similar to a spin echo that occurs before the next pulse is applied. Perfect nuclear focusing leads to a revival amplitude as large as the signal right after the pulse. This phenomenon is explained by a highly nonequilibrium distribution of the Overhauser field. Its distribution develops a comblike peak structure such that the difference between the Overhauser fields in two adjacent peaks implies precisely one additional spin revolution between consecutive pulses [25, 117, 122, 131, 139, 141, 142]. We distinguish between even and odd resonances for the peak positions in the distribution of the effective magnetic field, which is the sum of the external magnetic field and the Overhauser field. If the system is in even resonance, an integer number of electronic Larmor periods fits between consecutive pulses. For the odd resonance, a half-integer number of revolutions takes place.

The nuclear focusing induced by pulse model I is very efficient and the system favors the odd resonance. The buildup of the revival signal scales with $1/\sqrt{N_{\mathrm{eff}}}$, i.e., the nuclear focusing is slower by a factor of two if the spin bath is four times larger. Similarly, larger magnetic fields slow down the rate of nuclear focusing by $1/h$. These scaling laws result in excellent data collapses so that quantitative extrapolations to larger spin baths or magnetic fields are possible.

For pulse model II without nuclear Zeeman effect, nuclear focusing can arise in even or in odd resonance, with a transition between the two scenarios depending on the parameters $\gamma = 2/N_{\mathrm{eff}}$ and h. For QDs under typical experimental conditions, the odd resonance is the relevant one. The degree of nuclear focusing is always weaker than for pulse model I, i.e., the relative revival amplitude stays well below unity and the peak structure in the distribution of the Overhauser field does not approach a comb of δ peaks. Instead, the peaks retain a certain width. The scaling of the nuclear focusing rate is again proportional to $1/\sqrt{N_{\mathrm{eff}}}$ and stationary states are reached after at approximately the same number of scaled pulses n_{p}/h^2. The scaling laws only yield an approximate data collapse because of the nonmonotonic dependence on the parameters and because of the transition between even and odd resonance.

Next, we included the nuclear Zeeman effect using a generic value for an average isotope. For pulse model I, the nuclear focusing shifts from the odd to the even resonance because of its inclusion. The nuclear focusing is slowed down considerably since the nuclear Zeeman effect acts as a perturbation such that the hyperfine interaction determining the rate of change of the bath spins becomes a second-order effect. The rate of nuclear focusing is now proportional to $1/N_{\mathrm{eff}}$ and $1/h^2$. These scaling laws yield very good data collapses so that quantitative extrapolations are possible.

The inclusion of the nuclear Zeeman effect for periodic pulses of type II results in nuclear focusing fulfilling the ERC (5.18). The rate of nuclear focusing is proportional to $1/N_{\mathrm{eff}}$ and the accuracy of the scaling improves for larger baths N_{eff}. But since the dependence on the magnetic field h is nonmonotonic, no quantitative data collapse can be achieved by scaling with $1/h^2$. Instead, stationary states are reached after approximately the same number of scaled pulses n_{p}/h^2, i.e., the rate of nuclear focusing scales approximately with $1/h^2$, but not the degree. The quadratic scaling with the magnetic field is in agreement with the result of other research using quantum mechanical [141] or classical [131] approaches.

Using pulse model II in the presence of the nuclear Zeeman effect is a promising starting point for further improvements. Similar to the nonmonotonic magnetic field dependence of the revival amplitude on the external magnetic field found in experiments [117, 122], we find pronounced minima in this dependence at magnetic fields that fulfill a resonance condition for the nuclear spins. At these fields, the

nuclear spins perform a multiple of half-turn revolutions about the external field between consecutive pulses. Note that only an average isotope is considered here, whereas there are five different isotopes in InGaAs QDs. Hence, the complexity of the nonmonotonic behavior is expected to increase substantially when the isotope composition of the QDs is accounted for. This more complex situation is studied in Chap. 7.

We emphasize that our findings clearly show that a realistic description of the pulse matters. The qualitative differences in the results found between pulse model I and II underline that an accurate understanding of the pulse process is required. Even though the phenomenon of nuclei-induced frequency focusing appears to be robust, important features such as its rate, degree and the kind of resonance (even or odd) are very sensitive to the details of the pulse.

In the following chapter, we treat the pulse in a more realistic manner by describing its action as the result of the formation of trion states. Furthermore, we combine the ideas developed in this chapter with ideas from other research to gradually build a model that is capable of describing several effects seen in experiments.

Chapter 6

Interplay of spin mode locking and nuclei-induced frequency focusing

The results of the previous chapter demonstrate that the CSM subjected to periodic pulses shows the phenomenon of NIFF. But they also demonstrate that the behavior is sensitive to the properties of the pulse and to the nuclear Zeeman effect. In particular, the results of Sec. 5.4 underline the importance to account for the quantum mechanical nature of a pulse. The action of a pulse can be interpreted as a quantum mechanical measurement so that the uncertainty principle needs to be accounted for in the semiclassical approach.

In this chapter, we pursue this route further and extend the models studied in Chap. 5 in several steps.[1] In Chap. 5, the revival signal is solely caused by the emerging nonequilibrium distribution of the Overhauser field as a consequence of nuclear focusing. But it is known that there is also a contribution that can emerge without nuclear focusing, simply resulting from a selection of commensurable precession modes as a consequence of the pulse properties [24, 117, 122, 135, 141, 148]. In this regime, which takes place after very few pulses, we face spin mode locking *without* nuclei-induced frequency focusing. Clearly, this behavior is not described by the models used in Chap. 5. The main difference between them and other theoretical approaches is the applied pulse, which is considered as a simple alignment of the central spin (on average) along the z axis in Chap. 5. In experiments, however, the spin polarization of a localized electron spin in a singly-charged QD is induced by the optical excitation of trion states [23, 24, 112, 113, 117, 122, 141]. This mechanism is described in detail in Sec. 2.2.

[1] This chapter is based on the author's publication [254], ©2020 American Physical Society.

A fundamental question that we want to address is whether NIFF always acts constructively, i.e., does it always lead to an enhancement of the SML effect, and what is the influence of the external magnetic field on this interplay? Previous theoretical studies, both quantum mechanical [117, 142] and semiclassical [122], suggest that this is not necessarily the case. In these studies, additional resonances that can act destructively are found. The slow Larmor precession of the nuclear spins plays a major role in this context. In these studies, however, the dynamics of the unpaired heavy-hole spin in the excited trion [125, 255] is neglected. We lift this simplification and show that it influences the physics on a qualitative level.

This chapter is devoted to a better theoretical description and understanding of NIFF while being close to the experimental conditions. Existing (semi)classical precession models [117, 122, 131, 139, 252] are improved by interpreting the action of *each* pump pulse as a quantum mechanical measurement [117, 252], very similar to pulse model II studied in Chap. 5. In this sense, we apply the TWA [230] to the action of each pulse, which results in a reduced discrepancy of our semiclassical approach to a fully quantum mechanical description. Moreover, we investigate the role of the dynamics of the trion pseudospin during its lifetime and briefly analyze the role of an inhomogeneous ensemble of QDs.

First, the initial model is introduced in Sec. 6.1, which combines the semiclassical approach to the spin dynamics in QDs used in Chap. 5 with a pulse model resulting from the quantum mechanical description of the trion excitation [113]. We will see that the initial model does not describe some experimental results appropriately. In the subsequent sections, we extend the initial model step by step, leading to the extended models (EMs) I, II, and III. A nondeterministic description of the pulse model is introduced in Sec. 6.2 by interpreting each pulse as a quantum mechanical measurement, similarly to the pulse model II used in Chap. 5, but also accounting for the trion excitation. This reduces the discrepancy to a fully quantum mechanical model while still being able to treat large numbers of nuclear spins for a realistic distribution of the hyperfine couplings. In Sec. 6.3, the model is extended by including the dynamics of the trion pseudospin [125, 255], resulting in qualitatively different physics and also in the emergence of dynamic nuclear polarization [42, 115, 225], i.e., to the formation of a finite average polarization of the nuclear spin bath. The role of inhomogeneities in the QD ensemble is briefly discussed in Sec. 6.4. A minimal model to describe the qualitative interplay of SML and NIFF is presented in Sec. 6.5. Finally, a conclusion and an outlook are given in Sec. 6.6.

6.1 Initial model: Localized electron spin in a quantum dot subjected to periodic laser pulses

In this section, we introduce and numerically analyze the initial model. It is a combination of an established pulse model often used to describe the excitation of a trion [23, 113, 122, 135, 255, 256] with the efficient semiclassical Spectral Density approach to the nuclear spin dynamics in the CSM introduced in Sec. 4.2.3. This efficient approach enables us to simulate the spin dynamics for large or even infinite bath sizes up the experimentally relevant nonequilibrium steady states appearing on very long timescales.

6.1.1 Equations of motion

We consider a homogeneous ensemble of GaAs QDs, i.e., all QDs in the ensemble are assumed to be equal. The QDs are singly charged by electrons and a strong transverse magnetic field of up to several Tesla is applied perpendicular to the axis of light propagation (Voigt geometry), which is also parallel to the growth axis $\boldsymbol{e}_z$ of the QD. A graphical illustration depicting the basic model and setup is shown in Fig. 6.1.

We treat the spin dynamics in a QD using our semiclassical approach to the CSM (Sec. 3.3.2), i.e., we solve the corresponding classical equations of motion and aver-

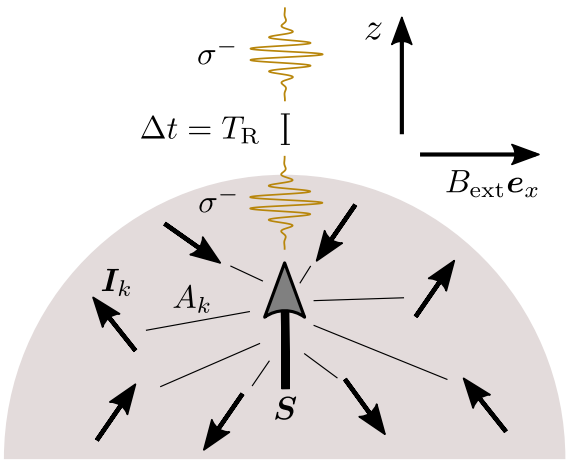

Figure 6.1: Illustration of the basic model and setup: A localized electron spin $\boldsymbol{S}$ in a QD is subjected to a train of periodic circularly polarized σ^- pulses, which are applied with repetition time T_R. The electron spin $\boldsymbol{S}$ couples to the surrounding nuclear spins $\boldsymbol{I}_k$ via the hyperfine interaction with coupling constants A_k. This interaction is described by the CSM (3.7). An external magnetic field $B_\mathrm{ext}\boldsymbol{e}_x$ is applied in Voigt geometry, i.e., perpendicular to the direction of light propagation. The direction of light propagation is parallel to the growth axis $\boldsymbol{e}_z$ of the QD.

age over an appropriate distribution for the initial conditions of the classical spins. Initially, the nuclear spins are completely disordered because the temperature in experiments ($\sim 4-6\,\mathrm{K}$ [24, 25, 117]) corresponds to a much larger energy than the individual hyperfine couplings. Thus, as a consequence of the central limit theorem, each component B_{ov}^{α}, $\alpha \in \{x, y, z\}$, of the Overhauser field comprising $10^4 - 10^6$ effectively coupled nuclear spins [19, 103–107] with $I = 3/2$ follows initially a normal distribution with expectation value $\mathrm{E}[B_{\mathrm{ov}}^{\alpha}] = 0$ and variance

$$\mathrm{Var}[B_{\mathrm{ov}}^{\alpha}] = \frac{5}{4} A_{\mathrm{Q}}^2 = \frac{2}{(T_{\mathrm{n}}^*)^2}\,, \tag{6.1}$$

Unless stated otherwise, we use the generic value $T_{\mathrm{n}}^* = 1\,\mathrm{ns}$ [19, 104]. We fix the variance of the Overhauser field via the dephasing time T_{n}^* because this time is accessible in the experiments. Physically, it is defined in Eq. (3.50) via the strength of the hyperfine interaction and the spin quantum number of the nuclei, resulting in $T_{\mathrm{n}}^* = \sqrt{8/5} A_{\mathrm{Q}}^{-1}$ for nuclear spins with $I = 3/2$.

In the semiclassical approach, the dynamics of the localized electron spin $\boldsymbol{S}$ and of the N nuclear spins $\boldsymbol{I}_k$ for a single random initial configuration of the full ensemble is determined by the classical equations of motion

$$\frac{\mathrm{d}}{\mathrm{d}t}\boldsymbol{S} = (\boldsymbol{B}_{\mathrm{ov}} + h\boldsymbol{e}_x) \times \boldsymbol{S} + \frac{1}{\tau_0} J^z \boldsymbol{e}_z\,, \tag{6.2a}$$

$$\frac{\mathrm{d}}{\mathrm{d}t} J^z = -\frac{1}{\tau_0} J^z\,, \tag{6.2b}$$

$$\frac{\mathrm{d}}{\mathrm{d}t}\boldsymbol{I}_k = (A_k \boldsymbol{S} + h_{\mathrm{n}} \boldsymbol{e}_x) \times \boldsymbol{I}_k\,, \qquad k \in \{1, 2, \ldots, N\}\,, \tag{6.2c}$$

with $h = \gamma_{\mathrm{e}} B_{\mathrm{ext}}$, $h_{\mathrm{n}} = \gamma_{\mathrm{n}} B_{\mathrm{ext}}$, $\gamma_{\mathrm{e}} = g_{\mathrm{e}} \mu_{\mathrm{B}} \hbar^{-1}$ is the electronic gyromagnetic ratio, $g_{\mathrm{e}} = 0.555$ [25] is the electronic g factor,[2] μ_{B} the Bohr magneton, B_{ext} the strength of the external magnetic field, and $\boldsymbol{e}_\alpha$ the unit vector in $\alpha \in \{x, y, z\}$ direction. For the gyromagnetic magnetic ratio of the nuclear spins, we use the value $\gamma_{\mathrm{n}} = \gamma_{\mathrm{e}}/800$ as in Chap. 5, which is approximately an average value for GaAs or InGaAs QDs [117, 122, 142, 167]. The intermediate trion state, which can

[2] Note that the electronic g factor is chosen to be positive here, whereas it is actually negative in InGaAs QDs [132]. But for the physics under investigation, its sign is not of particular importance because of symmetry reasons: the Overhauser field is represented as a random classical field centered around zero polarization. The sign is important whenever the direction of a certain polarization needs to be uniquely identified.

be excited by a circularly polarized pump pulse, is denoted by the z projection J^z of its pseudospin $\boldsymbol{J}$ [defined in Eq. (2.8c)] and has a recombination time of $\tau_0 = 400\,\mathrm{ps}$ [23, 111]. Its decay is simply described by $J^z(t) = J^z(0)\exp(-t/\tau_0)$. As a consequence of the radiative trion recombination, the polarization J^z is transferred back to the ground state S^z while emitting a photon. The recombination dynamics for the spin polarizations of the trion and ground state can be derived, e.g., from a Lindblad approach [121] incorporating a photonic bath. The combination with the semiclassical treatment of the CSM was carried out by Jäschke *et al.* [122, 257]. The terms describing the recombination dynamics also appear in several other works, e.g., in Refs. [23, 112–114, 124, 125, 135]. The implications of the recombination dynamics with and without contributions from other interactions are discussed in Sec. 2.2.2 around Eq. (2.15).

Crucially for the description of NIFF, the Overhauser field $\boldsymbol{B}_{\mathrm{ov}} = \sum_{k=1}^{N} A_k \boldsymbol{I}_k$ is a dynamic object since the individual nuclear spins $\boldsymbol{I}_k$ are also dynamic as described by Eq. (6.2c). Otherwise, no nuclear focusing could occur. The hyperfine coupling constants A_k are proportional to the probability density the localized electron at the position of the kth nucleus. As discussed in Sec. 3.1.2, the hyperfine couplings in approximately flat QDs can be parameterized exponentially by

$$A_k = C\exp(-k\gamma)\,, \qquad k \in \{1, 2, \ldots, N\}\,. \tag{6.3}$$

with $C = \sqrt{2\gamma}A_{\mathrm{Q}}$ for $N \to \infty$, $\gamma \ll 1$. The parameter γ defines the number of effectively coupled nuclear spins $N_{\mathrm{eff}} = 2/\gamma$. In the previous chapters, the couplings A_k are normalized with respect to A_{Q}. Here, we fix $A_{\mathrm{Q}} = \sqrt{8/5}(T_{\mathrm{n}}^*)^{-1}$ via the input parameter T_{n}^*.

Since it is unfeasible to solve the equations of motion (6.2c) for each individual nuclear spin $\boldsymbol{I}_k$ for a realistic bath size, we resort to the efficient Spectral Density approach, which is introduced in Sec. 4.2.3 and applied in Chap. 5 to simulate nonequilibrium spin dynamics in the CSM. In this approach, the total number of nuclear spins N is infinite while the number of effectively coupled nuclear spins N_{eff} is finite. The essence of the Spectral Density approach is the replacement of the individual nuclear spins $\boldsymbol{I}_k$ by appropriate sums of nuclear spins that are represented by the N_{tr} auxiliary fields $\boldsymbol{Q}_k$, where N_{tr} is a discretization parameter of a weight

function. The dynamics of these fields is governed by the equation of motion

$$\frac{\mathrm{d}}{\mathrm{d}t}\boldsymbol{Q}_k = (\varepsilon_k \boldsymbol{S} + h_\mathrm{n}\boldsymbol{e}_x) \times \boldsymbol{Q}_k\,, \qquad k \in \{1, 2, \ldots, N_\mathrm{tr}\}\,. \tag{6.4}$$

The effective coupling constants $\varepsilon_k \propto \sqrt{2\gamma}A_\mathrm{Q} \propto \sqrt{\gamma}/T_\mathrm{n}^*$ result from the parameterization (6.3) of the original couplings after discretization of the spectral density (4.36); see Sec. 4.2.3 around Eq. (4.40) for details. Finally, the Overhauser field in this approach is given by

$$\boldsymbol{B}_\mathrm{ov} = \sum_{k=1}^{N_\mathrm{tr}} \sqrt{W_k}\boldsymbol{Q}_k\,, \tag{6.5}$$

where the W_k are the weights that result from the discretization of the spectral density. The discretization procedure is visualized in Fig. 4.1. Since we focus on GaAs QDs, we have $I = 3/2$ for all nuclear spins. Thus, we sample the components of the vectors $\boldsymbol{Q}_k$ from a normal distribution around zero with variance 5/4 given by Eq. (4.45). This choice ensures that the resulting variances of the Overhauser field components respect Eq. (6.1).

6.1.2 Pulse model: Spin polarization induced by trion excitation

In the experiments, the periodic pumping with laser pulses is carried out with a repetition time of $T_\mathrm{R} = 13.2\,\mathrm{ns}$ [24, 25, 117, 122]. We focus on resonant pumping of the electron spin $\boldsymbol{S}$ by circularly polarized π pulses with helicity σ^- and a typical duration of 1.5 ps [23–26, 30, 117, 148]. Such pulses are very efficient in generating a sizable revival amplitude as a result of SML [24, 25, 113]. The pumping with the circularly polarized light leads to the excitation of a negatively-charged singlet trion T^- [112], which decays completely before the next pulse arrives under the experimental condition $\tau_0 \ll T_\mathrm{R}$. The trion consists of two electrons in a spin singlet state and a heavy hole with unpaired spin. We consider flat QDs where the lateral size by far exceeds their height, i.e., we can choose the growth axis $\boldsymbol{e}_z$ to be the quantization axis for the electron and heavy-hole spin states. As discussed in Sec. 2.2, the electron spin state with $S^z = -1/2$ and the heavy-hole spin state with $J^z = -3/2$ are responsible for the dominant optical transition when using σ^- pulses [19, 113–115]. Since a single Larmor period in a magnetic field as large

as 9 T lasts about 14 ps, the action of the pulse is approximated to be instantaneous because the pulse duration is shorter by one order of magnitude.

Under these conditions, the action of a pump pulse can be described by simple relations between the spin components before ($\boldsymbol{S}_\mathrm{b}$, $\boldsymbol{J}_\mathrm{b}$) and after ($\boldsymbol{S}_\mathrm{a}$, $\boldsymbol{J}_\mathrm{a}$) the pulse. The concrete relations have the form [113, 122]

$$S_\mathrm{a}^z = \frac{1}{4} + \frac{1}{2} S_\mathrm{b}^z \,, \tag{6.6a}$$

$$S_\mathrm{a}^x = S_\mathrm{a}^y = 0 \,, \tag{6.6b}$$

$$J_\mathrm{a}^z = S_\mathrm{b}^z - S_\mathrm{a}^z \,, \tag{6.6c}$$

$$J_\mathrm{a}^x = J_\mathrm{a}^y = 0 \,, \tag{6.6d}$$

where the J^α, $\alpha \in \{x, y, z\}$, represent the components of the trion pseudospin vector $\boldsymbol{J}$ defined in Eq. (2.8), which represents the unpaired heavy-hole spin in the excited trion [114, 115].[3] The transverse components J^x and J^y have no relevance in this section since we neglect possible trion pseudospin dynamics for now, but they become important later in Sec. 6.3. For a significantly longer pulse duration, the pulse efficiency is reduced when the external magnetic field is large [117, 147], but this is beyond the scope of this work.

The application of the pulse (6.6) aligns the electron spin along the z axis, similar to the pulse (5.11) used in Chap. 5 (pulse model I). The key difference is that the value S_a^z after the pulse now depends on the value S_b^z before the pulse. In the following, we will see that this dependence is responsible for the appearance of SML *without* NIFF because the spin polarization is amplified whenever the electronic precession frequency favors commensurable dynamics, i.e., such precession modes are enhanced.

6.1.3 Results for the initial model

We solve the coupled equations of motion (6.2a), (6.2b), and (6.4) describing the spin dynamics numerically for M random initial fields $\{\boldsymbol{Q}_k\}$ while applying the pulse relation (6.6) every $T_\mathrm{R} = 13.2\,\mathrm{ns}$ for n_p pulses. The actual dynamics of the electron spin polarization is given by the ensemble average (denoted by an overline)

[3] As discussed in Sec. 2.2.2, these relations follow from Eq. (2.13) for a resonant σ^- pulse ($\mathcal{P} = -1$) with pulse area $\Theta = \pi$ because of $Q = \cos(\Theta/2) = 0$.

over all $M \approx 10^4$ independent trajectories starting from random initial conditions. Concretely, the time evolution of the quantum mechanical average $\langle \hat{\boldsymbol{S}}(t) \rangle$ of the central spin is approximated in the semiclassical approach by

$$\overline{\boldsymbol{S}(t)} = \frac{1}{M} \sum_{m=1}^{M} \boldsymbol{S}_m(t) \,, \tag{6.7}$$

where $\boldsymbol{S}_m(t)$ represents one of the M independent trajectories.

Let us briefly review the basic phenomena of SML and NIFF, which can be already discussed qualitatively using the initial model. The typical time evolution between consecutive pulses influenced by these two effects is shown in Fig. 6.2. The first pulse creates a net spin polarization $\overline{\boldsymbol{S}(0)} = \boldsymbol{e}_z/4$, which precesses predominantly about the transverse magnetic field $B_{\text{ext}}\boldsymbol{e}_x$. As a consequence of the interaction with the random Overhauser field, the polarization dephases on the timescale $T_{\text{n}}^* = 1\,\text{ns}$ according to [104, 115, 200]

$$\overline{S^z(t)} = \overline{S^z(0)} \cos(\gamma_{\text{e}} B_{\text{ext}} t) \exp\left[-\left(\frac{t}{T_{\text{n}}^*} \right)^2 \right] . \tag{6.8}$$

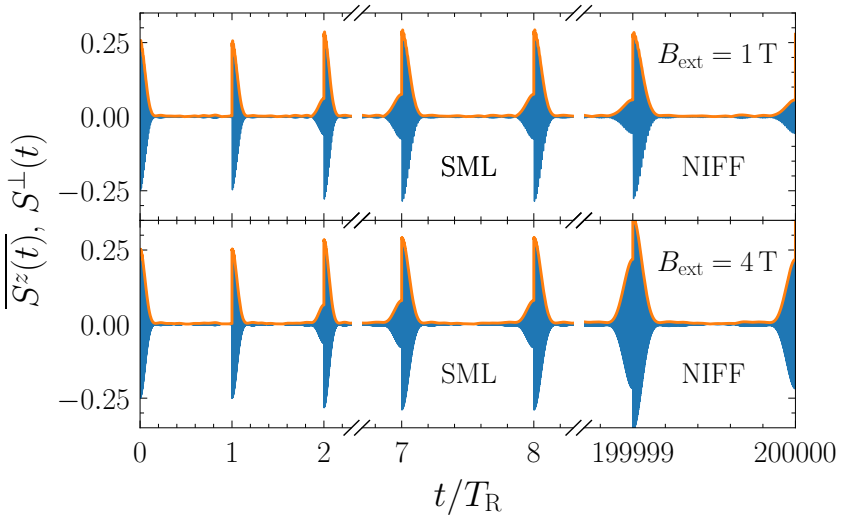

Figure 6.2: Initial model: Spin dynamics $\overline{S^z(t)}$ (blue lines display the fast oscillations) between consecutive pulses after the first pulse, after a few pulses (SML regime without NIFF), and after many pulses (NIFF regime) for two external magnetic fields B_{ext} at $\gamma = 0.02$. The envelope $S^{\perp}(t)$ defined analogously to Eq. (6.11) is plotted in orange.

This basic result follows from the frozen Overhauser field approximation for large transverse magnetic fields (see Sec. 3.3.4). But after applying only a few pulses, a revival of the spin polarization emerges just before the arrival of the next pulse. This effect is known as spin mode locking [24, 135]; see Sec. 2.4.1 for an overview. Here, it occurs because of an enhancement of commensurable precession modes as a consequence of the properties of the pulse (6.6). Qualitatively speaking, the modes corresponding to an integer number of Larmor periods between consecutive pulses lead to an enhancement of the spin polarization, whereas the polarization is destroyed for modes corresponding to a half-integer number. The physics behind this behavior is that the electron spin is optically inactive in the first case and active in the second case as a consequence of the selection rules governing the trion excitation.

It can be shown analytically that a steady state emerges for the revival amplitude when neglecting the Overhauser field dynamics and also the trion recombination ($\gamma_\mathrm{e} B_\mathrm{ext} \gg 1/\tau_0$) [117, 141]. It follows from the condition $S^z(n_\mathrm{p} T_\mathrm{R}) = S^z(n_\mathrm{p} T_\mathrm{R} + T_\mathrm{R})$ describing a steady state in combination with the periodic application of the pulse relation (6.6). After averaging over the initial Overhauser field distribution, the steady state in the SML regime without NIFF takes the value [117, 141]

$$S_\mathrm{SML} \coloneqq \lim_{n_\mathrm{p}\to\infty} \overline{S^z(n_\mathrm{p} T_\mathrm{R}^-)} = \frac{1}{\sqrt{3}} - \frac{1}{2} \approx 0.07735\,, \tag{6.9}$$

where the notation T_R^- indicates that the spin polarization immediately before the arrival of the next pulse is taken. The transverse components vanish on average so that the amplitude of the revival is equal to S_SML. In the following, this value is referred to as the SML steady-state value.[4] It is reached after about ten pulses, independent of the strength of the external magnetic field.

When driving the system by much longer pulse trains, the effect of NIFF comes into play [25], with a rate depending strongly on the parameters B_ext, γ, and T_n^*. This effect influences the amplitude of the revival signal. The periodic driving of the electron spin is transferred to the nuclear spin bath via the hyperfine interaction. The Overhauser field, which contributes to the effective electronic Larmor frequency mainly by its component B_ov^x because of $B_\mathrm{ext}\boldsymbol{e}_x$ being large, evolves in time until the effective magnetic field $B_\mathrm{eff} = |\boldsymbol{B}_\mathrm{ov} + \gamma_\mathrm{e} B_\mathrm{ext}\boldsymbol{e}_x|/\gamma_\mathrm{e}$, i.e., the sum of the Overhauser

[4] To be precise, it is the SML steady-state value without NIFF. In Ref. [117], it is referred to as the 'purely electronic steady state'.

and external magnetic field, fulfills a certain resonance condition. Initially, the Overhauser field and therefore also the effective magnetic field follows a normal distribution. As a consequence of the periodic application of pulses, nuclear focusing takes place so that the probability distribution $p(B_{\mathrm{eff}})$ of the effective magnetic field evolves towards a comblike structure; see Fig. 6.3. Initially, the distribution $p(B_{\mathrm{eff}})$ is simply a Gaussian because of the contribution from the random Overhauser field. Similarly to Chap. 5, two classes of resonance conditions determine the peak positions in the distribution [117, 122],

$$\gamma_{\mathrm{e}} B_{\mathrm{eff}} T_{\mathrm{R}} = 2\pi |k| \,, \tag{6.10a}$$

$$\gamma_{\mathrm{e}} B_{\mathrm{eff}} T_{\mathrm{R}} = 2\pi |k| + 2 \arctan\left(\gamma_{\mathrm{e}} B_{\mathrm{eff}} \tau_0\right) \approx (2|k| + 1)\pi \,, \tag{6.10b}$$

$k \in \mathbb{Z}$, where $\gamma_{\mathrm{e}} B_{\mathrm{eff}}$ is the precession frequency of the electron spin in the effective magnetic field and τ_0 is the trion recombination time. We refer to the first condition (6.10a) as the *even* resonance condition (ERC) because $2|k|$ is an even integer. It describes an integer number of electron spin revolutions about the effective magnetic field between consecutive pulses. The approximation in the second condition (6.10b) is valid for $\gamma_{\mathrm{e}} B_{\mathrm{eff}} \tau_0 \gg 1$, which is the case in our theoretical considerations and also under typical experimental conditions. Hence, we refer to it

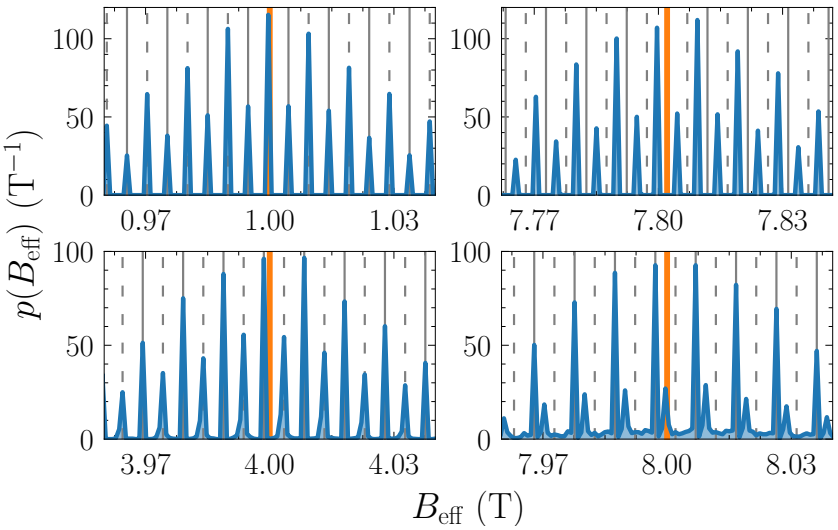

Figure 6.3: Initial model: Probability distribution $p(B_{\mathrm{eff}})$ of the effective magnetic field showing nuclear focusing in the NESS regime for various magnetic fields B_{ext} (orange vertical lines) and $\gamma = 0.02$. The gray solid and dashed vertical lines represent the values of B_{eff} fulfilling the ERC (6.10a) and ORC (6.10b), respectively.

as the odd resonance condition (ORC) because $(2|k|+1)$ is an odd integer, which means that the number of electron spin revolutions between consecutive pulses is a half-integer. Depending on which resonance condition is dominant, the revival amplitude is either increased or decreased with respect to the SML steady-state value S_{SML}. The description of this interplay as a function of the magnetic field is the main goal of this chapter.

One of the key quantities of interest is again the revival amplitude

$$S^{\perp}(n_{\mathrm{p}}) \coloneqq \sqrt{\left[\overline{S^{y}(n_{\mathrm{p}}T_{\mathrm{R}}^{-})}\right]^{2} + \left[\overline{S^{z}(n_{\mathrm{p}}T_{\mathrm{R}}^{-})}\right]^{2}}\,. \tag{6.11}$$

The trion does not contribute to the revival signal because it decays completely until $t = n_{\mathrm{p}}T_{\mathrm{R}}^{-}$ for $\tau_0 \ll T_{\mathrm{R}}$. In particular, we are interested in the long-time behavior of the revival amplitude and its corresponding saturation values

$$S^{\perp}_{\mathrm{NESS}} \coloneqq \lim_{n_{\mathrm{p}}\to\infty} S^{\perp}(n_{\mathrm{p}})\,, \tag{6.12a}$$

$$S^{z}_{\mathrm{NESS}} \coloneqq \lim_{n_{\mathrm{p}}\to\infty} \overline{S^{z}(n_{\mathrm{p}}T_{\mathrm{R}}^{-})}\,, \tag{6.12b}$$

which describes the NESS reached in the experiments where the pulses are applied for very long times. As discussed in Sec. 2.3, the spin polarization can be probed using weak linearly polarized pulses and measuring the Faraday rotation or ellipticity, yielding a signal proportional to $S^z - J^z$ [113, 114]. Since the pulse duration in experiments is finite (but very small), it is beneficial to study the envelope also in experiments so that possible phase shifts do not influence the results [117].

Figure 6.4 shows the buildup of spin polarization for various values of the inverse bath size γ. The revival amplitude increases to the SML steady-state value $S_{\mathrm{SML}} \approx 0.07735$ within the first few pulses, independent of γ and of the magnetic field B_{ext}. The regime of NIFF emerges after a long train of pulses, but there is an important qualitative difference between $B_{\mathrm{ext}} = 1\,\mathrm{T}$ and $2\,\mathrm{T}$: the revival amplitude decreases for $B_{\mathrm{ext}} = 1\,\mathrm{T}$, but it increases for $B_{\mathrm{ext}} = 2\,\mathrm{T}$. In both cases, saturation is reached eventually. Scaling the number of pulses n_{p} with γ leads to an almost perfect data collapse in Fig. 6.4 so that the saturation value $S^{\perp}_{\mathrm{NESS}}$ is independent of γ; differences stem from the statistical nature of the semiclassical approach. This is the same scaling behavior that we have found in Chap. 5 in the presence of the nuclear Zeeman effect. A linear scaling with the inverse of the bath size is also found in the semiclassical analysis of Ref. [122].

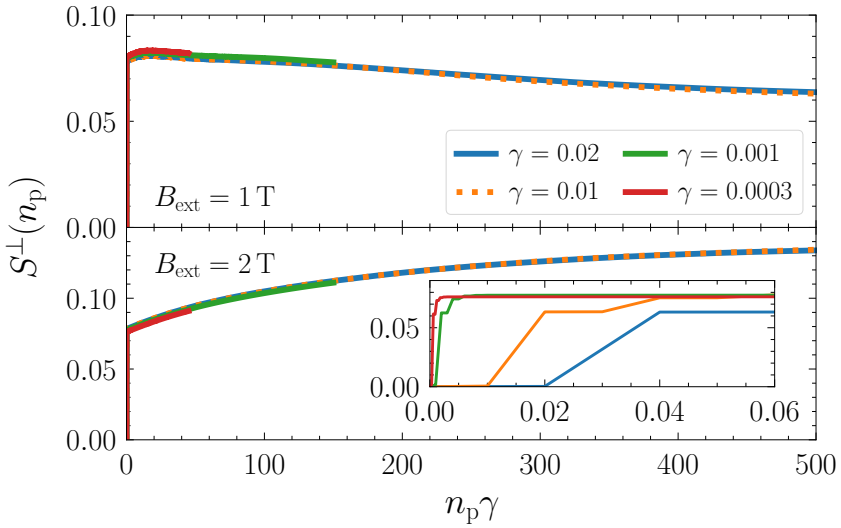

Figure 6.4: Initial model: Revival amplitude $S^{\perp}$ as a function of the scaled number of pulses $n_p\gamma$ for various inverse bath sizes γ at $B_{ext} = 1\,T$ (upper panel) and $2\,T$ (lower panel); note the data collapse for long trains of pulses. The inset shows the SML regime $n_p\gamma \ll 1$.

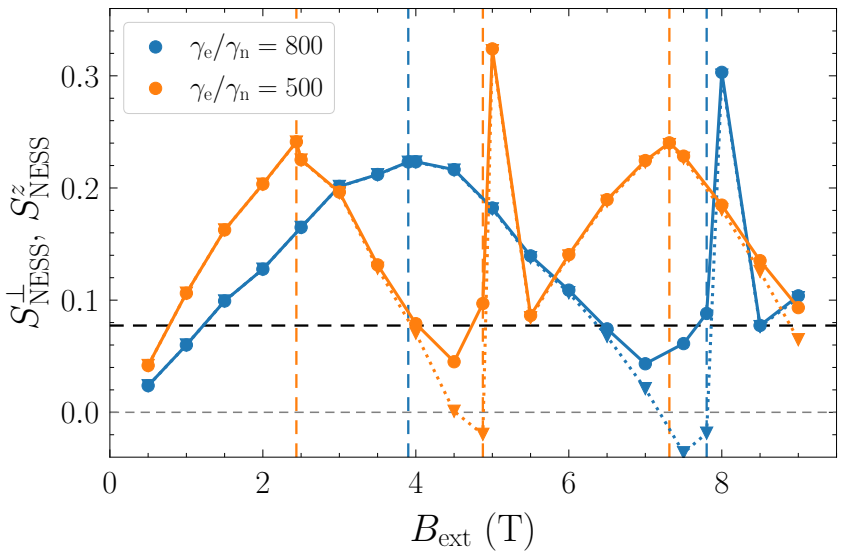

Figure 6.5: Initial model: Limiting values $S^{\perp}_{NESS}$ (sphere, solid) and S^{z}_{NESS} (triangle, dotted) of the revival amplitude as a function of the magnetic field B_{ext} for two ratios γ_n/γ_n and $\gamma = 0.02$. The vertical dashed lines represent the NRCs (6.13) for $k = 1$ and 2, the horizontal dashed line indicates the SML steady-state value S_{SML}.

Since $\gamma = 2/N_{\text{eff}}$ represents the inverse of the effective bath size, we are particularly interested in values $\gamma \approx 10^{-4} - 10^{-6}$. But the computational effort is too big for a direct simulation because the typical hyperfine coupling of a nuclear spin is proportional to $\sqrt{\gamma}$, i.e., the rate of nuclear focusing is much smaller for realistic bath sizes. In fact, the rate scales only linearly with γ as demonstrated in Fig. 6.4. The reason is that NIFF is only a second-order effect when the nuclear Zeeman term in Eq. (6.4) is present: The nuclear spin dynamics induced by the hyperfine interaction acts as a perturbation to the full Larmor precession and its leading effect occurs in second order. Thanks to the scaling, we can study the dependence of $S^{\perp}_{\text{NESS}}$ on the magnetic field B_{ext} for $\gamma = 0.02$ ($N_{\text{eff}} = 100$) in Fig. 6.5, which is also representative for the limit $\gamma \to 0$, i.e., the limit of interest for QDs with a huge number of effectively coupled nuclear spins. We also show S^{z}_{NESS} to identify possible phase shifts between the signal before and after the pulse.

Previous research has established another class of resonance conditions, namely for the nuclear spins [117, 142],

$$\gamma_{\text{n}} B_{\text{ext}} T_{\text{R}} = \pi |k| \,, \tag{6.13}$$

$k \in \mathbb{Z}$, which plays a crucial role for the magnetic field dependence of the saturated revival amplitude $S^{\perp}_{\text{NESS}}$. Its importance is already discussed in Sec. 5.4, where minima in the magnetic field dependence of the revival amplitude are found at the values of B_{ext} fulfilling this nuclear resonance condition (NRC). Similarly, we highlight these values in Fig. 6.5 as vertical dashed lines for the two different ratios $\gamma_{\text{e}}/\gamma_{\text{n}} = 800$ and 500. The NRC describes the number of half-turn revolutions of the nuclear spins between consecutive pulses caused by the Larmor precession in the external magnetic field. The influence of the small Knight field, i.e., the additional field seen by a nuclear spin because of its coupling to the electron spin, is neglected. It can be responsible for slight deviations from the expected resonances [253].

Let us discuss the details of Fig. 6.5. Essentially, the curve for $\gamma_{\text{e}}/\gamma_{\text{n}} = 500$ is a horizontally scaled version of the curve for $\gamma_{\text{e}}/\gamma_{\text{n}} = 800$. Maxima are found close to the values of B_{ext} fulfilling the NRC (6.13). The first maximum ($k = 1$, half turn) is rather broad, while the second maximum ($k = 2$, full turn) is quite sharp and slightly shifted to the right from the expected resonance. Since $S^{\perp}_{\text{NESS}}$ and S^{z}_{NESS} start to deviate from each other while approaching the second maximum, there must be a phase shift in the electron spin dynamics at the pulse boundary. Just after

the NRC for $k = 2$ is reached, this phase shift vanishes again. For $\gamma_e/\gamma_n = 500$, a third maximum ($k = 3$) appears, which is very similar to the first one and indicates a periodicity for larger values of B_{ext}. We expect a third maximum also for the ratio $\gamma_e/\gamma_n = 800$, but it is computationally out of reach. The heights of the broad maxima are very similar. The sharp maximum is slightly less pronounced for $\gamma_e/\gamma_n = 800$, but this behavior stems most likely from the discretization of the magnetic field.

The finding of a maximum at $B_{ext} \approx 3.9\,\mathrm{T}$ for $\gamma_e/\gamma_n = 800$ is the main downside of the initial model. As demonstrated in Sec. 5.4 and in Ref. [117], *minima* are expected at the values of B_{ext} fulfilling the NRC, which is also in much better agreement with the experimental results in the vicinity of $B_{ext} = 4\,\mathrm{T}$ [117, 122]; see also Fig. 2.5(b) taken from Ref. [117].

The dependence $S^{\perp}_{\mathrm{NESS}}(B_{ext})$ shown in Fig. 6.5 can be understood by studying the corresponding quasistationary probability distributions $p(B_{eff})$ of the effective magnetic field. The term 'quasistationary' implies that the distribution does not change noticeably anymore even though the Overhauser field is still dynamic. A nonequilibrium steady state (NESS) is reached. Characteristic examples for different magnetic fields are shown in Fig. 6.3 using the ratio $\gamma_e/\gamma_n = 800$ (only this ratio is used henceforth). For almost any magnetic field B_{ext}, highlighted by the orange vertical line in the plots, we find sharp peaks at the even (vertical solid black lines) and odd (vertical dashed black lines) resonance conditions, but with different weights. Since the ERC corresponds to full Larmor periods between consecutive pulses, the steady-state condition following from the pulse relation (6.6a) is $S^z_b = S^z_a = 1/2$. For the ORC, the steady state is determined by $S^z_b = -S^z_a = -1/6$. For this reason, odd resonances contribute with a three times smaller weight than even resonances when integrating over the full distribution of the effective magnetic field. For the same reason, the ERC dominates the SML regime without NIFF because the Overhauser field is normally distributed and this distribution by itself does not favor the ERC over the ORC or vice versa.

In Fig. 6.3, obvious deviations from the even and odd resonances are found in the vicinity of $B_{ext} \approx 7.8\,\mathrm{T}$, which is the resonant field resulting from the NRC (6.13) for $k = 2$. This finding explains the deviations of the z component from the envelope in Fig. 6.5. When increasing the magnetic field just slightly to $B_{ext} = 8\,\mathrm{T}$, sharp peaks are found at the ERC, but small side peaks that do not correspond to the

expected resonances remain. At $B_{\mathrm{ext}} = 8.5\,\mathrm{T}$ and $9\,\mathrm{T}$, the behavior is back to normal, i.e., with sharp peaks at the ERC and slightly broader peaks at the ORC (not shown).

6.1.4 Discussion of the initial model

The initial model reveals the coherent spin phenomena SML and NIFF and also a nonmonotonic dependence of the revival amplitude. However, the magnetic field dependence contradicts our previous results of Sec. 5.4 and the results of Kleinjohann *et al.* [117] where *minima* instead of maxima are found at the NRC, which is also in much better agreement with experimental observations [117, 122]. While there are experimental results that indicate that even and odd resonances can appear simultaneously in the frequency spectrum of the electron spin, this does not seem to be the case for every magnetic field [122]. Moreover, the peaks found in the experiments appear to be much broader than the peaks visible in Fig. 6.3. In this context, one has to keep in mind that the frequency spectrum of the electron spin is not completely equal to the probability distribution of the effective magnetic field. The main reason is that the ERC and the ORC contribute to the spin polarization with different weights, the precession modes are weighted differently when studying the frequency spectrum of the electron spin. In the following sections, the issues of the initial model are addressed by extending it in three steps.

6.2 Extended model I: Pulse as quantum mechanical measurement

Since we are modeling the system in a semiclassical picture, it is not clear how to treat the quantum mechanical action of a pulse on the electron spin. In fact, the pulse model (6.6) was derived quantum mechanically [113, 122], but the relations are only valid for the expectation values of the spins as discussed in Sec. 2.2.2. One could argue that the relations given by Eq. (6.6) must be applied to the spin polarization *after* calculating the ensemble average, but this approach destroys any correlation otherwise present in a single configuration. Since $\overline{\boldsymbol{S}(t = T_{\mathrm{R}}^{-})} \approx 0$ corresponds to the initial condition $\overline{\boldsymbol{S}(t = 0^{-})} = 0$ of an unpolarized electron spin, the action of every pulse (6.6) would be identical so that no revival amplitude can

build up without NIFF, i.e., there would be no initial buildup to the SML steady-state value. However, such correlations are preserved in the existing quantum mechanical approaches [117, 141] and hence, they should not be neglected.

In the following, we extend the pulse (6.6) by interpreting its application as a quantum mechanical measurement, i.e., we account for the uncertainty principle. To this end, we apply the TWA [230–232] and obtain a nondeterministic pulse description that reduces the discrepancy to the fully quantum mechanical description of the pulse. This is the same principle used for pulse model II in Chap. 5, which is the pulse model for which a minimum in the magnetic field dependence of the revival amplitude is found at around 3.9 T, similar to experimental observations [117, 122].

6.2.1 Nondeterministic pulse description

The essence of simulating quantum mechanics via classical equations of motion by means of the TWA is the choice of appropriate initial conditions. Typically, one tries to fulfill the quantum mechanical moments of the corresponding operators, in our case of the spin operators. We are already applying this principle to the Overhauser field by sampling it from the proper normal distribution, and in Chaps. 4 and 5 this principle is also applied to the central spin. In the case of the Overhauser field, the large number of nuclear spins forming the spin bath provides a valid justification of the semiclassical treatment based on the central limit theorem [200]. In contrast, this argument does not hold for the single electron spin that is excited by a pump pulse, so any semiclassical treatment is always an approximation. Nevertheless, we will see that the semiclassical treatment leads to promising results.

The main requirement is that the nondeterministic pulse retains the properties of pulse (6.6) in the SML regime. We consider *each* pulse to act as a quantum mechanical measurement, i.e., we have to account for the uncertainty principle as before in Chap. 5 for pulse model II. To be precise, the pulse needs to fulfill the quantum mechanical property for spin-1/2 operators $\langle(\hat{S}^\alpha)^2\rangle = 1/4$. Hence, the deterministic pulse relation (6.6) is extended to a nondeterministic description in which the electron spin $\boldsymbol{S}_\mathrm{a}$ after the pulse is sampled from normal distributions

characterized by

$$\mathrm{E}[S_\mathrm{a}^z] = \frac{1}{4} + \frac{1}{2} S_\mathrm{b}^z \,, \tag{6.14a}$$

$$\mathrm{E}[S_\mathrm{a}^x] = \mathrm{E}[S_\mathrm{a}^y] = 0 \,, \tag{6.14b}$$

$$\mathrm{Var}[S_\mathrm{a}^\alpha] = \begin{cases} \frac{1}{4} - \mathrm{E}[S_\mathrm{a}^\alpha]^2 \,, & \text{if } \mathrm{E}[S_\mathrm{a}^\alpha]^2 \leq \frac{1}{4} \,, \\ 0 \,, & \text{else.} \end{cases} \tag{6.14c}$$

The distribution is determined by the spin vector $\boldsymbol{S}_\mathrm{b}$ before the pulse, i.e., the distribution is different for every pulse application. Randomness is present even in a NESS so that such a nonequilibrium state can only be steady on average. Note that we have to set the variance to zero in some cases because we treat the spins as classical vectors, i.e., a spin component can be larger than 1/2 because of the sampling from a normal distribution. Practically, the issue only arises for the z component, but for about 25% of the pulses. This changes its effective variance to a certain extent, but it does not change the expectation value responsible for the correct revival amplitude in the SML steady state without NIFF. The treatment is in line with semiclassical approaches based on the TWA [230–232]. In such approaches, resorting to normal distributions often yields convincing results even though it is known that the Wigner functions reflecting quantum mechanical measurements involve negative probabilities [231].

The validity of the nondeterministic pulse description is established in Appendix C. There, various nondeterministic pulse descriptions are benchmarked in the SML regime without NIFF against the deterministic pulse (6.6) and its quantum mechanical counterpart used by Kleinjohann *et al.* [117]. The alternative nondeterministic pulse descriptions introduced in Appendix C do not reproduce the SML steady-state value correctly and hence, we do not consider them further. The approach promoted above turns out to be the only reliable one.

6.2.2 Results for the extended model I

As pointed out above and analyzed in detail in Appendix C, the nondeterministic pulse description (6.14) does not change the behavior in the SML regime without NIFF besides adding statistical fluctuations to the spin polarization. In the fol-

lowing, we study the interplay of SML and NIFF when long trains of pulses are applied.

Figure 6.6 shows the influence of NIFF on the revival amplitude for various magnetic fields B_{ext} given in the legend. Since the initial SML regime is reached after very few pulses, the curves appear to start with a revival amplitude $S^{\perp} \approx S_{\mathrm{SML}}$. All curves reach a saturation value after approximately the same number of scaled pulses $n_{\mathrm{p}}/B_{\mathrm{ext}}^2$, but the value depends strongly on the strength of the applied magnetic field. Since there are significant statistical fluctuations in the data resulting from the nondeterministic pulse description, we extract the saturation value $S_{\mathrm{NESS}}^{\perp}$ by fitting an appropriate function. As in Sec. 5.4, a suitable fit function is

$$S_{\mathrm{fit}}^{\perp}(n_{\mathrm{p}}) = A_{\mathrm{NIFF}} \frac{2}{\pi} \arctan\left(\frac{n_{\mathrm{p}}}{\eta}\right) + B_{\mathrm{SML}}\,, \tag{6.15}$$

which displays a $1/n_{\mathrm{p}}$ convergence towards saturation. The constant offset B_{SML} accounts for the sizable revival amplitude reached after very few pulses. This initial amplitude changes on the timescale η because of the contribution A_{NIFF} stemming from NIFF. The fits using Eq. (6.15) are included in Fig. 6.6 as black dashed curves.

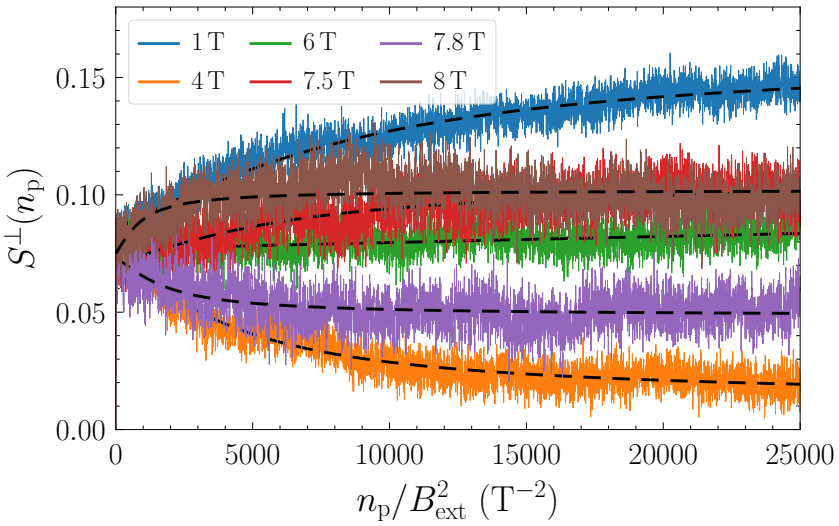

Figure 6.6: Extended model I: Revival amplitude $S^{\perp}$ as a function of the scaled number of pulses $n_{\mathrm{p}}/B_{\mathrm{ext}}^2$ for various magnetic fields B_{ext} given in the legend and $\gamma = 0.004$. The black dashed lines represent the corresponding fits using Eq. (6.15).

The saturation value reached for $n_\mathrm{p} \to \infty$ is given by

$$S^{\perp}_{\mathrm{NESS}} = \mathrm{sgn}(\eta) A_{\mathrm{NIFF}} + B_{\mathrm{SML}} \,. \tag{6.16}$$

Since the fit error turns out to be fairly small, we use the root-mean-square deviation of the last 10% data points as error estimate. It is a measure for both the fit quality and the statistical fluctuations. In the rare cases where the fit does not work appropriately, e.g., because almost no NIFF emerges for a given parameter set, we simply interpret the revival amplitude averaged over the last 10% pulses as the saturation value.

The quasistationary distributions of the effective magnetic field shown in Fig. 6.7 reveal much broader peaks than the distributions in Fig. 6.3 for the initial model. They are located at the values of B_eff corresponding either to the ERC *or* to the ORC, i.e., only a single kind of resonance appears, not both simultaneously as for the initial model.

In the extended model, the parameter $\gamma = 2/N_\mathrm{eff}$ defining the effective bath size plays an important role. While the number of pulses required to reach a NESS still increases linearly with γ, the saturation value $S^{\perp}_{\mathrm{NESS}}$ changes. A similar behavior

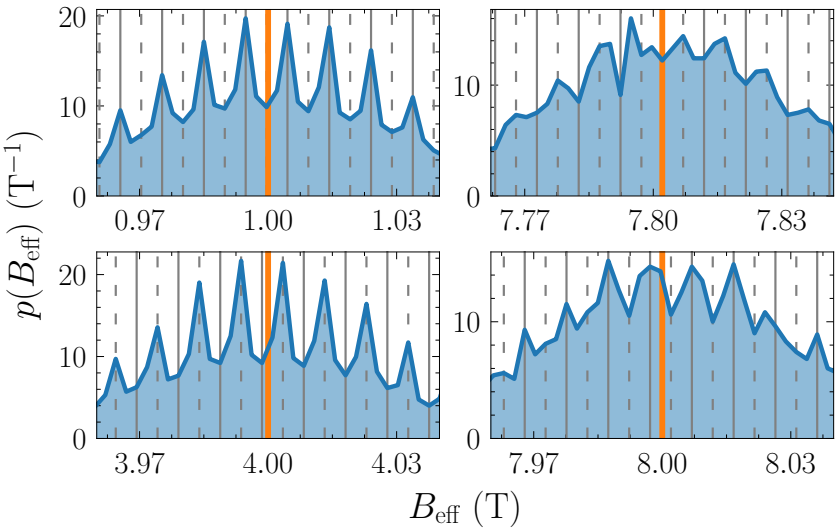

Figure 6.7: Extended model I: Probability distribution $p(B_\mathrm{eff})$ of the effective magnetic field showing nuclear focusing in the NESS regime for various magnetic fields B_ext (orange vertical lines) at $\gamma = 0.004$. The gray solid and dashed vertical lines represent the values of B_eff fulfilling the ERC (6.10a) and ORC (6.10b), respectively.

is found in Sec. 5.3 using pulse model II; see Figs. 5.14(a) and 5.18. It turns out that the typical hyperfine coupling, which is proportional to $\sqrt{\gamma}/T_\mathrm{n}^*$, determines the saturation value. In Fig. 6.8, we study $S_\mathrm{NESS}^\perp$ as a function of the typical hyperfine coupling for various combinations of B_ext and T_n^* while varying γ. Especially for $B_\mathrm{ext} = 1\,\mathrm{T}$ and $4\,\mathrm{T}$, there appears to be a linear dependence. It can be exploited for an extrapolation $\sqrt{\gamma} \to 0$, i.e., to an infinite bath size. This is the limit of interest for QDs with $10^4 - 10^6$ effectively coupled nuclear spins, i.e., $\sqrt{\gamma} \approx 10^{-3} - 10^{-2}$. Furthermore, the choice of the dephasing time T_n^*, which is an input parameter taken from experiments, appears to be of minor importance in the limit $\sqrt{\gamma} \to 0$ as long as it is significantly shorter than the pulse repetition time T_R. Otherwise, one would approach the regime of resonant spin amplification instead of SML, where the physics is qualitatively different [135]. We do not study this regime here. The data and their extrapolation is not as robust for $B_\mathrm{ext} = 2\,\mathrm{T}$ where almost no NIFF emerges, but this uncertainty is represented by the fit error being larger than the error of a single saturation value.

For too large values of $\sqrt{\gamma}/T_\mathrm{n}^*$ and independent of the magnetic field, there is almost no NIFF and the linear scaling is not applicable. Physically, the effective hyperfine couplings $\varepsilon_k \propto \sqrt{\gamma}/T_\mathrm{n}^*$ become too large in comparison to the nuclear Zeeman term $\gamma_\mathrm{n} B_\mathrm{ext}$ in Eq. (6.4). For this reason, the linear scaling is applicable for larger ratios $\sqrt{\gamma}/T_\mathrm{n}^*$ when a larger magnetic field is applied. For instance, the linear scaling in Fig. 6.8 for $B_\mathrm{ext} = 4\,\mathrm{T}$ is valid up to larger ratios $\sqrt{\gamma}/T_\mathrm{n}^*$ than for $B_\mathrm{ext} = 1\,\mathrm{T}$.

The fact that the influence of T_n^* on the revival amplitude $S_\mathrm{NESS}^\perp$ in the limit $\gamma \to 0$ is only minor is very beneficial because the number of pulses required to reach the saturated revival amplitude scales approximately with $(T_\mathrm{n}^*)^3$. Thus, we can stick to our initial choice $T_\mathrm{n}^* = 1\,\mathrm{ns}$ without worrying about a strong influence of this parameter, which can also be larger for some QD samples, e.g., $T_\mathrm{n}^* \approx 4\,\mathrm{ns}$ [23, 123]. Simulations for such a large value are out of reach because of the required computational effort. They require a perturbative treatment, which is developed and applied in Chap. 7 to study the influence of the isotope composition of the QDs on the nonequilibrium spin physics.

We put the new insight to use in Fig. 6.9 by plotting the saturated revival amplitude $S_\mathrm{NESS}^\perp$ as a function of B_ext for decreasing values of γ. The z component S_NESS^z is not shown because it is almost equal to $S_\mathrm{NESS}^\perp$. We also extrapolate the saturation values to an infinite bath size ($\gamma \to 0$) using the procedure described above and

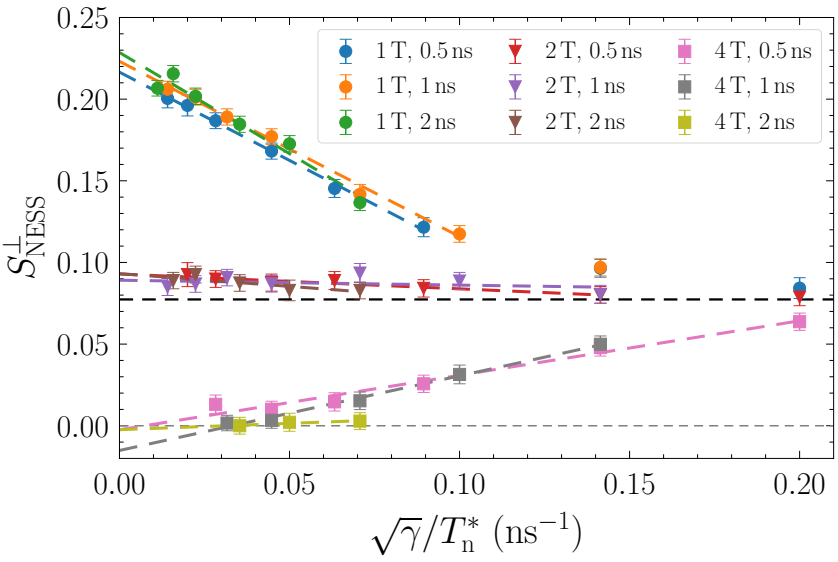

Figure 6.8: Extended model I: Limiting values $S^{\perp}_{\mathrm{NESS}}$ of the revival amplitude as a function of the typical hyperfine coupling $\sqrt{\gamma}/T_{\mathrm{n}}^{*}$ for various combinations of the magnetic field B_{ext} (in T) and the dephasing time T_{n}^{*} (in ns) given in the legend. Linear extrapolations $\sqrt{\gamma} \to 0$ (dashed lines) yield the limit of an infinite bath size. The horizontal dashed line represents the SML steady-state value S_{SML}.

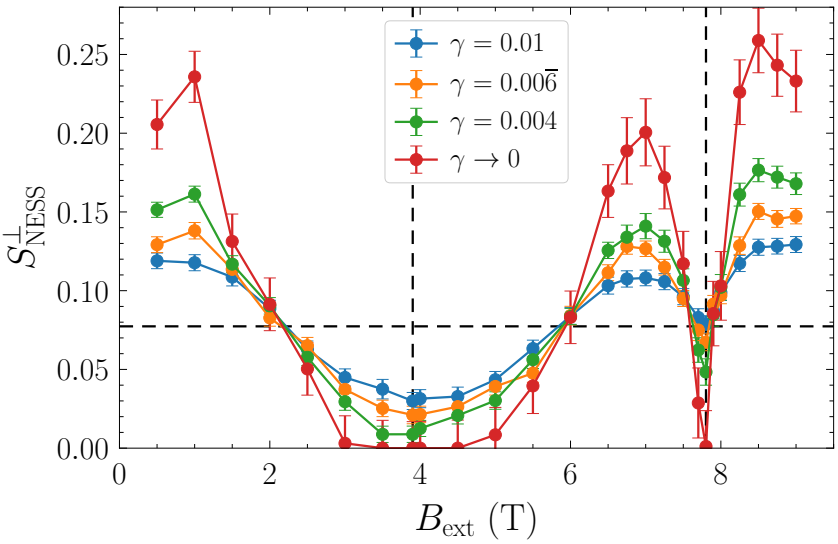

Figure 6.9: Extended model I: Limiting values $S^{\perp}_{\mathrm{NESS}}$ of the revival amplitude as a function of the magnetic field B_{ext} for various inverse bath sizes γ and extrapolated to $\gamma \to 0$. The vertical dashed lines represent the NRC (6.13) for $k = 1$ and 2, the horizontal dashed line indicates the SML steady-state value S_{SML}.

compare the results to the SML regime without NIFF. For the extrapolation, we enforce the physical lower bound $S^{\perp}_{\mathrm{NESS}} \geq 0$. This is realized by setting $S^{\perp}_{\mathrm{NESS}} = 0$ if the extrapolation yields a negative value, but we have checked that the actual extrapolation value and its error are in agreement with the bound. Turning to the results, we find two *minima* at the values of B_{ext} that fulfill the NRC (6.13), with the second one being much narrower. The minima and maxima become more pronounced for smaller values of γ, and the minima for $\gamma \to 0$ correspond to $S^{\perp}_{\mathrm{NESS}} \approx 0$, i.e., there is no revival amplitude. At around $B_{\mathrm{ext}} = 2\,\mathrm{T}$ and $6\,\mathrm{T}$, the revival amplitude is very close to S_{SML} for any choice of γ, which implies that there is almost no contribution NIFF. Between these two fields, we find a destructive interplay of SML and NIFF that is responsible for a decrease of the revival amplitude with respect to S_{SML}. This behavior is also evident in a narrow interval around $B_{\mathrm{ext}} = 7.8\,\mathrm{T}$. For the other values of B_{ext}, NIFF leads to an increase of the revival amplitude, i.e., it acts constructively by enhancing the revival amplitude S_{SML} already present after a few pulses in the SML regime without NIFF.

6.2.3 Discussion of the extended model I

Mimicking the quantum mechanical behavior of the system by interpreting the action of each pump pulse as a quantum mechanical measurement requires a non-deterministic pulse description in the framework of our semiclassical approach based on the TWA. As a result of this extension to the initial model, we find the expected minima in the magnetic field dependence of $S^{\perp}_{\mathrm{NESS}}$, similar to the experimental and theoretical results of Kleinjohann *et al.* [117], similar to our result for pulse model II in Sec. 5.4, and in contrast to the initial model studied in the previous section.

Overall, the results for the EM I are qualitatively very similar to the quantum mechanical results of Kleinjohann *et al.* [117]. This is a good message because they consider essentially the effects in their model, which suggests that our semiclassical approach mimics the quantum mechanical system well. Differences could stem from the considered bath sizes: the quantum mechanical approach is limited to only $N = 6$ nuclear spins, while our semiclassical approach can deal with much larger bath sizes.

Summarizing the results, the probability distributions of the effective magnetic field show much broader nuclear focusing peaks than those found for the initial model.

This is in much better agreement with the experimental observation [122, 148]. Moreover, only a single kind of resonance appears, corresponding to either an integer (ERC) *or* a half-integer (ORC) number of Larmor periods between consecutive pulses. Depending on the strength of the magnetic field, either the ERC or the ORC is fulfilled, which, in turn, leads to an increase (constructive interplay) or a decrease (destructive interplay) of the revival amplitude relative to the SML steady-state value, respectively. The minima and maxima in the magnetic field dependence of the revival amplitude become more pronounced for larger bath sizes. Furthermore, it is possible to extrapolate the revival amplitude to an infinite bath size. In this limit, the dephasing time T_n^*, which serves as an input parameter taken from experiment, only has a minor influence.

Note that in principle, the emergence of the ORC could also lead to an increase of the revival amplitude relative to the SML regime, given that the nuclear focusing is strong enough. S_NESS^z would be negative in this case, i.e., there would be a phase shift of $\Delta\varphi \approx \pi$ at the pulse boundary. This behavior, however, is not observed in the simulations. In this context, it is important to mention that the resonance favored by the effective magnetic field does not directly translate to a phase shift of either $\Delta\varphi \approx 0$ or π as in Chap. 5. The reason is the aforementioned difference between the distribution of the effective magnetic field and the frequency spectrum of the electron spin towards which the precession modes contribute with different weights.

6.3 Extended model II: Trion pseudospin dynamics

Up to this point, the trion is treated only on the level of an intermediate state that decays on the timescale $\tau_0 = 400\,\mathrm{ps}$ as described by Eq. (6.2b). We neglected the dynamics of its pseudospin $\boldsymbol{J}$, which can be described similarly to the dynamics of the electron spin $\boldsymbol{S}$. In the theoretical studies of Refs. [117, 122], this dynamics is not considered either. But its description, especially the coupling to the external magnetic field, is crucial for the correct description of the time evolution between consecutive pulses. In the context of spin inertia and polarization recovery measurements, where rather small magnetic fields up to a few 100 mT are applied in Faraday geometry, the detailed description of the trion pseudospin dynamics can be absolutely mandatory [93, 125]. In the following, we demonstrate that the trion

pseudospin dynamics also changes the behavior of NIFF. In addition, we observe the appearance of dynamic nuclear polarization [42, 115, 225], i.e., the formation of a nonzero average polarization of the nuclear spin bath, in the extended model.

6.3.1 Equations of motion of the trion pseudospin

A singlet T^- trion excited by the σ^- pulses consists of two electrons in a spin singlet state and a heavy hole with unpaired spin so that the effective type of the charge carrier spin in the excited state (hole) is opposite to the type in the ground state (electron). We recall that the relevant trion states, resulting from the unpaired heavy-hole spin, can be described by an effective pseudospin 1/2 denoted as $\boldsymbol{J}$; see Eq. (2.8) for its definition. Its dynamics is induced by its coupling to the effective magnetic field, but we need to consider that the hyperfine interaction is much weaker and anisotropic for hole spins because it is caused by the dipole-dipole interaction [156–158]. As discussed in Sec. 3.1.4, this interaction can be described by the anisotropic CSM [156, 157, 184]

$$\hat{\mathcal{H}}_{\mathrm{CSM,anisotropic}} = \sum_{k=1}^{N} \chi A_k \left[\hat{J}^z \hat{I}_k^z + \frac{1}{\lambda} (\hat{J}^x \hat{I}_k^x + \hat{J}^y \hat{I}_k^y) \right] . \tag{6.17}$$

Here, we assume the same parameterization for the couplings A_k as before and use the factor χ to describe how much weaker the hyperfine interaction is for hole spins than for electron spins. Typically, it is about five to ten times weaker [19, 93, 97] and thus, we use $\chi = 0.2$ in the simulations. A typical value for the degree of anisotropy is $\lambda \approx 5 - 10$ [93, 97]; we use $\lambda = 5$.

The Zeeman effect acting on the trion pseudospin also needs to be accounted for. Since we consider a magnetic field that is applied along the x axis, the corresponding Hamiltonian simply has the form

$$\hat{\mathcal{H}}_{\mathrm{hZ}} = h_{\mathrm{h}} \hat{J}^x , \tag{6.18}$$

with $h_{\mathrm{h}} = \gamma_{\mathrm{h}} B_{\mathrm{ext}}$. The subscript 'h' refers to the heavy hole in the trion. The g factor entering in the gyromagnetic ratio $\gamma_{\mathrm{h}} = g_{\mathrm{h}} \mu_{\mathrm{B}} \hbar^{-1}$ is also anisotropic. Typical values range from $g_{\mathrm{h}} = 0.05$ to 0.15, depending on the in-plane orientation of the QD sample [96, 132]. We focus on $g_{\mathrm{h}} = 0.15$ here and show in Appendix D that the results are very similar for $g_{\mathrm{h}} = 0.05$.

In the semiclassical approach, the classical equation of motion for the trion pseudospin $\boldsymbol{J}$ follows from application of Eq. (3.31). It has the form

$$\frac{\mathrm{d}}{\mathrm{d}t}\boldsymbol{J} = \chi\left(B_{\mathrm{ov}}^{z}\boldsymbol{e}_z + \frac{1}{\lambda}\boldsymbol{B}_{\mathrm{ov}}^{\perp}\right)\times\boldsymbol{J} + h_{\mathrm{h}}\boldsymbol{e}_x\times\boldsymbol{J} - \frac{1}{\tau_0}\boldsymbol{J}\,, \tag{6.19}$$

with $\boldsymbol{B}_{\mathrm{ov}}^{\perp} = B_{\mathrm{ov}}^{x}\boldsymbol{e}_x + B_{\mathrm{ov}}^{y}\boldsymbol{e}_y$. The first term describes the precession about the Overhauser field, but it is weaker (factor χ) and also anisotropic (factor $1/\lambda$). The second term describes the precession about the external magnetic field. The last term describing the trion recombination is included by hand in accordance with similar approaches [23, 125, 135]. Note that because of the selection rules governing the optical transitions between the bands Γ_6 and Γ_8 in GaAs-based semiconductors, only the z projection J^z contributes to the spin polarization in the ground state during the recombination [114, 124]. Thus, Eq. (6.2a) describing the dynamics of the electron spin $\boldsymbol{S}$ requires no change.

The equations of motion describing the dynamics of the Overhauser field $\boldsymbol{B}_{\mathrm{ov}}$ also need to be extended because the nuclei interact with the trion pseudospin during its lifetime τ_0. Again, the weaker and anisotropic hyperfine interaction is accounted for by the parameters λ and χ. Since we assume that the couplings for the trion pseudospin can be parameterized using the same exponential parameterization (6.3) as for the electron spin, the effective coupling constants ε_k and the weights W_k entering in the Spectral Density approach can be reused. Then, the extended equations of motion of the N_{tr} auxiliary fields $\boldsymbol{Q}_k$ result to be

$$\frac{\mathrm{d}}{\mathrm{d}t}\boldsymbol{Q}_k = \varepsilon_k\boldsymbol{S}\times\boldsymbol{Q}_k + \chi\varepsilon_k\left(J^z\boldsymbol{e}_z + \frac{1}{\lambda}\boldsymbol{J}^{\perp}\right)\times\boldsymbol{Q}_k + h_{\mathrm{n}}\boldsymbol{e}_x\times\boldsymbol{Q}_k\,, \tag{6.20}$$

with $\boldsymbol{J}^{\perp} = J^x\boldsymbol{e}_x + J^y\boldsymbol{e}_y$. The second term is the new one and describes the anisotropic coupling of the fields $\boldsymbol{Q}_k$ to the trion pseudospin $\boldsymbol{J}$.

6.3.2 Results for the extended model II

The numerical integration of the extended equations of motion (6.19) and (6.20) together with Eq. (6.2a) leads only to a negligible increase of computational complexity in comparison to the previous setup. In the following, we discuss the main changes appearing in comparison to the results of the EM I analyzed in Sec. 6.2.

Spin dynamics

In the pump-probe experiments under consideration, the Faraday rotation or ellipticity is measured by weak linearly polarized pulses. The probed signal is proportional to $S^z - J^z$ [113, 114], i.e., the spin polarization of the system is measured. Figure 6.10 shows the corresponding time evolution resulting from our model between two consecutive pulses in the NESS regime for the two magnetic fields $B_{\mathrm{ext}} = 1\,\mathrm{T}$ and $4\,\mathrm{T}$. The initial dephasing reveals additional beats that stem from the trion pseudospin precessing about the external magnetic field with a different Larmor frequency than the electron spin. The beats decay on the timescale $\tau_0 \ll T_{\mathrm{R}}$ so that they do not appear in the revival signal before the next pulse. They are also evident in experimental results [23–25, 117], see also Figs. 2.4(a) and 2.5(a), but they typically vanish much quicker than in our model calculations. This issue is related to the inhomogeneous nature of self-assembled QD ensembles and is addressed in Sec. 6.4.

Nuclei-induced frequency focusing

The most prominent difference to the EM I is visible in the magnetic field dependence of the revival amplitude, which is shown in Fig. 6.11 for various values of the inverse bath size γ. While there are still two minima at values of B_{ext} fulfilling the NRC (6.13), the first broad minimum hints at the emergence of even resonances instead of the previous odd ones because the revival amplitude is larger than S_{SML} and not smaller as for the EM I (Fig. 6.9). This finding is supported by the corresponding quasistationary distributions $p(B_{\mathrm{eff}})$ of the effective magnetic field, e.g., for $B_{\mathrm{ext}} = 4\,\mathrm{T}$ shown in Fig. 6.12 where nuclear focusing peaks appear at values of B_{eff} fulfilling the ERC. Hence, the values of the revival amplitude are larger than the mere SML steady-state value S_{SML} (highlighted in Fig. 6.11 as horizontal dashed line) thanks to a constructive interplay of SML and NIFF. But the overall NIFF degree in this regime is small, which differs from our findings for the EM I where the revival amplitude approaches zero in the vicinity of $B_{\mathrm{ext}} = 3.9\,\mathrm{T}$ (Fig. 6.9) because the nuclear focusing (favoring the ORC) is more efficient for smaller values of γ. For the EM II, the narrow minimum visible in Fig. 6.11 at $B_{\mathrm{ext}} = 7.8\,\mathrm{T}$ still results from the ORC being favored in the probability distribution $p(B_{\mathrm{eff}})$ as evident from Fig. 6.12. In contrast to the EM I, this minimum is slightly narrower.

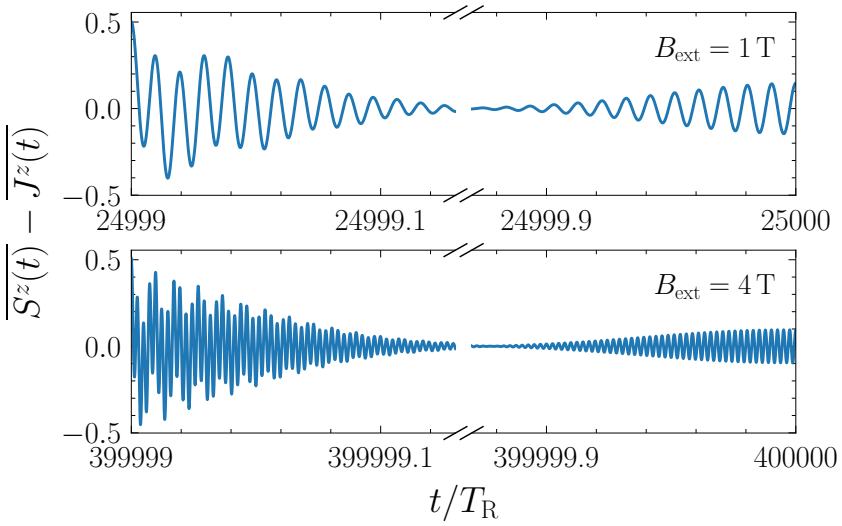

Figure 6.10: Extended model II: Spin dynamics between two consecutive pulses after a long train of pulses for the two magnetic fields $B_{\mathrm{ext}} = 1\,\mathrm{T}$ and $4\,\mathrm{T}$ at $\gamma = 0.004$. The beats visible in the initial dephasing signal result from the different Larmor frequencies of the electron spin $\boldsymbol{S}$ ($g_{\mathrm{e}} = 0.555$) and trion pseudospin $\boldsymbol{J}$ ($g_{\mathrm{h}} = 0.15$).

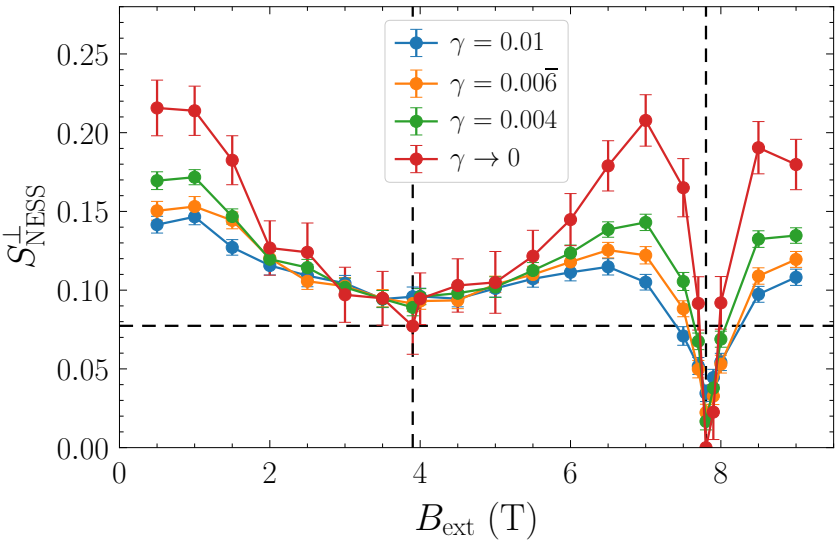

Figure 6.11: Extended model II: Limiting values $S^{\perp}_{\mathrm{NESS}}$ of the revival amplitude as a function of the magnetic field B_{ext} for various inverse bath sizes γ and for the infinite bath limit $\gamma \to 0$. The vertical dashed lines represent the NRC (6.13) for $k = 1$ and 2, the horizontal dashed line indicates the SML steady-state value S_{SML}.

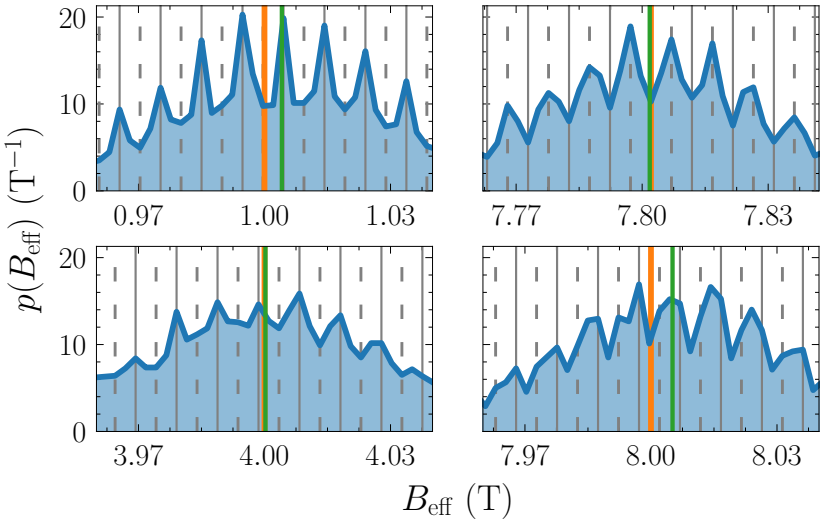

Figure 6.12: Extended model II: Probability distribution $p(B_{\mathrm{eff}})$ of the effective magnetic field in the NESS regime for various magnetic fields B_{ext} (orange vertical lines) at $\gamma = 0.004$. The gray solid and dashed vertical lines represent the values of B_{eff} fulfilling the ERC (6.10a) and ORC (6.10b), respectively. The green vertical lines represent the expectation value of the distributions.

The linear extrapolation $\sqrt{\gamma} \to 0$ to the infinite bath limit of the saturation value $S^{\perp}_{\mathrm{NESS}}$, which is established in Fig. 6.8 for the EM I, is still applicable when accounting for the trion pseudospin dynamics. As before, the exact choice of the dephasing time T_{n}^{*} has only a minor influence on the results. We apply the extrapolation procedure for the magnetic field dependence $S^{\perp}_{\mathrm{NESS}}(B_{\mathrm{ext}})$ of the revival amplitude in Fig. 6.11. Overall, the structure becomes more pronounced in the limit $\gamma \to 0$, but the revival amplitudes in the vicinity of $B_{\mathrm{ext}} = 3.9\,\mathrm{T}$ are almost independent of γ. Moreover, the maxima have a similar height as in Fig. 6.9 for the EM I. This implies that the degree of NIFF under optimal conditions is very similar, and the revival amplitude is about three times larger than without NIFF. Experimentally, a ratio of 3.6 for the revival amplitude with versus without NIFF is found at $B_{\mathrm{ext}} = 2\,\mathrm{T}$ [148]. For this particular magnetic field, we find a ratio of only 2. For the EM I, this ratio is barely larger than 1.

Dynamic nuclear polarization

In the probability distributions of the effective magnetic field shown in Fig. 6.12, a small shift of the distributions to the right can be discerned for $B_{\mathrm{ext}} = 1\,\mathrm{T}$

(upper left panel) and $B_{\mathrm{ext}} = 8\,\mathrm{T}$ (lower right panel). The shift is made visible by highlighting the expectation value $\overline{B_{\mathrm{eff}}}$ of the distribution as a green vertical line. The applied magnetic field B_{ext} is highlighted in orange. Remember that at the beginning of each simulation, $\overline{B_{\mathrm{eff}}} \approx B_{\mathrm{ext}}$ holds, with small deviations stemming only from the statistical nature of the semiclassical approach.

The shift results from dynamic nuclear polarization (DNP) [19, 42, 115, 225] in the Overhauser field, i.e., the nuclear spins align along the axis of the external magnetic field $B_{\mathrm{ext}}\boldsymbol{e}_x$ to a certain extent. First, there is the possibility of an internal alignment of the nuclear spins in each QD. Second, the Overhauser fields of all QDs in the ensemble could also align. This ensemble effect can be the result of the first mechanism, but the internal alignment of nuclear spins is not possible when a simple box model is used for the hyperfine couplings, i.e., when all couplings are considered to be equal.

In order to analyze this phenomenon in more detail, we define the DNP as

$$B_{\mathrm{DNP}}(n_{\mathrm{p}}) \coloneqq \frac{\overline{B^x_{\mathrm{ov}}(n_{\mathrm{p}}T_{\mathrm{R}})} - \overline{B^x_{\mathrm{ov}}(0)}}{\gamma_{\mathrm{e}}} \tag{6.21}$$

and study it as a function of the magnetic field for several values of γ in Fig. 6.13. The number of pulses n_{p} is chosen such that $S^{\perp}_{\mathrm{NESS}}$ is approximately in saturation. The spheres and solid lines represent B_{DNP}, the triangles and dashed lines its absolute value $|B_{\mathrm{DNP}}|$. The DNP B_{DNP} can be either positive or negative, i.e., it can point in the same direction as the external magnetic field ($B_{\mathrm{DNP}} > 0$) or in the opposite direction ($B_{\mathrm{DNP}} < 0$). Interestingly, the magnetic field dependence of $|B_{\mathrm{DNP}}|$ is very similar to that of $S^{\perp}_{\mathrm{NESS}}$ (Fig. 6.11) and we find no DNP at the magnetic fields fulfilling the NRC (6.13). This suggests that the underlying mechanisms of DNP and NIFF have a similar origin in the equations of motion. But considering that nuclear focusing displays also a kind of dynamic polarization of the nuclei, just with the polarization approaching stable points given by the resonance conditions, this finding is not a big surprise.

For most magnetic fields, the dependence of the DNP on the inverse bath size γ is only minor. But we stress that the values B_{DNP} plotted in Fig. 6.13 do not represent the stationary values of the DNP even though the values of $S^{\perp}_{\mathrm{NESS}}$ are approximately in saturation (number of pulses scaled with B^2_{ext}). The reason is that the saturation limit for the DNP is approached much slower than for the revival amplitude. It

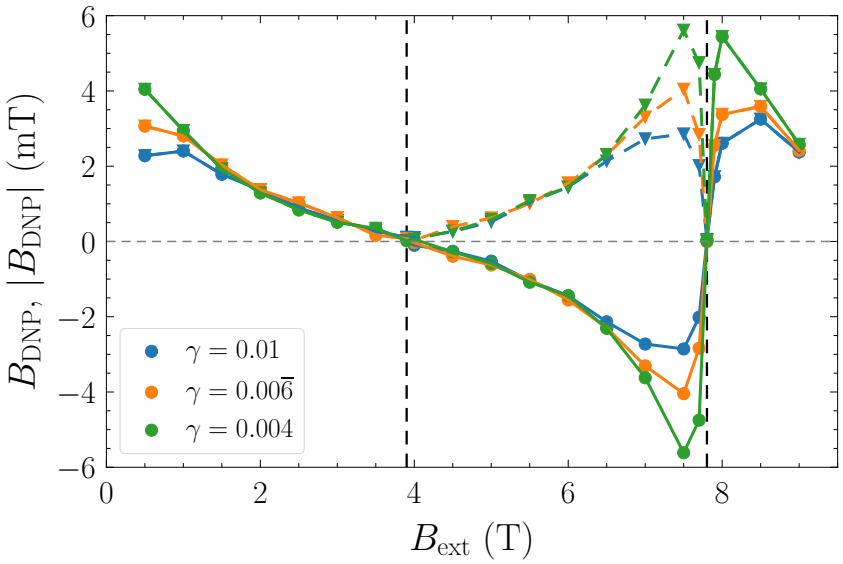

Figure 6.13: Extended model II: DNP B_{DNP} (circles, solid lines) and its absolute value (triangles, dashed lines) as a function of the magnetic field B_{ext} for various inverse bath sizes γ after the saturation of the revival amplitude is reached. The vertical dashed lines represent the NRCs (6.13) for $k = 1$ and 2.

appears that for the magnetic fields for which the DNP is most prominent, smaller values of γ correspond to a stronger DNP. Unfortunately, it is not possible to reach the stationary DNP regime for large magnetic fields because of its extremely slow convergence, but the DNP behavior for small magnetic fields is analyzed in the following.

In Fig. 6.14, we investigate the saturation behavior of DNP and the mechanisms leading to its emergence. Figure 6.14(a) demonstrates the buildup of B_{DNP} caused by periodic driving with pulses for $B_{\mathrm{ext}} = 0.5\,\mathrm{T}$ at $\gamma = 0.004$, eventually reaching a steady state of about 100 mT after more than 10^6 pulses. This DNP is fairly large in comparison to the initial standard deviation of the Overhauser field components of about 29 mT. Note that the revival amplitude $S^{\perp}_{\mathrm{NESS}}$ is already saturated after about 5000 pulses for this set of parameters, i.e., a two orders of magnitude longer pulse train is required to reach the saturation regime for DNP.

The DNP buildup and saturation as a function of the number of pulses can be

described by the function

$$f_{\mathrm{DNP}}(n_{\mathrm{p}}) = A_{\mathrm{DNP}} \frac{2}{\pi} \arctan\left(\frac{n_{\mathrm{p}}}{\eta}\right) + B_{\mathrm{DNP}}\,, \tag{6.22}$$

where A_{DNP}, B_{DNP}, and η are the fit parameters. As before, the function displays a $1/n_{\mathrm{p}}$ convergence towards saturation and it is the same function that describes the buildup of the revival amplitude.

The average length of the Overhauser field vector

$$\overline{B_{\mathrm{ov}}} := \frac{\overline{|\boldsymbol{B}_{\mathrm{ov}}|}}{\gamma_{\mathrm{e}}} \tag{6.23}$$

increases as a consequence of an alignment of the individual nuclear spins. The dependence of $\overline{B_{\mathrm{ov}}}$ on the number of pulses can also be described by the function (6.22). However, this lengthening alone does not explain the appearance of DNP completely as we see next.

Figure 6.14(c) shows the average angles

$$\overline{\theta^{\alpha}} := \overline{\arccos\left(\frac{B^{\alpha}_{\mathrm{ov}}}{|\boldsymbol{B}_{\mathrm{ov}}|}\right)}\,, \tag{6.24}$$

$\alpha \in \{x, y, z\}$, between the Overhauser field components B^{α}_{ov} and the unit vectors $\boldsymbol{e}_{\alpha}$ as a function of the number of pulses. The average of the initial angle is given by $\pi/2$ for all components because the components B^{α}_{ov} are sampled from the same normal distribution. Driving the system with periodic pulses does not influence the average angles $\overline{\theta^{y}}$ and $\overline{\theta^{z}}$, but the average angle $\overline{\theta^{x}}$ is reduced to about $\pi/12$, implying that the Overhauser field aligns along the direction of the external magnetic field pointing along the x axis, which is confirmed by $B_{\mathrm{DNP}} > 0$. The dependence of $\overline{\theta^{x}}$ on the number of pulses can again be described by the function (6.22). Note that $\overline{\theta^{x}}$ does not shrink to zero because of the finite components B^{y}_{ov} and B^{z}_{ov}. These components still follow a normal distribution but with a reduced variance.

The corresponding probability distributions of the angles θ^{α} after different numbers of pulses are plotted in Fig. 6.14(d). Initially, all components follow the same distribution with a maximum at $\pi/2$. As a consequence of the periodic driving with pulses, the distributions of all components become narrower, i.e., more focused

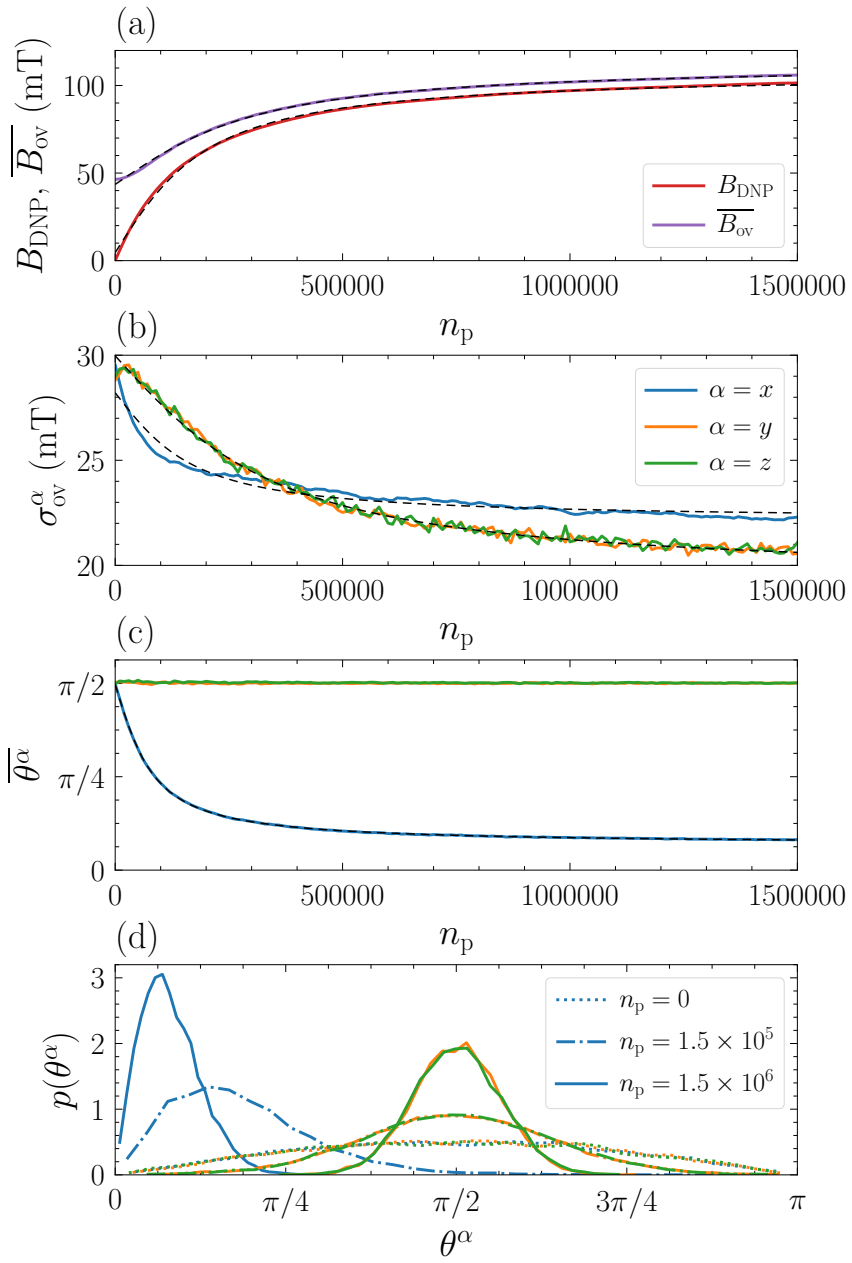

Figure 6.14: Analysis of the DNP behavior in the extended model II for $B_{\mathrm{ext}} = 0.5\,\mathrm{T}$ at $\gamma = 0.004$ caused by periodic driving with n_{p} pulses. All fits (black dashed lines) are of the type (6.22). **(a)** Buildup of the DNP B_{DNP} (blue line) defined in Eq. (6.21). The purple line shows the simultaneous increase of the average Overhauser field length $\overline{B_{\mathrm{ov}}}$. **(b)** Decrease of the standard deviations $\sigma_{\mathrm{ov}}^{\alpha}$, $\alpha \in \{x, y, z\}$, of the Overhauser field components. **(c)** Average angles $\overline{\theta^{\alpha}}$ between the Overhauser field and the unit vectors $\boldsymbol{e}_{\alpha}$. **(d)** Probability distributions of the angles θ^{α} after different numbers of pulses.

around a certain angle. The angles θ^y and θ^z remain centered around $\pi/2$, but the angle θ^x becomes significantly smaller; see also Fig. 6.14(c) for the average angles.

An important consequence of DNP is a narrowing of the Overhauser field distribution, which is analyzed in Fig. 6.14(b). The standard deviations of the Overhauser field components

$$\sigma_{\mathrm{ov}}^{\alpha} := \frac{\sqrt{\mathrm{Var}[B_{\mathrm{ov}}^{\alpha}]}}{\gamma_{\mathrm{e}}}\,, \tag{6.25}$$

$\alpha \in \{x, y, z\}$, are reduced from their initial value of approximately 29 mT to about $21 - 22$ mT. This process is faster for the x component and the precise saturation value differs slightly from that of the y and z components. A fit with the function (6.22) works well again, allowing for an extrapolation $n_{\mathrm{p}} \to \infty$. The narrowing of the Overhauser field distribution implies an increase of the coherence because the dephasing time T_{n}^{*} is inversely proportional to the standard deviations of the Overhauser field components according to Eq. (6.1).

What is the influence of the system parameters, especially of the inverse effective bath size γ, on the DNP behavior? First, we find that the rate of DNP scales linearly with γ and the data available for $B_{\mathrm{ext}} = 0.5\,\mathrm{T}$ and 1 T suggests a B_{ext}^{-2} dependence. These are the same scaling laws as for NIFF.

For a more detailed analysis of the influence of the bath size, we fit the function (6.22) to the data at $B_{\mathrm{ext}} = 0.5\,\mathrm{T}$ (circles) and 1 T (triangles) for various values of γ and plot the resulting saturation values in Fig. 6.15. It turns out that the dependence on γ is linear for all observables and hence, linear fits enable extrapolations to the limit $\gamma \to 0$, i.e., the limit of interest for QDs with $N_{\mathrm{eff}} = 10^4 - 10^6$ effectively coupled nuclear spins. For B_{DNP}, this extrapolation yields a value of 117 mT for $B_{\mathrm{ext}} = 0.5\,\mathrm{T}$ and a value of 102 mT for $B_{\mathrm{ext}} = 1\,\mathrm{T}$. For $B_{\mathrm{ext}} = 0.5\,\mathrm{T}$, the standard deviations σ_{ov}^{y} and σ_{ov}^{z} are reduced by about 40% from their initial value of about 29 mT to only 17.4 mT. The standard deviation σ_{ov}^{x} decreases slightly less to 21.2 mT. For $B_{\mathrm{ext}} = 1\,\mathrm{T}$, this anisotropy is less pronounced with limiting values of $\sigma_{\mathrm{ov}}^{x} = 21.7\,\mathrm{mT}$ and $\sigma_{\mathrm{ov}}^{y} = \sigma_{\mathrm{ov}}^{z} = 20\,\mathrm{mT}$. Comparing the results for the limit $\gamma \to 0$ to the data for finite values of γ, we conclude that all main effects are already present for, e.g., $\gamma = 0.01$. The size of the spin bath influences only the precise values of the observables, but their order of magnitude turns out to be robust.

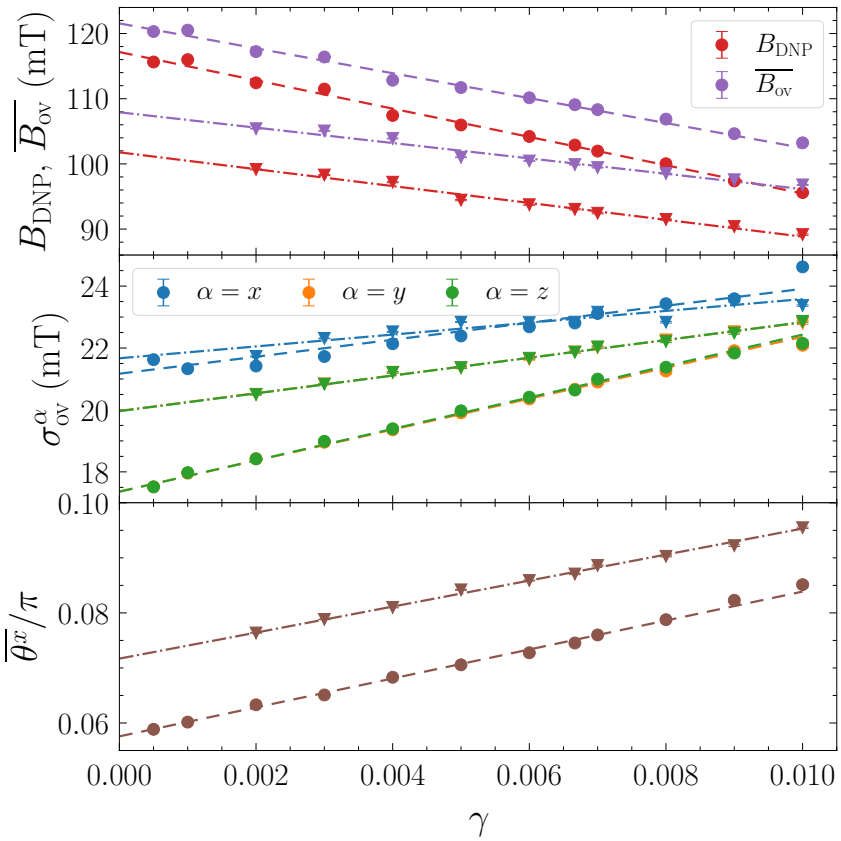

Figure 6.15: Extended model II: Limiting values of the DNP B_{DNP}, the average length $\overline{B_{\mathrm{ov}}}$ of the Overhauser field, the standard deviations $\sigma_{\mathrm{ov}}^{\alpha}$ of the Overhauser field components, and the average angle $\overline{\theta^x}$ as a function of the inverse bath size γ, calculated by fitting the function (6.22) to the data for $B_{\mathrm{ext}} = 0.5\,\mathrm{T}$ (circles) and $1\,\mathrm{T}$ (triangles). The fit errors shown for each data point are usually too small to be discernible. The dashed ($B_{\mathrm{ext}} = 0.5\,\mathrm{T}$) and dash-dotted ($B_{\mathrm{ext}} = 1\,\mathrm{T}$) lines represent linear fits, which enable an extrapolation to the infinite bath limit $\gamma \to 0$.

Let us briefly discuss the role of the dephasing time T_{n}^* on DNP. According to Eq. (6.1), the initial fluctuation strength of the Overhauser field is proportional to $(T_{\mathrm{n}}^*)^{-1}$ and hence, we also expect this dependence for the DNP in the saturation limit. For QDs with $\gamma = 0.01$ at $B_{\mathrm{ext}} = 0.5\,\mathrm{T}$, we find a DNP of $B_{\mathrm{DNP}} = 127\,\mathrm{mT}$ for $T_{\mathrm{n}}^* = 0.5\,\mathrm{ns}$, $B_{\mathrm{DNP}} = 96\,\mathrm{mT}$ for $T_{\mathrm{n}}^* = 1\,\mathrm{ns}$, and $B_{\mathrm{DNP}} = 45\,\mathrm{mT}$ for $T_{\mathrm{n}}^* = 2\,\mathrm{ns}$. For $B_{\mathrm{ext}} = 1\,\mathrm{T}$, the dependence is similar, i.e., a larger dephasing time T_{n}^* corresponds to a smaller DNP. We cannot confirm the $(T_{\mathrm{n}}^*)^{-1}$ dependence for this data with certainty, but it fits sufficiently well to provide an educated guess. For $\gamma \to 0$ and $T_{\mathrm{n}}^* \approx 4\,\mathrm{ns}$, which corresponds to the QD sample studied in Refs. [23, 123], we estimate a DNP of about $30\,\mathrm{mT}$ based on the scaling with $(T_{\mathrm{n}}^*)^{-1}$. A direct

simulation of the DNP for this particular sample is out of reach because the required computational effort scales roughly with $(T_n^*)^3$. In any case, the DNP is expected to be noticeably larger than the typical Overhauser field fluctuations.

6.3.3 Discussion of the extended model II

The inclusion of the trion pseudospin dynamics is a crucial step towards the correct description of the underlying pump-probe experiments. It turns out to have an important qualitative influence on the interplay of SML and NIFF. For the EM I studied in Sec. 6.2, a broad range of magnetic fields is found for which nuclear focusing appears in the probability distribution $p(B_{\text{eff}})$ of the effective magnetic field at values of B_{eff} fulfilling the ORC. In contrast, when including the trion pseudospin dynamics, the majority of magnetic fields B_{ext} reveal nuclear focusing at the ERC, with the only exception being the very narrow but apparently robust regime around $B_{\text{ext}} = 7.8\,\text{T}$ for which the system chooses the ORC. This means that for the majority of magnetic fields, the interplay of SML and NIFF is constructive. In the vicinity of the broad minimum at $B_{\text{ext}} = 3.9\,\text{T}$, we find very weak nuclear focusing in the Overhauser field (Fig. 6.12) and it is almost independent of the effective bath size. In contrast, the nuclear focusing in this regime for the EM I is fairly pronounced (Fig. 6.7), but the system chooses the ORC instead of the ERC so that the revival amplitude is strongly suppressed because of a destructive interplay of SML and NIFF (Fig. 6.9).

In the quantum mechanical model with $N = 6$ nuclear spins studied by Kleinjohann *et al.* [117], odd resonances emerge in the vicinity of the NRC (6.13) for $B_{\text{ext}} = 3.9\,\text{T}$ ($k = 1$) with an accompanied minimum of the revival amplitude. A minimum is also found around $B_{\text{ext}} = 7.8\,\text{T}$ ($k = 2$), but it is much broader than the one appearing in our semiclassical simulations. At this particular value, neither the ERC nor the ORC is fulfilled in their model, similar to the behavior of the initial model (Fig. 6.3). But the trion pseudospin dynamics is not accounted for in Ref. [117]. We expect that its inclusion also has a significant influence on the results of the fully quantum mechanical approach.

Why do even instead of odd resonances appear around $B_{\text{ext}} = 3.9\,\text{T}$ when the trion pseudospin dynamics is included? One can think of the Larmor precession of the trion pseudospin as a perturbation to the transfer of spin polarization during the

trion recombination, especially when the external magnetic field is large. Effectively, this leads to a decoupling of the trion pseudospin $\boldsymbol{J}$ from the electron spin $\boldsymbol{S}$ so that the equations of motion become very similar to those studied by Glazov *et al.* [131], who neglect the radiative trion recombination and observe only the ERC. Note that in the derivation of the ORC (6.10b) [122], the trion decays only exponentially as described by Eq. (6.2b) of the initial model, i.e., no further dynamics of its pseudospin is considered. For this reason, the ORC (6.10b) in its original form does not hold anymore when the dynamics of the trion is more complex such as in Eq. (6.19).

At present, the origin of the persistent sharp minimum in the magnetic field dependence of the revival amplitude at $B_{\mathrm{ext}} = 7.8\,\mathrm{T}$ remains unclear and it is very difficult to come up with a mechanism because of the nondeterministic pulse description. But it is plausible that something different happens whenever the NRC (6.13) with k being an even integer is fulfilled. In this case, the Larmor period of the nuclear spins is equal to the pulse repetition time so that without the Knight field, the nuclei would have the same orientation at the incidence of each pulse. Thus, the process of nuclear focusing induced by the hyperfine interaction is not disturbed as much by the nuclear Larmor precession as when the NRC with even k is not fulfilled. This reminds us of Chap. 5, where we have analyzed in detail that the nuclear Zeeman effect acts as a perturbation to the process of nuclear focusing, resulting in a very different qualitative behavior of the nonequilibrium spin physics.

The experimental situation on the aforementioned issues is unclear, but techniques that allow for a systematic study are available. By applying a radio frequency field, Evers *et al.* [148] are able to scramble the nuclear spins in the QDs such that they do not contribute to the revival amplitude by means of NIFF. Applying this approach to a broad range of magnetic fields allows for a systematic comparison between SML without NIFF and SML with NIFF. Such an experimental study is likely to clarify whether or not NIFF always leads to an increase of the revival amplitude. Moreover, a detailed experimental search for sharp features in the vicinity of the NRC (6.13), especially for $k = 2$, would be very interesting. Note that multiple NRCs are possible when considering all the different isotopes in the QDs instead of an average one. Indeed, accounting for the various isotopes results in a much more complex structure in the magnetic field dependence of the revival amplitude as we will see in Chap. 7.

The finding of a DNP of up to 120 mT in the simulation is interesting since it implies a certain increase of the dephasing time because of the associated narrowing of the Overhauser field distribution. But for a substantial increase, a much larger DNP is required [18, 19, 42]. Yet, the DNP found in our simulations is significantly larger than the magnitude of the Overhauser field fluctuations. We point out that hints for DNP are also visible in Fig. 5.19 of Sec. 5.4, where the NESS emerging from the application of pulse model II combined with the nuclear Zeeman effect is studied.

We stress that the nondeterministic pulse description is not responsible for DNP. It also appears when using the deterministic pulse (6.6) in combination with the inclusion of the trion pseudospin dynamics. For this combination, DNP as a function of the magnetic field shows a fairly similar behavior as depicted in Fig. 6.13. But at the same time, NIFF fulfilling the ERC with $S^{\perp}_{\mathrm{NESS}} \to 0.5$ occurs. Only for $B_{\mathrm{ext}} = 7.8\,\mathrm{T}$, the ORC with $S^{\perp}_{\mathrm{NESS}} \to -1/6$ appears instead of the ERC. But since the broad minimum around $B_{\mathrm{ext}} = 3.9\,\mathrm{T}$ is missing and NIFF is almost perfect (unlike in experiments [117, 122, 148]), we do not study the combination in more detail.

As argued above, the equations of motion studied by Glazov *et al.* [131] are similar to those of the EM II because the trion pseudospin effectively decouples from the ground state for large magnetic fields so that almost no spin polarization is transferred during the trion recombination. In their model, DNP is predicted analytically by studying the stability of fixed points given by the ERC (6.10a). Without any additional nuclear spin relaxation, the resonance condition turns out to describe an unstable fixed point so that DNP is possible. In agreement with Ref. [131], changing the helicity of the pulses does not change the direction of the DNP in our semiclassical simulations. In experiments, the buildup of DNP could be less efficient because of weak nuclear spin relaxation [131].

Experimental hints for DNP in the related experiments exist. In Ref. [122], the distribution of Larmor frequencies, extracted from the real-time evolution of the spin polarization measured via pump-probe spectroscopy, is shown. There, the mean value of the distribution is shifted from the bare Larmor frequency stemming only from the external magnetic field, possibly as a result of DNP.

Since about two orders of magnitude more pulses are required to reach the saturation of the DNP than for the revival amplitude caused by NIFF, it is well possible that the DNP steady state is not reached in the experiments under investigation.

Experimentally, it takes about a minute to reach an almost saturated revival amplitude for a magnetic field of 6 T [25]. By applying the suggested scaling with B_{ext}^{-2}, which has yet to be confirmed experimentally, we estimate that a sizable DNP should emerge within 5 minutes for a magnetic field of 1 T and within 3 hours for a magnetic field of 6 T.

6.4 Extended model III: Inhomogeneous ensemble of quantum dots

When using the EM II of the previous section, beats that decay during the trion lifetime $\tau_0 = 400\,\mathrm{ps}$ are visible in the initial dephasing of the signal $\overline{S^z(t)} - \overline{J^z(t)}$ shown in Fig. 6.10. However, the beats vanish noticeably faster in experiments [23, 117] as can be seen in Figs. 2.4(a) and 2.5(a). Moreover, the total dephasing time T_2^* shows a strong magnetic field dependence in experiments [23, 24, 123], see also Fig. 2.4(c), which cannot be explained by the random Overhauser field.

Until now, we have considered a homogeneous ensemble of QDs with dephasing time $T_{\mathrm{n}}^* = 1\,\mathrm{ns}$. This is, however, a simplification. In self-assembled QDs, the g factor of the localized electron spin varies slightly from QD to QD because they are not identical, leading to a faster dephasing for large magnetic fields as shown by the experimental results in Fig. 2.4(c) and as discussed at the end of Sec. 3.3.4. Here, we only consider resonant optical pumping, i.e., the g factor of the electron spin in each QD can be modeled by the normal distribution given in Eq. (3.51) with expectation value $\overline{g_{\mathrm{e}}} = 0.555$ [25] and standard deviation $\Delta g_{\mathrm{e}} = 0.005$ [24, 123]. The result is that the spin polarization now dephases within the total dephasing time T_2^* defined by

$$(T_2^*)^{-2} = (T_{\mathrm{n}}^*)^{-2} + (T_{\mathrm{inh}}^*)^{-2}\,, \tag{6.26}$$

where the dephasing time $(T_{\mathrm{inh}}^*)^{-1} = \Delta g_{\mathrm{e}} \mu_{\mathrm{B}} \hbar^{-1} B_{\mathrm{ext}}/\sqrt{2}$ results from the spread of g factors in the inhomogeneous ensemble of QDs. The total dephasing time decreases for large magnetic fields, while its upper bound is given by T_{n}^* for $B_{\mathrm{ext}} \to 0$ (see Fig. 3.4). Because of the computational reasons mentioned before and for a better comparability with the previous results, we still use $T_{\mathrm{n}}^* = 1\,\mathrm{ns}$.

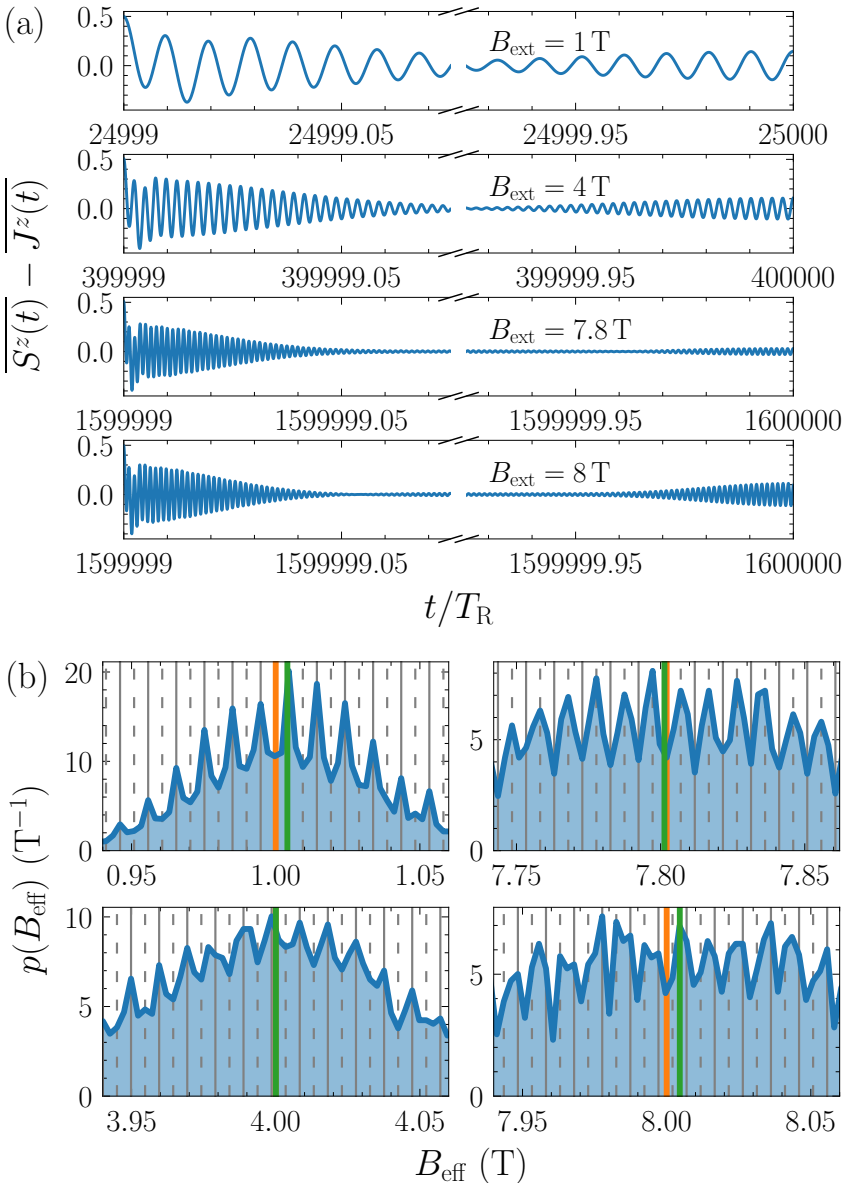

Figure 6.16: Extended model III: **(a)** Spin dynamics for an inhomogeneous ensemble of QDs in the NESS regime for various magnetic fields B_{ext}. **(b)** Probability distribution $p(B_{\mathrm{eff}})$ of the effective magnetic field in the NESS regime for various magnetic fields B_{ext} (orange vertical lines). The gray solid and dashed vertical lines represent the values of B_{eff} fulfilling the ERC (6.10a) and (6.10b), respectively. The green vertical lines represents the expectation value of the distributions. Parameters: $\gamma = 0.004$, $T_{\mathrm{n}}^{*} = 1\,\mathrm{ns}$, $\overline{g_{\mathrm{e}}} = 0.555$, $\Delta g_{\mathrm{e}} = 0.005$, $\overline{g_{\mathrm{h}}} = 0.15$, $\Delta g_{\mathrm{h}} = 0.05$, $T_{\mathrm{R}} = 13.2\,\mathrm{ns}$.

We apply the same modeling to the g factor of the heavy hole in the trion with standard deviation $\Delta g_\mathrm{h} = 0.05$ [132] to account for the fast vanishing of the beats in the time evolution of the spin polarization as observed in experiments. When including the spread Δg_h, the spin polarization stemming from the ensemble of photoexcited trions can dephase on a timescale shorter than the radiative trion lifetime τ_0. The average gyromagnetic ratio of the nuclei is not altered, i.e., it is still chosen to be $\gamma_\mathrm{n} = \gamma_\mathrm{e}/800$.

The implementation of the spread of the g factors is straightforward in the simulations. It is realized by sampling the g factors from the aforementioned normal distributions around their expectation values given by $\overline{g_\mathrm{e}} = 0.555$ and $\overline{g_\mathrm{h}} = 0.15$. Results for a different in-plane orientation of the QD sample with $\overline{g_\mathrm{h}} = 0.05$ are presented in Appendix D, but they reveal only slight quantitative differences.

Let us discuss the differences to the results of the previous section (EM II) when accounting for an inhomogeneous ensemble of QDs (EM III). Figure 6.16(a) shows the overall faster dephasing for larger magnetic fields B_ext, as expected from Eq. (6.26). The beats also vanish much quicker, which is in better agreement with the experimental observations [23, 117]. An even better agreement could be achieved by explicitly fitting the system parameters to experimental results, e.g., the g factor of the heavy hole in the trion, but this is not our goal here.

Instead, we are interested if and how an inhomogeneous ensemble of QDs influences the interplay of SML and NIFF. Obviously, modeling the g factor of the electron spin by a normal distribution leads to a broadening of the distribution of the effective magnetic field $p(B_\mathrm{eff})$ for large magnetic fields as demonstrated in Fig. 6.16(b), but the width of each individual peak caused by nuclear focusing does not change noticeably.

Without the spread of the electronic g factor, the nuclear focusing peaks are also visible in the probability distribution of the mere Overhauser field $p(B_\mathrm{ov}^x)$ as demonstrated in Chap. 5 (see, e.g., Fig. 5.15). The peaks are slightly shifted from the expected resonance and they are also a bit broader compared to peaks in the probability distribution $p(B_\mathrm{eff})$ of the effective magnetic field. In contrast, for the inhomogeneous ensemble of QDs under study even a rather small magnetic field of 0.5 T is enough to smear out the resonances such that no peaks are discernible in the distribution $p(B_\mathrm{ov}^x)$, i.e., it keeps its initial Gaussian shape (not shown). The minimal peak width is determined by the spread of the g factor Δg_e of the electron

spin. Once the minimal width is larger than the distance $2\pi/T_{\mathrm{R}}$ between adjacent resonances, i.e., for $T_{\mathrm{R}}^{-1} \lesssim \Delta g_{\mathrm{e}} \mu_{\mathrm{B}} \hbar^{-1} B_{\mathrm{ext}}$, no peaks can be discerned. Hence, we find no peaks in the Overhauser field distribution $p(B_{\mathrm{ov}}^{x})$ here, only the distribution of the effective magnetic field $p(B_{\mathrm{eff}})$ reveals a comblike structure.

In Fig. 6.17, the magnetic field dependence of the revival amplitude is shown for the EMs I, II, and III in the limit of an infinite bath size ($\gamma \to 0$). It turns out that no significant difference can be found between the EM II (homogeneous) and the EM III (inhomogeneous), i.e., the qualitative interplay of SML and NIFF does not change when a finite spread for the g factors is included. From the comparison we conclude that the minimum at $B_{\mathrm{ext}} = 7.8\,\mathrm{T}$ is even narrower for the EMs II and III in comparison to the EM I. Possibly, this narrow feature remains undiscovered in experiments if the discretization of the magnetic field is chosen too coarse; we find it only when simulating closely around $B_{\mathrm{ext}} = 7.8\,\mathrm{T}$. Hence, a systematic experimental search for such narrow features in the vicinity of the magnetic fields fulfilling the NRC (6.13) is called for.

We point out that DNP also occurs even when studying an inhomogeneous ensemble of QDs (see Appendix D), with an almost identical DNP behavior as in Fig. 6.13. The strong similarity was expected because the additional small variances of the

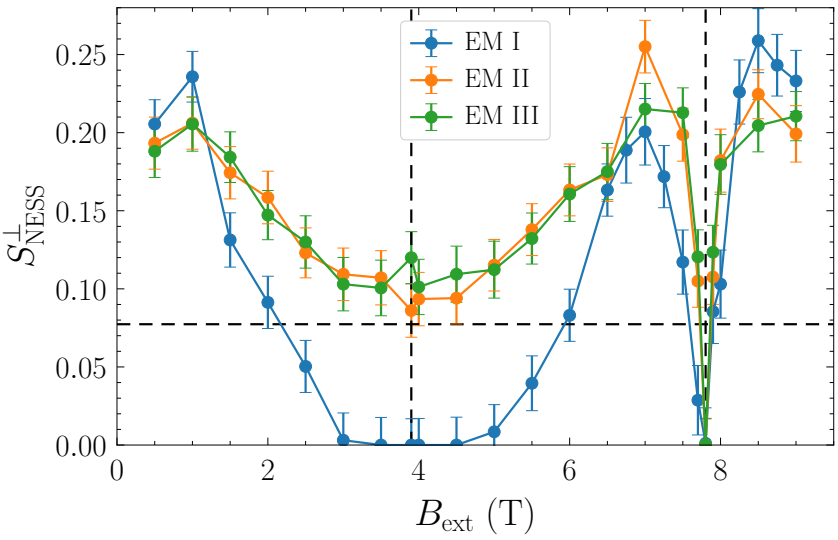

Figure 6.17: Limiting values $S_{\mathrm{NESS}}^{\perp}$ of the revival amplitude as a function of the magnetic field B_{ext} in the infinite bath limit ($\gamma \to 0$) for the three extended models (EMs) I, II, and III. The vertical dashed lines represent the NRC (6.13) for $k = 1$ and 2, the horizontal dashed line indicates the SML steady-state value S_{SML}.

g factors barely change the dynamics from QD to QD, i.e., the qualitative physics remains the same as in the EM II. The same argument holds for the strong similarity of the magnetic field dependence of the revival amplitude in Fig. 6.17 for the EMs II and III.

For an inhomogeneous ensemble of QDs, the influence of DNP on the total dephasing time T_2^* is smaller than for the homogeneous case. DNP only implies a decrease of the dephasing time T_n^*, which is determined by the variance of the random Overhauser field, and this variance reduces as a consequence of DNP. The inhomogeneous dephasing time T_inh^*, however, does not change. For this reason, the relative influence of the narrowed Overhauser field distribution on the total dephasing time T_2^* defined in Eq. (6.26) is diminished, especially for large magnetic fields where the influence of T_n^* on T_2^* is minimal (see Fig. 3.4).

6.5 Minimal model

The qualitative interplay of SML and NIFF described by the EM II can be captured by a simpler, minimal model. For simplicity, we neglect the spread of the g factors introduced for the EM III because it barely influence the NESS for the revival amplitude. Note that it needs to be included to describe the spin dynamics between consecutive pulses and of course, also the broadening of the probability distribution of the effective magnetic field is missing. Furthermore, we set $\chi = 0$ in the equations of motion (6.19) and (6.20), i.e., the interaction between the trion pseudospin and the nuclear spins is neglected. This approximation is justified because the hyperfine interaction between the unpaired heavy hole in the trion and the nuclei is much weaker than for the electron and only present on the short timescale of $\tau_0 = 400\,\mathrm{ps}$. As demonstrated in Fig. 6.18(a), only small differences between the results for $\chi = 0$ and $\chi = 0.2$ are found when studying magnetic field dependence of the revival amplitude in the NESS. The qualitative behavior is the same.

The next simplification has a bigger impact, but only on a quantitative level. We consider all hyperfine couplings A_k in the equation of motion (6.2c) to be equal, i.e., we set them to

$$A_k = \frac{1}{\sqrt{N}} A_\mathrm{Q}\,, \tag{6.27}$$

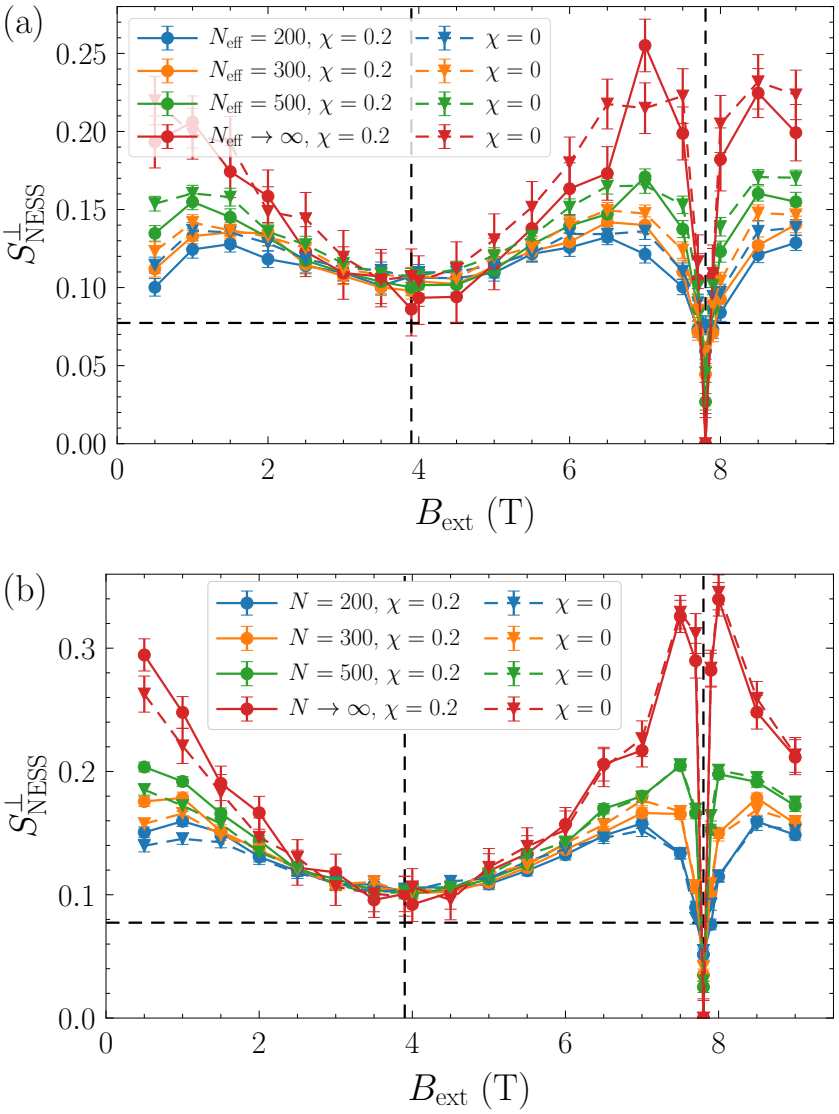

Figure 6.18: Limiting values $S^{\perp}_{\text{NESS}}$ of the revival amplitude as a function of the magnetic field B_{ext}: **(a)** Comparison using the EM II for $\chi = 0$ and $\chi = 0.2$ in Eqs. (6.19) and (6.20) for various effective bath sizes $N_{\text{eff}} = 2/\gamma$ and extrapolated to the infinite bath limit corresponding to $\gamma \to 0$. **(b)** Combination of the EM II with the box model for the hyperfine couplings (see main text) for various bath sizes N using $\chi = 0.2$ or $\chi = 0$. The vertical dashed lines represent the NRC (6.13) for $k = 1$ and 2, the horizontal dashed line indicates the SML steady-state value S_{SML}.

with A_{Q}^2 being the square root of the square sum of all couplings. Equation (3.50) describes its relation with the dephasing time T_{n}^*,

$$A_{\mathrm{Q}} = \sqrt{\sum_{k=1}^{N} A_k^2} = \sqrt{\frac{6}{I(I+1)}} \frac{1}{T_{\mathrm{n}}^*} = \sqrt{\frac{8}{5}} \frac{1}{T_{\mathrm{n}}^*} \,. \tag{6.28}$$

The approximation that all couplings A_k are assumed to be equal is referred to as the box model [115, 191]. It assumes that the electronic wave function in Eq. (3.9) is a constant with a certain spatial cutoff that determines the number of nuclear spins N coupled to the electron spin. The advantage is that we do not have to resort to the spectral density approach to describe the Overhauser field dynamics. Instead, since all nuclear spins precess with the same frequency, the dynamics of the Overhauser field is described by the single equation of motion

$$\frac{\mathrm{d}}{\mathrm{d}t} \boldsymbol{B}_{\mathrm{ov}} = \left[A_k \boldsymbol{S} + \chi A_k \left(J^z \boldsymbol{e}_z + \frac{1}{\lambda} \boldsymbol{J}^{\perp} \right) + h_{\mathrm{n}} \boldsymbol{e}_x \right] \times \boldsymbol{B}_{\mathrm{ov}} \,. \tag{6.29}$$

The results for the box model combined with the choices $\chi = 0.2$ and $\chi = 0$ are compiled in Fig. 6.18(b). Clearly, the qualitative behavior is very similar in comparison to the results for the EM II: The revival amplitude is overall larger when comparing the results for a given N to the same value of $N_{\mathrm{eff}} = 2/\gamma$, but the qualitative behavior is the same. The influence of χ is again small, noticeable differences are only present for small values of B_{ext}. The physical reason is that for finite χ, the extra terms in the equations of motion (6.19) and (6.20) become less important for larger magnetic fields.

The minimal model, which consists of using the box model and setting $\chi = 0$, is much easier to deal with numerically. First, only the z projection of the trion pseudospin $\boldsymbol{J}$ enters in the model. If a pulse creates an initial polarization $J^z(0)$, the pseudospin dynamics for $\chi = 0$ is fully described by

$$J^z(t) = J^z(0)\, \mathrm{e}^{-t/\tau_0} \cos(h_{\mathrm{h}} t) \,. \tag{6.30}$$

Thanks to the box model, the dimension of the remaining ODE system is reduced from $3(N_{\mathrm{tr}} + 1)$ to 6, rendering the numerical treatment much easier. Thus, larger and more accurate simulations are possible, or the model can be extended in another direction. In Chap 7, it constitutes the starting point to investigate the influence of the isotope composition of InGaAs QDs on the nonequilibrium spin physics.

6.6 Chapter conclusion

We developed an improved semiclassical model for the spin mode locking effect in combination with nuclei-induced frequency focusing in QDs, which yields an improved numerical description of various experimental results. The final model is the result of a combination of several key points while exploiting various scaling arguments.

First, we combined an established semiclassical pulse model [113, 122] often used to describe the excitation of a trion with an efficient approach to the spin dynamics of the Overhauser field presented in Sec. 4.2.3. But the results do not match our expectations stemming from a quantum mechanical description of the problem [117], and they also disagree with the experimental results presented in Refs. [117, 122].

Consequently, we improved the pulse model by introducing a nondeterministic description (EM I) in which we interpret the pulse as a quantum mechanical measurement. This reduces the discrepancy to a quantum mechanical approach while being able to cope with large nuclear spin baths. This step led to considerably improved results, which are in qualitative agreement with what is found in Ref. [117] using a fully quantum mechanical approach. But there, only a small bath consisting of $N = 6$ nuclear spins is studied, which is a disadvantage compared to our semiclassical approach. In this improved model and in agreement with Ref. [117], both even and odd resonances caused by nuclear focusing are found in the probability distribution of the effective magnetic field, but they appear for different strengths of the external magnetic field, not simultaneously. The corresponding nuclear focusing peaks turn out to be rather broad. For a broad range of magnetic fields, the resulting NIFF leads to a reduction of the revival amplitude because of the emergence of odd resonances in the distribution of the effective magnetic field, i.e., the interplay of SML and NIFF can be destructive.

We improved our model further by including the dynamics of the trion pseudospin, resulting in the EM II. It turns out that the Larmor precession of the trion pseudospin acts as a perturbation that suppresses the appearance of the odd resonances. As a consequence, the behavior of NIFF studied as a function of the magnetic field is qualitatively different than that of the previous model. In the EM II, NIFF acts constructively towards SML, except for a very narrow regime around a resonance condition for the nuclear spins where their Larmor period between consecutive

pulses matches the pulse repetition time. Even though the g factor of the unpaired heavy-hole spin of the negatively-charged trion depends strongly on the in-plane orientation of the QD sample [96, 132], the differences between the results are minor.

Furthermore, we observed the emergence of DNP of the order of 100 mT, i.e., the formation of a nonzero average polarization of the nuclear spin ensemble, which can be significantly larger than the typical fluctuations of the Overhauser field. It is caused by an alignment of the nuclear spins along the external magnetic field. A similar behavior can be inferred from the experimental results presented in Ref. [122], where the spectrum of Larmor frequencies of the localized electron spins is studied. Importantly, the saturation of the DNP takes about two orders of magnitude longer than the saturation of the revival amplitude stemming from NIFF. Its emergence leads to a slight narrowing of the Overhauser field distribution by about one third and thus, also to a slight increase of the dephasing time. Moreover, the dependence of the DNP on external magnetic field is very similar to that found for NIFF. The absolute value of the DNP is minimal (almost zero) whenever the pulse repetition time is a multiple of half the nuclear Larmor period, i.e., whenever the nuclear spins perform a multiple of half-turn revolutions about the external field between consecutive pulses. For a typical experiment, we estimate the maximum DNP to be 30 mT for a magnetic field of 1 T, which can be reached by applying pulses for about 5 minutes. This DNP is noticeably larger than the assumed magnitude of the Overhauser field fluctuations of about 7 mT per component ($T_\mathrm{n}^* \approx 4$ ns).

Accounting for an inhomogeneous ensemble of QDs led to the EM III. This extension in combination with the trion pseudospin dynamics (introduced in the EM II) is crucial for a correct description of the measured spin dynamics between two consecutive pulses. But it does neither lead to a qualitatively different DNP behavior nor to a different interplay of SML and NIFF.

In all three extended models, the peaks in the Overhauser field distribution are fairly broad compared to, e.g., the initial model studied in Sec. 6.1. This is similar to what is found for the quantum mechanical model studied in Ref. [117]. Thus, we attribute this behavior to quantum fluctuations captured by the randomness of the nondeterministic pulse description introduced for the EM I. Note that the peak widths are not determined by some additional relaxation time induced by further interactions such as the quadrupolar or dipole-dipole interaction. Their finite width

is intrinsic to the studied model at hand. But such further interactions are another possible mechanism that could hinder the efficiency of NIFF. For instance, it is found in Ref. [143] that the quadrupolar interaction acts against nuclear focusing. Moreover, weak nuclear spin relaxation resulting from such interactions could lead to a reduced DNP efficiency.

The qualitative behavior of the system can be reproduced by a rather simple, minimal model. The essential ingredients are the hyperfine interaction of the electron spin with the nuclear spin bath (for which a simple box model is sufficient to achieve a good description), the coupling of *all* spins to the external magnetic field, the nondeterministic pulse description to account for the uncertainty principle in the semiclassical approach. This model should be realizable on a fully quantum mechanical level, and the simplification of using the box model might help to overcome the issue of being limited to a small bath size.

Further extensions of the model are conceivable. First, the model should be extended to account for the various isotopes in InGaAs QDs so that several NRCs for the different isotopes act in a combined way. Indeed, we will see in Chap. 7 that this extension leads to a more complex structure in the magnetic field dependence of the revival amplitude.

In the present chapter, only the resonant trion excitation is considered. However, the applied pulse model can be easily generalized to detuned pulses (Sec. 2.2.2) [113]. Thereby, one can account for the influence of the inhomogeneous broadening of the trion transition energies present in a real QD ensemble [95, 120, 146] and explicitly calculate the Faraday rotation and ellipticity [113], which show different dependencies on certain parameters [95, 113]. Moreover, this step would enable us to simulate two-color pump-probe experiments [95, 113, 146]. Detuned pulses can also lead to the emergence of different resonances as demonstrated in Refs. [145, 148]. There, the influence of a positive and negative detuning on NIFF is discussed, but a different model is used to describe for the spin dynamics. Furthermore, the optical Stark effect induced by detuned pulses appears to be important to accurately describe the phenomenon of DNP [98, 149].

A third relevant aspect is the inclusion of a finite pulse duration. It leads to a reduced efficiency of the pulse for very large magnetic fields and can also induce phase shifts for the emerging resonances [117, 147].

From the experimental side, several clarifications could stimulate progress in understanding the relevant physics. First, the dependence of the rate with which NIFF emerges has not been analyzed in experiments yet. Our model suggests that the rate is proportional to B_{ext}^{-2}. Second, a systematic comparison of the revival amplitude as a function of the magnetic field for the cases *with* and *without* NIFF would be helpful, accompanied by an analysis of the Larmor frequency spectrum with respect to the kind of resonance. Such an experimental study could also reveal the influence of the pulse duration on spin mode locking *without* NIFF by comparing the measured revival amplitude with the analytically obtained steady-state value S_{SML}. In our model, this value does not depend on external magnetic field, but a reduced pulse efficiency for large fields caused by a finite pulse duration could be revealed by the suggested experimental analysis. Evers *et al.* [148] demonstrated that such experiments are realizable by applying an appropriate radiofrequency field that hinders nuclear focusing to the QDs. But so far, measurements at various strengths of the magnetic field have not been carried out. Finally, the emergence of DNP in the system, for which some evidence exists in the experimental data of Ref. [122], is another subject calling for further investigation.

Chapter 7

Nuclear magnetic resonance spectroscopy of nonequilibrium steady states

In the previous chapter, we have established a model that captures various effects in the context of SML and NIFF observable in experiments. We have also found that the qualitative nonequilibrium spin physics can be described by the minimal model described in Sec. 6.5. Notably, a resonance condition for the nuclear spins determines the magnetic field dependence of the revival amplitude, which has minima at the magnetic fields fulfilling the NRC (6.13). When considering $In_xGa_{1-x}As$ QDs, there are various NRCs (6.13) arising from the different isotopes present in the QDs and hence, we expect that the QD composition influences the nonequilibrium physics. Up to now, the role of the QD composition was only investigated by a perturbative quantum mechanical approach comprising a rather small number of nuclear spins ($N = 17$) [142], but this approach cannot reach the NESS present in experiments and it also neglects the dynamics of the unpaired heavy-hole spin in the excited T^- trions.

The main goal of this chapter[1] is to establish a model accounting for the various isotopes in an $In_xGa_{1-x}As$ QD and analyze its influence on the nonequilibrium spin physics with a particular focus on the various nuclear magnetic resonances. Since we are facing computational constraints in the exact numerics, a powerful framework is developed in which the equations of motion governing the spin dynamics are expanded in the inverse of the magnetic field, speeding up the calculations by two orders of magnitude.

[1]This chapter is based on the author's publication [258], ©2021 Europhysics Letters Association (EPLA). Preliminary calculations were performed by P. W. Scherer in the context of his master's thesis [259], supervised by G. S. Uhrig and by the author.

7.1 Accounting for the quantum dot composition

We start from the minimal semiclassical model established in Sec. 6.5, which we extend to account for the various nuclei in $In_xGa_{1-x}As$ QDs. The optical spin orientation is still described by the nondeterministic pulse (6.14) introduced in Sec. 6.2, i.e., we consider the periodic application (repetition time $T_R = 13.2\,s$) of resonant π pulses with helicity σ^- and a pulse duration of the order of picoseconds, which is much shorter than all other timescales of the system. The nondeterministic pulse description is required in the semiclassical approach to account for the uncertainty principle, i.e., each application of a pulse is considered as a quantum mechanical measurement.

Let us turn to the spin dynamics, which we describe by the classical precession equations

$$\frac{\mathrm{d}}{\mathrm{d}t}\boldsymbol{S} = (\boldsymbol{B}_{\mathrm{ov}} + h\boldsymbol{e}_x) \times \boldsymbol{S} + \frac{1}{\tau_0} J^z \boldsymbol{e}_z \,, \tag{7.1a}$$

$$\frac{\mathrm{d}}{\mathrm{d}t}\boldsymbol{B}_{\mathrm{ov},j} = (A_j \boldsymbol{S} + h_{\mathrm{n},j}\boldsymbol{e}_x) \times \boldsymbol{B}_{\mathrm{ov},j} \,. \tag{7.1b}$$

The electron spin $\boldsymbol{S}$ precesses in the superposition of the time-dependent Overhauser field $\boldsymbol{B}_{\mathrm{ov}} = \sum_{k=1}^{N} A_k \boldsymbol{I}_k$, which is the sum over all N nuclear spins $\boldsymbol{I}_k$ weighted by their individual hyperfine coupling A_k, and the transverse external magnetic field $h\boldsymbol{e}_x = \gamma_e B_{\mathrm{ext}} \boldsymbol{e}_x$. Here, B_{ext} denotes the magnetic field, $\gamma_e = g_e \mu_B \hbar^{-1}$ the gyromagnetic ratio, $g_e = 0.555$ [25] the electronic g factor, and μ_B the Bohr magneton. The total Overhauser field is the sum of the subfields of each nuclear species numbered by the index j, i.e., $\boldsymbol{B}_{\mathrm{ov}} = \sum_j \boldsymbol{B}_{\mathrm{ov},j}$. Each subfield precesses in the Knight field $A_j \boldsymbol{S}$ caused by hyperfine interaction with the electron spin and also in the external magnetic field with Larmor frequency $h_{\mathrm{n},j} = \gamma_{\mathrm{n},j} B_{\mathrm{ext}}$. The gyromagnetic ratios relevant for the influence of the external field are very small, $\gamma_{\mathrm{n},j}/\gamma_e = \mathcal{O}(10^{-3})$ [167]. Yet, since $h_{\mathrm{n},j}$ can be of similar order of magnitude as A_j, the nuclear Zeeman effect determines the nonequilibrium spin physics decisively. The strength of the hyperfine interaction is proportional to the probability density of the electron at the position of the nuclei. For simplicity, we approximate this density as a box with a certain spatial cutoff, i.e., we use the box model [115, 191] as in Sec. 6.5. In this approximation, all nuclear spins of species j have the same coupling constant A_j.

The optically excited singlet trion T^- consists of two electrons in a spin singlet

and a heavy hole with unpaired spin, which can be described by the pseudospin $\boldsymbol{J}$ defined in Eq. (2.8) [114, 115]. The dynamics of its z projection is given by

$$J^z(t) = J^z(0)\,\mathrm{e}^{-t/\tau_0}\cos(h_\mathrm{h} t)\,, \tag{7.2}$$

where $h_\mathrm{h} = \gamma_\mathrm{h} B_\mathrm{ext}$ and $g_\mathrm{h} = \gamma_\mathrm{h}\hbar/\mu_\mathrm{B} = 0.15$ [132] is the g factor of the heavy hole in the trion. The pseudospin precesses about the transverse magnetic field while the trion decays radiatively into the ground state, characterized by the electron spin $\boldsymbol{S}$. The radiative trion lifetime is $\tau_0 = 400\,\mathrm{ps}$ [23, 111]. The hyperfine interaction is a magnitude smaller for heavy holes than for electrons and also strongly anisotropic [93, 156, 157]. As shown in Sec. 6.5, this interaction barely affects the nonequilibrium physics and hence, we neglect it here for simplicity.

Applying the same semiclassical approach based on the TWA (see Sec. 3.3) as in the previous chapters, the classical equations of motion (7.1) are solved for M random configurations of the initial conditions. Averages over the resulting M independent classical trajectories approximate the quantum mechanical expectation values of the spin operators. The initial conditions for the electron spin are determined by the nondeterministic pulse (6.14). The Overhauser field comprising $10^4 - 10^6$ effectively coupled nuclear spins [19, 103–107] is treated as a classical field based on the central limit theorem [104, 200]. For temperatures of $\sim 4 - 6\,\mathrm{K}$ as in the experiments [23, 25, 117], the nuclear spin bath is completely disordered and its fluctuations follow a normal distribution with mean value zero. To capture its variance, we define the dephasing time

$$T_\mathrm{n}^* \coloneqq \sqrt{2}\left(\sum_{k=1}^{N} \frac{I_k(I_k+1)}{3} A_k^2\right)^{-1/2} \tag{7.3}$$

based on the hyperfine interaction of the electron with N nuclei with spin I_k. This definition is an extension of Eq. (3.50) to account for the different nuclear species. Next, we define the ratios of couplings α_j between the different species according to $A_j = \alpha_j A$ with $A \coloneqq A_1$. Moreover, $N_j = n_j N$ is the number of nuclei of species j so that n_j describes its relative abundance in an $\mathrm{In}_x\mathrm{Ga}_{1-x}\mathrm{As}$ QD. Then, we have

$$A = \frac{\sqrt{2}}{T_\mathrm{n}^*\sqrt{N}}\left(\sum_j n_j \alpha_j^2 \frac{I_j(I_j+1)}{3}\right)^{-1/2}, \tag{7.4}$$

which sets the low-energy scale $\propto 1/(T_\mathrm{n}^*\sqrt{N})$ here. It depends on T_n^*, N, sample specific parameters, and known properties of the various nuclear species. Using the quantum mechanical second moment of a nuclear spin given by Eq. (3.34b), the variances for the components of the nuclear subfields result to

$$\mathrm{Var}\left[B_{\mathrm{ov},j}^{\alpha}\right] = \sum_{j=1}^{N_j} \frac{I_j(I_j+1)}{3} A_j^2 = n_j N \alpha_j^2 A^2 \frac{I_j(I_j+1)}{3}\,, \tag{7.5}$$

$\alpha \in \{x, y, z\}$. Since variances are additive, the fluctuations of the Overhauser field can be characterized by the dephasing time T_n^*

$$\mathrm{Var}\left[B_{\mathrm{ov}}^{\alpha}\right] = \sum_{k=1}^{N} \frac{I_k(I_k+1)}{3} A_k^2 = \frac{2}{(T_\mathrm{n}^*)^2}\,. \tag{7.6}$$

Thus, T_n^* serves as an input parameter taken from experiments. In contrast to the previous chapters, we focus on a particular QD sample with approximately $T_\mathrm{n}^* = 4\,\mathrm{ns}$ [23, 123]. This dephasing time captures only the dephasing caused the random Overhauser field. In an inhomogeneous ensemble of QDs, the actually observed dephasing time T_2^* shows a strong magnetic field dependence, which is caused by a spread of the electronic g factors [23, 123] as discussed at the end of Sec. 3.3.4. In Sec. 6.4, it turned out that this inhomogeneity barely affects the revival amplitude in the NESS and hence, we do not account for it here for simplicity. In the simulations, we use $N = 60$ nuclear spins because the number of pulses and therefore also the run time required to reach the NESS scales linearly with N. Note that the number of equations does not depend on N because all nuclear spins of the same species have the same coupling constant in the box model, which is the important feature of this approximation. We will see, however, that a larger number of nuclei N has only a small influence on the results.

The relevant parameters for the nuclei in $\mathrm{In}_x\mathrm{Ga}_{1-x}\mathrm{As}$ QDs are listed in Table 3.1. We consider an average isotope for ^{113}In and ^{115}In weighted by their natural abundances and denoted by $\overline{\mathrm{In}}$ because their parameters are almost identical. Eventually, we consider four different nuclear species: ^{69}Ga, ^{71}Ga, ^{75}As, and $\overline{\mathrm{In}}$. Note that only the ratios of the hyperfine interaction strength for the various nuclear species enter in our model. The low-energy scale set by Eq. (7.4) determines the magnitude of the different coupling constants and is proportional to $1/(T_\mathrm{n}^*\sqrt{N})$, similar to the models studied in the previous chapters.

7.2 Fast and slow degrees of freedom

The numerical integration of the equations of motion (7.1) seems to be straightforward, but it requires massive parallelization to solve them $M = \mathcal{O}(10^4)$ times. We use $M = 32512$ if not stated otherwise. Moreover, reaching the NESS for realistic parameters requires hundred millions of pulses, rendering a direct simulation elusive. On the one hand, the fast Larmor frequency of the electron spin needs to be resolved numerically, so only small time steps proportional to the Larmor period $2\pi h^{-1} \propto B_{\mathrm{ext}}^{-1}$ are possible.[2] On the other hand, the time to reach the NESS scales like B_{ext}^2. Eventually, the computational effort scales worse than B_{ext}^3. For this reason, we split the fast and the slow spin dynamics in the equations of motion (7.1), solve the fast part analytically and expand the slow dynamics in the first order of h^{-1}. This expansion turns out to be remarkably accurate for magnetic fields $B_{\mathrm{ext}} \gtrsim 1\,\mathrm{T}$ and the simulation runs two orders of magnitude faster than the brute force approach. This methodical achievement is the key element that enables us to study the influence of several nuclear species on the nonequilibrium spin physics under realistic conditions.

We split the equations of motion (7.1) into a part describing the fast Larmor precession and a part for the slow dynamics by applying a suitable ansatz. Corrections of the order $\mathcal{O}(h^{-2})$ are neglected because they are strongly suppressed for large magnetic fields B_{ext}. To this end, we introduce the composite variables

$$z \coloneqq S^y + \mathrm{i}S^z\,, \tag{7.7a}$$

$$b_j \coloneqq B_{\mathrm{ov},j}^y + \mathrm{i}B_{\mathrm{ov},j}^z\,, \tag{7.7b}$$

$$B_j^x \coloneqq B_{\mathrm{ov},j}^x\,. \tag{7.7c}$$

[2] This is also the case when using the rotating frame approach described in Sec. 3.3.3. The reason is that the fast electronic Larmor precession is transferred to the nuclear spin dynamics via the interaction with the electron spin.

In this notation, the classical equations of motion (7.1) have the form

$$\frac{\mathrm{d}}{\mathrm{d}t}z = \mathrm{i}(B^x + h)z - \mathrm{i}bS^x + \mathrm{i}\frac{1}{\tau_0}J^z\,, \tag{7.8a}$$

$$\frac{\mathrm{d}}{\mathrm{d}t}b_j = \mathrm{i}(A_jS^x + h_{\mathrm{n},j})b_j - \mathrm{i}A_jzB_j^x\,, \tag{7.8b}$$

$$\frac{\mathrm{d}}{\mathrm{d}t}S^x = \mathrm{Im}(zb^*)\,, \tag{7.8c}$$

$$\frac{\mathrm{d}}{\mathrm{d}t}B_j^x = -A_j\,\mathrm{Im}(zb_j^*)\,, \tag{7.8d}$$

with $b = \sum_j b_j$, $B^x = \sum_j B_j^x$, and

$$J^z(t) = J^z(0)\,\mathrm{e}^{-t/\tau_0}\cos(h_{\mathrm{h}}t)\,. \tag{7.9}$$

7.2.1 Expansion of the equations of motion in the magnetic field

A suitable ansatz to split the fast and slow degrees has the form

$$z(t) = z_0(t) + z_1(t)\,\mathrm{e}^{\mathrm{i}ht} + z_2(t)\,\mathrm{e}^{\mathrm{i}h_{\mathrm{h}}t} + z_3(t)\,\mathrm{e}^{-\mathrm{i}h_{\mathrm{h}}t}\,, \tag{7.10a}$$

$$b_j(t) = b_{0,j}(t) + b_{1,j}(t)\,\mathrm{e}^{\mathrm{i}ht}\,, \tag{7.10b}$$

$$\begin{aligned} S^x(t) &= S_0^x(t) + \mathrm{Re}\left[S_1^x(t)\,\mathrm{e}^{\mathrm{i}ht}\right] \\ &= S_0^x(t) + \frac{1}{2}\left(S_1^x\,\mathrm{e}^{\mathrm{i}ht} + S_1^{x*}\,\mathrm{e}^{-\mathrm{i}ht}\right), \end{aligned} \tag{7.10c}$$

$$\begin{aligned} B_j^x(t) &= B_{0,j}^x(t) + \mathrm{Re}\left[B_{1,j}^x(t)\,\mathrm{e}^{\mathrm{i}ht}\right] \\ &= B_{0,j}^x(t) + \frac{1}{2}\left(B_{1,j}^x\,\mathrm{e}^{\mathrm{i}ht} + B_{1,j}^{x*}\,\mathrm{e}^{-\mathrm{i}ht}\right). \end{aligned} \tag{7.10d}$$

It already includes all relevant terms stemming from the fast Larmor precession with frequencies h and h_{h}. This ansatz is inserted into Eq. (7.8). We identify and keep all terms that are $\mathcal{O}(1)$ or $\mathcal{O}(h^{-1})$ and impose $\mathcal{O}(h_{\mathrm{h}}) = \mathcal{O}(h)$ and $\mathcal{O}(h_{\mathrm{n},j}) = \mathcal{O}(1)$. The first relation is justified because the g factors of electrons and holes are of similar magnitude ($g_{\mathrm{e}} = 0.555$ [25], $g_{\mathrm{h}} = 0.15$ [132]). The second relation is justified because the gyromagnetic ratios of the nuclei in $\mathrm{In}_x\mathrm{Ga}_{1-x}\mathrm{As}$ QDs are smaller by three orders of magnitude than the electronic one [19, 167]. In $\mathcal{O}(h^{-1})$ the resulting

relations are algebraic,

$$z_0(t) = \frac{1}{h} b_0 S_0^x \,, \tag{7.11a}$$

$$z_2(t) = -\frac{J^z(0)}{2\tau_0(h - h_\mathrm{h})} \, \mathrm{e}^{-t/\tau_0} \,, \tag{7.11b}$$

$$z_3(t) = -\frac{J^z(0)}{2\tau_0(h + h_\mathrm{h})} \, \mathrm{e}^{-t/\tau_0} \,, \tag{7.11c}$$

$$b_{1,j}(t) = -\frac{A_j}{h} z_1 B_{0,j}^x \,, \tag{7.11d}$$

$$S_1^x(t) = -\frac{1}{h} z_1 b_0^* \,, \tag{7.11e}$$

$$B_{1,j}^x(t) = \frac{A_j}{h} z_1 b_{0,j}^* \,, \tag{7.11f}$$

$$S_0^x(t) = S_0^x(0) \,, \tag{7.11g}$$

while in $\mathcal{O}(1)$ we obtain the ordinary differential equations

$$\frac{\mathrm{d}}{\mathrm{d}t} z_1 = \mathrm{i} \left(B_0^x z_1 - b_1 S_0^x + \frac{1}{2} b_0 S_1^x \right) , \tag{7.12a}$$

$$\frac{\mathrm{d}}{\mathrm{d}t} b_{0,j} = \mathrm{i} \left[(A_j S_0^x + h_{\mathrm{n},j}) b_{0,j} - A_j z_0 B_{0,j}^x - \frac{A_j}{2} z_1 B_{1,j}^{x*} \right] , \tag{7.12b}$$

$$\frac{\mathrm{d}}{\mathrm{d}t} B_{0,j}^x = -A_j \, \mathrm{Im}(z_0 b_{0,j}^*) \,. \tag{7.12c}$$

It turns out that z_1, $b_{0,j}$, S_0^x, and $B_{0,j}^x$ are of the order $\mathcal{O}(1)$, whereas the remaining variables z_0, z_2, z_3, $b_{1,j}$, S_1^x, and $B_{1,j}^x$ are of the order $\mathcal{O}(h^{-1})$. All other conceivable corrections are of the order $\mathcal{O}(h^{-2})$. They can be omitted because they are strongly suppressed for the large magnetic fields to be considered here.

Next, we insert the algebraic relations (7.11) into Eq. (7.12) and obtain

$$\frac{\mathrm{d}}{\mathrm{d}t} z_1 = \mathrm{i} \left(B_0^x + \sum_j \frac{A_j}{h} B_{0,j}^x S_0^x + \frac{|b_0|^2}{2h} \right) z_1 \,, \tag{7.13a}$$

$$\frac{\mathrm{d}}{\mathrm{d}t} b_{0,j} = \mathrm{i} \left[\left(A_j S_0^x + h_{\mathrm{n},j} - \frac{A_j^2}{2h} |z_1|^2 \right) b_{0,j} - \frac{A_j}{h} S_0^x B_{0,j}^x b_0 \right] , \tag{7.13b}$$

$$\frac{\mathrm{d}}{\mathrm{d}t} B_{0,j}^x = -\frac{A_j}{h} S_0^x \, \mathrm{Im} \left(\sum_{j \neq l} b_{0,j} b_{0,l}^* \right) . \tag{7.13c}$$

Equation (7.13a) can be simplified by applying the complex exponential ansatz

$$z_1(t) = z_1(0)\,\mathrm{e}^{\mathrm{i}\varphi_{z_1}(t)}\,. \tag{7.14}$$

The result is the new differential equation

$$\frac{\mathrm{d}}{\mathrm{d}t}\varphi_{z_1} = B_0^x + \sum_j \frac{A_j}{h} B_{0,j}^x S_0^x + \frac{|b_0|^2}{2h}\,. \tag{7.15}$$

The set of differential equations (7.13b), (7.13c), and (7.15) needs to be solved numerically starting from appropriate initial conditions. Note that the correct initial conditions (see below) must be calculated after *each* pulse application.

If the case is considered where only a single nuclear species is present, there are no sums in the equations so that the differential equations can be solved analytically. In this simpler case, the dynamics in order $\mathcal{O}(h^{-1})$ is fully determined by a set of algebraic relations, i.e., no numerical integration is required. Details on the analytical treatment are given in Appendix E.

7.2.2 Initial conditions of the expansion variables

To determine the initial conditions of all time-dependent variables, we insert $t = 0$ into the algebraic relations (7.11). For brevity, the time argument $t = 0$ is omitted in the following. The initial conditions for the variables z, b_j, S^x, B_j^x, and J^z are known: z, S^x, and J^z are determined by the nondeterministic pulse (6.14), while b_j and B_j^x representing the Overhauser subfields are determined by the Gaussian initial conditions (7.5). The task is to deduce from them the initial conditions of the expansion variables z_0, z_1, $b_{0,j}$, $b_{1,j}$, S_0^x, S_1^x, $B_{0,j}^x$, and $B_{1,j}^x$. To this end, we define the auxiliary quantities

$$P_j \coloneqq \mathrm{Re}(z_1 b_{0,j}^*) \tag{7.16}$$

and insert the relation

$$b_{0,j} = b_j - b_{1,j} = b_j + \frac{A_j}{h} z_1 B_{0,j}^x\,. \tag{7.17}$$

After a few algebraic transformations, we obtain

$$P_j = \frac{\mathrm{Re}(z_1 b_j^*) + \frac{A_j}{h} B_j^x |z_1|^2}{1 + \frac{A_j^2}{h^2}|z_1|^2}\,, \tag{7.18}$$

which depends only on known initial conditions except z_1. In addition, we have

$$B_{0,j}^x = B_j^x - \frac{A_j}{h} P_j\,, \tag{7.19a}$$

$$S_0^x = S^x + \frac{1}{h}\sum_j P_j\,, \tag{7.19b}$$

which we insert into $z_1 = z - z_0 - z_2 - z_3$ and find

$$z_1 = z - \frac{1}{h}\sum_j \left[b^k - \frac{A_j}{h} z_1 \left(B_j^x - \frac{A_j}{h} P_j\right)\right] \left(S^x + \frac{1}{h}\sum_j P_j\right) + \frac{J^z}{2\tau_0}\left(\frac{1}{h + h_\mathrm{h}} + \frac{1}{h - h_\mathrm{h}}\right). \tag{7.20}$$

Since the P_j depend only on z_1, the nonlinear and nonpolynomial relation (7.20) determines z_1. All terms on the right-hand side except z are suppressed by at least a factor of h^{-1}. Hence, the relevant zero for z_1 is quickly found by iteration starting from $z_1 = z$. Fast convergence is reached within approximately five iteration steps. Afterwards, the quantities P_j can be calculated from z_1. Thus, all initial conditions are now fully determined. The missing ones are given by

$$z_0 = z - z_1 + \frac{J^z}{2\tau_0}\left(\frac{1}{h + h_\mathrm{h}} + \frac{1}{h - h_\mathrm{h}}\right), \tag{7.21a}$$

$$z_2 = -\frac{J^z}{2\tau_0(h - h_\mathrm{h})}\,, \tag{7.21b}$$

$$z_3 = -\frac{J^z}{2\tau_0(h + h_\mathrm{h})}\,, \tag{7.21c}$$

$$b_{1,j} = -\frac{A_j}{h} z_1 B_{0,j}^x\,, \tag{7.21d}$$

$$S_1^x = -\frac{1}{h} z_1 \sum_j b_{0,j}^*\,, \tag{7.21e}$$

$$B_{1,j}^x = \frac{A_j}{h} z_1 b_{0,j}^*\,. \tag{7.21f}$$

Notably, the trion pseudospin component J^z does not appear in any of the equations governing the time evolution the other quantities; it only has an influence on their initial values. The reason is that any contribution from the trion pseudospin to the dynamics is of the order $\mathcal{O}(h^{-2})$ thanks to its precession about the external magnetic field. In contrast, for $h_\mathrm{h} = 0$, i.e., neglecting its Larmor precession, the contribution from J^z to the dynamics of z_0 is of the order $\mathcal{O}(h^{-1})$. Physically, this implies that the trion pseudospin decouples from the remaining dynamics if it precesses about the external magnetic field fast enough.

7.2.3 Validity of the expansion

In the following, we establish the validity of the expansion derived above. To this end, the time evolution of the electron spin $\boldsymbol{S}$ and of the Overhauser field $\boldsymbol{B}_\mathrm{ov}$ is calculated for $M = 256$ random initial conditions by solving the original equations of motion (7.1) numerically and also applying the expansion in $\mathcal{O}(h^{-1})$. The mean absolute error calculated for each component at $t = T_\mathrm{R}^- = 13.2\,\mathrm{ns}$, i.e., at the end of the first pulse period and before the application of the second pulse, is plotted in Fig. 7.1 in a double logarithmic manner. Linear fits reveal a clear B_ext^{-2} dependence for all errors. This confirms that the accuracy of the derived equations is of the order $\mathcal{O}(h^{-1})$ as intended.

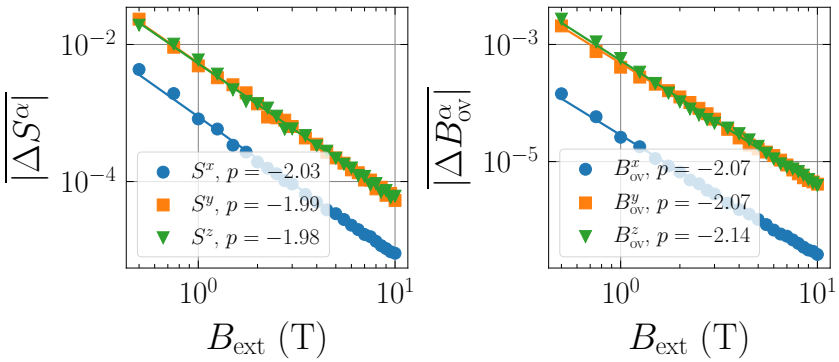

Figure 7.1: Error analysis of the $\mathcal{O}(h^{-1})$ expansion of the equations of motion for the electron spin $\boldsymbol{S}$ and the Overhauser field $\boldsymbol{B}_\mathrm{ov}$. The mean absolute errors calculated for the $M = 256$ random configurations at $t = T_\mathrm{R}^-$, i.e., at the end of the first pulse period and before the arrival of the second pulse, are shown in a double logarithmic plot. The slopes p of the applied linear fits (solid lines) are given in the legends; they all have a fit error of ± 0.02. Clearly, the error scales like $B_\mathrm{ext}^{-2} \propto h^{-2}$ for all components. Parameters: $N = 200$, $T_\mathrm{n}^* = 1\,\mathrm{ns}$, $x = 0.3$.

Figure 7.2 demonstrates the remarkable accuracy of the expansion in $\mathcal{O}(h^{-1})$ for the magnetic field dependence of the revival amplitude in the NESS for the case where only an average isotope ($\gamma_e/\gamma_n = 800$) is considered. For magnetic fields $B_{ext} \gtrsim 1\,T$, the deviations of the results obtained using the $\mathcal{O}(h^{-1})$ approach from the numerically exact results are within the statistical accuracy displayed by the error bars. The revival amplitude in the NESS is calculated as the arithmetic mean over the last 10% data points, the error bar represents the corresponding root-mean-square deviation.

We also compare the numerically exact results to the approximate results in $\mathcal{O}(h^{-1})$ for the revival amplitude as a function of the number of nuclei N for various dephasing times T_n^* in Fig. 7.3 for an $In_{0.3}Ga_{0.7}As$ QD sample. The comparison is only carried out for $B_{ext} = 1\,T$ because the computational demand for the exact numerics is too large for larger magnetic fields. The agreement between the numerically exact and approximate results is within the statistical accuracy for all combinations of N and T_n^*, but the approximate solution slightly overestimates the real revival amplitude for this rather small magnetic field. For larger fields, the agreement is expected to be better because the approximation is based on a sys-

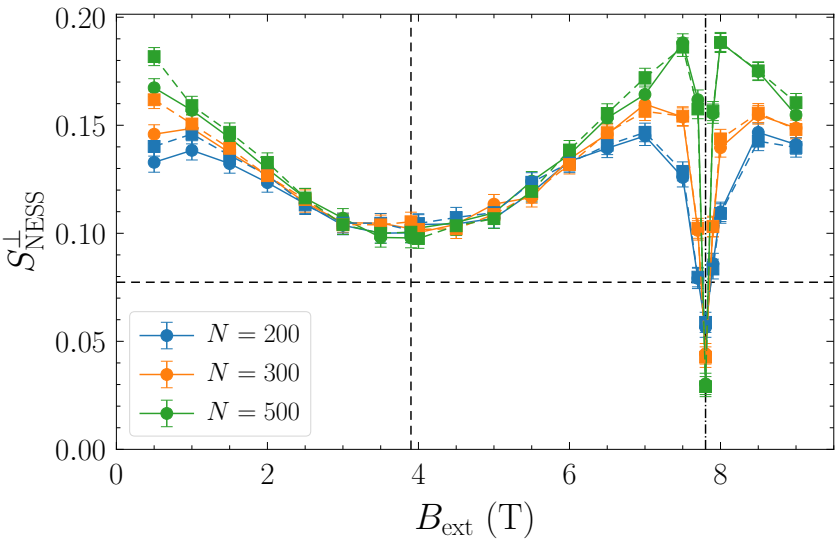

Figure 7.2: Revival amplitude $S^{\perp}_{NESS}$ in the NESS as a function of the magnetic field B_{ext} for the model where only an average isotope is considered. The numerically exact (spheres, solid lines) and the approximate $\mathcal{O}(h^{-1})$ (squares, dashed lines) results are shown for various bath sizes N. The agreement is within the statistical accuracy for magnetic fields $B_{ext} \gtrsim 1\,T$. Parameters: $T_n^* = 1\,ns$, $\gamma_e/\gamma_n = 800$, $I = 3/2$, $M = 10240$.

tematic expansion in $h^{-1} \propto B_{\mathrm{ext}}^{-1}$; see also Fig. 7.2 where the accuracy improves for larger magnetic fields.

Physically, the results shown in Fig. 7.3 demonstrate the influence of the dephasing time T_{n}^{*} on the revival amplitude. For $T_{\mathrm{n}}^{*} = 1\,\mathrm{ns}$, the revival amplitude is only slightly larger than the SML steady-state value $S_{\mathrm{SML}} \approx 0.077$ given by Eq. (6.9), i.e., the degree of NIFF is small. For the value $T_{\mathrm{n}}^{*} = 4\,\mathrm{ns}$, there is a noticeable dependence on the number of nuclei. But for our choice $N = 60$, the revival amplitude is already close to the maximum value that is in the limit $1/\sqrt{N} \to 0$, i.e., it does not change significantly for larger bath sizes. For the case of a single nuclear species studied in Chap. 6, the choice of T_{n}^{*} in the limit of an infinite bath size has no significant influence on the revival amplitude (Fig. 6.8). This limit is the experimentally relevant case with $10^4 - 10^6$ effectively coupled nuclear spins in a QD [19, 103–107]. But for the case of several nuclear species as considered here, there is a significant influence of T_{n}^{*} on the revival amplitude, even in the limit of an infinite bath size. For this reason, we use the value $T_{\mathrm{n}}^{*} = 4\,\mathrm{ns}$ chosen in accordance with previous analyses [23, 123].

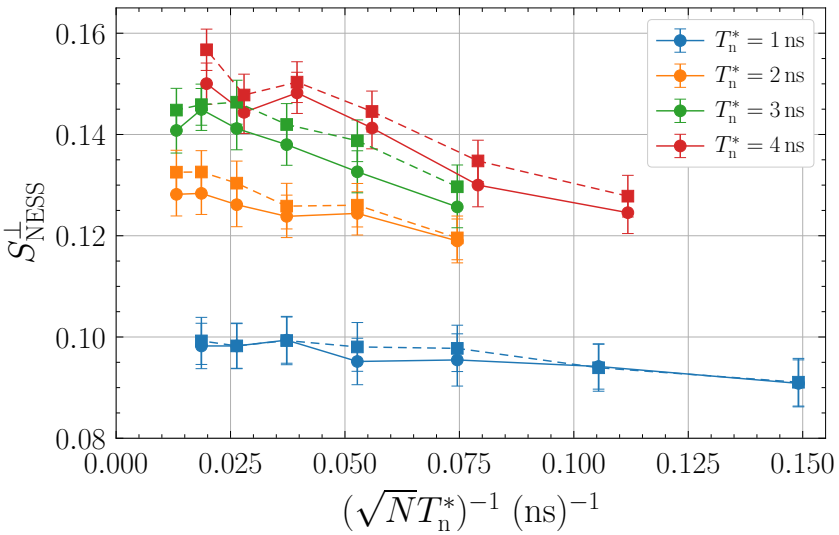

Figure 7.3: Revival amplitude $S_{\mathrm{NESS}}^{\perp}$ in the NESS as a function of the typical hyperfine coupling $(\sqrt{N}T_{\mathrm{n}}^{*})^{-1}$ at a magnetic field of $B_{\mathrm{ext}} = 1\,\mathrm{T}$. The numerically exact results (spheres, solid lines) and approximate results in $\mathcal{O}(h^{-1})$ (squares, dashed lines) are shown for various dephasing times T_{n}^{*}. The agreement is within the statistical accuracy, but the approximate solution slightly overestimates the numerically exact result. Parameters: $x = 0.3$, $M = 11520$.

7.3 Nonequilibrium spin physics

The general nonequilibrium spin physics is very similar to the behavior studied in detail in Chap. 6. As a brief recapitulation, the electron spin dynamics in the NESS for various external magnetic fields B_{ext} is shown in Fig. 7.4(a). The optically induced spin polarization precesses about the external field and dephases within $T_{\text{n}}^{*} = 4\,\text{ns}$. As discussed in Sec. 6.1, already $\mathcal{O}(10)$ pulses induce a revival of the spin polarization with amplitude $S^{\perp} = 1/\sqrt{3} - 1/2 = S_{\text{SML}}$ [117, 122, 141] before the next pulse as a consequence of SML in the random Overhauser field, i.e., without any nuclear focusing. The figure shows that applying many more pulses (for up to minutes in experiments) changes the amplitude $S^{\perp}$ of the revival as a consequence of NIFF [25], eventually approaching a NESS. In most cases, the revival amplitude is enhanced as a consequence of NIFF, but under certain conditions a destructive effect occurs as analyzed in Chap. 6. For instance, there is barely any revival at $B_{\text{ext}} = 8.072\,\text{T}$, but for the slightly larger field $B_{\text{ext}} = 8.5\,\text{T}$ the revival has a substantial amplitude even though $\mathcal{O}(10^{8})$ pulses are applied in both cases.

The origin of NIFF, which is partially responsible for the revival signal if very long pulse trains are applied, is visualized in Fig. 7.4(b) by showing the probability distribution $p(B_{\text{eff}})$ of the effective magnetic field

$$B_{\text{eff}} := \frac{|\boldsymbol{B}_{\text{ov}} + \gamma_{\text{e}} B_{\text{ext}} \boldsymbol{e}_x|}{\gamma_{\text{e}}} \tag{7.22}$$

for three different external magnetic fields B_{ext}. Initially, it follows a normal distribution with mean value B_{ext} and a variance resulting from the random Overhauser field described by Eq. (7.6) But the long sequences of pulses train the system to favor commensurable precession modes so that the distribution evolves towards a comblike structure until reaching a NESS. Hence, certain polarizations resulting in commensurable dynamics are selected. The positions of the nuclear focusing peaks match either the even [Eq. (6.10a)] or the odd [Eq. (6.10b)] resonance condition for the Larmor precession of the electron spin. The precise behavior of NIFF and its impact on the revival amplitude strongly depends on the strength of the applied magnetic field. In most cases, the ERC (6.10a) is fulfilled. But as analyzed in Sec. 6.3, the system tends towards the ORC (6.10b) if the nuclear resonance

condition

$$\gamma_{\mathrm{n},j} B_{\mathrm{ext}} T_{\mathrm{R}} = 2\pi |k| \,, \qquad k \in \mathbb{Z} \,, \tag{7.23}$$

is met. We refer to this resonance condition, which describes nuclear magnetic resonances (NMRs) of the species j, as the even NRC because $2|k|$ is an even integer.

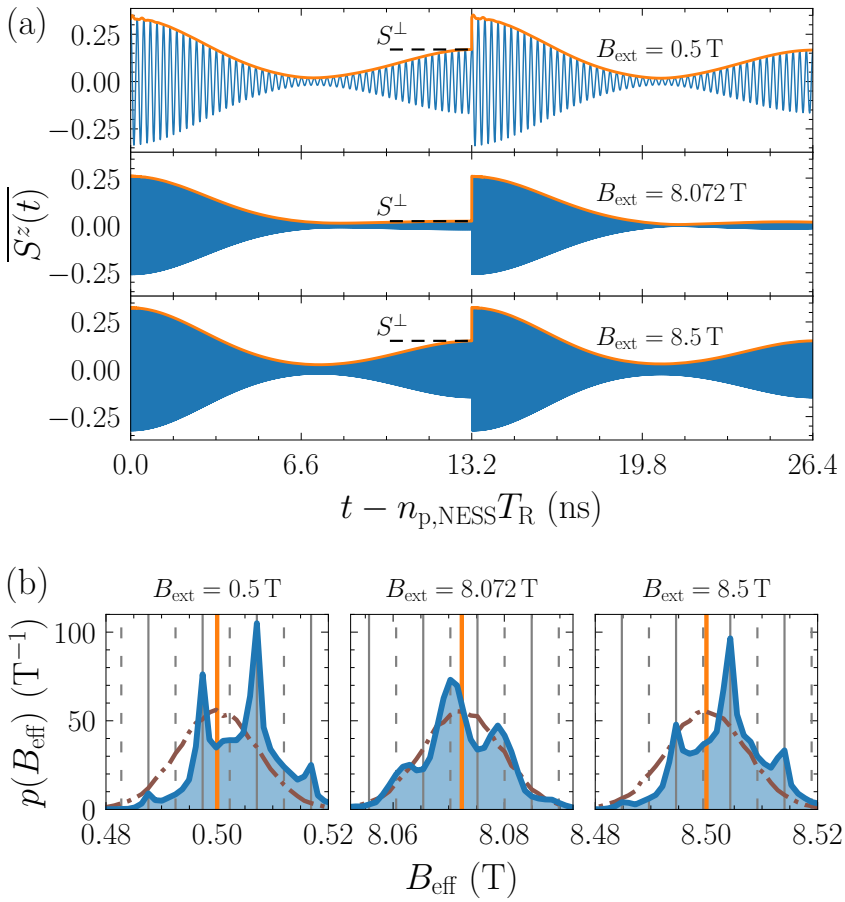

Figure 7.4: (a) Electron spin dynamics $\overline{S^z(t)}$ showing spin mode locking in the NESS after $n_{\mathrm{p,NESS}} = 4.5 \times 10^5$ ($B_{\mathrm{ext}} = 0.5\,\mathrm{T}$), 1.174×10^8 ($B_{\mathrm{ext}} = 8.072\,\mathrm{T}$), and 1.301×10^8 ($B_{\mathrm{ext}} = 8.5\,\mathrm{T}$) pulses. The envelope is highlighted in orange, the fast Larmor precession (blue) is not discernible for large fields. A pump pulse arrives at 0 and 13.2 ns, respectively. The In concentration is $x = 0.3$. **(b)** Corresponding nonequilibrium probability distribution $p(B_{\mathrm{eff}})$ of the effective magnetic field (external plus Overhauser field) revealing the selection of special polarizations in the nuclear spin bath. The solid and dashed gray lines represent the even and odd resonance conditions (6.10a) and (6.10b) for the electron spin, respectively. The orange vertical lines highlight the applied magnetic fields B_{ext}. The initial normal distributions are depicted in brown for comparison.

In Fig. 7.4, it is fulfilled for $B_{\mathrm{ext}} = 8.072\,\mathrm{T}$, which is the NMR field of the nuclear spin of $\overline{\mathrm{In}}$ for the mode number $k = 1$. In this case, the Larmor period of the In nuclear spins is equal to the pulse repetition time $T_{\mathrm{R}} = 13.2\,\mathrm{ns}$ and the revival amplitude shows a sharp local minimum when studied as a function of the magnetic field B_{ext} as we will see below.

If a nuclear spin revolves an odd multiple of half Larmor precessions between two consecutive pulses, i.e., if

$$\gamma_{\mathrm{n},j} B_{\mathrm{ext}} T_{\mathrm{R}} = (2|k| + 1)\pi\,, \qquad k \in \mathbb{Z}\,, \tag{7.24}$$

is met, the revival amplitude studied as a function of the magnetic field shows a broad local minimum around the magnetic fields fulfilling this resonance condition. In the following, we refer to this condition as the odd NRC because $2|k| + 1$ is an odd integer. It describes an odd number of half-turn revolutions of the nuclear spins about the magnetic field within the pulse interval. But in this regime, the effective magnetic field still favors the even resonance (6.10a) for the electronic Larmor precession. So far, we have analyzed the magnetic field dependence of the revival amplitude only for an average isotope in Chap. 6. In the following, we analyze the role of simultaneously present different nuclear species j. This extension gives rise to several possible NRCs and thus, increases the complexity of the results by a substantial amount.

7.4 Nuclear magnetic resonance spectroscopy

The magnetic field dependence of the revival amplitude

$$S^{\perp}(n_{\mathrm{p}}) \coloneqq \sqrt{\left[\overline{S^{y}(n_{\mathrm{p}} T_{\mathrm{R}}^{-})}\right]^2 + \left[\overline{S^{z}(n_{\mathrm{p}} T_{\mathrm{R}}^{-})}\right]^2}\,, \tag{7.25}$$

as a function of the number of applied pulses n_{p} and of the magnetic field B_{ext} for the In concentration $x = 0.3$ is shown in Fig. 7.5(a) as a heatmap; the revival amplitude is encoded in the color. The notation T_{R}^{-} indicates that the spin polarization is probed immediately before the arrival of the pump pulse; the overline denotes the ensemble-averaged quantity in the semiclassical approach. The revival amplitude starts at $S^{\perp} = 0$ and rises quickly to the SML steady-state value $S_{\mathrm{SML}} \approx 0.077$ within $\mathcal{O}(10)$ pulses. At this stage, the Overhauser field still follows its initial

normal distribution. Subsequently, the revival amplitude changes as a consequence of the slowly emerging nuclear focusing over a timescale covered by millions of pulses, eventually approaching a NESS where the revival amplitude does not change anymore on average (it still fluctuates because of the nondeterministic pulses). The deviation of the amplitude from the SML steady state is representative for the degree of NIFF in most cases; exceptions are discussed below. The number of pulses $n_{\mathrm{p,NESS}}$ necessary to reach the NESS scales like B_{ext}^2 as before in Sec. 5.3.2 and Chap. 6. For instance, at $B_{\mathrm{ext}} = 10\,\mathrm{T}$ one must apply $n_{\mathrm{p,NESS}} = 1.8 \times 10^8$ pulses to approximately reach the NESS. As discussed before, the dependence of the revival amplitude on the magnetic field is strongly nonmonotonic. The amplitude is large at small magnetic fields, then decreases with a broad minimum in the vicinity of $B_{\mathrm{ext}} = 4.5\,\mathrm{T}$, and increases thereafter. For fields $B_{\mathrm{ext}} \gtrsim 8.1\,\mathrm{T}$, the amplitude decreases again. Importantly, several sharp minima are discernible at larger magnetic fields.

The nonmonotonic behavior is easier to analyze when focusing solely on the NESS regime, which is shown in Fig. 7.5(b) for various In concentrations x. The sharp minima are located exactly at the positions determined by the NMRs (7.23) for $k = 1$ (vertical dash-dotted lines), i.e., whenever the Larmor period of a nuclear spin is equal to the pulse repetition time T_{R}. The broad minimum appears in the range of magnetic fields in which the fields fulfilling the odd NRC (7.24) with $k = 1$ are located (vertical dashed lines). This minimum appears to be a robust feature: it also appears in our previous investigations using an average isotope, in the quantum mechanical model of Ref. [117], and a similar feature is found experimentally for various QD samples [117, 122]; see also Fig. 2.5(b) taken from Ref. [117]. The key difference to the previous theoretical studies is the larger number of sharp minima and the much more complex behavior of the revival amplitude at large magnetic fields. The depths of these minima strongly depend on the In concentration x. Only the minimum at the NMR field of about 10.4 T, corresponding to the nuclear spin of As, is almost independent of x. This was to be expected because varying x does not change the number of As isotopes in the QDs (its relative abundance in $\mathrm{In}_x\mathrm{Ga}_{1-x}\mathrm{As}$ QDs is always 0.5). The more In is present (larger x), the deeper and sharper is the minimum related to the nuclear spin of In at its NMR field $B_{\mathrm{ext}} = 8.072\,\mathrm{T}$. In return, the two minima related to the NMR fields of ^{69}Ga and ^{71}Ga become deeper when the concentration of In is decreased. Even for the small concentration $x = 0.0\overline{3}$, In prevails over the other isotopes because of its larger

spin and larger hyperfine coupling strength (see Table 3.1). Obviously, the sharp minimum at $B_{\text{ext}} = 8.072\,\text{T}$ vanishes completely without any In ($x = 0$). Likewise, the sharp minima related to the two Ga isotopes at the corresponding NMR fields $B_{\text{ext}} = 5.819\,\text{T}$ and $7.403\,\text{T}$ vanish without any Ga in the QDs ($x = 1$). In this case, the maximum of the revival amplitude at around $8\,\text{T}$ increases because the

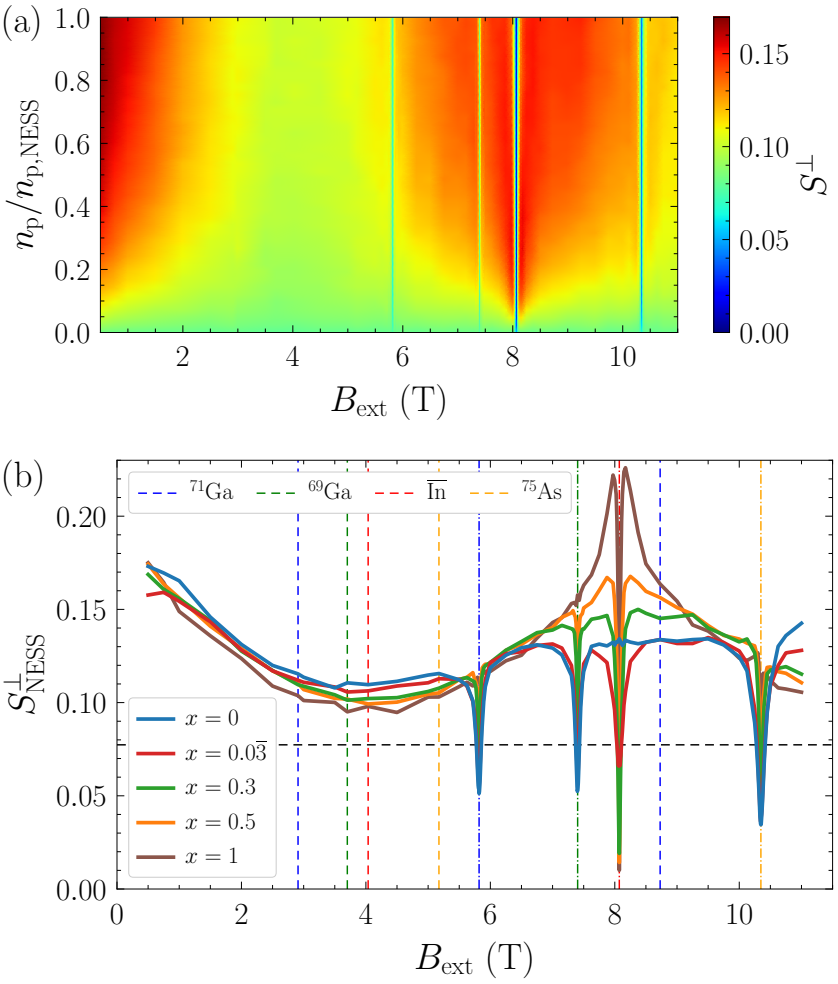

Figure 7.5: (a) Revival amplitude $S^{\perp}$ as function of the magnetic field B_{ext} and of the normalized number of pulses $n_{\text{p}}/n_{\text{p,NESS}}$, where $n_{\text{p,NESS}} \propto B_{\text{ext}}^2$ denotes the number of pulses necessary to reach the NESS. The In concentration is $x = 0.3$. The positions of the sharp minima coincide with the NMR fields resulting from the even NRC (7.23). **(b)** Revival amplitude $S^{\perp}_{\text{NESS}}$ in the NESS regime (averaged over the last 10% data points) as a function of the magnetic field B_{ext} for various In concentrations x. The fields fulfilling the NRCs (7.23) (even, dash-dotted) and (7.24) (odd, dashed) for the various nuclear species in $\text{In}_x\text{Ga}_{1-x}\text{As}$ QDs are highlighted by vertical lines. The horizontal dashed line marks the SML steady-state value S_{SML} as a reference to assess the degree of NIFF.

odd NRC (7.24) for $k = 2$ related to ^{71}Ga at around 8.7 T plays no role. But if Ga is present in the QDs ($x < 1$), this odd NRC limits the degree of NIFF in the regime around 8.7 T. The resulting magnetic field dependence of the revival amplitude for $x = 0.3$ has some similarities to the experimental observation [117] shown in Fig. 2.5(b), where the revival amplitude also has the trend to decrease for larger magnetic fields. Note that a similar trend could be induced by the reduced pulse efficiency appearing for large magnetic fields if the pulse duration is not much shorter than the electronic Larmor period [117]. In our case, they differ by an order of magnitude as discussed in Sec. 6.1, but still, there could be a small effect.

Overall, the magnetic field dependence of the revival amplitude appears to be fairly independent of the QD composition up to about 5 T. For larger fields, however, the behavior is complex and strongly depends on the In concentration. In this regime, various nuclear magnetic resonances influence the NESS and appear as sharp dips in the revival amplitude studied as a function of the magnetic field. These sharp resonance suggest themselves to be exploited for a so far not known kind of NMR spectroscopy.

Figure 7.6 shows the revival amplitude in the NESS around the fields meeting the even NRC (7.23). Obviously, the widths of the minima are related to the amount of In in the QD: a larger x corresponds to a narrower minimum. This is also the case for the dip related to As even though the number of As isotopes does not change with x.

The deviation of the revival amplitude from the SML steady-state value S_{SML} does not necessarily represent the degree of NIFF for fields close to the NMRs. In these cases, the probability distribution $p(B_{\mathrm{eff}})$ of the effective field does not always single out the ERC (6.10a) or the ORC (6.10b). Instead, the nuclear focusing peaks can appear at slightly irregular positions. This behavior can be seen in Fig. 7.7 where the probability distribution $p(B_{\mathrm{eff}})$ is shown for external magnetic fields approaching the NMRs for an In concentration of $x = 0.3$. Around the NMR fields for In and As, a change of resonance from the ERC to the ORC (or to a mixture) can be discerned. In contrast, the degree of NIFF for the two Ga isotopes decreases when approaching the respective NMR field, but the system sticks to the ERC. But the details depend on the In concentration, e.g., for smaller x there is also a change of resonance at the NMR fields for ^{69}Ga and ^{71}Ga (not shown).

Slight shifts of the expectation value of the probability distributions $p(B_{\mathrm{eff}})$ from its initial value B_{ext} are discernible in Figs. 7.4(b) and 7.7. They stem from dynamic

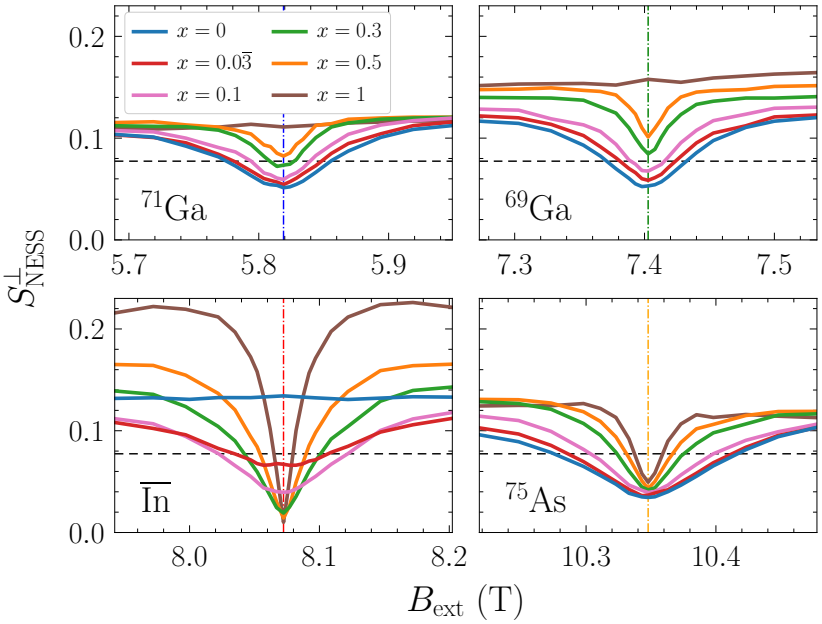

Figure 7.6: Revival amplitude $S^{\perp}_{\text{NESS}}$ in the NESS in close vicinity to the NMR fields fulfilling (7.23) for $k = 1$ for various In concentrations x. The panels show $S^{\perp}_{\text{NESS}}$ in the range $\pm 0.13\,\text{T}$ around the NMR fields (dash-dotted) for ^{71}Ga, ^{69}Ga, $\overline{\text{In}}$, and ^{75}As. The SML steady-state value S_{SML} is marked by the horizontal dashed line.

nuclear polarization, i.e., from the formation of a nonzero polarization of the nuclear spins parallel to the external magnetic field. This phenomenon is analyzed in detail in Sec. 6.3 for the case of an average isotope. Its analysis for the case of various nuclear species is beyond the scope of the present chapter, but it is an interesting subject for future research.

Finally, let us discuss if and how the predicted features are accessible in experiments. The two $\text{In}_x\text{Ga}_{1-x}\text{As}$ QD samples studied experimentally in Ref. [117] [see Fig. 2.5(b)] were thermally annealed at different temperatures, resulting in an estimated In concentration of $x \approx 0.3$ (Sample 1) and $x \approx 0.4$ (Sample 2).[3] Thus, all nuclear species are present. Most of the In isotopes should be located in the center of the QDs [88, 260]. But the applied magnetic field was varied in steps of 0.5 T, which is too coarse to reveal sharp features. In principle, however, the external field can be tuned with mT accuracy so that sharp features such as those promoted in Fig. 7.6 should be resolvable. We stress that the inhomogeneity of self-assembled QD ensembles is not detrimental to these features because the gy-

[3]The concentrations were estimated by A. Greilich.

romagnetic ratios $\gamma_{\mathrm{n},j}$ do not depend on details of the QDs, i.e., they are physical constants. Furthermore, the electronic g factor, which has a small spread in real QD ensembles, does not influence the NMRs.

Further experimental support could potentially be obtained by applying continuous radiation at the NMR frequency of a particular isotope for a fixed magnetic field. Such related experiments were performed recently by Evers *et al.* [148], demonstrating that this procedure also leads to a substantial reduction of the revival amplitude because of a reduced nuclear focusing efficiency.

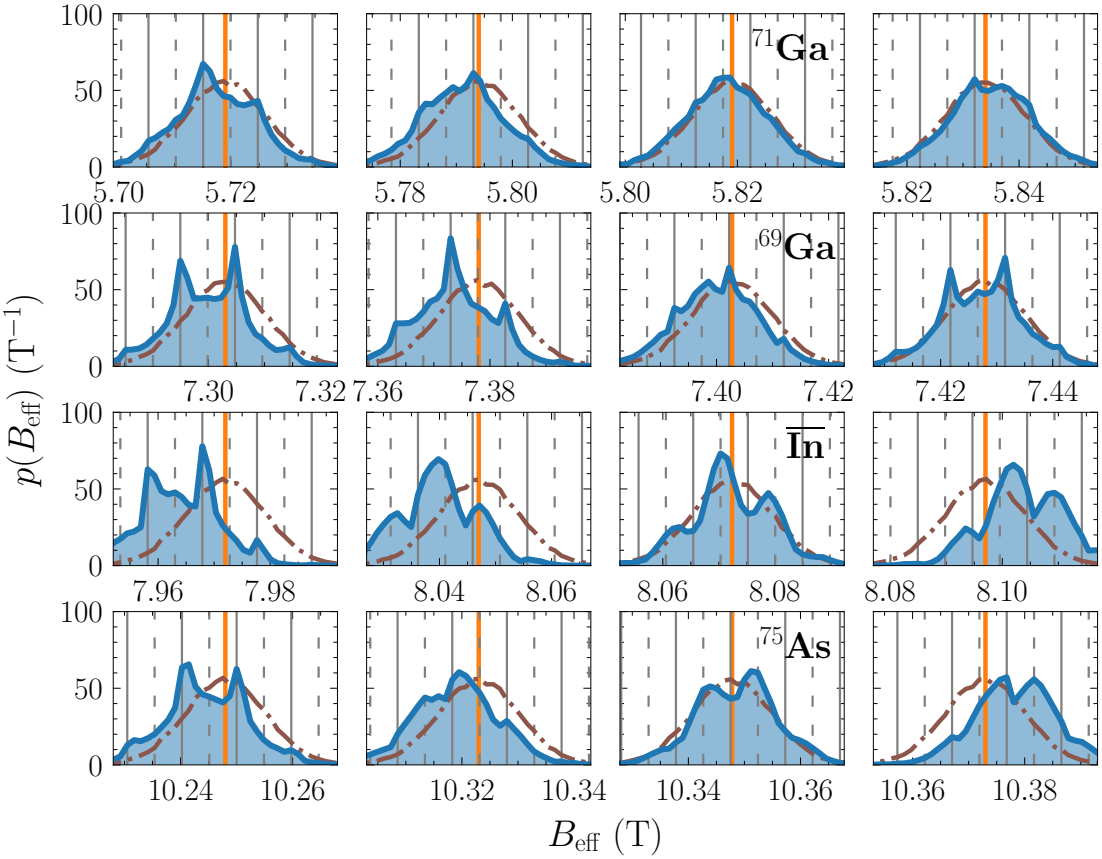

Figure 7.7: Probability distribution $p(B_{\mathrm{eff}})$ of the effective magnetic field in the NESS in the vicinity of the NMR fields fulfilling the even NRC (7.23) at $k = 1$ for an In concentration $x = 0.3$. Each row corresponds to the NMR for ^{71}Ga, ^{69}Ga, $\overline{\mathrm{In}}$, and ^{75}As, respectively. In the third column, $p(B_{\mathrm{eff}})$ is shown at the respective NMR field. In the other columns, this magnetic field is changed by $-0.1\,\mathrm{T}$ (first), $-0.025\,\mathrm{T}$ (second), and $+0.025\,\mathrm{T}$ (fourth). The applied magnetic field B_{ext} is always highlighted in orange. The solid and dashed gray lines represent the ERC (6.10a) and ORC (6.10b) for the electron spin. The initial normal distributions are depicted in brown for comparison.

7.5 Chapter conclusion

By methodical progress we are able to simulate the dynamics of the localized electron spin in a QD in presence of a nuclear spin bath comprising several nuclear species under nonequilibrium conditions where trains of up to $\mathcal{O}(10^8)$ pulses are applied to the system. Considering the pulse repetition time $T_\mathrm{R} = 13.2\,\mathrm{ns}$, the simulations cover a real-time scale of the order of seconds, i.e., very close to the duration of the pulse trains applied in experiments (up to minutes) [25]. The key step is to separate fast and slow spin dynamics, solve the fast part analytically, and expand the slow part in the inverse of the applied magnetic field. Numerically, only the slow dynamics needs to be integrated, which runs two orders of magnitude faster than the brute force approach. The approximation turns out to be remarkably accurate for magnetic fields $B_\mathrm{ext} \gtrsim 1\,\mathrm{T}$ and clearly, it can also be applied to many other related physical problems. For instance, if there is only a single nuclear species, the spin dynamics between two pulses can be obtained algebraically. This enables extremely efficient simulations and can be used to deal with other issues such as the inhomogeneous broadening of the trion transition energies appearing in real QD ensembles (adding another statistical component), or with two-color pump-probe experiments [95, 113, 146]. The technique should be also applicable to the Spectral Density approach (Sec. 4.2.3) for the Overhauser field dynamics.

The periodic application of the pulses for extremely long times drives the system to a nonequilibrium steady state. This state is imprinted in the nuclear spin bath and has a lifetime of the order of minutes in experiments [25]. As a consequence of the spin mode locking effect combined with nuclei-induced frequency focusing, a revival of the electron spin polarization created by a pulse, which dephases as a result of the interaction with the random nuclear spin bath, appears before the arrival of the next pulse. Several resonances related to the Larmor precession of the different nuclear spins in the QD determine the nonequilibrium behavior decisively. Whenever the Larmor period of a nuclear spin matches the pulse repetition time, the amplitude of the revival becomes minimal. This results in a number of very sharp minima when studying its magnetic field dependence. Similar nonequilibrium steady states have been proposed to allow for the distillation of quantum coherent states [253]. We suggest that these minima stemming from nuclear magnetic resonances are observable in tailored experiments. This would constitute a novel kind of NMR spectroscopy.

III

Nonequilibrium spin phenomena in a longitudinal magnetic field

Chapter 8

Spin inertia and polarization recovery: Influence of pumping strength

The progress in the field of spintronics [77, 78] over the past two decades lead to several experimental tools for the investigation and characterization of the spin dynamics in semiconductor nanostructures. One of the main characteristics is the spin lifetime. Most of the tools are based on the interrelation between the spin of a charge carrier and the polarization of a photon emitted or absorbed by the semiconductor structure [108]. The most popular ones are the Hanle effect [261] and the time-resolved pump-probe spectroscopy. The latter is based on the pulsed-laser excitation [127, 128] and can be extended to detect spin dynamics on arbitrary timescales with femtosecond resolution [129]. Other powerful tools are the resonant spin amplification [77, 133, 135–137], the spin-noise spectroscopy [262–264], the spin inertia technique [93, 125, 159], and measurements of the polarization recovery [93, 125, 126]. The latter two are the subject of this chapter; see Secs. 2.4.2 and 2.4.3 for an introduction to the corresponding effects. The spin inertia technique can be used to measure slow spin dynamics on the timescale of microseconds. Combined with measurements of polarization recovery curves, many parameters governing the spin dynamics can be determined [93, 125, 126].

The spin inertia technique is based on the pump-probe spectroscopy [159], in which the spin polarization induced by periodically applied circularly polarized laser pulses is measured. The spin inertia effect occurs when the helicity of the circularly polarized pump pulses is modulated with a finite frequency f_m. When this frequency increases and becomes larger than the inverse spin relaxation time, the spin polarization decreases and eventually vanishes for very large modulation frequencies. This led to calling the effect *spin inertia* because it can be understood as an inertia of the spin polarization that prevents it from following an external

switching of the pulse helicity arbitrarily quickly. The measurement of the dependence of the spin polarization on the modulation frequency allows one to determine the spin relaxation time of the resident charge carriers, e.g., the longitudinal spin relaxation time often denoted as T_1.

Generally, this method is useful to measure long spin relaxation times, e.g., of localized electrons and holes in a longitudinal magnetic field [93]. A natural physical system for this kind of study are localized charge carriers in ensembles of self-assembled QDs [19, 38] or localized charge carriers bound to impurities in bulk semiconductors [36]. The spin dynamics in such systems is mainly driven by the hyperfine interaction with the nuclear spins of the host lattice [19, 115]. The simple phenomenological model used for the description of the first experiments [159] was later extended to account for non-Markovian spin dynamics typical for localized electrons [125]. But up to now, the effects caused by saturation limit of the spin polarization, where all spins point in the same direction, was not analyzed in detail.

Motivated by the recent experiments presented in Ref. [93] (see also Secs. 2.4.2 and 2.4.3), we develop a theory of the spin inertia effect for electrons and holes localized in QDs and account for an arbitrarily strong pumping of the system. We take into account the interplay between the hyperfine interaction of the localized charge carrier with the nuclear spin bath and the external magnetic field for both the ground state and the excited trion state. The simulations and analytical calculations demonstrate a decrease of the effective spin relaxation time with an increase of the pump power, which is also found in pump-probe experiments [124, 265] and in measurements of the spin inertia [93, 159]. We also study the dependence of the spin polarization on the applied longitudinal magnetic field and discuss possible effects that could be induced by nonresonant pump pulses. Finally, a regime is predicted where resonant spin amplification occurs, i.e., the probed spin polarization resonantly depends on whether the Larmor period of the localized carrier spins is commensurable with the time between consecutive pump pulses [135]. Thanks to the contribution from the random Overhauser field, such a Larmor precession takes place in spite of the pulses orienting the localized carrier spin along the axis of the longitudinal magnetic field (Faraday geometry).

The chapter is set up as follows.[1] In the next section, we present the model that we consider for simulations of the spin inertia effect and its analytical description in limiting cases. Two different methods that we apply for this purpose are introduced in Sec. 8.2. In Sec. 8.3, we first consider the limit of a strong magnetic field in which the hyperfine interaction can be neglected. Afterwards, the dependence of the spin polarization on the magnetic field is studied and possible effects induced by nonresonant pump pulses are discussed. Finally, we predict and describe the emergence of resonant spin amplification in Faraday geometry. The results are summarized in Sec. 8.4.

8.1 Phenomenological model

We consider a homogeneous ensemble of singly-charged QDs subjected to a longitudinal magnetic field under the condition of a pump-probe experiment [93]. The QDs can be charged either by electrons (n doped) or by holes (p doped). We treat these two cases, for which the parameters governing the spin dynamics are drastically different [93], on equal footing. The pump pulses excite singlet trion states, leading to the spin orientation of the resident charge carriers as discussed in Sec. 2.2. The spin polarization can be probed by weak linearly polarized pulses measuring the Faraday rotation or ellipticity [113, 114].

In measurements of the spin inertia, the QDs are excited by a long train of $n_\mathrm{p} \gg 1$ pump pulses following one another with the repetition time $T_\mathrm{R} = 13.2\,\mathrm{ns}$ [93, 159]. Each pulse is circularly polarized and the helicity of the pulses is alternated with the frequency f_m. The spin inertia effect manifests itself in the dependence of the spin polarization on f_m. The spin polarization is probed by weak probe pulses with the same repetition time. Experimentally, they arrive shortly before the next pump pulse, e.g., with a delay of $\tau_\mathrm{d} = -50\,\mathrm{ps}$ [93]. In our model, we assume an infinitesimal negative delay $\tau_\mathrm{d} = -0$ for simplicity, but the influence of a small delay is minor [125]. The Faraday ellipticity or rotation measured for the probe pulses yields the projection of the spin polarization on the axis of light propagation, which is also the growth direction of the QDs. As in the previous chapters, we refer to it

[1] This chapter is based on the author's publication [255], published by the American Physical Society under the terms of the CC BY 4.0 license (https://creativecommons.org/licenses/by/4.0). All numerical calculations were conducted by the author. Analytical support based on the steady-state approach was provided by D. S. Smirnov.

as the z axis. The spin inertia signal as a function of the modulation frequency f_m as measured in experiments is defined as [125, 159]

$$L(f_\mathrm{m}) \coloneqq \frac{1}{n_\mathrm{p}} \left| \sum_{k=1}^{n_\mathrm{p}} \overline{S^z(kT_\mathrm{R} + \tau_\mathrm{d})}\, \mathrm{e}^{\mathrm{i}2\pi f_\mathrm{m}(kT_\mathrm{R}+\tau_\mathrm{d})} \right| , \tag{8.1}$$

where n_p is the total number of applied pump pulses. The overline denotes the required ensemble average over the Overhauser field distribution introduced later in this section. Qualitatively, the expression describes the amplitude of the Fourier component of the spin polarization $\overline{S^z(kT_\mathrm{R} + \tau_\mathrm{d})}$ at the modulation frequency f_m. Note that the probed spin polarization as defined by Eq. (8.1) is also modulated with frequency f_m. Otherwise, the time-averaged spin polarization would vanish because the helicity of the pump pulses is modulated with the same frequency.

The goal is to describe the relevant spin dynamics and calculate $L(f_\mathrm{m})$ for various system parameters and magnetic fields. In order to address experimentally relevant conditions, we take into account the hyperfine interaction and the external magnetic field. Spin relaxation induced by other mechanisms is accounted for by phenomenological relaxation terms. In contrast to the theory presented in Ref. [125], we do not impose any restrictions on the system parameters. In particular, we do not assume that the pump pulses are infinitely weak. We will see that avoiding this simplification gives rise to interesting and new effects. In contrast to the previous chapters, the model presented in the following has a partially phenomenological character. But it has turned out that it describes the experiments of interest quite well [93, 125], and we extend it further to achieve an even better description.

We describe the spin dynamics of the resident charge carrier in a QD between consecutive pump pulses by the equation of motion[2]

$$\frac{\mathrm{d}}{\mathrm{d}t}\boldsymbol{S} = (\boldsymbol{\Omega}_\mathrm{n} + \boldsymbol{\Omega}_\mathrm{L}) \times \boldsymbol{S} - \frac{\boldsymbol{S}}{\tau_\mathrm{s}} + \frac{J^z}{\tau_0}\boldsymbol{e}_z \,, \tag{8.2}$$

where $\boldsymbol{\Omega}_\mathrm{n}$ represents the frequency of the spin precession about the Overhauser field, $\boldsymbol{\Omega}_\mathrm{L} = g_z \mu_\mathrm{B} \hbar^{-1} B_\mathrm{ext} \boldsymbol{e}_z$ represents the Larmor frequency of the spin precession about the longitudinal magnetic field $B_\mathrm{ext}\boldsymbol{e}_z$, g_z is the longitudinal g factor of the resident charge carrier, μ_B is the Bohr magneton, and $\boldsymbol{e}_\alpha$ is the unit vector in

[2] The notation used in this and the following chapter differs slightly from that used in the previous chapters to facilitate a comparison with the literature [93, 94, 125, 126, 255]. The Overhauser field is referred to as $\boldsymbol{\Omega}_\mathrm{n}$ (instead of $\boldsymbol{B}_\mathrm{ov}$) and the Larmor frequency as Ω_L (instead of h).

$\alpha \in \{x, y, z\}$ direction. The phenomenological term $-\boldsymbol{S}/\tau_\mathrm{s}$ describes the typically slow spin relaxation unrelated to the hyperfine interaction. Possible mechanisms result from the spin-orbit, dipolar, or quadrupolar interaction. Phonon-assisted spin relaxation is another possible mechanism, which could also explain the observed temperature dependence of the polarization recovery curves presented in Ref. [93]. The component J^z is the z projection of the trion pseudospin $\boldsymbol{J}$ and τ_0 is the trion lifetime related to the radiative trion recombination. The last term in Eq. (8.2) describes the input of spin polarization caused by this process [113, 124]. In contrast to Ref. [125], we neglect the dynamics of the Overhauser field, i.e., we consider it to be frozen in time as in Sec. 3.3.4. At least for the time T_R between two pulses, this approximation is justified, and we assume that no nonequilibrium effects similar to those studied in Part II become important on long timescales. Possible effects stemming from the nuclear spin dynamics are studied in Refs. [125, 126], but they appear to be of minor importance.

In the presence of an external longitudinal magnetic field, the Zeeman effect will lead to a residual spin polarization $S_0^z \boldsymbol{e}_z = \tanh[g_z \mu_\mathrm{B} B_\mathrm{ext}/(2k_\mathrm{B}T)]/2\, \boldsymbol{e}_z$, where T is the temperature and k_B is the Boltzmann constant. This residual polarization could be accounted for in the equations of motion, but its contribution is negligibly small under experimental conditions. For instance, in a magnetic field of $B_\mathrm{ext} = 200\,\mathrm{mT}$ at temperature $T = 4\,\mathrm{K}$ [93], the thermal equilibrium spin polarization amounts to only 1% of the maximum possible value. Moreover, the thermal contribution to the spin polarization increases the polarization slightly for one helicity of the pump pulse but decreases it for the other one so that the total effect cancels in linear order for the measured quantity defined in Eq. (8.1). Only in second order, a minute effect can occur.

Similarly to Eq. (8.2), the dynamics of the trion pseudospin between the pump pulses can be described by

$$\frac{\mathrm{d}}{\mathrm{d}t}\boldsymbol{J} = \left(\boldsymbol{\Omega}_\mathrm{n}^\mathrm{T} + \boldsymbol{\Omega}_\mathrm{L}^\mathrm{T}\right) \times \boldsymbol{J} - \frac{\boldsymbol{J}}{\tau_\mathrm{s}^\mathrm{T}} - \frac{\boldsymbol{J}}{\tau_0}\,. \tag{8.3}$$

The superscript ‘T’ refers to the parameters of the unpaired charge carrier spin in the trion. For resident electrons the trion consists of the two electrons in a spin singlet state and a hole with unpaired spin, while for resident holes it consists of two holes in a spin singlet state and an electron with unpaired spin. Thus, the effective type of the charge carrier in the trion state is opposite to the type of

the resident charge carrier. The spin relaxation unrelated to the hyperfine interaction is accounted for by the phenomenological relaxation time $\tau_\mathrm{s}^\mathrm{T}$. Combined with Eq. (8.2), only the z component of the trion pseudospin $\boldsymbol{J}$ is transferred back to the spin polarization S^z in the ground state during the trion recombination. This follows from the optical selection rules for the optical transitions between the bands Γ_6 and Γ_8 in GaAs-based semiconductors [114, 124].

The Overhauser field caused by the hyperfine interaction with the nuclear spins is treated as a random classical field. Since it comprises $10^4 - 10^6$ effectively coupled nuclear spins [19, 103–107], its probability distribution is a multivariate normal distribution as a consequence of the central limit theorem [104, 200, 219],

$$p(\boldsymbol{\Omega}_\mathrm{n}) = \frac{\lambda^2}{(\sqrt{\pi}\omega_\mathrm{n})^3} \exp\left(-\lambda^2 \frac{(\Omega_\mathrm{n}^x)^2 + (\Omega_\mathrm{n}^y)^2}{\omega_\mathrm{n}^2} - \frac{(\Omega_\mathrm{n}^z)^2}{\omega_\mathrm{n}^2}\right). \tag{8.4}$$

Its variance is characterized by ω_n^2 and the potential anisotropy of the hyperfine interaction is parameterized by λ. Thus, ω_n is a measure for the typical fluctuation strength of the Overhauser field and characterizes the typical precession frequency of the resident charge carrier spin in this field. In the case of electrons $\lambda = 1$ holds, while for heavy holes $\lambda \gg 1$ (see Sec. 3.1). The hyperfine interaction for the trion pseudospin is related to the same nuclear spin bath and we assume that it is given by

$$\Omega_\mathrm{n}^{\mathrm{T},x} = \chi \frac{\lambda}{\lambda^\mathrm{T}} \Omega_\mathrm{n}^x, \tag{8.5a}$$

$$\Omega_\mathrm{n}^{\mathrm{T},y} = \chi \frac{\lambda}{\lambda^\mathrm{T}} \Omega_\mathrm{n}^y, \tag{8.5b}$$

$$\Omega_\mathrm{n}^{\mathrm{T},z} = \chi \Omega_\mathrm{n}^z, \tag{8.5c}$$

where $\chi = \omega_\mathrm{n}^\mathrm{T}/\omega_\mathrm{n}$ describes the relative strength of the hyperfine interaction for the trion state and λ^T quantifies the degree of anisotropy. These relations are exact when the trion wave function is a product of identical wave functions of the three charge carriers forming the trion, which is a reasonable approximation for QDs providing a strong confinement, i.e., small QDs [266].

Let us turn to the description of the pump pulses of arbitrary strength. For this purpose, we apply the pulse model developed in Ref. [113] and presented in Sec. 2.2.2. We still assume that the trion state is unoccupied at the arrival of a pump pulse.

This assumption is perfectly valid in the usual case $\tau_0 \ll T_\mathrm{R}$, but it needs to be lifted in Chap. 9 where pulses with repetition time $T_\mathrm{R} = 1\,\mathrm{ns}$ instead of 13.2 ns are considered. In the experiments of Ref. [93], the pulses have a duration of 1.5 ps, which is much shorter than all the above time scales of the spin dynamics. Under these conditions, the action of a pump pulse can be described by a relation between the spin components before ($\boldsymbol{S}_\mathrm{b}$, $\boldsymbol{J}_\mathrm{b}$) and after ($\boldsymbol{S}_\mathrm{a}$, $\boldsymbol{J}_\mathrm{a}$) the pulse [113],

$$S_\mathrm{a}^z = -\mathcal{P}\frac{1-Q^2}{4} + \frac{1+Q^2}{2} S_\mathrm{b}^z\,, \tag{8.6a}$$

$$S_\mathrm{a}^x = Q\cos(\Phi) S_\mathrm{b}^x + \mathcal{P}Q\sin(\Phi) S_\mathrm{b}^y\,, \tag{8.6b}$$

$$S_\mathrm{a}^y = Q\cos(\Phi) S_\mathrm{b}^y - \mathcal{P}Q\sin(\Phi) S_\mathrm{b}^x\,, \tag{8.6c}$$

$$J_\mathrm{a}^z = S_\mathrm{b}^z - S_\mathrm{a}^z\,, \tag{8.6d}$$

$$J_\mathrm{a}^x = J_\mathrm{a}^y = 0\,. \tag{8.6e}$$

The probability *not* to excite a trion is given by $0 \leq Q^2 \leq 1$ and $-\pi \leq \Phi \leq \phi$ describes the angle of a spin rotation induced by detuned pulses. The helicity of the circularly polarized light is represented by $\mathcal{P} = \pm 1$. The parameter Q is a measure for the pumping strength. Previous theoretical treatment [125] assumed the limit $Q \to 1$ and $\Phi = 0$, which corresponds to very weak pulses. In this limit, the pulse adds a constant spin polarization to the value S_b^z before the pulse while preserving the transverse components. But here, we are interested in arbitrarily strong pulses and particularly in π pulses corresponding to $Q = 0$, which is the most efficient case.

Note that there is a difference between the semiclassical approach used here and the semiclassical approach used in Part II. As discussed at the end of Sec. 3.3.2, the averaging over random initial conditions does not only mimic the quantum mechanical behavior of the system. In experiments, the spin polarization is accumulated over repeated measurements to obtain a decent signal-to-noise ratio. Since the Overhauser field is not static but fluctuates, mainly as a consequence of the hyperfine interaction, its temporal fluctuations but also the fluctuations in a homogeneous ensemble of QDs can be modeled by the probability distribution (8.4). Here, we consider $\boldsymbol{S}$ and $\boldsymbol{J}$ to represent the average spin polarizations in a single QD while also accounting for phenomenological relaxation terms, but we do not account for the nuclear spin dynamics. The pulse relations are directly applicable to this case because they describe the action of a pump pulse on the quantum

mechanical averages of the spins (see Sec. 2.2.2) [113]. In contrast, in the previous chapters, the quantum mechanical spin dynamics without phenomenological terms is mimicked by applying the Gaussian TWA to account for the uncertainty principle whenever a pump pulse acts on the electron spin (see Sec. 6.2), which is important to account for its non-classical backaction on the nuclear spins in the semiclassical approach. Since we neglect this backaction here, it is not necessary to include the additional statistical overhead imposed by the resulting nondeterministic pulse description. Note that we still apply the Gaussian TWA to the Overhauser field, for which this approximation is very well justified thanks to the central limit theorem [183, 200, 229], but it happens automatically when averaging over the distribution (8.4).

8.2 Methods

We apply the following two approaches to analyze the spin inertia signal for various parameters: the full solution of the equations governing the spin dynamics for finite modulation frequency and a simplified approach for the steady-state limit. Overall, we have checked that our results are in agreement with the approach developed in Ref. [125] for weak pump pulses. Slight deviations are found only when the assumptions made in Ref. [125] are not completely valid.

8.2.1 Finite modulation frequency

In order to calculate the spin inertia signal defined by Eq. (8.1) for a finite modulation frequency f_m, we solve the equations of motion (8.2) and (8.3) numerically by applying the Dormand-Prince method [241], which is an adaptive fifth-order Runge-Kutta algorithm. The numerical calculation of the spin dynamics is performed for $M = 10^5$ random initial conditions of the Overhauser field $\mathbf{\Omega}_\mathrm{n}$ sampled from the normal distribution (8.4). All components of the vectors $\boldsymbol{S}$ and $\boldsymbol{J}$ are set equal to zero before the arrival of the first pump pulse, i.e., the system is in the ground state and unpolarized. Then, periodic pulses are applied with repetition time T_R by solving the equations of motion on a grid given by the intervals $t \in [kT_\mathrm{R}, (k+1)T_\mathrm{R}]$ and applying the pulse (8.6) at the boundaries. The helicity of the pulse is alternated

between σ^+ and σ^- by switching the sign of $\mathcal{P}$ in the pulse relation (8.6) every $T_\mathrm{m}/2 = 1/(2f_\mathrm{m})$. Finally, we calculate the average

$$\overline{S^z(t)} = \frac{1}{M}\sum_{m=1}^{M} S_m^z(t) \tag{8.7}$$

over all M trajectories $S_m^z(t)$ resulting from the random initial conditions of the Overhauser field and calculate from it the spin inertia signal L using Eq. (8.1). The numerical effort is realized by massive parallelization. General remarks on the numerical treatment are given in Sec. 3.3.3.

Depending on the modulation frequency, the number of pulses to be simulated can become fairly large. For instance, at $f_\mathrm{m} = 40\,\mathrm{kHz}$ and $T_\mathrm{R} = 13.2\,\mathrm{ns}$, about 1894 pulses fit into a single modulation period, whereas for $f_\mathrm{m} = 4000\,\mathrm{kHz}$, the number of pulses reduces to roughly 19. In Chap. 9, the combination of $f_\mathrm{m} = 10\,\mathrm{kHz}$ with $T_\mathrm{R} = 1\,\mathrm{ns}$ is studied in detail. In this case, 10^6 pulses fit into a modulation period. In the experiments analyzed there, however, the magnetic field is varied with a rate of $45\,\mathrm{mT\,min^{-1}}$ with a minimal resolution of approximately 0.1 mT [94]. This implies that a single measurement is averaged at least over a time of 133.3 ms, which translates to $n_\mathrm{p} = 1333$ modulation periods, i.e., more than 10^9 pulses. Fortunately, it is not required to replicate this situation because the first few modulation periods already contain the relevant information.

In practice, we simulate $n_\mathrm{period} = 5$ modulation periods and calculate L using only the last two periods for the summation in Eq. (8.1) to exclude effects of transient behavior (occurring because every simulation starts from the equilibrium initial condition $\boldsymbol{S}(0) = 0$). This procedure provides a good compromise between efficiency and accuracy and in most cases, the relative error of L is well below 1%. For high modulation frequencies where only a few pulses fit into a modulation period, the relative error can grow because of the generic non-commensurability of T_m and T_R. It is difficult to give an error estimate, but using $f_\mathrm{m} \approx 4000\,\mathrm{kHz}$ and $T_\mathrm{R} = 13.2\,\mathrm{ns}$ as an example, the error can be as large as $\sim 5\%$, depending on the precise choice of n_period in combination with f_m. As a trend, the error is smaller for larger magnetic fields. The influence of the non-commensurability is reduced for smaller f_m because the impact of a single pulse on L is diminished when more pulses fall into the modulation period. Overall, we have checked that the error does not have a noticeable influence on the results presented in this chapter.

For very small modulation frequencies, the computational effort can still be quite large. In this case, it is sufficient to consider only $n_{\mathrm{period}} = 2$ modulation periods and consider only the second (final) one to calculate L. This is what we do in Chap. 9 because the simulations would be too expensive otherwise. We still neglect the first period because of the transient behavior. Its influence on L vanishes in the steady-state limit $f_{\mathrm{m}} \to 0$.

8.2.2 Steady-state limit

When considering the limit of zero modulation frequency $f_{\mathrm{m}} \to 0$, it is not necessary to solve the equations for the spin dynamics explicitly over a time interval covered by many pump pulses. Instead, one can exploit the fact that in this case the spin polarization is a periodic function with period T_{R} [114], i.e., the system approaches a steady state if the pump helicity is not modulated. Provided the spin polarization $\boldsymbol{S}_{\mathrm{b}}$ before a pulse is known, one can calculate the polarizations $\boldsymbol{S}_{\mathrm{a}}$ and $\boldsymbol{J}_{\mathrm{a}}$ after the pulse using Eq. (8.6) and then solve Eqs. (8.2) and (8.3) on the time interval $t \in [0, T_{\mathrm{R}}]$ for a given Overhauser field $\boldsymbol{\Omega}_{\mathrm{n}}$. In the steady state, the result at $t = T_{\mathrm{R}}$ has to coincide with $\boldsymbol{S}_{\mathrm{b}}$ because of the periodicity, which we exploit to find the steady-state value for $\boldsymbol{S}_{\mathrm{b}}$. Finally, the spin inertia signal $L(f_{\mathrm{m}} \to 0)$ is proportional to the steady-state value $S^z_{\mathrm{b,NESS}}$ averaged over the Overhauser field distribution (8.4). To be precise, $L(f_{\mathrm{m}} \to 0) = 2\overline{S^z_{\mathrm{b,NESS}}}/\pi$, which follows from the definition (8.1).

The analytical integration of Eq. (8.3) yields the time evolution of the trion pseudospin. The dynamics of its z component after a pump pulse are described by

$$J^z(t) = J^z_{\mathrm{a}} \left[\cos^2\left(\theta^{\mathrm{T}}\right) + \sin^2\left(\theta^{\mathrm{T}}\right) \cos\left(\Omega^{\mathrm{T}}_{\mathrm{eff}} t\right)\right] \mathrm{e}^{-t/\tau_{\mathrm{s}}^{\mathrm{T}}} \mathrm{e}^{-t/\tau_0} \,. \tag{8.8}$$

Here, $\boldsymbol{\Omega}^{\mathrm{T}}_{\mathrm{eff}} = \boldsymbol{\Omega}^{\mathrm{T}}_{\mathrm{n}} + \boldsymbol{\Omega}^{\mathrm{T}}_{\mathrm{L}}$ is the total precession frequency of the trion pseudospin and θ^{T} is the angle between $\boldsymbol{\Omega}^{\mathrm{T}}_{\mathrm{eff}}$ and the z axis. Analogously, we define θ as the angle between $\boldsymbol{\Omega}_{\mathrm{eff}} = \boldsymbol{\Omega}_{\mathrm{n}} + \boldsymbol{\Omega}_{\mathrm{L}}$ and the z axis.

The spin dynamics of the resident charge carrier between consecutive pulses is determined by Eq. (8.2). In the steady state, its solution at time $t = T_{\mathrm{R}}$ must

coincide with $\boldsymbol{S}_\mathrm{b}$ [24, 112, 113], leading to the equations [255]

$$S_\mathrm{b}^x = S_\mathrm{a}^x \left[\sin^2(\theta) + \cos^2(\theta)\cos(\Omega_\mathrm{eff} T_\mathrm{R})\right] \mathrm{e}^{-T_\mathrm{R}/\tau_\mathrm{s}} - S_\mathrm{a}^y \cos(\theta)\sin(\Omega_\mathrm{eff} T_\mathrm{R})\,\mathrm{e}^{-T_\mathrm{R}/\tau_\mathrm{s}} + \int \left(S_\mathrm{a}^z \delta(\tau) + \frac{J^z(\tau)}{\tau_0}\right) \cos(\theta)\sin(\theta)\left\{1 - \cos\left[\Omega_\mathrm{eff}(T_\mathrm{R} - \tau)\right]\right\} \mathrm{e}^{-(T_\mathrm{R}-\tau)/\tau_\mathrm{s}}\,\mathrm{d}\tau\,, \tag{8.9a}$$

$$S_\mathrm{b}^y = S_\mathrm{a}^x \cos(\theta)\sin(\Omega_\mathrm{eff} T_\mathrm{R})\,\mathrm{e}^{-T_\mathrm{R}/\tau_\mathrm{s}} + S_\mathrm{a}^y \cos(\Omega_\mathrm{eff} T_\mathrm{R})\,\mathrm{e}^{-T_\mathrm{R}/\tau_\mathrm{s}} - \int \left(S_\mathrm{a}^z \delta(\tau) + \frac{J^z(\tau)}{\tau_0}\right) \sin(\theta)\sin\left[\Omega_\mathrm{eff}(T_\mathrm{R} - \tau)\right] \mathrm{e}^{-(T_\mathrm{R}-\tau)/\tau_\mathrm{s}}\,\mathrm{d}\tau\,, \tag{8.9b}$$

$$S_\mathrm{b}^z = S_\mathrm{a}^x \cos(\theta)\sin(\theta)\left[1 - \cos(\Omega_\mathrm{eff} T_\mathrm{R})\right] \mathrm{e}^{-T_\mathrm{R}/\tau_\mathrm{s}} + S_\mathrm{a}^y \sin(\theta)\sin(\Omega_\mathrm{eff} T_\mathrm{R})\,\mathrm{e}^{-T_\mathrm{R}/\tau_\mathrm{s}} + \int \left(S_\mathrm{a}^z \delta(\tau) + \frac{J^z(\tau)}{\tau_0}\right) \left\{\cos^2(\theta) + \sin^2(\theta)\cos\left[\Omega_\mathrm{eff}(T_\mathrm{R} - \tau)\right]\right\} \mathrm{e}^{-(T_\mathrm{R}-\tau)/\tau_\mathrm{s}}\,\mathrm{d}\tau\,. \tag{8.9c}$$

Here, without loss of generality, we assume that both $\boldsymbol{\Omega}_\mathrm{eff}$ and $\boldsymbol{\Omega}_\mathrm{eff}^\mathrm{T}$ lie in the (xz) plane. We also assume that τ_0 is much shorter than τ_s and $J^z(\tau) = 0$ at $\tau < 0$, so the limits of the integration over τ can be extended to run from $-\infty$ to $+\infty$. Both assumptions are valid in InGaAs QDs; see Table 8.1 for typical parameters. After inserting $J^z(t)$ given by Eq. (8.8), the integrals can be solved analytically by a computer algebra system such as Wolfram Mathematica, but the solution is lengthy. The spin polarization $S_\mathrm{b,NESS}^z$ in the steady state results from solving the coupled set of linear equations (8.6) and (8.9). Finally, averaging the steady-state value $S_\mathrm{b,NESS}^z$ over the distribution of the Overhauser field (8.4) yields the spin inertia signal $L(f_\mathrm{m} \to 0) = 2\overline{S_\mathrm{b,NESS}^z}/\pi$ in the limit of zero modulation frequency. We point out that a similar approach is used, e.g., in Refs. [23–25].

Note that in order to correctly obtain the limit $f_\mathrm{m} \to 0$, the solution has to be averaged over the two pump helicities $\mathcal{P} = \pm 1$. Technically, this is equivalent to averaging over two opposite detunings corresponding to opposite signs of the rotation angle Φ as can be seen from the pulse relation (8.6). Thus, calculating the average is only required for $\Phi \neq 0$.

8.3 Results

In this section, we analyze the spin inertia signal for various parameters, in particular for different pumping strengths and as function of the applied longitudinal magnetic field. First, we illustrate the typical spin dynamics arising from the modulated pumping scheme. We then focus on the case of a strong magnetic field using resonant pulses. Afterwards, the dependence of the spin polarization on the magnetic field is discussed and possible effects resulting from the application of detuned pulses are highlighted. At the end of this section, we predict and describe the effect of resonant spin amplification in Faraday geometry.

The calculations are performed for the two sets of parameters summarized in Table 8.1. The parameters correspond to n-doped and p-doped InGaAs QD samples [93, 97] and illustrate the qualitative differences between these two kinds of systems. The main difference is the strength of the hyperfine interaction ω_n. In n-doped QDs, the electrons are in an s-type Bloch band and the hyperfine interaction stems from the Fermi-contact interaction, which is strong thanks to the confinement provided by the QD. For holes (p doped) the hyperfine interaction is caused by the dipole-dipole interaction, which is much weaker and anisotropic [97, 156–158, 184]. The different interactions are discussed in detail in Sec. 3.1. As mentioned above, the effective type of charge carrier in the trion state is opposite to the type of the resident charge carrier. The longitudinal g factors of electrons and holes are of the

Table 8.1: Choice of parameters and their physical meaning used for the n- and p-doped QDs. The values are based on the experimental results of Ref. [93].

Parameter	n doped	p doped	Physical meaning
$\omega_\mathrm{n}/(2\pi)$	70 MHz	16 MHz	hyperfine interaction strength (ground state)
$\omega_\mathrm{n}^\mathrm{T}/(2\pi)$	16 MHz	70 MHz	hyperfine interaction strength (trion state)
λ	1	5	hyperfine interaction anisotropy (ground state)
λ^T	5	1	hyperfine interaction anisotropy (trion state)
g_z	−0.61	−0.45	longitudinal g factor (ground state)
g_z^T	−0.45	−0.4	longitudinal g factor (trion state)
τ_s	500 ns	5200 ns	spin relaxation time (ground state)
$\tau_\mathrm{s}^\mathrm{T}$	10 ns	35 ns	spin relaxation time (trion state)
τ_0	0.4 ns	0.4 ns	radiative trion lifetime
T_R	13.2 ns	13.2 ns	pulse repetition time

same order, but the spin relaxation time in the ground state τ_s is found experimentally to be about one order shorter for electrons than for holes. For both kinds of QDs (n or p doped), the spin relaxation time τ_s^T in the trion state is much shorter than the spin relaxation time τ_s in the ground states.

8.3.1 Typical spin dynamics resulting from modulated pumping

The characteristic behavior of the spin polarization $\overline{S^z(n_p T_R^-)}$ caused by the modulated pumping scheme, where the notation T_R^- means that the spin polarization is probed immediately before the arrival of a pump pulse, is shown in Fig. 8.1. for two different modulation frequencies f_m while applying a strong longitudinal magnetic field of $B_{ext} = 300\,\mathrm{mT}$. Here, we use the parameters typical for n-doped QDs given in Table 8.1. The switching of the helicity takes place at the positions highlighted by the vertical dashed lines.

In Fig. 8.1(a) with $f_m = 100\,\mathrm{kHz}$, the spin polarization reaches a steady state before the helicity is switched. After switching from $\mathcal{P} = +1$ to -1, the spin polarization approaches a steady state with the same absolute value but opposite sign. Generally, the spin polarization is smaller for weaker pulses corresponding to larger values of Q. Simply integrating over the full time interval essentially yields zero if the pulse sequence is applied long enough. Hence, the probed spin inertia

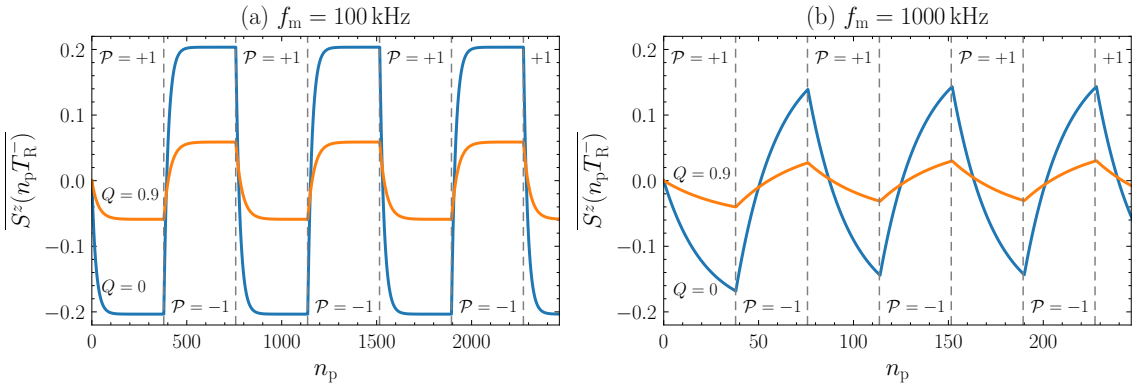

Figure 8.1: Spin polarization $\overline{S^z(n_p T_R^-)}$ for n-doped QDs probed immediately before the arrival of the next pump pulse while a longitudinal magnetic field of $B_{ext} = 300\,\mathrm{mT}$ is applied. The pump helicity $\mathcal{P}$ is modulated with frequency (a) $f_m = 100\,\mathrm{kHz}$ and (b) $f_m = 1000\,\mathrm{kHz}$, respectively. The vertical dashed lines highlight the moments in time at which the helicity is switched.

signal needs to be modulated as described by Eq. 8.1 to obtain a nonzero value. If the modulation frequency is chosen large enough, e.g., $f_\mathrm{m} = 1000\,\mathrm{kHz}$ as in Fig. 8.1(b), the helicity is switched before the spin polarization can reach a steady state. The result is that the spin inertia signal 8.1 yields a smaller value. Generally, the dependency on the modulation frequency depends on the spin relaxation rate, which is the essence of the spin inertia effect. It is described in detail in the following section.

Since the spin polarization $\boldsymbol{S}(0) = 0$ is zero at the start of a simulation, there is a transient behavior for the first few modulation periods (mainly in the first one). As discussed in Sec. 8.2.1, this transient part needs to be omitted when calculating the spin inertia signal. In the limit of zero modulation frequency $f_\mathrm{m} \to 0$, the influence of the initial buildup on the spin inertia signal vanishes so that we can simply apply the steady-state approach introduced in Sec. 8.2.2.

8.3.2 Spin inertia in a strong longitudinal magnetic field

As discussed in Sec. 3.3.4, the application of a strong longitudinal magnetic field $\Omega_\mathrm{L} \gg \Omega_\mathrm{n}$ suppresses the nuclei-induced spin relaxation. In this limit, the influence of the hyperfine interaction can be neglected. Instead of Eqs. (8.2) and (8.3), the spin dynamics can be described by the two coupled scalar equations

$$\frac{\mathrm{d}}{\mathrm{d}t} S^z = -\frac{S^z}{\tau_\mathrm{s}} + \frac{J^z}{\tau_0}\,, \tag{8.10a}$$

$$\frac{\mathrm{d}}{\mathrm{d}t} J^z = -\frac{J^z}{\tau_\mathrm{s}^\mathrm{T}} - \frac{J^z}{\tau_0}\,. \tag{8.10b}$$

In the realistic situation $\tau_\mathrm{s} \gg T_\mathrm{R}$, Eq. (8.10) can be solved for the initial conditions determined by the pulse relation (8.6). For now, we consider resonant pulses with $\Phi = 0$. For $t \gg \tau_0$ and $t < T_\mathrm{R}$, the solution is given by

$$S^z(t) = (S_\mathrm{b}^z + \Delta S^z)\,\mathrm{e}^{-t/\tau_\mathrm{s}}\,, \tag{8.11}$$

where

$$\Delta S^z = -\left(\frac{\mathcal{P}}{4} + \frac{S_\mathrm{b}^z}{2}\right)(1 - Q^2)\left(\frac{\tau_0}{\tau_\mathrm{s}^\mathrm{T} + \tau_0} - \frac{\tau_0}{\tau_\mathrm{s}}\right) \tag{8.12}$$

is the difference of the spin polarization after the trion recombination and before the arrival of the next pump pulse. In contrast to the theory of Ref. [125], the time τ_s^T can be comparable to τ_0.

Still assuming $\tau_s \gg T_R$ and $t \gg \tau_0$, the train of pump pulses can be replaced on average by a continuous pumping such that the spin dynamics is described by

$$\frac{d}{dt}S^z = \frac{\Delta S^z}{T_R} - \frac{S^z}{\tau_s}. \tag{8.13}$$

The first term represents the generation rate of the spin polarization. In this limit, the spin inertia dependency is described by the relation [159]

$$L(f_m) = \frac{L(0)}{\sqrt{1+(2\pi\tau_s^* f_m)^2}}, \tag{8.14}$$

where τ_s^* is the effective spin relaxation time defined by [125]

$$\frac{1}{\tau_s^*} = \frac{1}{\tau_s} + \frac{(1-Q^2)\tau_0}{2T_R(\tau_s^T+\tau_0)}. \tag{8.15}$$

In the limit of weak pulses with $Q \to 1$, the intrinsic spin relaxation time τ_s is retained. But for $Q < 1$, the effective spin relaxation time τ_s^* is shorter than τ_s because of an effective quenching of the spin relaxation time induced by strong pump pulses. This effect can be seen by insert Eq. (8.12) into Eq. (8.13) and assuming $\tau_s \gg \tau_s^T$. The spin inertia signal at zero modulation frequency is determined by the balance between spin generation and spin relaxation

$$L(0) = \frac{1-Q^2}{2\pi}\frac{\tau_s^*}{T_R}\left|\frac{\tau_0}{\tau_s^T+\tau_0} - \frac{\tau_0}{\tau_s}\right|, \tag{8.16}$$

where we take into account that according to the definition (8.1) the steady-state spin polarization is $\pi/2$ times larger than $L(0)$ [125]. The pump pulse creates a spin polarization proportional to $(1-Q^2)$, which has opposite directions in the ground and trion states as can be seen from Eq. (8.6d), e.g., for $S_b^z = 0$. Hence, the spin relaxations in the ground and trion states during the trion lifetime result in two competing contributions to the total spin polarization as described by the two terms under the modulus.

Note that it can be deduced from Eq. (8.12) that the effect of spin polarization

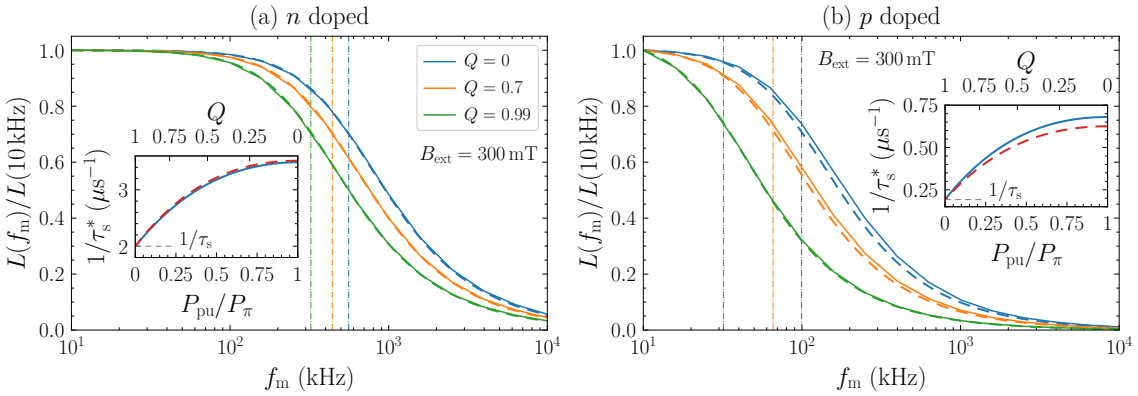

Figure 8.2: Dependence of the spin inertia signal L on the modulation frequency f_m at a magnetic field of $B_\mathrm{ext} = 300\,\mathrm{mT}$ for (a) n-doped and (b) p-doped QDs, calculated by numerical simulations (solid lines) and by Eqs. (8.14) and (8.15) (dashed lines). The vertical dash-dotted lines represent the corresponding cutoff frequencies $1/(2\pi\tau_\mathrm{s}^*)$, where the effective spin relaxation time τ_s^* is calculated using Eq. (8.15). The inset shows the inverse effective spin relaxation time $1/\tau_\mathrm{s}^*$ as a function of Q and P/P_π, calculated by fitting Eq. (8.14) to data obtained from the numerical simulation for $B_\mathrm{ext} = 300\,\mathrm{mT}$ (blue solid line) and calculated according to Eq. (8.15) (red dashed line).

saturation results from an effective decrease of the spin generation rate. However, it is not straightforward in this interpretation to explain the change of the cutoff frequency $1/(2\pi\tau_\mathrm{s}^*)$ in Eq. (8.14). Thus, we prefer the interpretation based on the effective decrease of the spin relaxation time for stronger pump pulses as described by Eq. (8.15). But sometimes, the other interpretation is also convenient to explain certain effects.

The spin inertia dependence $L(f_\mathrm{m})$ at a strong magnetic field of $B_\mathrm{ext} = 300\,\mathrm{mT}$ using different pumping efficiencies Q is shown in Fig. 8.2 for n- and p-doped QDs. The dependence described by Eq. (8.14) combined with Eq. (8.15) is depicted by the dashed curves in Fig. 8.2. The spin polarization decreases significantly when the modulation frequency f_m becomes larger than the cutoff frequency $1/(2\pi\tau_\mathrm{s}^*)$, which is the essence of the spin inertia effect. For $f_\mathrm{m} \gg 1/(2\pi\tau_\mathrm{s}^*)$, the dependence on the modulation frequency is reciprocal, $L(f_\mathrm{m}) \propto 1/f_\mathrm{m}$. In the opposite limit, the system approaches the steady-state spin polarization $L(0)$. The small differences between the analytical (dashed lines) and numerical (solid lines) results are related to the large but finite ratio of the external magnetic field and the Overhauser field in the numerical simulations.

Since the hyperfine interaction can be neglected in the limit of a strong longitudinal magnetic field, the results are very similar for n- and p-doped QDs. The main difference is a shift of the spin inertia dependence to smaller modulation frequencies for the p-doped case, which results from the ground state spin relaxation time τ_s being larger by one order of magnitude than in the n-doped case (see Table 8.1).

Let us turn to the dependence on the pump power. In the case of resonant pulses, the pumping efficiency is determined by $Q = \cos(\Theta/2)$, where Θ is the effective area of the pump pulse [113]; see Sec. 2.2.2 for more details and for the definition of Θ given in Eq. (2.14). In parallel, the pump pulse power scales like $P_{\mathrm{pu}} \propto \Theta^2$ for small powers [23, 113, 135]. Thus, for a power smaller than the power of a π pulse ($\Theta = \pi \Rightarrow Q = 0$), denoted by P_π, we obtain the relation

$$Q = \cos\left(\frac{\pi}{2}\sqrt{\frac{P_{\mathrm{pu}}}{P_\pi}}\right), \tag{8.17}$$

which facilitates the investigation of the spin inertia as a function of the pump power P_{pu} because the proportionality factor depends on many details related to the specific QD sample. The power P_π can be determined in experiments by increasing P_{pu} until the spin polarization shows a maximum (pulses with $\Theta = \pi$ are most efficient) [23].

Measurements of the spin inertia allow one to determine the effective spin relaxation time τ_s^* in the limit of a large magnetic field because the only other relevant parameter in this limit is the modulation frequency f_m. The inset in Fig. 8.2 shows the dependence of the inverse effective spin relaxation time on Q and on the normalized pump power P_{pu}/P_π, which is related to Q by Eq. (8.17). The solid line is obtained from the numerical simulation by fitting the dependence $L(f_m)$ for $B_{\mathrm{ext}} = 300\,\mathrm{mT}$ with Eq. (8.14), and the dashed lines are calculated using Eq. (8.15). In the limit of zero pump power ($Q \to 1$), τ_s^* is equal to the intrinsic spin relaxation time τ_s, as expected. With an increase of the pump power, the rate of spin relaxation effectively increases. Its dependence on the pump power in the regime of small powers appears to be linear. This justifies a linear extrapolation to zero pump power in order to extract the intrinsic spin relaxation time τ_s from measurements of the spin inertia as performed in Refs. [93, 159]; see also the insets in Figs. 2.6(c) and 2.6(d) taken from Ref. [93].

The dependence of the spin inertia signal on the pump power in the strong field

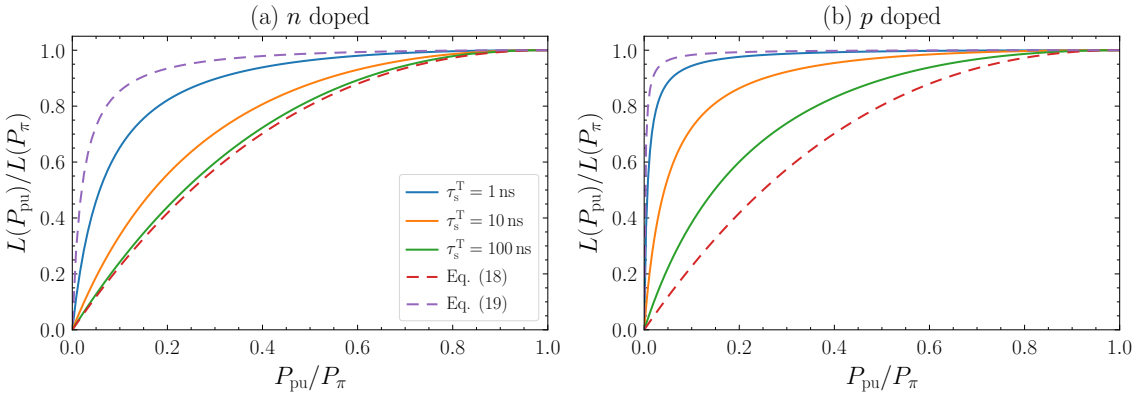

Figure 8.3: Dependence of the spin inertia signal L on the normalized pump power P_{pu}/P_π at a magnetic field of $B_{\mathrm{ext}} = 300\,\mathrm{mT}$ in the steady-state limit for various trion spin relaxation times τ_s^T and remaining parameters chosen to represent (a) n-doped and (b) p-doped QDs. For comparison, the limiting cases of large and small τ_s^T, described by Eqs. (8.19) and (8.20), are depicted as dashed lines.

limit is shown in Fig. 8.3 for n- and p-doped QDs in the steady-state limit $f_m \to 0$. The slope depends on the ratio τ_s^T/τ_0 of the trion spin relaxation time and the trion recombination time and is larger for smaller ratios. The reason is that a smaller ratio implies that a larger degree of spin polarization remains in the ground state after the trion recombination, i.e., spin generation rate is increased as can be seen from Eq. (8.12) for $\tau_s \gg \tau_s^T \gg \tau_0$. Potentially, this allows one to determine this ratio by measuring the dependence of the spin polarization on the pump power. If the recombination time τ_0 is known, e.g., from time-dependent photoluminescence measurements, this dependence gives access to the spin relaxation time τ_s^T of the trion, which is not easy to determine by other means. Note that in Fig. 8.3, we vary only τ_s^T while keeping τ_0 constant, but we have checked that varying $1/\tau_0$ by the same factors has the same effect.

Let us analyze $L(0)$ given by Eq. (8.16), which describes the spin polarization in the steady state induced by an infinite train of pulses with the same helicity. Usually, the spin relaxation in the trion state is much faster than in the ground state so that $\tau_s^T \ll \tau_s$ holds and it follows

$$L(0) = \frac{(1-Q^2)\tau_s^* \tau_0}{2\pi T_R(\tau_s^T + \tau_0)}\,. \tag{8.18}$$

The dependence of $L(0)$ on the pump power P_{pu} in a large external magnetic field

stems directly from the multiplier $1 - Q^2 = \sin^2\left(\sqrt{P_{\mathrm{pu}}/P_\pi}\pi/2\right)$ and also from the dependence of the effective spin relaxation time τ_{s}^* on P_{pu}. For long trion spin relaxation times $\tau_{\mathrm{s}}^{\mathrm{T}} \gg \tau_{\mathrm{s}}\tau_0/T_{\mathrm{R}}$, the latter dependence is negligible and it follows

$$\frac{L(P_{\mathrm{pu}})}{L(P_\pi)} = \sin^2\left(\frac{\pi}{2}\sqrt{\frac{P_{\mathrm{pu}}}{P_\pi}}\right). \tag{8.19}$$

This function, which does not depend on any system parameter besides the pump power, is displayed by the red dashed curve in Fig. 8.3. In the opposite limit $\tau_{\mathrm{s}}^{\mathrm{T}} \ll \tau_0$, we obtain

$$\frac{L(P_{\mathrm{pu}})}{L(P_\pi)} = \frac{\sin^2\left(\frac{\pi}{2}\sqrt{P_{\mathrm{pu}}/P_\pi}\right)}{\sin^2\left(\frac{\pi}{2}\sqrt{P_{\mathrm{pu}}/P_\pi}\right) + 2T_{\mathrm{R}}/\tau_{\mathrm{s}}}. \tag{8.20}$$

This dependence is displayed by the purple dashed curve in Fig. 8.3. In this limit, the spin inertia signal quickly increases for powers $P_{\mathrm{pu}} \gtrsim P_\pi T_{\mathrm{R}}/\tau_{\mathrm{s}}$ until saturation because an increase of the pump power not only increases the spin generation efficiency but also shortens the effective spin relaxation time τ_{s}^* so that both effects compensate each other. Since the spin relaxation times τ_{s} for n- and p-doped QDs differ by one order of magnitude, saturation is reached faster for the p-doped case. For intermediate values of $\tau_{\mathrm{s}}^{\mathrm{T}}$, the dependence on the pump power of the spin inertia signal smoothly changes from one limit to the other as demonstrated in Fig. 8.3.

8.3.3 Polarization recovery

Next, we analyze the dependence of the spin inertia signal on the strength of the applied longitudinal magnetic field. It is commonly accepted that the application of an external magnetic field in Faraday geometry suppresses nuclei-induced spin relaxation. Hence, increasing its strength typically leads to an increase of the spin polarization [104, 115]. This effect is known as *polarization recovery* and the related dependence is referred to as polarization recovery curve (PRC). Recently, it was shown that the polarization recovery can manifest itself in a surprising nonmonotonic way for p-doped QDs [93, 125]; see also Fig. 2.6(b) taken from Ref. [93].

Figure 8.4 depicts the spin inertia signal as a function of the external magnetic field B_{ext}. The calculations are performed for n-doped and p-doped QDs at low and high modulations frequencies f_{m} combined with various pumping strengths Q.

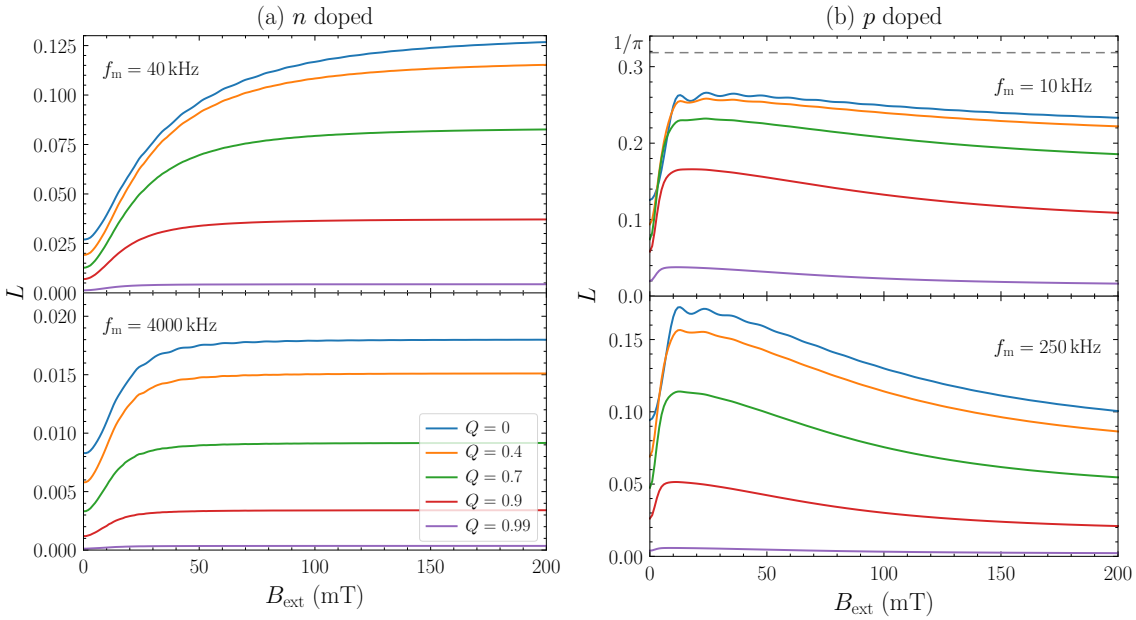

Figure 8.4: Polarization recovery curves: spin inertia signal L as a function of the external magnetic field B_{ext} at low and high modulation frequencies f_{m} for various pumping strengths Q. The parameter choice for n- and p-doped QDs are listed in Table 8.1. The gray dashed line in (b) indicates the maximum possible value $L_{\mathrm{max}} = 1/\pi$.

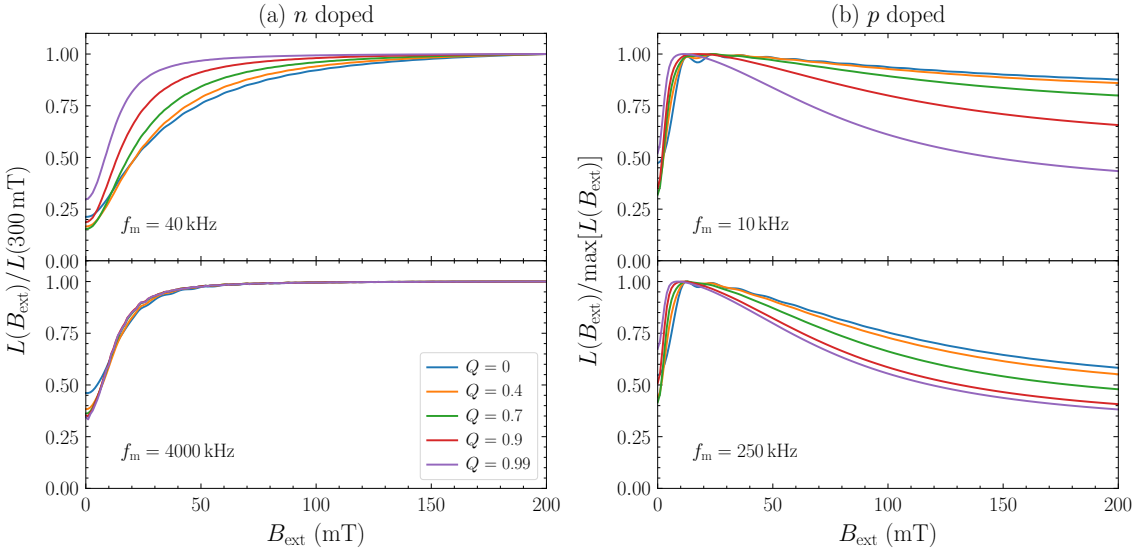

Figure 8.5: Normalized version of Fig. 8.4 to highlight changes in the shapes of the PRCs resulting from the variation of the pumping strength Q or the modulation frequency f_{m}.

Obviously, the shapes of the PRCs displayed in Fig. 8.4 are qualitatively different for the two sets of system parameters: for n-doped QDs the PRC is monotonic, whereas for p-doped QDs the spin polarization has a maximum at $B_{\mathrm{ext}} \approx 15\,\mathrm{mT}$. Because the spin inertia signal is an even function of B_{ext}, these shapes are referred to as V- and M-like, respectively [93, 125].

As discussed in Sec. 2.4.2, the different PRC shapes are caused by differing mechanisms leading to the spin polarization generation [93, 125], which is related to the complete relaxation mechanism of the trion state. For p-doped QDs, in contrast to the n-doped case, a major part of the relaxation stems from the hyperfine interaction of the unpaired electron spin in the positively-charged trion with the surrounding nuclei. Therefore, the application of a longitudinal magnetic field suppresses a part of the total trion relaxation mechanism, which leads to a reduced spin polarization generation rate. As a result, the probed spin polarization is reduced for large magnetic fields, leading to the characteristic M-like shape of the PRC for p-doped QDs. In contrast, for n-doped QDs, the hyperfine interaction of the hole in the trion with the surrounding nuclei is weak so that a reduction of the spin polarization is not observed for large magnetic fields. The result is the well-known V-like shape of the PRC, which is the shape that also follows from the frozen Overhauser field approximation under equilibrium conditions (see Fig. 3.3). But here, the nonequilibrium situation gives rise to several interesting effects.

Let us analyze the dependence of the PRCs on the pumping strength Q and on the modulation frequency f_{m}. Complementary to Fig. 8.4, normalized versions of the PRCs are shown in Fig. 8.5, which make it easier to notice changes of the PRC shapes. For the n-doped case at $f_{\mathrm{m}} = 40\,\mathrm{kHz}$, a strong broadening of the zero-field minimum is visible for stronger pulses corresponding to smaller values of Q. No broadening can be discerned when using the large modulation frequency $f_{\mathrm{m}} = 4000\,\mathrm{kHz}$. But when fixing, e.g., $Q = 0$ while decreasing f_{m}, a strong broadening is evident again. A similar but less pronounced behavior is also visible for the p-doped case. This phenomenon is closely related to the pulse properties. Strong pulses with $Q \to 0$ destroy the transverse spin components as can be seen from Eq. 8.6. But as discussed in Sec. 8.3.2, these components are only important if the magnetic field is not too large. For finite magnetic fields, the Overhauser field contributes to the effective magnetic field $\mathbf{\Omega}_{\mathrm{eff}} = \mathbf{\Omega}_{\mathrm{L}} + \mathbf{\Omega}_{\mathrm{n}}$, which results in a tilt from the z axis. Thus, the transverse spin components are larger on average for smaller external magnetic fields so that more spin polarization is

destroyed by strong pulses. The result is the observed broadening of the zero-field minimum.

The broadening observed for smaller modulation frequencies is related to the saturation limit of the spin polarization (all spins pointing in the same direction). The relative change of S^z induced by a single pulse (8.6a), which is responsible for the buildup of the spin polarization, reduces while approaching the saturation limit. But at the same time, the relative change of the transverse components does not depend on the degree of spin polarization. Hence, the broadening effect becomes more pronounced for a spin polarization closer to the saturation limit therefore for small modulation frequencies.

Notably, a similar broadening effect is observed in Ref. [93] for a decreasing modulation frequency, which could not be explained by the theory. The respective PRCs are visible in Fig. 2.6(a). Our results suggest that accounting for a finite pump power could lead to an improved agreement between experiment and theory. While we do not try to obtain better fits for these experimental results here, we will see in Chap. 9 that our extended theory can indeed describe the broadening of the zero-field minimum observed in experiments.

In the limit of very small spin polarization, i.e., when the modulation frequency is very large or when very weak pulses are applied, the width of the zero-field minimum of the PRC is determined by the frequency ω_n characterizing the hyperfine interaction of the resident charge carriers. Often, the PRC described by Eq. (3.47), which follows from the frozen Overhauser field approximation under equilibrium conditions [88], is fitted to measured data to determine ω_n [88]. We will see in Chap. 9 that this procedure is not sufficient if strong pump pulses are applied. At least an extrapolation to zero pump power is required.

The nonequilibrium conditions are responsible for another interesting effect. As demonstrated in Fig. 8.5(b), the application of stronger pulses can result in a change of the PRC shape from M- to V-like for p-type QDs. The reason for this behavior is similar to the mechanism leading to the broadening of the zero-field minimum. The larger the spin polarization, the less efficient is the spin generation of a single pump pulse as described by Eq. (8.6a). Thus, starting from a pronounced M-like shape, an increase of the pumping strength has a reduced effect on the regime around $B_\mathrm{ext} \approx 15\,\mathrm{mT}$ where the spin polarization is already large. In contrast, the spin polarization at large magnetic fields is much smaller so that the spin generation is

more efficient at large magnetic fields than at $B_{\mathrm{ext}} \approx 15\,\mathrm{mT}$. The consequence is that the PRC shape evolves from M- to V-like. This means that the decrease of the total trion spin relaxation rate by an increase of the magnetic field does not necessarily lead to a significant decrease of the spin polarization in the limit of strong pumping if the overall degree of spin polarization is large. The maximum possible value of the spin inertia signal corresponds to the case in which the spin polarization amounts to $S_{\mathrm{b}}^{z} = -\mathcal{P}/2$ before a pump pulse. In this case, Eq. (8.1) yields $L = 1/\pi$, which is highlighted in Fig. 8.4(b) as upper bound (gray dashed line).

In Fig. 8.5, it can be also seen that the pumping strength affects the depth of the zero magnetic field for both the n- and p-doped case. The expected ratio for n-doped QDs in the limit of small spin polarization is $L(0\,\mathrm{mT})/L(B_{\mathrm{ext}} \to \infty) = 1/3$ as described by Eq. (3.47). But for small modulation frequencies or strong pulses, we clearly find a difference from this ratio. This effect is similar to what is observed when including slow nuclear spin dynamics in the model [125]. Thus, the finite nuclear spin correlation time of about 200 ns obtained in Ref. [93] could be related to the assumption of very weak pumping. Certainly, there is an effect stemming from nuclear spin dynamics, which is omitted in our approach. But our results demonstrate that other effects can lead to a similar behavior so that the importance of the nuclear spin dynamics is difficult to judge in this context.

8.3.4 Nonresonant pumping

Up to now, we have considered resonant pump pulses by setting $\Phi = 0$ in the pulse relation (8.6). Let us briefly discuss the role of detuned pulses with $\Phi \neq 0$. Figure 8.6 shows the normalized PRCs for n-doped and p-doped QDs for moderate pump pulses with $Q = 0.7$ in combination with various values of the rotation angle Φ. There are a number of changes visible in the PRCs when increasing Φ, but they are qualitatively similar for large (solid lines) and zero (dash-dotted lines) modulation frequencies.

In the first place, an increase of Φ leads to an increase of the spin polarization for small to intermediate magnetic fields. From the unscaled versions of the PRCs in Fig. 8.6 (not shown), we find that the degree of spin polarization does not depend on Φ at large magnetic fields. To explain this effect, we recall that a finite value

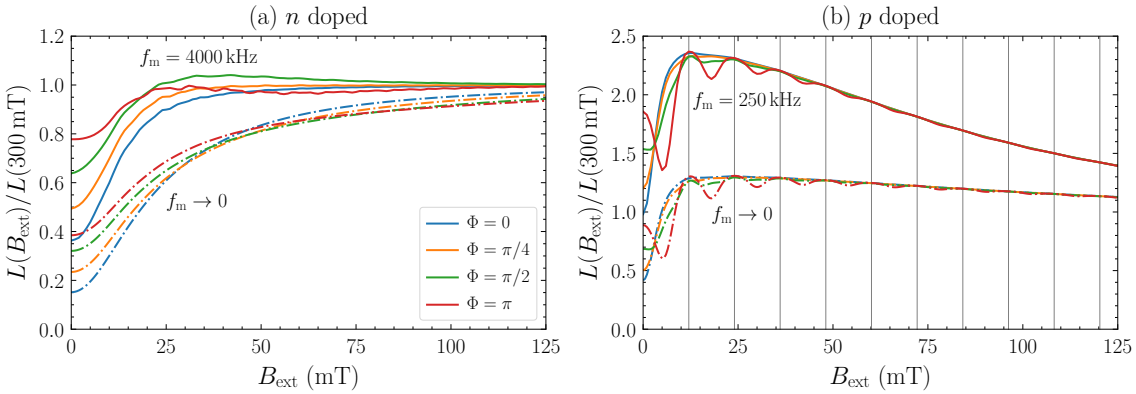

Figure 8.6: PRCs for various rotation angles Φ using moderate pump pulses with $Q = 0.7$ for n- and p-doped QDs. The numerical simulations (solid lines) are performed at $f_m = 4000$ kHz (n doped) and $f_m = 250$ kHz (p doped) and for the steady-state limit $f_m \to 0$ (dash-dotted lines). The vertical lines in panel (b) represent the phase synchronization condition (8.24). The parameter choices for n- and p-doped QDs are listed in Table 8.1.

of Φ corresponds to a spin rotation in the (xy) plane as described by the pulse relation (8.6). We recall that the spin rotation be understood as a consequence of a dynamic Zeeman effect: The electric field of the circularly polarized light induces a splitting of the spin states with z projections $\pm 1/2$ through the optical Stark effect, which is equivalent to an additional magnetic field parallel to the z axis acting only in the presence of the pump pulse [115, 118]. Qualitatively, this effective magnetic field increases the spin polarization similarly to the external magnetic field, i.e., it effectively suppresses the role of the random Overhauser field.

As discussed above, strong pump pulses partially destroy the transverse components of the spin polarization; see Eq. (8.6) for $Q \to 0$. Thus, the influence of Φ is reduced for smaller values of Q, i.e., the in-plane spin rotation becomes less important for stronger pulses.

In order to describe the effect of a finite rotation angle Φ on the spin polarization analytically, we consider the limit of very short trion spin relaxation time $\tau_s^T \ll \tau_0$ for isotropic hyperfine interaction in the ground state ($\lambda = 1$), long spin relaxation time $\tau_s \gg T_R$, strong hyperfine interaction $\omega_n T_R \gg 1$, and weak pump pulses with $(1 - Q^2)\tau_s/T_R \ll 1$. The precession of the trion pseudospin has no effect in this limit because the assumption $\tau_s^T \ll \tau_0$ implies that it its decay is basically immediate and also nonradiative. Under these assumptions, the system of equations (8.6) and (8.9)

can be solved analytically in the steady-state limit, yielding

$$S^z_{\mathrm{b,NESS}} = -\frac{\mathcal{P}}{4}(1-Q^2)\frac{\tau_\mathrm{s}}{T_\mathrm{R}}\frac{\kappa^2}{\kappa^2+\sin^2(\theta)\sin^2(\phi/2)}\,, \tag{8.21}$$

with

$$\kappa = \cos(\theta)\cos(\Phi/2)\sin(\phi/2) - \mathcal{P}\cos(\phi/2)\sin(\Phi/2) \tag{8.22}$$

and $\phi = \Omega_\mathrm{eff} T_\mathrm{R}$. Averaging this solution over the Overhauser field distribution (8.4) yields the ratio

$$\frac{L(B_\mathrm{ext}=0\,\mathrm{mT})}{L(B_\mathrm{ext}\to\infty)} = 1 - \frac{2}{\sin^2(\Phi/2)} + \frac{2\pi\sin^4(\Phi/4)+|\Phi|\cos(\Phi/2)}{\sin^3(|\Phi|/2)} \tag{8.23}$$

for $0<|\Phi|<\pi$. At $\Phi=0$ and $\Phi=\pi$, we obtain $L(0\,\mathrm{mT})/L(B_\mathrm{ext}\to\infty)=1/3$ and $\pi/2-1$, respectively, with a monotonic increase described by Eq. (8.23) in between. Thus, a finite rotation angle Φ leads to an increase of the spin polarization at zero magnetic field relative to its value at large field.

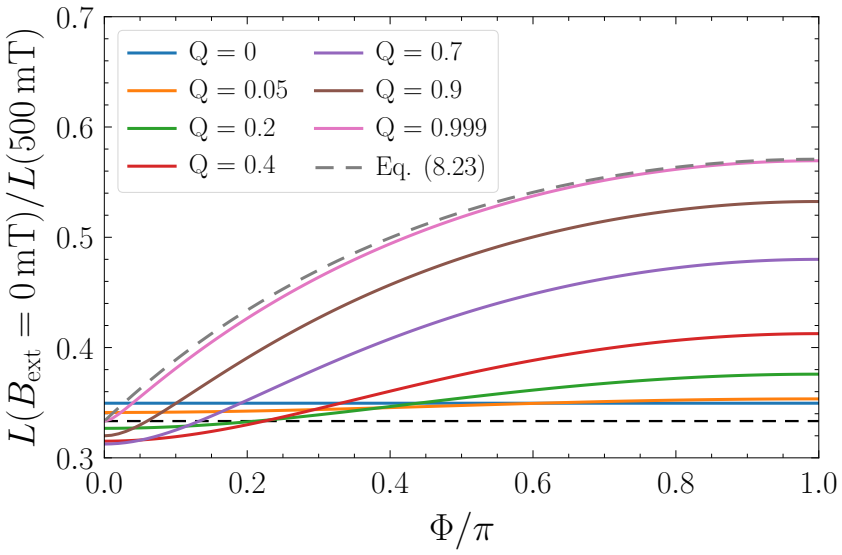

Figure 8.7: Ratio $L(B_\mathrm{ext}=0\,\mathrm{mT})/L(500\,\mathrm{mT})$ in the steady-state limit as a function of Φ for various pumping strengths Q. The trion spin relaxation time is chosen to be $\tau_\mathrm{s}^\mathrm{T}=0.04\,\mathrm{ns}$, the other parameters are taken from Table 8.1 for n-doped QDs. The gray dashed curve represents the analytical solution for the limit of weak pump pulses given by Eq. (8.23).

In order to check the validity of Eq. (8.23), we compare it to the numerical calculations with appropriate parameter choices ($\tau_s^T = 0.01\,\mathrm{ns}$) in Fig. 8.7. The convergence to the weak pump pulse limit $Q \to 1$, which was used for the derivation of Eq. (8.23), is evident. In the case of resonant pulses with $\Phi = 0$, we obtain $L(B_{\mathrm{ext}} = 0\,\mathrm{mT})/L(500\,\mathrm{mT}) \approx 1/3$, which is the ratio following from the frozen Overhauser field approximation [88, 104]; see Eq. (3.48b) and Fig. 3.3. Notably, an increase of Φ leads to a deviation from the ratio 1/3 in agreement with Eq. (8.23). At the same time, an increase of the pump power (or a decrease of Q) leads to a flattening of this dependence and to a slight deviation of the ratio from 1/3 even for $\Phi = 0$. For π pulses ($Q = 0$), a finite value of Φ has no effect because the transverse spin components in the pulse relation (8.6) vanish for $Q = 0$. In summary, we find that detuned pulses with fixed $Q > 0$ and $\Phi \neq 0$ lead to an increase of the spin polarization at zero magnetic field relative to the polarization at large field.

The most interesting effect is a qualitative change of the PRC shapes shown in Fig. 8.6 for larger values of Φ. For the n-doped case, the PRC can become non-monotonic, while for p-doped QDs, additional modulations appear in the PRC. The additional modulations are the result of a novel effect that we term *resonant spin amplification in Faraday geometry*. It is studied in the following section and also in Chap. 9.

8.3.5 Resonant spin amplification in Faraday geometry

The spin polarization studied as a function of the longitudinal magnetic field in Fig. 8.6(b) shows additional periodic modulations for large values of Φ. They are the result of resonant spin amplification (RSA) in Faraday geometry. The RSA effect is well established in Voigt geometry where a transverse external magnetic field is applied [77, 133, 135–137]. This effect leads to a considerable enhancement of the spin polarization whenever the Larmor frequency $\Omega_L = \mu_B |g_z B_{\mathrm{ext}}| \hbar^{-1}$ fulfills the phase synchronization condition (PSC)

$$\Omega_L T_R = 2\pi |k|\,, \qquad k \in \mathbb{Z}\,. \tag{8.24}$$

If this condition is fulfilled, the Larmor period of the resident charge carrier spin is a multiple of the pulse repetition time, which leads to a constructive interplay

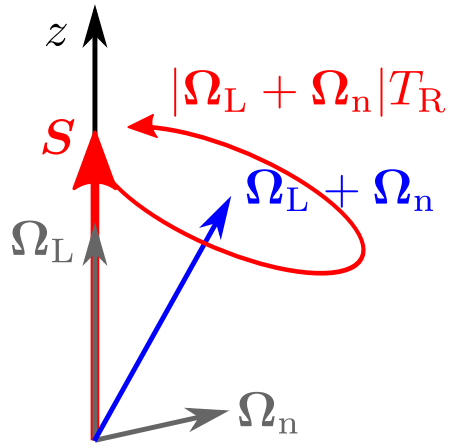

Figure 8.8: Illustration of the mechanism leading to RSA in Faraday geometry. The transverse component of the Overhauser field $\mathbf{\Omega}_\mathrm{n}$ tilts the effective field $\mathbf{\Omega}_\mathrm{eff} = \mathbf{\Omega}_\mathrm{n} + \mathbf{\Omega}_\mathrm{L}$ from the z axis, inducing a precession of the spin $\boldsymbol{S}$ with frequency Ω_eff. As a result, the z projection of $\boldsymbol{S}$ oscillates with the same frequency and the amplitude of this oscillation depends on the tilt angle. Thanks to the properties of the pulse (8.6), its application results in RSA for a single QD whenever the PSC (8.25) is fulfilled.

between the spin polarizations induced by consecutive pulses. We label these discrete resonance frequencies by their mode number k. The magnetic fields fulfilling this condition are highlighted as vertical lines in Fig. 8.6(b), perfectly matching the periodicity of the modulations.

In Ref. [137], it is demonstrated that applying a magnetic field that is slightly tilted from the longitudinal configuration reveals RSA in measurements of the PRC. In the setup under study, however, the external field is applied purely along the z axis without any tilt, so the spin component S^z does not precess on average and one expects that no RSA takes place. But in reality, the Overhauser field tilts the resulting effective magnetic field slightly from the z axis in each QD as illustrated in Fig. 8.8. This mechanism renders RSA in Faraday geometry possible under certain conditions. It is the same mechanism that is responsible for the visible oscillations in the time domain of an initially created spin polarization S^z in QDs subjected to a finite, longitudinal magnetic field (see Fig. 3.2). One requirement to observe this effect is that Ω_n and Ω_L are of similar magnitude because the tilt from the z axis vanishes for $\Omega_\mathrm{L} \gg \Omega_\mathrm{n}$. Thus, the effect vanishes for large external magnetic fields, i.e., for large ratios $\Omega_\mathrm{L}\lambda/\omega_\mathrm{n}$ because $\omega_\mathrm{n}/\lambda$ characterizes the transverse component of the Overhauser field in the ensemble of QDs according to its distribution (8.4). Typically, the random Overhauser field smears out the RSA modes so that they are not visible, e.g., for the n-doped case where ω_n is quite large. Hence, only a very small modulation is discernible in Fig. 8.4(a) for $Q = 0$.

A rough estimate of a condition under which RSA in Faraday geometry should be observable is $\omega_\mathrm{n} \lesssim \sqrt{2}\pi/T_\mathrm{R}$. Otherwise, the potential RSA modes are too broad. This estimate is motivated by Ref. [135], where the regimes for the standard RSA

and spin mode locking in Voigt geometry are established. Consequently, decreasing the pulse repetition time T_R should lead to an increase of the visibility of the RSA modes. Indeed, we will see in Chap. 9 that this is the guiding idea to reveal RSA in Faraday geometry under experimental conditions.

As explained above, the RSA modes result from the transverse components Ω_n^x and Ω_n^y of the Overhauser field. If these components are small because of a large anisotropy degree λ [see Eq. (8.4)], the RSA modes are less pronounced. Figure 8.9 shows the spin polarization in the steady-state limit for π pulses ($Q = 0$) for various anisotropies of the hyperfine interaction λ. For comparison, vertical lines represent the values of B_ext that fulfill the PSC (8.24), which perfectly match the positions of the periodic maxima. As expected, smaller values of λ are favorable to observe the RSA modes because the transverse components of the Overhauser field are less suppressed.

A tiny shift of the peak position from the PSC (8.24) can be discerned for the first maximum at $|k| = 1$. This deviation is expected for small magnetic fields. For each

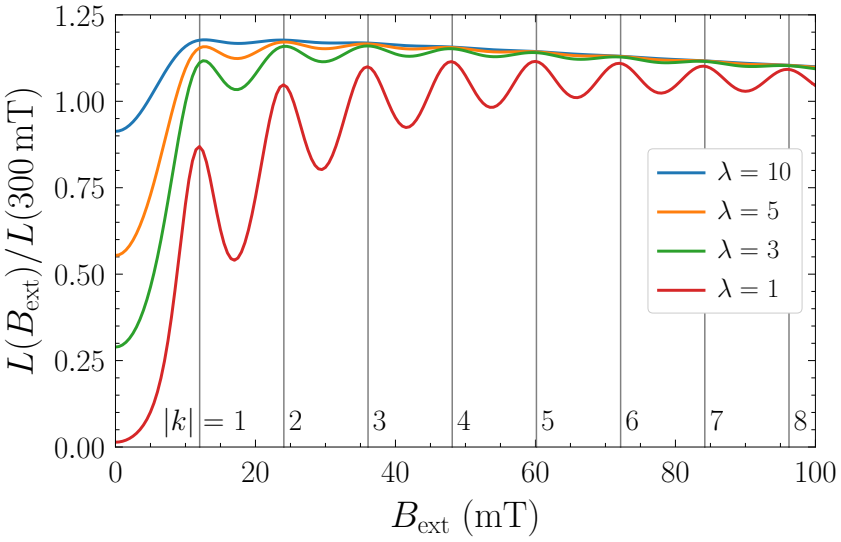

Figure 8.9: PRCs in the steady-state limit showing RSA in Faraday geometry for various anisotropy degrees λ while using π pulses with $Q = 0$. The other parameters are representative for p-doped QDs (see Table 8.1). The vertical lines represent the values of B_ext that fulfill the PSC (8.24) for the mode numbers $|k|$.

individual QD of the ensemble, the relevant PSC is given by

$$\Omega_{\text{eff}} T_{\text{R}} = |\mathbf{\Omega}_{\text{L}} + \mathbf{\Omega}_{\text{n}}| T_{\text{R}} = 2\pi |k| \,, \qquad k \in \mathbb{Z} \,, \tag{8.25}$$

because the precession takes place about the complete magnetic field consisting of the external magnetic field plus the Overhauser field. Assuming that the external field is nevertheless larger than the characteristic value ω_{n} of the Overhauser field, $\Omega_{\text{L}} \gtrsim \omega_{\text{n}}$, one can expand the modulus in Eq. (8.25) in powers of ω_{n} and average the resulting expression over the distribution (8.4), yielding

$$\overline{|\mathbf{\Omega}_{\text{L}} + \mathbf{\Omega}_{\text{n}}|} = \Omega_{\text{L}} \left[1 + \frac{\omega_{\text{n}}^2}{2\lambda^2 \Omega_{\text{L}}^2} + \mathcal{O}\left(\frac{\omega_{\text{n}}^4}{\Omega_{\text{L}}^4} \right) \right] . \tag{8.26}$$

Contributions from odd orders cancel because of the symmetry of the distribution (8.4). Qualitatively, the expansion implies that the real resonance frequencies are actually slightly larger than the bare resonant Larmor frequency resulting from the PSC (8.24). This slight deviation can be discerned in the vicinity of the mode $|k| = 1$ in Fig. 8.9. For larger magnetic fields, the deviation vanishes as described by the expansion.

Resonant spin amplification is less pronounced for weaker pulses corresponding to larger values of Q. This can be easily understood because strong pump pulses generate a spin polarization parallel to the z axis as can be seen from the pulse relation (8.6) for $Q \to 0$. The consequence is the resonant buildup of spin polarization in a single QD whenever the PSC (8.25) is fulfilled. But for weaker pulses corresponding to larger values of Q, the resonant buildup of the spin polarization has less of an effect because weak pulses do not push the spin polarization towards the z axis. Since rather weak pulses were applied for the PRC measurements presented in Ref. [93], it is no surprise that indications of RSA are not observed.

We stress that the assumption of a static Overhauser field does not restrict the observation of RSA in Faraday geometry. The nuclear spin dynamics in QDs with $10^4 - 10^6$ effectively coupled nuclear spins takes place on a timescale of the order of 100 to 1000 ns [104], which is much larger than the pulse repetition time T_{R}. Hence, it has no noticeable effect on the resonant buildup of the spin polarization and it does not lead to a further smearing of the RSA modes either.

The effect of RSA in Faraday geometry is not restricted to ensembles of QDs. We

recall that the averaging over the Overhauser field distribution (8.4) models two physical scenarios: (i) the average over a homogeneous ensemble of QDs and (ii) the time average in an experiment where the signal is probed over a time much longer than the typical correlation time of the nuclei. Since single QDs can be modeled by the latter scenario, the effect should also take place for them.

From a methodical perspective, RSA in Faraday geometry opens the possibility to measure the longitudinal g factor g_z of the resident charge carriers in small to intermediate magnetic fields[3] with high accuracy. It is the only uncontrollable parameter appearing in the PSC (8.24) so that g_z can be determined from the periodicity of the RSA modes. In Chap. 9, we will see that this novel effect can indeed be measured and modeled by theory.

8.4 Chapter conclusion

We have developed an extension of the theory of Ref. [125] to describe the spin inertia and polarization recovery effect for localized charge carriers in singly-charged QDs while taking into account a finite pump power and also nonresonant pump pulses. In strong longitudinal magnetic fields, the spin dynamics can be described by a single effective spin relaxation time that shortens if the pump power is increased. In this limit, the dependence of the spin polarization on the pump power can help to determine the ratio of the trion spin relaxation time and the radiative trion lifetime.

The dependence of the spin polarization on the longitudinal magnetic field, called the polarization recovery curve, can be V- or M-like for the parameters generic for n- or p-doped QDs, respectively. For small modulation frequencies, an increase of the pump power leads to a gradual change of the shape from M-like to V-like. Furthermore, the application of strong pump pulses can increase the width of the zero-field minimum of the PRC if the degree of spin polarization is large, e.g., for small modulation frequencies. Vice versa, since the modulation frequency has a strong impact on the degree of spin polarization, this broadening is also visible when reducing the modulation frequency while applying strong pulses. All these effects result from the spin polarization approaching the saturation limit where all

[3]The effective g factor in a real system may change at large magnetic fields as a result of band mixing.

spins point in the same direction. But it needs to be stressed that they also appear when the saturation limit is fairly far away. The effects vanish only in the limit where the degree of spin polarization is very small.

Furthermore, the application of nonresonant pulses leads to an increase of the spin polarization at zero magnetic field relative to its value at large field. Notably, this generalizes the established ratio 1/3 appearing under equilibrium conditions. Generally, also for resonant pulses, the depth of the zero-field minimum of the PRC depends strongly on the pumping strength. The ratio 1/3 is approximately retained for n-doped QDs in the limit of very weak pulses.

Finally, we have predicted the emergence of resonant spin amplification in Faraday geometry. This effect, which is enabled by the transverse component of the Overhauser field, manifests itself as a periodic modulation of the spin polarization studied as a function of the external magnetic field. It is a clear identifying characteristic of the commensurability of the Larmor precession with the periodic pumping. In the following chapter, this novel effect is analyzed in more detail. There, we analyze recent measurements performed on an inhomogeneous ensemble of QDs, which demonstrate its realization.

The observation of RSA in our calculations highlights the importance of commensurability also in Faraday geometry. Hence, it is an interesting subject for future research to investigate whether effects similar to nuclear focusing can emerge. Obviously, such a study requires the inclusion of the nuclear spin dynamics in the simulations, which is beyond the scope of this thesis.

Chapter 9

Resonant spin amplification in Faraday geometry in inhomogeneous ensembles of quantum dots

The g factor is one of the most basic parameters for the spin dynamics in QDs or generally in semiconductor nanostructures. By means of the standard RSA method [136], it is possible to measure its transverse component with high accuracy. This technique is based on the pump-probe technique (see Sec. 2.3) while a magnetic field is applied perpendicular to the optical axis (Voigt geometry). As a consequence of RSA, the spin polarization is resonantly amplified whenever the Larmor period is multiple integer of the laser repetition time [77]. The RSA effect is not only suitable to determine the transverse g factor but also to evaluate parameters such as its spread, spin relaxation times, or the strength of the hyperfine interaction [267]. This method has been successfully applied to a variety of systems, e.g., bulk GaAs [136], III-V and II-VI quantum wells and epilayers [137, 265, 268], and also QDs [133, 135].

In Faraday geometry where the magnetic field is parallel to the optical axis, there is no spin precession of the resident charge carriers on average so that it is difficult to determine their g factor. Up to now, it needs to be measured indirectly: First, the transverse g factor is determined in Voigt geometry, e.g., by standard RSA [136] or from time-resolved measurement of quantum beats [23, 132, 269]. Repeating the measurements in an oblique geometry (e.g., tilted by 45°) gives access to the longitudinal g factor [137, 269]. But the method suggested in Sec. 8.3.5 based on RSA in Faraday geometry can be used to measure the longitudinal g factor *directly* and with high accuracy.

In this chapter, we model and analyze recent measurements, which confirm experimentally that RSA can indeed emerge in Faraday geometry for an ensemble of n-doped InGaAs QDs.[1] For this purpose, the model used in Chap. 8 is extended to account for inhomogeneous ensembles of QDs based on the formalism of Ref. [113]. We analyze results of experiments performed for two different samples of n-doped InGaAs QDs. Sample B is the n-doped QD ensemble studied in Ref. [93], whose parameters also motivated the choice of parameters in Chap. 8. Sample A is a QD ensemble with a stronger hyperfine interaction and longer spin relaxation times.

9.1 Modeling an inhomogeneous ensemble of quantum dots

We describe the spin dynamics in the n-doped QDs by the phenomenological model introduced in Sec. 8.1. To account for the experimental situation of an inhomogeneous ensemble of QDs, we apply the formalism of Ref. [113], which allows for a detailed description of the pumping and probing of the spins as a function of the trion transition energy. Since a pulse repetition time of $T_\mathrm{R} = 1\,\mathrm{ns}$ is used in the experiments (instead of the common choice $T_\mathrm{R} = 13.2\,\mathrm{ns}$), we need to account for trion states that have a finite population at the arrival of a pump pulse. For this reason, we resort to the pulse relations (2.9), (2.10), and (2.11), which are derived in Sec. 2.2.2 and generalize the pulse relations derived in Ref. [113] to this situation.

For n-doped QDs, it is typically sufficient to neglect the precession term in the equation of motion (8.3). The reason is that in this case, the trion pseudospin stems from the heavy hole with weak and anisotropic hyperfine interaction, i.e., its contribution to the generation rate of spin polarization is minor [125]. The ensemble of InGaAs QDs studied in Sec. 9.3 (Sample B) is well characterized [93]. This is not the case for Sample A so that more parameters need to be fitted. Hence, we neglect the unimportant precession term in Eq. (8.3) in the analysis of Sample A but include it for Sample B for which the relevant parameters are already known. Despite the better characterization of Sample B, the results for Sample A are more suitable to demonstrate the effect of RSA in Faraday geometry because the stronger hyperfine interaction leads to larger number of visible RSA modes.

[1] This chapter is based on the author's publication [94], ©2021 American Physical Society. The author performed the numerical simulations to analyze the experimental data and to study the RSA visibility. The analysis of the spin inertia dependence was performed by A. Greilich. The experiments were performed by E. Evers, V. Nedelea, and A. Greilich.

In our model calculations presented in Sec. 9.3 and 9.2, we use the parameters listed in Table 9.1. The two fit parameters varied to reproduce the experimental results for Sample B are the longitudinal electronic g factor, which is determined by the positions of the experimentally observed RSA modes, and the trion spin relaxation time τ_s^T (estimated in Ref. [93] to be $\tau_s^T < 1000\,\mathrm{ns}$). For Sample A, the longitudinal electronic g factor is also determined by the positions of the RSA modes. The spin relaxation time τ_s is determined from measurements of the spin inertia, the value of ω_n is determined such that the width of the RSA modes fits the experimental results.

It should be mentioned that the simulated PRCs are fairly sensitive to the choice of the trion spin relaxation time τ_s^T and of the effective pulse area Θ entering in the pulse relations, and both quantities can only be estimated. It is possible that there are other combinations that yield a similarly good agreement between experiment and theory.

Table 9.1: Parameters and their physical meaning used in the model calculations for the two different n-doped InGaAs QD ensembles. The parameters for Sample B are based on the previous sample characterization of Ref. [93].

Parameter	Value	Physical meaning
Sample A:		
$\omega_n/(2\pi)$	140 MHz	hyperfine interaction strength (electron)
τ_s	22 μs	spin relaxation time (electron)
τ_s^T	0.45 μs	spin relaxation time (hole in trion)
g_z	−0.69	longitudinal g factor (electron)
Sample B:		
$\omega_n/(2\pi)$	70 MHz	hyperfine interaction strength (electron)
$\omega_n^T/(2\pi)$	16 MHz	hyperfine interaction strength (hole in trion)
λ^T	5	hyperfine interaction anisotropy (hole in trion)
τ_s	1.3 μs	spin relaxation time (electron)
τ_s^T	0.06 μs	spin relaxation time (hole in trion)
g_z	−0.64	longitudinal g factor (electron)
g_z^T	−0.45	longitudinal g factor (hole in trion)
Common parameters:		
τ_0	0.4 ns	radiative trion lifetime
λ	1	hyperfine interaction anisotropy (electron)

9.1.1 Inhomogeneous ensemble of quantum dots

All QDs in a real ensemble are slightly different, e.g., in size, shape, composition, and strain. In particular, as a consequence of the inhomogeneous broadening of the trion transition, each QD of the ensemble has a slightly different trion transition energy E_T. We model this situation by assuming that the transition energies follow the normal distribution

$$p(E_\mathrm{T}) = \frac{1}{\sqrt{2\pi}\Delta E_\mathrm{T}} \exp\left[-\frac{1}{2}\left(\frac{E_\mathrm{T} - \overline{E_\mathrm{T}}}{\Delta E_\mathrm{T}}\right)^2\right] \tag{9.1}$$

with mean value $\overline{E_\mathrm{T}}$ and variance $(\Delta E_\mathrm{T})^2$. The situation implies that for a fixed energy of the pump pulses, each QD of the ensemble is pumped with a different efficiency because of the inevitable detuning between the trion transition and the pump energy. Eventually, this can be described by an associated pair $\{Q, \Phi\}$ of the pulse parameters for each QD. Similarly, different QDs have a different contribution to the probed Faraday ellipticity or rotation. Tuning the pump and probe energies allows one to analyze different subsets of the QD ensemble. For more details, we refer the interested reader to Ref. [113], where this formalism is established.

9.1.2 Pulse parameters for a single quantum dot

We now turn to the pulse parameter pair $\{Q, \Phi\}$ for a single QD, which must be known to apply the pump pulse relations (2.9), (2.10), and (2.11) for a given detuning. The energies of the pump and probe pulses are denoted as E_pu and E_pr, respectively. In the experiments to be analyzed, a degenerate pump-probe setup is used so that $E_\mathrm{pu} = E_\mathrm{pr}$. The duration of the pulses is much smaller than all other time scales of the system. The finite spectral width of the pulses is accounted for by the inverse pulse duration τ_p^{-1}, i.e., we assume that the pulses are Fourier-transform limited. For simplicity, we model the pulses to have a hyperbolic secant shape [270] because for this case, analytical expressions for the pulse parameters Q and Φ can be derived [113]. The envelope of the electric field of such a pulse with duration τ_p has the form

$$f(t) = \mu \operatorname{sech}\left(\pi \frac{t}{\tau_\mathrm{p}}\right), \tag{9.2}$$

where μ is a measure for the electric field strength. In the experiments, the value of μ is not known. Furthermore, the actual pulse shape is a Gaussian and the pulses are not perfectly Fourier-transform limited. However, the shape of a hyperbolic secant is qualitatively very similar to a Gaussian, with slightly more pronounced tails if the FWHMs are identical.

In the simulations, we use the pulse duration $\tau_\mathrm{p} = 1.3\,\mathrm{ps}$. The proper value to account for the FWHM of 1.3 meV of the photoluminescence intensity of the pulses, which is proportional to $|f(\omega)|^2$, would actually be $\tau_\mathrm{p} \approx 1.8\,\mathrm{ps}$. But we have checked that the difference between the results is only of statistical nature and therefore negligible.[2] This value corresponds to the minimal pulse duration that results from the minimal time-bandwidth product $\delta t \delta\omega \approx 1.978$ for a pulse with an intensity profile $|f(x)|^2 \propto \mathrm{sech}^2(x/X)$, where δt and $\delta\omega$ are the FWHM in the time ($x = t$) and frequency ($x = \omega$) domain, respectively [270]. The FWHM of $|f(x)|^2$ is $\delta x \approx 1.763X$.

As mentioned above, the pulse parameters Q and Φ can be calculated analytically for pulses with a hyperbolic secant shape. For the corresponding envelope $f(t)$ of the electric field given in Eq. (9.2), it follows [113]

$$Q = \sqrt{1 - \frac{\sin^2(\Theta/2)}{\cosh^2(\pi y)}}\,, \tag{9.3a}$$

$$\Phi = \arg\left[\frac{\Gamma^2\left(\frac{1}{2} - \mathrm{i}y\right)}{\Gamma\left(\frac{1}{2} - \frac{\Theta}{2\pi} - \mathrm{i}y\right)\Gamma\left(\frac{1}{2} + \frac{\Theta}{2\pi} - \mathrm{i}y\right)}\right], \tag{9.3b}$$

with the Gamma function $\Gamma(z)$, the effective pulse area

$$\Theta = 2\int_{-\infty}^{\infty} f(t)\,\mathrm{d}t = 2\mu\tau_\mathrm{p} \tag{9.4}$$

and the dimensionless detuning of the pump pulse

$$y = \frac{(E_\mathrm{pu} - E_\mathrm{T})\tau_\mathrm{p}}{2\pi\hbar}\,. \tag{9.5}$$

The parameters Q and Φ along with the probability $1 - Q^2$ to excite a trion are plotted in Fig. 9.1 as a function of the dimensionless pump detuning y for various

[2] The simulations are computationally too expensive to redo all calculations.

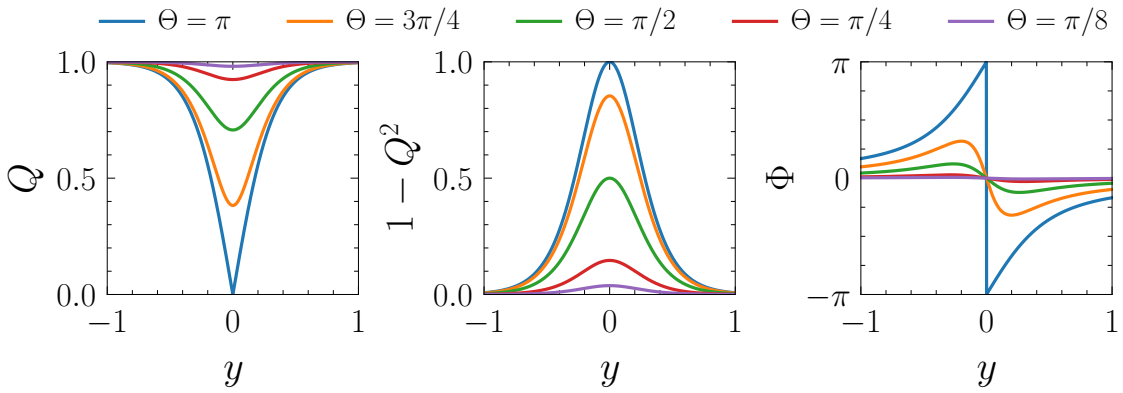

Figure 9.1: Pump pulse parameters Q and Φ resulting from Eq. (9.3) along with the probability $1-Q^2$ to excite a trion as a function of the dimensionless pump detuning y defined in Eq. (9.5) for various effective pulse areas Θ.

effective pulse areas Θ. The value $1-Q^2$ has a major influence on the spin polarization after a pulse as can be seen from Eq. (2.9c). Pulses with $\Theta = \pi$ (we do not consider $\Theta > \pi$ here) without detuning ($y = 0$) are most efficient because this combination yields $Q = 0$. This is, of course, only a theoretical consideration because $E_{\mathrm{pu}} = E_{\mathrm{T}}$ will never be exactly fulfilled for an inhomogeneous ensemble of QDs. The rotation induced by the pulse also depends on the pulse area, with a decreasing rotation angle Φ for small pulse areas. Pulses with a strong detuning from the trion transition energy barely influence the spin polarization in the QD because $Q \to 1$ and $\Phi \to 0$ results in this case.

For small pump powers, the pulse area scales like $\Theta \propto \sqrt{P_{\mathrm{pu}}}$ [23, 113, 135]. If the pulse area at a some pump power is already known from previous experiments, this scaling can be used to estimate the effective pulse area prevalent in new experiments.

9.1.3 Probing the Faraday ellipticity and rotation

The Faraday ellipticity and rotation, which are proportional to the spin polarization, can be probed by weak linearly polarized pulses. Depending on the energy E_{pr} of the probe pulse, different subsets of the QD ensemble are probed, i.e., the contribution of a single QD to the probed signal depends on the detuning of the probe pulse from the trion transition energy E_{T}. In the experiments to be analyzed, the energy of pump and probe are degenerate, $E_{\mathrm{pu}} = E_{\mathrm{pr}}$.

For a single QD, the Faraday ellipticity $\mathcal{E}$ and rotation $\mathcal{R}$ are proportional to the spin polarization $J^z - S^z$ weighted by an additional function that depends on the probe detuning and pulse duration [113],

$$\mathcal{E} \propto (J^z - S^z)\,\mathrm{Re}\,G(E_{\mathrm{pr}} - E_{\mathrm{T}}, \tau_{\mathrm{p}})\,, \tag{9.6a}$$

$$\mathcal{R} \propto (J^z - S^z)\,\mathrm{Im}\,G(E_{\mathrm{pr}} - E_{\mathrm{T}}, \tau_{\mathrm{p}})\,, \tag{9.6b}$$

with

$$G(E_{\mathrm{pr}} - E_{\mathrm{T}}, \tau_{\mathrm{p}}) = \frac{\tau_{\mathrm{p}}^2}{\pi^2}\,\zeta\left(2,\, \frac{1}{2} - \mathrm{i}\frac{(E_{\mathrm{pr}} - E_{\mathrm{T}})\tau_{\mathrm{p}}}{2\pi\hbar}\right), \tag{9.7}$$

where $\zeta(z)$ is the Hurwitz Zeta function. The prefactors in Eq. (9.6) are identical but sample dependent. Their exact values do not matter for our considerations because we scale the simulated PRCs to the experimental data by a global factor.

With respect to the probe detuning $E_{\mathrm{pr}} - E_{\mathrm{T}}$, the real part of $G(E_{\mathrm{pr}} - E_{\mathrm{T}}, \tau_{\mathrm{p}})$ is an even function, whereas the imaginary part is an odd function as can be seen in Fig. 9.2. Clearly, the Faraday ellipticity has the largest response if the spin polarization in QD is probed without detuning. In contrast, the Faraday rotation yields zero in this case; its response is the largest for a small but finite probe detuning. In an inhomogeneous ensemble of QDs, however, it is inevitable that each QD is probed (and also pumped) with a finite detuning. For the Faraday rotation, the situation becomes more complicated because the fact that $\mathrm{Im}\,G$ is an odd function results in contributions with opposite signs for opposite detunings. This results in

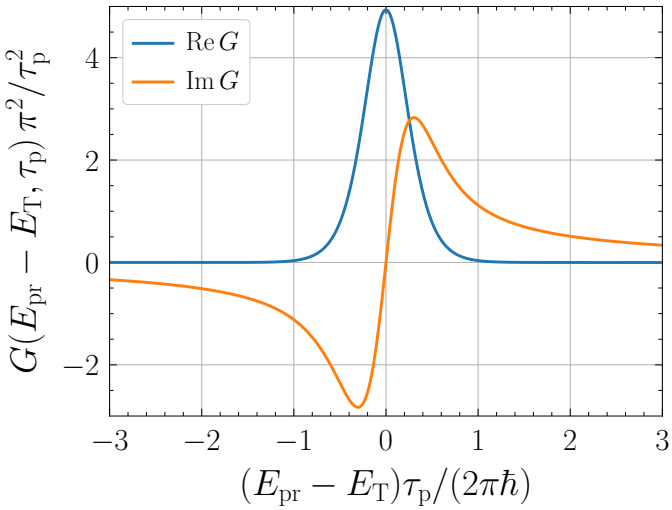

Figure 9.2: Visualization of the real and imaginary part of the function $G(E_{\mathrm{pr}} - E_{\mathrm{T}}, \tau_{\mathrm{p}})$ given by Eq. (9.7). The real part is an even function of the probe detuning, whereas the imaginary part is an odd function.

a certain cancellation effect that depends on the shape of the distribution $p(E_\mathrm{T})$ of the trion transition energies (modeled as a normal distribution), on the difference between the probe energy E_pr and the mean trion transition energy $\overline{E_\mathrm{T}}$, on the pump energy E_pu (determines which subset of the QD ensemble is excited), and also on the spectral pulse width proportional to τ_p^{-1}. For instance, the Faraday rotation yields zero if $E_\mathrm{pr} = E_\mathrm{pu} = \overline{E_\mathrm{T}}$ as a consequence of the symmetry of the assumed normal distribution $p(E_\mathrm{T})$. If $E_\mathrm{pr} = E_\mathrm{pu}$ is shifted to the low or high energy flank of this distribution, there is a finite but small Faraday rotation because the contributions from most but not all QDs cancel out. For this reason, calculating the Faraday rotation numerically is computationally much more expensive than calculating the Faraday ellipticity: The required Monte Carlo sampling suffers from a sign problem because of the cancellation of the probed spin polarizations with opposite signs so that the relative statistical error increases. In the case of a finite pump-probe detuning, this is less of an issue because the spin polarization of the QDs that are pumped with a finite detuning is probed. In this chapter, however, we only consider degenerate pump-probe setups.

9.1.4 Averaging over the inhomogeneous ensemble

Accounting for an inhomogeneous ensemble of QDs requires the calculation of two averages. First, we have to average over the random Overhauser field described by the distribution (8.4). Second, we have to average over the distribution (9.1) of the trion transition energies. If not stated otherwise, we calculate the ensemble average over $M = 2.6 \times 10^5$ (Sample A) or $M = 5 \times 10^6$ (Sample B) independent trajectories starting from random initial conditions that are sampled from these two distributions. Numerically, this is extremely expensive and requires massive parallelization; see Sec. 3.3.3 for general remarks on the numerical treatment. The parameters $\overline{E_\mathrm{T}}$, ΔE_T, E_pu, and E_pr are obtained from fits to the photoluminescence spectra.

As discussed above, the Faraday ellipticity and rotation reveal the spin dynamics of different subsets of the QD ensemble. In the experiments performed on Sample B (Sec. 9.3), a degenerate pump-probe setup is used with the pulse energy shifted by 2.4 meV to the low-energy flank of the average trion transition energy of about 1.3908 eV (see Fig. 9.9). In this case, the probed Faraday rotation effectively reveals the spin dynamics of the QDs that are pumped by detuned pulses for which the

pumping strength is rather weak (large Q). However, as demonstrated in Sec. 8.3.4, the spin rotation induced by detuned pulses can lead to an increase of the visibility of RSA in Faraday geometry, which could potentially counter the detrimental influence of the reduced pumping strength.

9.1.5 Signal accumulation in the modulated pulse scheme

In the experiments, the helicity of the pump pulses is modulated with frequency f_m. As discussed in Sec. 8.3.1, this modulation scheme results in an alternating spin polarization that is zero on average if it is simply integrated. For this reason, the probed signal is also modulated. Analogously to spin inertia signal defined in Eq. (8.1), the actually measured Faraday ellipticity E or rotation R is given by [125, 159]

$$E(f_\mathrm{m}) = \frac{1}{n_\mathrm{p}} \left| \sum_{k=1}^{n_\mathrm{p}} \overline{\mathcal{E}(kT_\mathrm{R} + \tau_\mathrm{d})}\, \mathrm{e}^{\mathrm{i}2\pi f_\mathrm{m}(kT_\mathrm{R}+\tau_\mathrm{d})} \right| , \tag{9.8a}$$

$$R(f_\mathrm{m}) = \frac{1}{n_\mathrm{p}} \left| \sum_{k=1}^{n_\mathrm{p}} \overline{\mathcal{R}(kT_\mathrm{R} + \tau_\mathrm{d})}\, \mathrm{e}^{\mathrm{i}2\pi f_\mathrm{m}(kT_\mathrm{R}+\tau_\mathrm{d})} \right| . \tag{9.8b}$$

These expressions represent the accumulation of the probed signal for the ensemble of QDs (ensemble average denoted by the overline), modulated with frequency f_m and averaged over the number of applied pulses $n_\mathrm{p} \gg 1$. The spin polarization is probed slightly before the arrival of each pump pulse with a negative delay $\tau_\mathrm{d} = -60\,\mathrm{ps}$ (Sample A) or $-50\,\mathrm{ps}$ (Sample B).

In the numerical simulations, it is again not feasible to calculate the spin dynamics for more than a few modulation periods $1/f_\mathrm{m}$, whereas in the experiments, many modulation periods take place (see the discussion in Sec. 8.2.1). However, for small enough modulation frequencies as studied in this chapter, it is sufficient to simulate only two modulation periods and then to calculate E or F by summing only over the second (last) period. The first period is neglected because it shows a transient behavior as discussed in Sec. 8.3.1.

9.2 Analysis of Sample A

In the following two sections, experiments [94] performed on two different samples of InGaAs QDs are analyzed. First, we analyze the experiments performed on Sample A. The important experimental details for the theoretical analysis are summarized in the following.

9.2.1 Experimental details

Sample A consists of 20 layers of InGaAs QDs that are separated by 70 nm barriers of GaAs and grown by molecular beam epitaxy on an (100)-oriented GaAs substrate. The QD density per layer is $10^{10}\,\mathrm{cm}^{-2}$. On average, each QD is singly-charged by an electron, which is provided by a δ-doping layer of Si 16 nm above each QD layer. The sample was thermally annealed at 880 °C for 30 s, which homogenized the QD size distribution and shifted the average trion transition energy to 1.3662 eV. The photoluminescence spectrum for this sample is shown in Fig. 9.3.

The sample is cooled to 5.3 K. An external magnetic field $B_{\mathrm{ext}}\boldsymbol{e}_z$ is applied in the direction of light incidence, i.e., along the optical z axis with an accuracy of 2° (Faraday geometry). Periodic laser pulses with a mean photon energy of $E_{\mathrm{pu}} = E_{\mathrm{pr}} = 1.3655\,\mathrm{eV}$ and a FWHM of 1.3 meV are applied to the sample. The pulses are emitted with a repetition frequency of 1 GHz, corresponding to a repetition time of $T_{\mathrm{R}} = 1\,\mathrm{ns}$. They are split into degenerate pump and probe pulses,

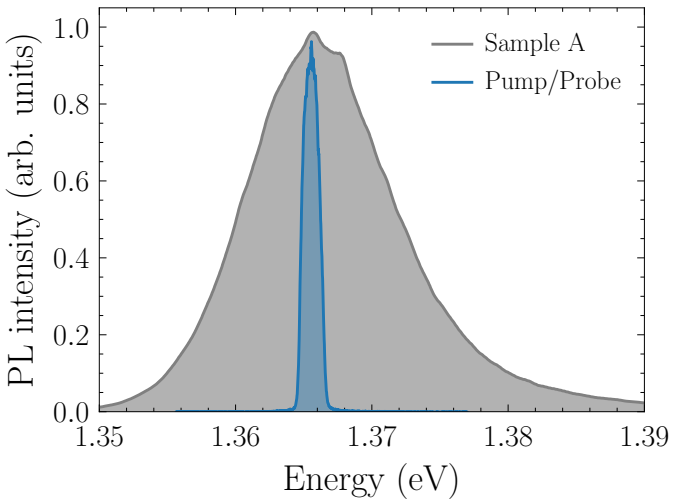

Figure 9.3: Sample A: Photoluminescence (PL) spectrum of the InGaAs QD ensemble (gray) at temperature $T = 5.3\,\mathrm{K}$ along with the spectrum of the laser used in the pump-probe experiments (blue). The pump and probe pulses are degenerate in photon energy.

which are shifted by 0.7 meV to the low-energy flank of the QD photoluminescence spectrum (see Fig. 9.3 for a visualization). A double modulation scheme is used to reduce the noise arising from separate detection of the scattered pump and probe light. The helicity of the pump is modulated between σ^+ and σ^- with frequency $f_\mathrm{m} = 0.1 - 10^4$ kHz, preventing the buildup of significant dynamic nuclear polarization [271]. The Faraday ellipticity amplitude of the linearly-polarized probe pulses is measured at a delay of $\tau_\mathrm{d} = -60$ ps, i.e., slightly before the arrival of the pump pulses. Further details on the experimental setup are given in Ref. [94].

9.2.2 Spin inertia dependence

As described in detail in Chap. 8, measurements of the spin inertia dependence yield the effective spin relaxation time τ_s^* of the resident charge carrier. Figure 9.4 shows the dependence of the measured Faraday ellipticity on the pump modulation frequency f_m at a magnetic field of $B_\mathrm{ext} = 400$ mT while using a pump power of $P_\mathrm{pu} = 7$ mW [94]. Typically, the spin inertia dependence can be described

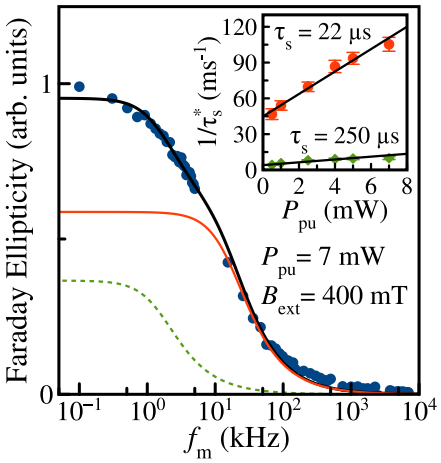

Figure 9.4: Spin inertia dependence measured for Sample A: Faraday ellipticity as a function of the pump modulation frequency f_m at a magnetic field of $B_\mathrm{ext} = 400$ mT for a pump power of $P_\mathrm{pu} = 7$ mW measured with a pump-probe delay of -60 ps (blue circles). The black line represents the fit using two-components of Eq. (8.14). The contribution of each component are shown by the solid-orange and dashed-green curves. The inset shows the power dependence of the two corresponding inverse effective spin lifetimes $1/\tau_\mathrm{s}^*$. A linear extrapolation to zero power (black lines) yields $\tau_\mathrm{s} = (22 \pm 1)\,\mu$s (orange) and $\tau_\mathrm{s} = (250 \pm 27)\,\mu$s (green) for the intrinsic spin relaxation times. The figure, created by A. Greilich, is reprinted with permission from Ref. [94], ©2021 American Physical Society.

by Eq. (8.14), but such a fit does not work properly here. Probably, there is a continuous distribution of spin relaxation times caused by the inhomogeneous character of the QD ensemble, but this situation is difficult to describe by our model in which only a single spin relaxation time enters for the resident charge carrier. Hence, we use a two-component fit of the spin inertia dependence, which works much better than a single-component fit and captures all effects important for the following analysis. Concretely, we assume that the ensemble can be described by two subsets of electrons, each following the spin inertia dependence (8.14). As demonstrated in Fig. 9.4, this two-component fit describes the measured dependence fairly well. Both components are described by different effective spin relaxation times τ_s^*, which are plotted in the inset as a function of the pump power P_{pu}. A linear extrapolation to zero power yields the intrinsic spin relaxation times $\tau_s = (22 \pm 1)\,\mu s$ (orange) and $\tau_s = (250 \pm 27)\,\mu s$ (green).

Nevertheless, the straightforward application of our model is only possible for a single component, i.e., a single spin relaxation time.[3] But for pump modulation frequencies $f_m \geq 5\,\mathrm{kHz}$, only the shorter living sub-ensemble with $\tau_s = 22\,\mu s$ has a significant contribution. For this reason, we focus on this regime in the following and use $\tau_s = 22\,\mu s$ in the simulations.

9.2.3 Polarization recovery curves

Let us turn to the PRCs displayed in Fig. 9.5, which were measured using various pump powers at $f_m = 10\,\mathrm{kHz}$. The colored data depicts the measured Faraday ellipticity E, the black curves represent the simulated PRCs. All PRCs have a V-like shape, which is typical for n-doped QDs, and generally, the spin polarization increases if a larger pump power is used. As predicted in Chap. 8, the width of the zero-field minimum broadens when stronger pulses are applied so that a larger magnetic field is required to reach saturation. The characteristic frequency ω_n, which describes the strength of the hyperfine interaction of the electron spins, is determined to be $\omega_n/(2\pi) = 140\,\mathrm{MHz}$ (equivalent to a magnetic field of 14.5 mT). This value is obtained by fitting simulated PRCS to the measured ones. Since there appear to be contributions from resident or photoexcited holes in the experimental data at small magnetic fields (discussed below), ω_n cannot be deduced reliably from

[3] Both components could be simulated separately, but it requires to know their contribution to the joint signal. This could be estimated based on the fit parameters.

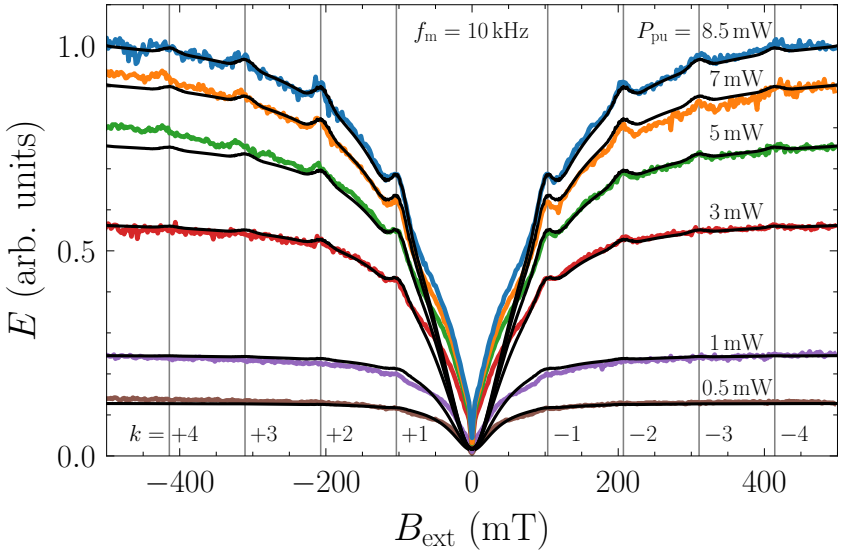

Figure 9.5: PRCs measured and simulated for Sample A using different pump powers P_{pu} (given next to the curves) at a pump modulation frequency of $f_m = 10\,\mathrm{kHz}$. The colored data depicts the experimentally measured Faraday ellipticity E, the smooth black curves represent the corresponding simulated PRCs. The pulse area in the simulations is chosen to fit the experimentally obtained power dependence of the Faraday ellipticity at large magnetic field ($\Theta = 0.07\pi$ at $P\mathrm{pu} = 8.5\,\mathrm{mW}$). The positions of the small peaks visible in the PRCs for larger pump powers match the positions resulting from the PSC (9.9) for the kth RSA modes (vertical gray lines).

the width of the zero-field minimum. For this reason, ω_n is tuned such that the simulated PRCs reproduce the width of the RSA modes, which appears to be robust against variations of the other parameters.

Most strikingly, there are small additional peaks in the PRCs at certain values of the magnetic field for large pump powers. They are the result of RSA in Faraday geometry and appear at magnetic fields B_{ext} that fulfill the PSC

$$\Omega_L T_R = 2\pi|k|\,, \qquad k \in \mathbb{Z}\,, \tag{9.9}$$

where $\Omega_L = \mu_B|g_z B_{ext}|\hbar^{-1}$ is the electronic Larmor frequency. These discrete resonance frequencies are multiples of the laser repetition frequency $\omega_R = 2\pi/T_R$; we label them by their mode number k. The corresponding magnetic fields are highlighted in Fig. 9.5 as vertical lines. Generally, the amplitude of the peaks decreases for larger ratios $\Omega_L\lambda/\omega_n$ as explained in Sec. 8.3.5. This behavior is also evident in Fig. 9.5 for both experiment and theory. Importantly, the mode positions are

solely determined by the longitudinal electronic g factor $|g_z|$. While we cannot determine its sign from this effect, we know that the longitudinal g factor is negative in similar InGaAs QDs [132]. By taking all peak positions into account, we obtain $g_z = -0.69 \pm 0.01$. For comparison, the transverse g factor of the electrons in this sample amounts to $g_\perp = -0.599 \pm 0.001$ [94].

The numerical simulations, depicted by the smooth black curves in Fig. 9.5, reproduce the experimental data very well for magnetic fields $|B_{\mathrm{ext}}| \gtrsim 75\,\mathrm{mT}$. The main deviation is found in the regime of small magnetic fields. It has a narrow M-like shape, which is typical for p-doped QD samples [93, 125]. Hence, we attribute the deviation to resident or photoexcited hole spins with weak hyperfine interaction that contribute to the measured Faraday ellipticity. The applied parameters are listed in Table 9.1. The effective pulse area is $\Theta = 0.07\pi$ at a pump power of $P_{\mathrm{pu}} = 8.5\,\mathrm{mW}$; for the other pump powers, the pulse area is adjusted to fit the Faraday ellipticity at large magnetic fields.

9.2.4 Visibility of resonant spin amplification in Faraday geometry

The prerequisites to observe RSA in Faraday geometry are

(i) a strong hyperfine interaction of the resident charge carriers,

(ii) application of strong pump pulses,

(iii) and a laser repetition time T_{R} that on the one hand allows for RSA modes that are separated enough not to overlap significantly, but on the other hand fall into magnetic field ranges where the spin polarization is not yet saturated.

The conditions (i) and (ii) are typically fulfilled for singly-charged n-type InGaAs QDs [19]. For p-type QDs with a strongly anisotropic hyperfine interaction [93, 97, 156–158, 184], the effect is expected to be much harder to observe (see Fig. 8.9). In Sec. 8.3.5, the condition $\omega_{\mathrm{n}} T_{\mathrm{R}} \lesssim \sqrt{2}\pi$ known from standard RSA [135] is mentioned as a first estimate for the realization of RSA in Faraday geometry. Thus, the condition (iii) requires to choose a proper laser source, which is of course interrelated with the condition (i). In the experiments studied here, a laser source that emits pulses with repetition time $T_{\mathrm{R}} = 1\,\mathrm{ns}$ is implemented.

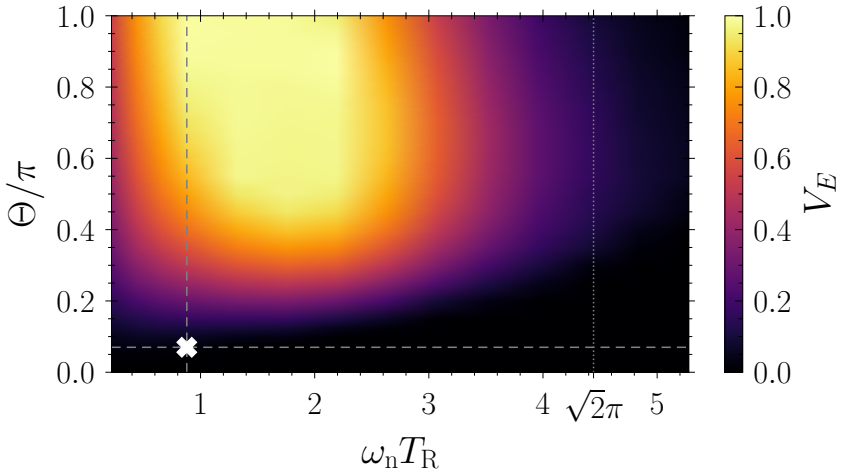

Figure 9.6: Visibility map of the RSA mode $|k| = 1$ of Sample A modeled for detection by Faraday ellipticity. The pump-probe delay is set to $\tau_\mathrm{d} = -0$, the pump modulation frequency to $f_\mathrm{m} = 10\,\mathrm{kHz}$. The white cross marks the experimental conditions for a pump power of $P_\mathrm{pu} = 8.5\,\mathrm{mW}$ ($\Theta = 0.07\pi$) and a pulse repetition time of $T_\mathrm{R} = 1\,\mathrm{ns}$ with $\omega_\mathrm{n}/(2\pi) = 140\,\mathrm{MHz}$. The vertical dotted line marks the value $\omega_\mathrm{n} T_\mathrm{R} = \sqrt{2}\pi$.

To provide a quantitative basis for the prerequisites (ii) and (iii), we study the RSA visibility defined as [126]

$$V_E := \frac{E_\mathrm{max} - E_\mathrm{min}}{E_\mathrm{max}}\,, \tag{9.10}$$

where E_max is the Faraday ellipticity of the first maximum at the RSA mode $|k| = 1$ and E_min denotes the adjacent minimum for larger magnetic field $|B_\mathrm{ext}|$. In order to average out statistical fluctuations in both the model and experiment, we fit polynomials to the region around the $|k| = 1$ mode to calculate its visibility. A map of the RSA visibility in dependence of the pulse area Θ and of the product $\omega_\mathrm{n} T_\mathrm{R}$ is shown in Fig. 9.6. Note that T_R is varied while ω_n is kept constant. The visibility map reveals that the visibility is enhanced by an increase of the pulse area Θ corresponding to stronger pulses. For a too large or too small repetition time T_R, the visibility decreases. The condition $\omega_\mathrm{n} T_\mathrm{R} \lesssim \sqrt{2}\pi$ turns out to be only a first rough estimate; the situation is more complex. Observing RSA in Faraday geometry turns out to be easiest in the intermediate regime $\omega_\mathrm{n} T_\mathrm{R} \sim 1 - 2$. The white cross on the heatmap indicates that the laser source used in the experiments is operating at a too small power, with a resulting visibility of merely $V_E \approx 0.02$ at $P_\mathrm{pu} = 8.5\,\mathrm{mW}$. Under optimal conditions, the visibility could reach unity. For the

commonly used pulse repetition times $T_R = 13.2$ and 6.6 ns ($\omega_n T_R \approx 10.6$ and 5.8), the RSA modes overlap significantly so that they are not visible for Sample A with $\omega_n/(2\pi) = 140$ MHz.

The main obstacle to reach a larger visibility is the small pulse area realized by the pump pulses because a too large pump power would heat the sample too much. Possibly, it could be enhanced by focusing the pump beam on a smaller spot diameter. Yet, we can study the power dependence of the experimentally seen and theoretically modeled visibility in the accessible range. Clearly, as demonstrated in Fig. 9.7(a) by experiment and theory, a reduction of the pump power results in the disappearance of the RSA modes represented by a vanishing visibility.

Remarkably, the RSA visibility can be enhanced by exploiting the spin inertia effect. This is demonstrated in Fig. 9.8 where PRCs for various pump modulation frequencies f_m are plotted using a pump power of $P_{pu} = 8.5$ mW. The PRCs are normalized with respect to the Faraday ellipticity at $B_{ext} = \pm 500$ mT to highlight the enhanced visibility of the RSA modes for larger f_m. The deviation between experiment (colored) and theory (black) for large f_m is related to the fact that

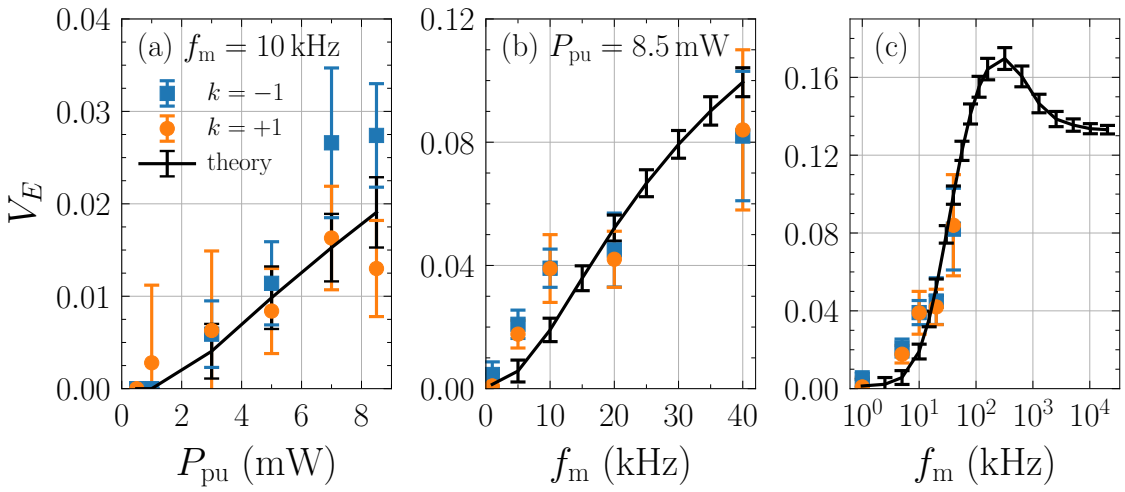

Figure 9.7: RSA visibility V_E of the RSA mode $|k| = 1$ of Sample A as a function of the (a) pump power P_{pu} and (b) pump modulation frequency f_m. The experimental data is plotted as blue squares ($k = -1$) and orange circles ($k = 1$), the theoretical data in black. The error bars represent the root-mean-square deviations of the polynomial fits around the respective RSA mode. Panel (c) shows the visibility for a broader range of modulation frequencies f_m at $P_{pu} = 8.5$ mW.

the spin inertia dependence for the QD sample is not perfectly captured by the monoexponential spin relaxation entering in our model. But generally, the spin inertia effect leads to a reduction of the average degree of spin polarization when increasing the modulation frequency f_m as shown earlier in Fig. 9.4. The key idea is the following: The application of a larger modulation frequency results in a decrease of the average absolute spin polarization and in turn, each pump pulse can better orient the spins along the optical axis because a larger number is disordered. In a nutshell, the spin inertia effect allows one to reduce the influence of saturation limit of the spin polarization where all spins already point along the same direction. Clearly, this limit is detrimental to RSA in Faraday geometry because there are simply less spins to be resonantly amplified. Note also that for a similar reason, a larger modulation frequency results in a narrowing of the zero-field minimum of the PRCs as visible in Fig. 9.8. This behavior is predicted and explained in Chap. 8.

To be more quantitative, we plot the extracted RSA visibility V_E as a function of f_m in Fig. 9.7(b). Clearly, an increase of the modulation frequency results in a significant increase of the visibility V_E, in agreement with the theoretical prediction. For instance, the visibility in the experiment for the $k = +1$ mode using $f_\mathrm{m} = 40\,\mathrm{kHz}$ amounts to $V = 0.08 \pm 0.02$. From Fig. 9.7(c), we assess the maximum possible enhancement that can be achieved by exploiting the spin inertia effect at a pump

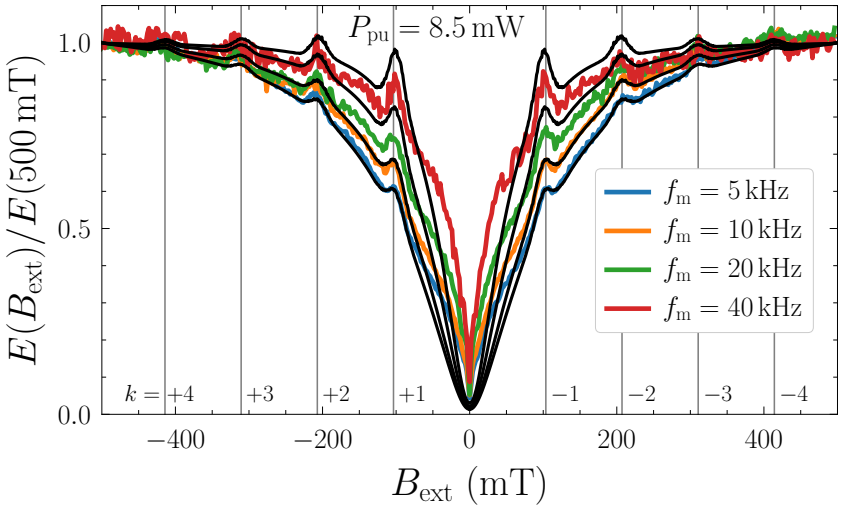

Figure 9.8: Normalized PRCs for sample A using various pump modulation frequencies f_m at a pump power of $P_\mathrm{pu} = 8.5\,\mathrm{mW}$. Except for the normalization with respect to the Faraday ellipticity E at $B_\mathrm{ext} = 500\,\mathrm{mT}$, the layout of the plot is analogous to Fig. 9.5. Clearly, the RSA modes are more pronounced for larger modulation frequencies.

power of $P_{\mathrm{pu}} = 8.5\,\mathrm{mW}$. The largest visibility $V_E \approx 0.17$ is found at a pump modulation frequency of $f_{\mathrm{m}} = 320\,\mathrm{kHz}$. For larger frequencies, the visibility decreases slightly until it saturates at $V_E \approx 0.13$. This decrease seems confusing at first glance. It results from the fact that in this particular case, the RSA mode $|k| = 1$ falls into a range of magnetic fields that belongs to the zero-field minimum, which becomes narrower for larger modulation frequencies as discussed above. For instance, the 'hump' is less pronounced when using, e.g., $\omega_{\mathrm{n}}/(2\pi) = 70\,\mathrm{MHz}$, implying a narrower zero-field minimum also for the smaller modulation frequencies. In experiments, a limitation of enhancing the visibility by means of the spin inertia effect, especially for the higher RSA modes $|k|$, is imposed by the deteriorated signal-to-noise ratio in the PRCs for larger frequencies as noticeable in Fig. 9.8. The signal-to-noise ratio can be improved by accumulating the signal over a longer period of time for each data point.

9.3 Analysis of Sample B

In this section, we provide and analyze complementary results demonstrating RSA in Faraday geometry for another QD ensemble (Sample B) with weaker hyperfine interaction. In contrast to the previous section, the Faraday rotation instead of the ellipticity is measured in the experiments.

9.3.1 Experimental details

Sample B consists of 20 layers of InGaAs QDs separated by 60 nm barriers of GaAs and grown by molecular beam epitaxy on a (100)-oriented GaAs substrate. A δ-doping layer of Si 16 nm above each QD layer provides a single electron per QD on average. The QD density per layer amounts to $10^{10}\,\mathrm{cm}^{-2}$. The sample was thermally annealed at 945 °C for 30 s, which homogenized the QD size distribution and shifted the average emission energy to 1.3908 eV.

The experimental setup is very similar to the one described in Sec. 9.2.1; the differences are the following (see the Supplemental Material of Ref. [94] for details). The sample is illuminated with a mean photon energy of 1.3884 eV and a FWHM of 1.3 meV. The pump and the probe pulses are degenerate in photon energy, which

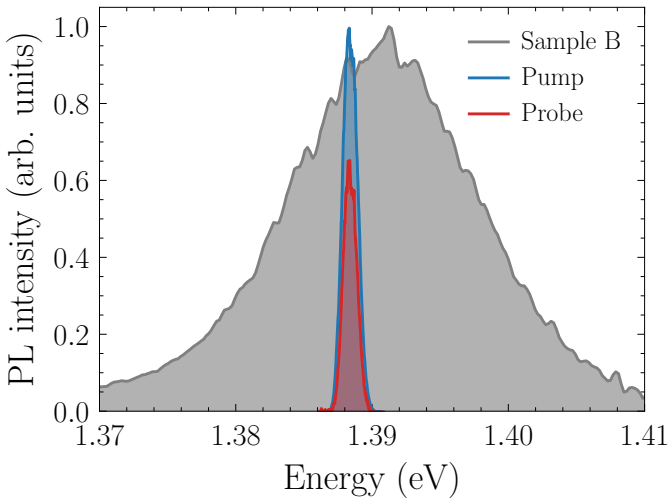

Figure 9.9: Sample B: Photoluminescence (PL) spectrum of the InGaAs QD ensemble (gray) at temperature $T = 5.3\,\mathrm{K}$ along with the spectra of the pump (blue) and probe (red) pulses used in the pump-probe experiments, which are degenerate in photon energy.

is shifted by 2.4 meV to the low-energy flank of the QD photoluminescence as visualized in Fig. 9.9. The helicity of the pump pulses is modulated with frequency $f_\mathrm{m} = 84\,\mathrm{kHz}$ between σ^+ and σ^-. The Faraday rotation amplitude of the linearly polarized probe pulses is measured with a delay of $\tau_\mathrm{d} = -50\,\mathrm{ps}$, i.e., slightly before the arrival of the pump pulses.

9.3.2 Polarization recovery curves

The Faraday rotation R measured as a function of the magnetic field B_ext for a wide range of pump powers is shown in Fig. 9.10. The colored data depicts the experimentally measured Faraday rotation, the smooth black curves represent the simulated PRCs. The very good agreement between experiment and theory is achieved despite having only three fit parameters: the effective pulse area Θ, the trion spin relaxation time $\tau_\mathrm{s}^\mathrm{T} = 0.06\,\mu\mathrm{s}$, and the longitudinal electronic g factor $g_z = -0.64$. The remaining parameters are taken from the earlier sample characterization of Ref. [93]; they are listed in Table 9.1.

All PRCs have a V-like shape, which is typical for n-doped QDs. Often, the PRC given by Eq. (3.48b) is used to characterize such PRCs [88], but it fixes the ratio of the spin polarizations at zero and large magnetic field to 1/3. But the ratio for the PRCs shown in Fig. 9.10 clearly differs from this value because we are dealing with nonequilibrium conditions thanks to the periodic application of strong pump pulses. For this reason, we fit the measured and simulated PRCs using the

generalized dependence

$$R(B_{\text{ext}}) = A\left(1 - \frac{C}{1 + (B_{\text{ext}} - B_0)^2/\Delta B^2}\right). \tag{9.11}$$

The parameter A describes the saturation level for large magnetic fields, $1 - C$ is the ratio of spin polarizations at zero and large field (if $B_0 \approx 0$), ΔB characterizes the width of the zero-field minimum of the PRC, and B_0 accounts for a potential shift (there is almost none). The fit parameters are shown in Fig. 9.11 as a function of the pump power P_{pu}. Figure 9.11(a) shows the increase of the saturation level A caused by the increase of the pump power. As predicted in Chap. 8, the application of a larger pump power results in a broadening of the zero-field minimum, which is displayed in Fig. 9.11(b) by an increase of ΔB. The width of the zero-field minimum in the limit of zero pump power is determined by random Overhauser field characterized by the characteristic frequency ω_{n}, corresponding to $\Delta B \approx 11\,\text{mT}$. From the previous sample characterization of Refs. [93, 97], we know that $\omega_{\text{n}}/(2\pi) = 70\,\text{MHz}$,

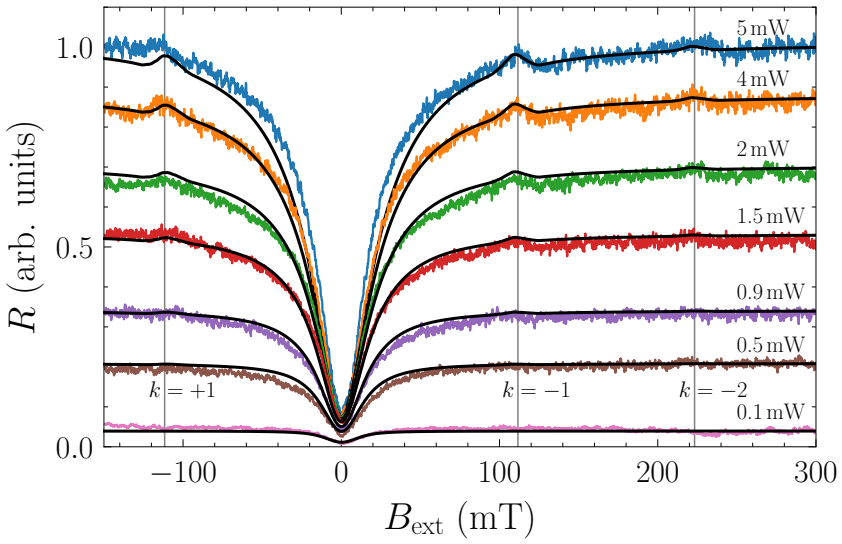

Figure 9.10: PRCs measured and modeled for Sample B for different pump powers P_{pu} (given next to the curves) at a pump modulation frequency of $f_{\text{m}} = 84\,\text{kHz}$. The colored data depicts the experimentally measured Faraday rotation R, the smooth black curves are the simulated curves. The simulated PRCs are smoothed by a moving average over a range of 7 mT, the pulse area in the simulations is chosen to fit the experimentally obtained power dependence of the saturation level A as shown in Fig. 9.11(a). The positions of the small peaks at around $B_{\text{ext}} = -112\,\text{mT}$, 112 mT, and 224 mT match the positions resulting from the PSC (9.9) for the kth RSA modes (vertical gray lines).

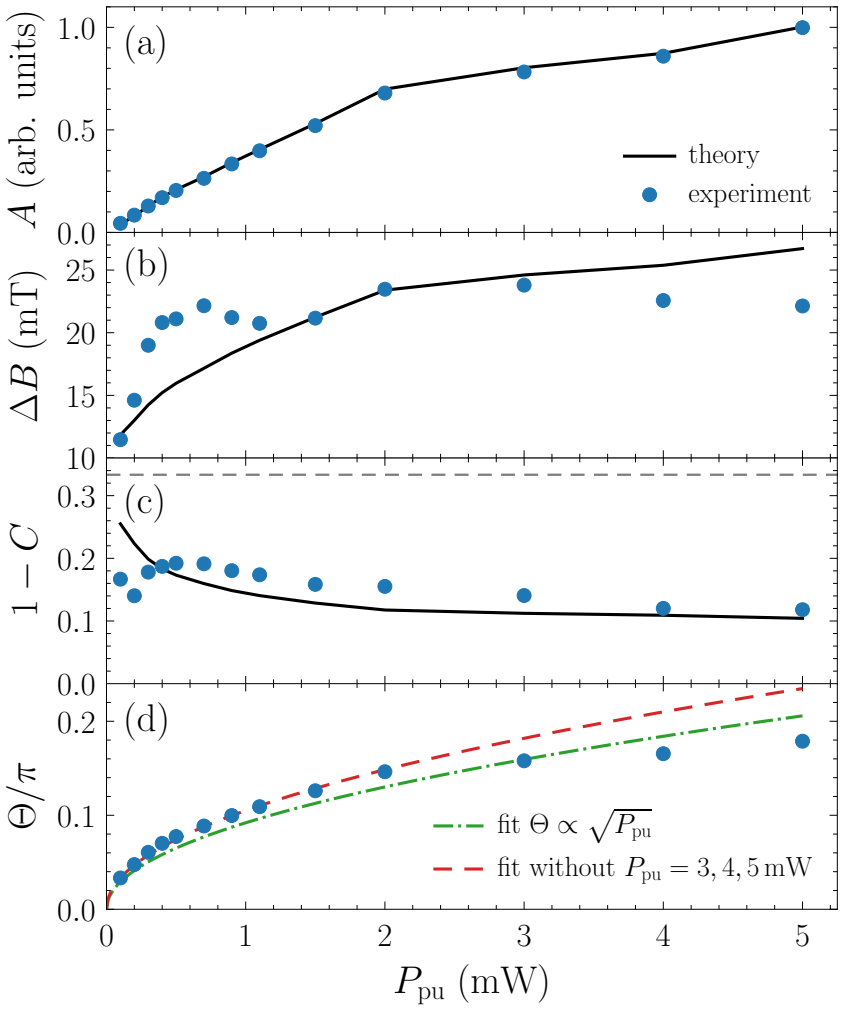

Figure 9.11: Characterization of the PRCs for Sample B for experiment (blue spheres) and theory (black lines). The saturation level A, the width ΔB of the zero-field minimum, the ratio $1-C$ describing the depth of the zero-field minimum relative to A, and the pulse area Θ are shown as a function of the pump power P_{pu}. The pulse area in the simulations is chosen such that A fits the experimentally observed dependence, the parameters ΔB and C follow from fitting Eq. (9.11) to the PRCs. The horizontal dashed line in (c) marks the ratio $1-C = 1/3$, which is expected in the limit of very weak pump pulses. For small powers, the pulse area shown in (d) scales like $\Theta \propto \sqrt{P_{\mathrm{pu}}}$, as expected.

which is equivalent to a field of 7.8 mT. In the limit of very weak pump pulses where Eq. (3.48b) is applicable, we find $\Delta B = \sqrt{2}\omega_\mathrm{n}/(g_z\mu_\mathrm{B}\hbar^{-1}) \approx 11\,\mathrm{mT}$, which is in excellent agreement with the previous sample characterization. The ratio $1-C$ shown in Fig. 9.11(c) deviates from the standard ratio 1/3 [88, 104] appearing in Eq. (3.48b), which is only valid in the limit of very weak pulses [126]. As demonstrated in Fig. 9.11(d), the pulse area scales like $\Theta \propto \sqrt{P_\mathrm{pu}}$ for small pump powers up to approximately $P_\mathrm{mW} = 2\,\mathrm{mW}$ [23, 113, 135]. The pulse area at $P_\mathrm{pu} = 5\,\mathrm{mW}$ is estimated very roughly to be $\Theta \approx 0.18\pi$; the pulse areas at the other pump powers are fitted such that the saturation level A fits to the experimentally observed dependence; see Fig. 9.11(a).

Very similar to the PRCs measured for Sample A, additional modulations of the spin polarization are visible in the PRCs for large pump power at magnetic fields B_ext fulfilling the PSC (9.9). This is again the result of RSA in Faraday geometry. By determining the maxima of the RSA modes, we deduce $g_z = -0.64 \pm 0.01$ for the longitudinal electronic g factor. In comparison, a value of $g_z = -0.61$ is obtained in Refs. [93, 132, 272] for the same sample. The difference could be related to a better accuracy of our novel technique or to the varying g factor and its spread in the inhomogeneous ensemble of QDs, i.e., different spots on the sample could be analyzed.

9.3.3 Visibility of resonant spin amplification in Faraday geometry

Analogously to Sec. 9.2.4, we study the RSA visibility [126]

$$V_R := \frac{R_\mathrm{max} - R_\mathrm{min}}{R_\mathrm{max}}\,, \tag{9.12}$$

where R_max is the Faraday rotation of the first maximum at the RSA mode $|k| = 1$ and R_min denotes the adjacent minimum at a larger magnetic field $|B_\mathrm{ext}|$. As explained in Sec. 9.1.3, the numerical calculation of the Faraday rotation is much more difficult than calculating the Faraday ellipticity. The reason is a sign problem arising in the applied Monte Carlo sampling, which results in much larger statistical fluctuations in the Faraday rotation than in the ellipticity. Since these fluctuations hinder the reliable detection of physical minima and maxima in the simulated PRCs, we set $V_R = 0$ whenever $V_R < 0.02$. A map of the RSA visibility in dependence of the pulse area Θ and of the product $\omega_\mathrm{n}T_\mathrm{R}$ with $\omega_\mathrm{n}/(2\pi) = 70\,\mathrm{MHz}$ is shown in

Fig. 9.12(a). The visibility becomes larger when the pulse area is increased, which corresponds to the usage of a larger pump power. For a too large or too small repetition time T_R, the visibility vanishes. Observing RSA in Faraday geometry by measuring the Faraday rotation appears to be easiest in the intermediate regime $\omega_\mathrm{n} T_\mathrm{R} \sim 1$. As indicated by the white cross on the heatmap, the laser source used in the experiments does not operate at optimal conditions. For a pump power of $P_\mathrm{pu} = 5\,\mathrm{mW}$, the experimentally observed visibility amounts to only $V_R \approx 0.02$. Under better conditions, the visibility could reach up to $V_R \approx 0.51$. No RSA

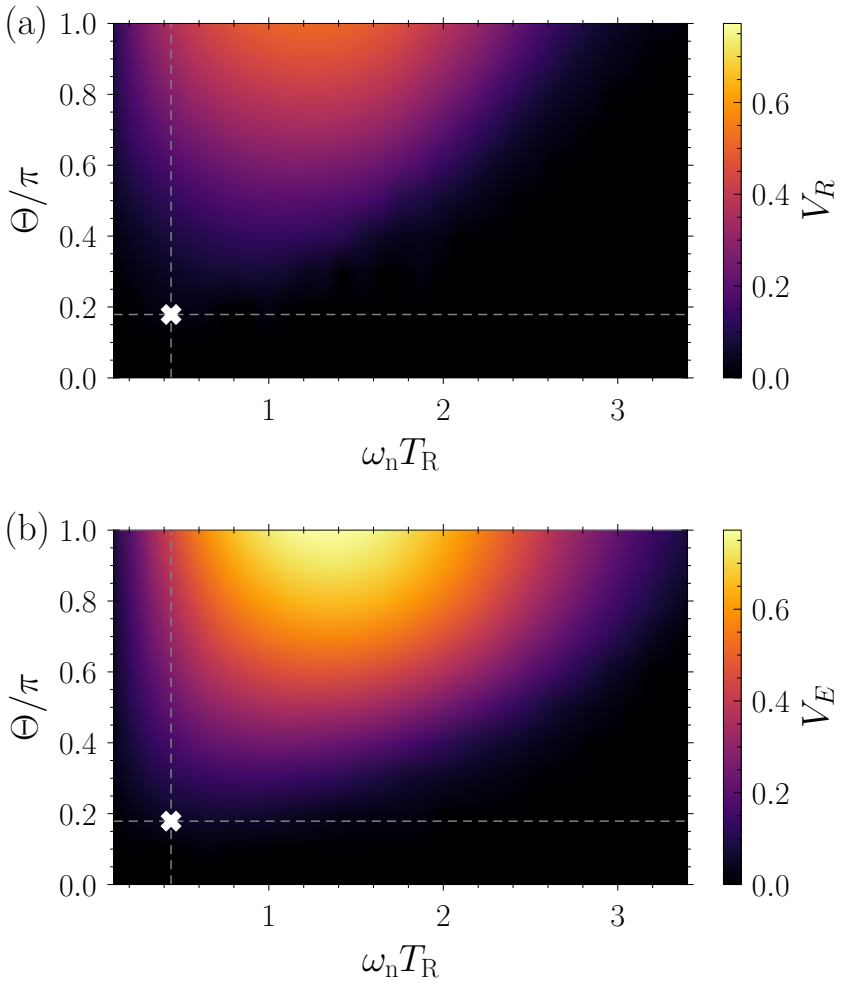

Figure 9.12: Visibility map of the RSA mode $|k| = 1$ for Sample B modeled for detection by (a) Faraday rotation (visibility V_R) and (b) Faraday ellipticity (visibility V_E). The white cross marks the experimental conditions for a pump power of $P_\mathrm{pu} = 5\,\mathrm{mW}$ ($\Theta \approx 0.18\pi$) and a pulse repetition time of $T_\mathrm{R} = 1\,\mathrm{ns}$ with $\omega_\mathrm{n}/(2\pi) = 70\,\mathrm{MHz}$. The pump-probe delay is set to $\tau_\mathrm{d} = -0$ and the number of configurations to $M = 10^6$.

modes are visible for the commonly used repetition times $T_R = 13.2$ and $6.6\,\mathrm{ns}$ ($\omega_n T_R \approx 5.8$ and 2.9) in theory nor in experiment.

The RSA visibility for Sample B with $\omega_n/(2\pi) = 70\,\mathrm{MHz}$ can be improved by increasing the pump power and by using a laser with a slightly larger repetition time of about $T_R = 2 - 3\,\mathrm{ns}$. A larger repetition time would also increase the number of visible RSA modes, allowing for an even more accurate determination of the longitudinal electronic g factor. In contrast, the choice $T_R = 1\,\mathrm{ns}$ is perfectly suited to reveal the RSA modes for Sample A because the Overhauser field characterized by $\omega_n/(2\pi) = 140\,\mathrm{MHz}$ is twice as large on average. The larger value also results in a broader zero-field minimum of the PRC and hence, the RSA modes are also visible at larger magnetic fields.

The theoretical modeling reveals that measuring the Faraday ellipticity instead of the Faraday rotation for the applied degenerate pump-probe setup yields a larger RSA visibility of up to $V_E \approx 0.77$. This is visualized in the corresponding visibility map displayed in Fig. 9.12(b), which needs to be compared to Fig. 9.12(a).

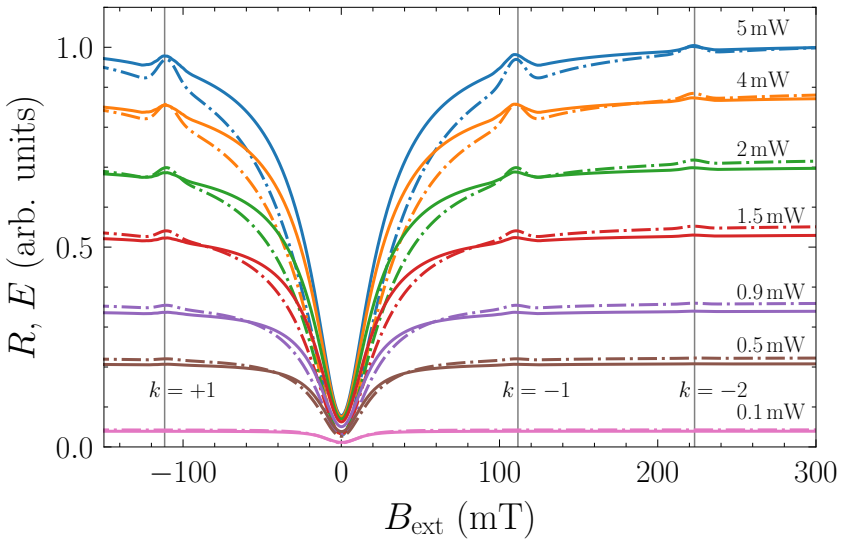

Figure 9.13: Comparison of the simulated PRCs for Sample B when probing the Faraday rotation R (solid curves) or the Faraday ellipticity E (dash-dotted curves) for various pump powers P_{pu} given next to the curves; see Fig. 9.11(d) for the corresponding pulse areas Θ. The PRCs are scaled such that $R(B_{ext} = 300\,\mathrm{mT}, P_{pu} = 5\,\mathrm{mW})$ is equal to $E(B_{ext} = 300\,\mathrm{mT}, P_{pu} = 5\,\mathrm{mW})$ and they are smoothed by a moving average over a range of 7 mT. The vertical gray lines highlight the values of the magnetic field B_{ext} that fulfill the PSC (9.9) for the mode numbers k.

Under the best realized experimental conditions (white cross), we find a visibility of $V_E \approx 0.05$ for the Faraday ellipticity and $V_R \approx 0.03$ for the Faraday rotation. We point out that the situation could be different if a controlled pump-probe detuning is used [146], which is question for future research. Another possibility to enhance the visibility consists of exploiting the spin inertia effect as demonstrated for Sample A.

For completeness, we compare in Fig. 9.13 the PRCs for the Faraday rotation R (solid curves) and Faraday ellipticity E (dash-dotted curves) for the pump powers used in Fig. 9.10. The PRCs are scaled such that $R(B_{\text{ext}} = 300\,\text{mT}, P_{\text{pu}} = 5\,\text{mW})$ is equal to $E(B_{\text{ext}} = 300\,\text{mT}, P_{\text{pu}} = 5\,\text{mW})$; the Faraday rotation is actually smaller by approximately a factor of 40. Clearly, the RSA modes are more pronounced when probing the Faraday ellipticity instead of the rotation. Moreover, the zero-field minimum of $E(B_{\text{ext}})$ is broader than the zero-field minimum of $F(B_{\text{ext}})$. The better visibility of the RSA modes results from the fact that in a degenerate pump-probe setup, the Faraday ellipticity probes the QDs that are pumped with minimal detuning and hence, with a better efficiency (smaller values of Q on average). At the same time, the average degree of spin polarization in these QDs is also larger, i.e., closer to the saturation limit, so that the zero-field minimum is broader. Similarly, the PRCs for R and E do not differ much when a small pump power is applied because the degree of spin polarization is small.

As a final point, let us briefly discuss the role of the trion spin relaxation time $\tau_{\text{s}}^{\text{T}}$. Approaching the saturation limit of the spin polarization is detrimental for RSA in Faraday geometry and hence, its visibility is fairly sensitive to the value of $\tau_{\text{s}}^{\text{T}}$. Smaller values result in a larger degree of spin polarization, which implies less pronounced RSA modes. In this sense, it should be beneficial to exploit the spin inertia effect to decrease the degree of spin polarization when trying to reveal RSA modes for samples with a fast trion spin relaxation.

9.4 Chapter conclusion

Measurements on two different ensembles of n-doped InGaAs QDs reveal RSA in Faraday geometry under experimental conditions. The experimental results can be described very well by our model. The positions of the RSA modes directly yield the longitudinal electronic g factor, which we determine to be $g_z = -0.69 \pm 0.01$

for Sample A and $g_z = -0.64 \pm 0.01$ for Sample B. Using strong pump pulses in combination with a suitable pulse repetition time ($\omega_n T_R \sim 1-2$) is the requirement to reveal RSA modes. A significant enhancement can be achieved by exploiting the spin inertia effect, which allows one to reduce the degree of spin polarization as a consequence of the modulated helicity of the pump pulses. For the considered degenerate pump-probe setup, probing the Faraday ellipticity instead of the rotation turns out to yield a better RSA visibility.

In order to understand the effect in more detail, a systematical analysis of the influence of important parameters (such as the spin relaxation times) on the visibility and on the width of the RSA modes is called for. For the mode width, a finite spread of the longitudinal electronic g factor, which we did not account for in our analysis, certainly plays a role for the higher modes. Analytical support [126] would be beneficial because the current approach relies on expensive numerical simulations.

An important task for future research is to enhance the RSA visibility further. Thanks to the very good agreement between experiment and theory, our model can be used to guide future experiments. For instance, the suggestion to exploit the spin inertia effect turned out to be successful. Another option is to study the influence of a controlled pump-probe detuning. As an exciting alternative, one could try to conceive advanced pulse protocols. Typically, laser sources with a specific repetition time are at one's disposal, but they do not necessarily represent the optimal choice for a particular sample. By adding a second laser with the same repetition time but with a pump incidence shifted by a certain delay, it could be possible to enforce the appearance of certain RSA modes. The idea is to tune the delay to enforce a different commensurability than the one imposed by the pulse repetition time. In a second step, the helicity of the two laser sources could be modulated in different ways, e.g., such that the helicity of consecutive pulses is alternating.

Chapter 10

Conclusion

Several nonequilibrium spin phenomena in quantum dots (QDs) arising in pump-probe experiments are addressed theoretically in this thesis. The studied experimental setups can be classified into two types: application of (i) a transverse magnetic field (Chaps. 5, 6, and 7) or of (ii) a longitudinal magnetic field (Chaps. 8 and 9). Both types require different approaches to describe the arising effects theoretically, but they share the underlying central spin model (CSM) describing the hyperfine interaction of a central spin with a surrounding spin bath. Depending on which particular effect shall be described, further influences need to be taken into account and sometimes, a phenomenological description can be sufficient.

One major goal of this thesis is the description of the nuclei-induced frequency focusing effect, which requires the description of the nuclear spin dynamics in the QDs caused by the hyperfine interaction with the spin of a localized charge carrier. But the number of effectively coupled nuclear spins $N_{\mathrm{eff}} = 10^4 - 10^6$ [19, 103–107] is huge in a QD and hence, it is not feasible to treat realistic system sizes fully quantum mechanically. To study the spin dynamics nevertheless, we apply a semiclassical approach based on the truncated Wigner approximation (TWA, Sec. 3.3), which amounts to solving classical equations of motion starting from random initial conditions. The ensemble average over all trajectories mimics the quantum mechanical expectation value. Even though the numerical effort scales linearly with the system size in this approach (instead of exponentially), the effort is still too large to calculate the dynamics for up to 13 orders of magnitude in time. Massive parallelization enabled by high-performance computing is one of the key solutions to this tremendous task, but it would not have been sufficient without significant progress on the algorithmic side. The application of the efficient algorithms to the spin dynamics in the semiclassical CSM established in Chap. 4 to reduce the complexity of the

classical equations of motion is the other key component. The most advanced algorithm, the Spectral Density approach, enables the simulation of an *infinite* number of bath spins by accounting for a limited number of auxiliary dynamic variables, whereas the number of *effectively* coupled bath spins N_{eff} remains large but finite. By analyzing the long-time dynamics of the central spin, we identify the low-energy scale $A_{\text{Q}}/\sqrt{N_{\text{eff}}}$ arising from the slow nuclear spin dynamics, which also appears in other investigations [163, 178]. The short-time dynamics of the central spin in the Overhauser field is governed by the energy scale A_{Q}.

10.1 Transverse magnetic field

Starting in Chap. 5, we put the efficient semiclassical Spectral Density approach to use to analyze the effect of nuclei-induced frequency focusing (NIFF), which arises from the application of long trains of pulses to a central spin coupled to a nuclear spin bath while a strong transverse magnetic field is applied (Voigt geometry). This nonequilibrium effect leads to the appearance of a revival signal of a dephasing spin polarization before the arrival of the pulse. It is caused by a selection of certain polarizations in the Overhauser field (referred to as nuclear focusing) as a consequence of the periodic application of pulses. Two generic pulse models are considered in this chapter. The first one is a classical pulse that simply rotates the classical central spin vector onto the z axis while preserving its length. For the second pulse model, each application is considered as a quantum mechanical measurement with the definite outcome of a spin state $|\uparrow\rangle$. Because of the uncertainty principle, a statistical component for the transverse spin components needs to be included in the semiclassical description, which can be realized by means of the Gaussian TWA. The first crucial insight gained in this chapter is that the properties of the pulse have a strong impact on the arising nonequilibrium spin physics. While the application of both pulse models results in the emergence of nuclear focusing, the qualitative behavior differs substantially. For instance, different classes of resonances (even or odd, corresponding to an integer or half-integer number of Larmor periods between two pulses) can appear and the nuclear focusing can be perfect (pulse model I) or imperfect (pulse model II). Perfect nuclear focusing means that the emerging nuclear focusing peaks in the probability distribution of the effective magnetic field (sum of external and Overhauser field) approach δ peaks. Imperfect nuclear focusing means that the peaks retain a finite width even in the nonequilibrium steady

state. Another crucial component is the inclusion of the nuclear Zeeman effect, which changes the scaling behavior of the long-time dynamics. Upon its inclusion, the low-energy scale is proportional to $1/N_{\mathrm{eff}}$ and the scaling with the applied magnetic field B_{ext} is proportional to B_{ext}^2. Without the nuclear Zeeman effect, the low-energy scale is proportional to $1/\sqrt{N_{\mathrm{eff}}}$ and the scaling with the magnetic field is proportional to B_{ext} (pulse model I) or B_{ext}^2 (pulse model II). The combination of the nondeterministic pulse with the nuclear Zeeman effect constitutes a model that yields a nonmonotonic magnetic field dependence of the revival amplitude arising as a consequence of NIFF. Pronounced minima are visible whenever the pulse repetition time is a multiple of half the nuclear Larmor period. This dependence has strong similarities with experimental results [117, 122] and quantum mechanical calculations performed for very a small number of nuclear spins [117].

Motivated by these similarities, a more elaborate model is established in Chap. 6. For instance, it is well known that a sizable revival amplitude can appear even without NIFF, simply as a consequence of pulse properties that describe the optical excitation of trion states [24, 113, 117, 122, 135, 141], which result in a selection of Larmor frequencies that are commensurable with the pulse repetition rate. This behavior cannot be described by the models studied in Chap. 5. This more general phenomenon, to which the effect of NIFF can contribute, is known as spin mode locking (SML). To study the interplay of SML and NIFF, a well known pulse model describing the resonant excitation of trion states [24, 113, 122] is combined with the efficient Spectral Density approach to the nuclear spin dynamics. The results are rich, e.g., the different classes of resonances (even and odd) appear simultaneously and there is a sizable revival amplitude after a few pulses without nuclear focusing. However, the magnetic field dependence of the revival amplitude contradicts the previous experimental [117, 122] and theoretical results [117]. Inspired by the pulse model II used in Chap. 5, the action of each pump pulse is treated as a quantum mechanical measurement as a first improvement of the semiclassical approach. This interpretation requires nondeterministic pulse description to account for the uncertainty principle, which can be realized by means of the Gaussian TWA. This step has a significant impact on the qualitative physics. Now, the two classes of resonances do not appear simultaneously anymore and the magnetic field dependence of the revival amplitude resembles the previous experimental and theoretical results much better. Importantly, a revival signal still appears after application of a few pulses without any nuclear focusing, which is the main improvement over

pulse model II used in Chap. 5. Interestingly, there can be a destructive interplay of SML and NIFF such that the revival amplitude is smaller than its value without NIFF for certain ranges of magnetic fields. In some cases, the revival amplitude can actually vanish as a consequence of NIFF.

The next improvement of the model consists in the inclusion of the trion pseudospin dynamics stemming from the unpaired heavy-hole in the trion. It is a crucial component to describe the spin dynamics between two pulses observed in experiments, but also to describe measurements of the polarization recovery effect for p-doped QDs. Especially the Larmor precession of the trion pseudospin turns out to be important for the qualitative nonequilibrium behavior because it acts as a perturbation to the trion recombination dynamics. The result is that only even resonances appear in the probability distribution of the effective magnetic field, with the only exception of a narrow range of magnetic fields where the nuclear Larmor period is almost equal to the pulse repetition time. But for the majority of magnetic fields, the interplay of SML and NIFF is constructive, i.e., NIFF leads to an enhancement of the revival signal. As a side effect, the emergence of dynamic nuclear polarization is observed, i.e., the formation of a nonzero average polarization of the Overhauser field parallel to the external magnetic field. The DNP can be larger than the typical magnitude of the random Overhauser field, leading to a small increase of the dephasing time. Interestingly, the magnetic field dependence has strong similarities with the one of the revival amplitude. But since the buildup of this effect is two order of magnitude slower than nuclear focusing, the corresponding nonequilibrium steady states can only be investigated for rather small magnetic fields of up to 1 T. Studying the steady states for larger fields is an interesting subject for future research, but methodical progress is required. As a promising outlook, the simulations can potentially be sped up significantly by resorting to the equations of motion expanded in the magnetic field (Chap. 7) in combination with their algebraic solution (Appendix E). Yet, the validity on the longer timescale must be verified first.

The influence of the finite g factor spread of an inhomogeneous ensemble of QDs on the behavior of NIFF is investigated next. While its inclusion is crucial to describe the experimentally observed spin dynamics between two pulses, it has no qualitative influence on the revival amplitude and the actual differences are only minor. Furthermore, it turns out that the actual distribution of the hyperfine couplings is only important on a quantitative level. Compiling all the gained knowledge, a

minimal model is established in which the nondeterministic pulse model describing the resonant trion excitation is combined with a simplified semiclassical model for the spin dynamics. Here, all hyperfine couplings are considered to be identical (box model) and the hyperfine interaction of the heavy-hole spin in the trion with the nuclear spin bath is neglected. Especially the application of the box model facilitates the numerical treatment because it reduces the dimension of the system of differential equations from $\mathcal{O}(200)$ to 6.

Building on this foundation, the influence of nuclear magnetic resonances on the nonequilibrium behavior is investigated in Chap. 7. Here, we take the isotope composition of $In_xGa_{1-x}As$ QDs into account. It turns out that the width of the Overhauser field distribution, characterized by the inverse dephasing time $1/T_n^*$, has a relevant influence on the revival amplitude. This is not the case for the models analyzed in Chap. 6 in the limit of an infinite effective bath size and it is related to the inclusion of multiple nuclear species in the model. Motivated by previous investigations [23, 123], a QD sample with $T_n^* = 4\,\mathrm{ns}$ is studied here, whereas the generic value $T_n^* = 1\,\mathrm{ns}$ is considered in Chap. 6. But the numerical effort scales worse than $(T_n^*)^3$ so that further methodical progress is required despite building on the previously established minimal model. In order to simulate the nonequilibrium steady states prevalent under experimental conditions nevertheless, we split the classical equations of motion into two parts: one part describing the fast Larmor precession, which is numerically expensive, and another part describing the slow dynamics. The fast Larmor precession with frequency $h \propto B_{\mathrm{ext}}$ is treated analytically, whereas the slow part of the dynamics is expanded in the large magnetic field while neglecting corrections of the order $\mathcal{O}(h^{-2})$. This approach turns out to work with a remarkable accuracy for large magnetic fields while reducing the runtime by two orders of magnitude. As a side product, an algebraic solution is derived for the case where only a single nuclear species is considered (Appendix E), opening promising routes for future research. By putting the efficient approach to use, the magnetic field dependence of the revival amplitude is analyzed for various compositions of $In_xGa_{1-x}As$ QDs, i.e., for various In concentrations x. Generally, the magnetic field dependence becomes more complex and better resembles the experimental results [117]. Several nuclear magnetic resonances are responsible for this behavior, which reveal themselves as narrow minima in the magnetic field dependence. Their depth and width depend on the isotope composition of the QDs. This opens up the possibility of a novel kind of nuclear magnetic resonance spectroscopy of the aris-

ing nonequilibrium steady states. It would be very interesting to see if these sharp minima can be observed experimentally to test the model and its predictions.

In conclusion, a sophisticated semiclassical model is developed that describes several effects related to spin mode locking and nuclei-induced frequency focusing in QDs. The key components are:

- the hyperfine interaction between the localized electron spin and the surrounding nuclear spins,
- the excitation of negatively-charged trions by the pump pulses,
- the interpretation of the pump pulse action as a quantum mechanical measurement to account for the uncertainty principle in the semiclassical approach,
- the Zeeman effect for *all* spins, including the unpaired heavy-hole spin of a negatively-charged trion,
- the isotope composition of the QDs, giving rise to several nuclear magnetic resonances with respect to the repetition rate of the pump pulses.

Possible extensions of the model are pointed out in the outlook given in Sec. 10.3.

10.2 Longitudinal magnetic field

In Chap. 8, the focus shifts to a different type of pump-probe experiment in which a longitudinal magnetic field is applied to the QDs (Faraday geometry). The polarization recovery effect is one of the effects to be described for n- and p-doped QDs [93]. It describes the dependence of the spin polarization on the strength of the longitudinal magnetic field. In addition, the helicity of the pump pulses is modulated, giving rise to the spin inertia effect [93, 125]. The spin inertia effect describes the dependence of the spin polarization on the modulation frequency and enables the measurement of long spin relaxation times. Our model developed in Chap. 8 accounts for an arbitrary pumping strength, extending the theory of Ref. [125] valid in the limit of weak pump pulses. Moreover, it accounts for the hyperfine interaction of the resident and photoexcited charge carrier spins with the Overhauser field, which is assumed to be static, the coupling to the external magnetic field, and

for the radiative trion recombination. Further spin relaxation induced by other interactions are accounted for by phenomenological relaxation terms. Notably, the approach does not impose any restrictions on the model parameters.

In our analysis, we find that the pumping strength has a significant effect on the effective spin relaxation time of the resident charge carriers. The extrapolation of this time to the limit of zero pump power yields the intrinsic spin relaxation time. Turning to the polarization recovery curves (PRCs), the model reproduces the V- and M-like shapes characteristic for n- and p-doped QDs, respectively [93, 125]. Importantly, an increase of the pump power influences the shape of the PRCs as a consequence of the spin polarization approaching the saturation limit in which all spins point in the same direction. Various effects are the result: First, a broadening of the zero field minimum of the PRCs is found for larger pump powers, which is also confirmed by an analysis of the experiments in Chap. 9. The same behavior is observed when the pump modulation frequency is reduced. Furthermore, a pronounced M-like shape can gradually change towards a V-like shape when increasing the pump power. All these effects are more pronounced if the degree of spin polarization is large, e.g., if the pump power is large or if the modulation frequency of the pump pulses is small. To mitigate the influence of the saturation limit of spin polarization, it is advised to apply very weak pulses combined with a large modulation frequency. In this limit, the width of the zero field minimum of the PRC is solely determined by the strength of the hyperfine interaction ω_n [88, 125] so that ω_n can be determined from measured PRCs without an extrapolation to zero pump power

Most strikingly, we predict the emergence resonant spin amplification (RSA) in Faraday geometry, which is enabled by the transverse component of the random Overhauser field under certain conditions. The effect reveals itself as an additional periodic modulation of the spin polarization in the PRCs and allows for a direct and accurate measurement of the longitudinal g factor of the resident charge carriers. Recent experiments demonstrate the realization of this novel effect for two different ensembles of n-doped InGaAs QDs [94]. These experiments are analyzed in Chap. 9, wherefore the model used in Chap. 8 is extended to account for the inhomogeneous broadening of the trion transition energy in inhomogeneous ensembles of QDs by resorting to the formalism developed in Ref. [113]. Furthermore, the pulse model developed in Ref. [113], which describes the excitation of trion states, is generalized in Sec. 2.2.2 to account for a finite trion population at the arrival of a pump

pulse. This extension is required because a laser with a short pulse repetition time of $T_\mathrm{R} = 1\,\mathrm{ns}$ is used in the experiments to reveal RSA in Faraday geometry. The comparison of simulations with the experimental data shows a remarkable agreement. An analysis of the RSA visibility reveals the optimal conditions to observe the effect, which helps to guide future experiments. The best visibility can be achieved by using a laser with a suitable pulse repetition time ($\omega_\mathrm{n} T_\mathrm{R} \sim 1 - 2$) together with a large pump power. It is expected to be hard to observe the effect in QDs with a strongly anisotropic hyperfine interaction, e.g., in p-doped QDs, because the transverse component of the Overhauser field $\propto \omega_\mathrm{n}/\lambda$ ($\lambda \gg 1$) is smaller than the longitudinal one $\propto \omega_\mathrm{n}$ that smears the RSA modes. A significant further enhancement of the RSA visibility can be achieved by exploiting the spin inertia effect, which leads to a substantial decrease of the degree of spin polarization if the pump modulation frequency is larger than the spin relaxation rate. In turn, the RSA visibility increases because it is less influenced by the saturation limit of the spin polarization in which no polarization can be resonantly amplified.

In conclusion, the analysis demonstrates that our model is capable of describing measurements of the spin inertia and polarization recovery. Accounting for the pumping strength instead of assuming the weak pulse limit has a significant effect on the results. Most importantly, the effect of resonant spin amplification in Faraday geometry is predicted. Optimal conditions to achieve an optimal RSA visibility are explored. Recent measurements confirm the existence of this effect under experimental conditions [94], with a remarkable agreement between experiment and theory.

10.3 Outlook

As always, the description of different effects requires tailored effective models. To model the effect of NIFF, the nuclear spin dynamics caused by the hyperfine interaction need to be taken into account, requiring a microscopic theory. In contrast, it appears to be sufficient for the description of polarization recovery and spin inertia measurements to consider a static nuclear spin bath, but phenomenological relaxation terms need to be included to describe slow but relevant spin relaxation processes. Nevertheless, effects stemming from nuclear spin dynamics can have an impact for small magnetic fields [125, 126]. But since there are other mechanisms

that can lead to similar effects, it is not straightforward to judge the importance of the nuclear spin dynamics for the PRCs. Yet, the different approaches also display synergetic effects: The inclusion of the trion pseudospin dynamics in Sec. 6.3 is motivated by the description of the M-shaped PRCs characteristic for p-doped QDs, for which this dynamics is the key component to describe the generation of spin polarization correctly. Importantly, the commensurability of the pulse repetition time and the Larmor period of the resident charge carriers plays a central role in all different types of pump-probe experiments studied in this thesis.

First, let us focus on the pump-probe experiments in which a transverse magnetic field is applied. Since our approach is based on a microscopic theory, several extensions are conceivable. For instance, the quadrupolar interaction of nuclear spins with $I > 1/2$ (see Sec. 3.1.5) could be taken into account [97, 185–190]. A recent theoretical study [143] shows that this interaction acts against nuclear focusing.

Another area for improvements is the description of QD ensembles with an inhomogeneous broadening of the trion transition energy. For this purpose, the formalism developed in Ref. [113] can be applied again. This extension would allow one to investigate the influence of the type of measurement (Faraday rotation versus Faraday ellipticity) and also the influence of the pump-probe detuning on the magnetic field dependence of the revival amplitude [95, 113, 146]. Furthermore, other effects related to detuning could be analyzed [98, 148]. The algebraic approach derived in Appendix E provides a suitable foundation provided the external magnetic field is large enough to justify the expansion in the external magnetic field ($B_{\mathrm{ext}} \gtrsim 1\,\mathrm{T}$).

Recently, it was demonstrated that by applying periodic pulses with repetition time $T_{\mathrm{R}} = 1\,\mathrm{ns}$ in Voigt geometry, it is possible to drive the electron spins in an ensemble of singly-charged InGaAs QDs towards a single Larmor precession mode, resulting in a substantial increase of the dephasing time [76]. The underlying idea is that the width of the Overhauser field distribution needs to be small compared to the distance between adjacent commensurable precession modes, which is proportional to T_{R}^{-1}. Earlier experiments used $T_{\mathrm{R}} = 6.6\,\mathrm{ns}$ [75], i.e., the distance between the modes is smaller compared to the experiments with $T_{\mathrm{R}} = 1\,\mathrm{ns}$. It needs to be tested if our model is capable of describing this effect in a suitable manner or whether further extensions are required.

In a related experimental and theoretical study [130] also using a pulse repetition time of $T_{\mathrm{R}} = 1\,\mathrm{ns}$, two novel phenomena termed ‘mode dragging’ and ‘mode pick-up’

are proposed. Combined, they can be used to generate a substantial dynamic nuclear polarization. In this exciting experiment, a sweeping transverse magnetic field is applied. Certainly, an investigation of this novel experimental setup with the aid of our model, potentially with the aforementioned extension to account for detuned pulses, is a very interesting subject for future research.

Turning to RSA in Faraday geometry, the current model is already capable of describing the relevant effects observed in experiments quantitatively and it can also predict conditions to achieve the optimal RSA visibility. Hence, it can be used to conceive advanced pulse protocols that potentially render the effect easier to observe for a variety of semiconductor nanostructures. First ideas consist in applying two pump beams with the same repetition time, but with a tunable delay to enforce a certain commensurability of the Larmor precession. Potentially, the helicity of the two different pump pulses could be modulated in different ways, e.g., such that the helicity of consecutive pulses is alternating. It might also be worth exploring whether a controlled pump-probe detuning can be used to increase the RSA visibility. Further support from analytical considerations such as the ones presented in Ref. [126] is certainly helpful to understand this novel effect better. A different question to be explored is whether nonequilibrium effects similar to nuclear focusing occur when the nuclear spin dynamics caused by the hyperfine interaction is taken into account.

Clearly, there is a variety of fascinating effects in the field of spin physics in QDs to be analyzed and probably, there are even more effects to be discovered. Since the models developed in this thesis for the different magnetic field orientations already explain many effects, they provide a promising foundation for future research.

Appendix

Appendix A

Derivation of the classical equations of motion

In the following, we derive the classical equations of motion for the spin dynamics resulting from the classical Hamiltonian (3.32). For this purpose, we use the notation

$$\mathcal{H}_{\mathrm{QD}} = \left(\sum_{k=1}^{N} A_k \boldsymbol{I}_k + \boldsymbol{h}\right) \cdot \boldsymbol{S} + \sum_{k=1}^{N} \boldsymbol{h}_{\mathrm{n},k} \cdot \boldsymbol{I}_k \,, \tag{A.1}$$

with $\boldsymbol{h} = \gamma_{\mathrm{e}} B_{\mathrm{ext}} \boldsymbol{n}_B$ and $\boldsymbol{h}_{\mathrm{n},k} = \gamma_{\mathrm{n},k} B_{\mathrm{ext}} \boldsymbol{n}_B$. The classical equations of motion follow from the application of Eq. (3.31). For the central spin components S^α, $\alpha \in \{x, y, z, \}$, we deduce

$$\frac{\mathrm{d}}{\mathrm{d}t} S^\alpha = \sum_{\beta,\gamma} \varepsilon_{\alpha\beta\gamma} \frac{\partial \mathcal{H}_{\mathrm{QD}}}{\partial S^\beta} S^\gamma \tag{A.2a}$$

$$= \sum_{\beta,\gamma} \varepsilon_{\alpha\beta\gamma} \left(\sum_{k=1}^{N} I_k^\beta + h^\beta\right) S^\gamma \,. \tag{A.2b}$$

Analogously, the equations of motion for the components I_k^α of the bath spins result to

$$\frac{\mathrm{d}}{\mathrm{d}t} I_k^\alpha = \sum_{\beta,\gamma} \varepsilon_{\alpha\beta\gamma} \frac{\partial \mathcal{H}_{\mathrm{QD}}}{\partial I_k^\beta} I_k^\gamma \tag{A.3a}$$

$$= \sum_{\beta,\gamma} \varepsilon_{\alpha\beta\gamma} \left(S^\beta + h_{\mathrm{n},k}^\beta\right) I_k^\gamma \,. \tag{A.3b}$$

It is clear from the properties of the Levi-Civita symbol $\varepsilon_{\alpha\beta\gamma}$ that for fixed α while summing over β and γ, only two terms with opposite signs remain. In fact, the

structure of the equation is identical to the structure of the cross product

$$(\boldsymbol{a} \times \boldsymbol{b})_\alpha = \sum_{\beta,\gamma} \varepsilon_{\alpha\beta\gamma} a^\beta b^\gamma \tag{A.4}$$

of the three-dimensional vectors $\boldsymbol{a}$ and $\boldsymbol{b}$. The notation $(\boldsymbol{a} \times \boldsymbol{b})_\alpha$ refers to the α component of the cross product. Making use of this property, we can write the full system of equations of motion in the compact form

$$\frac{\mathrm{d}}{\mathrm{d}t}\boldsymbol{S} = \left(\sum_{k=1}^{N} A_k \boldsymbol{I}_k + \boldsymbol{h}\right) \times \boldsymbol{S}\,, \tag{A.5a}$$

$$\frac{\mathrm{d}}{\mathrm{d}t}\boldsymbol{I}_k = (A_k \boldsymbol{S} + \boldsymbol{h}_{\mathrm{n},k}) \times \boldsymbol{I}_k\,, \qquad k \in \{1, 2, \ldots, N\}\,. \tag{A.5b}$$

These equations are essentially Bloch equations describing precessions about time-dependent, effective magnetic fields. The time dependence results from the interrelated dynamics of the central spin $\boldsymbol{S}$ and the N bath spins $\boldsymbol{I}_k$.

Appendix B

Phase shifts at the pulse boundaries

Extending the resonance analysis of Chap. 5, we calculate the phase shift $\Delta\varphi$ of the central spin precession at the pulse boundaries to determine the occurring resonance by fitting the function

$$S_{\mathrm{fit}}(t) = |A| \exp\left[-\frac{5A_{\mathrm{Q}}^2}{8}(t-t_0)^2\right] \cos\left(ht-\varphi\right) \tag{B.1}$$

to the autocorrelation function $S^{zz}(t)$ before and after the pulse separately. The fit parameters are A, t_0, and φ. Generally, they are different for the fits of the dynamics before and after the pulse. The function $S_{\mathrm{fit}}(t)$ is chosen to comprise a Gaussian envelope modulating the amplitude of the Larmor precession with frequency h. Figure B.1 illustrates this kind of fit, displaying a very nice agreement with the numerical data. From the two fits, the phase shift $\Delta\varphi$ at the pulse boundary can be calculated as

$$\Delta\varphi = |\varphi_{\mathrm{before}} - \varphi_{\mathrm{after}}| \mod 2\pi. \tag{B.2}$$

The labels 'before' and 'after' refer to the fit parameter φ obtained before and after the pulse, respectively.

For pulse model I without nuclear Zeeman effect (Sec. 5.2.1), we always find phase shifts of $\Delta\varphi \approx \pi$ with deviations of up to 3%, i.e., odd resonances in accordance with the analysis of the weight $\Sigma_{\mathrm{even}} < 0.5$.

For pulse model II without nuclear Zeeman effect (Sec. 5.2.2), the phase shift takes values of zero or π depending on the combination of γ and h. The corresponding resonance always matches the resonance displayed by the weight Σ_{even}. Table B.1 provides some phase shifts obtained for different combinations of h and γ.

Note that for combinations of h and γ close to the resonance transition marked by $P = h\gamma^2 = 9 \times 10^{-5} A_\mathrm{Q}$, e.g., $\{h = 80A_\mathrm{Q}, \gamma = 1/\sqrt{2} \times 10^{-3}\}$, it is hard to obtain a reliable value for $\Delta\varphi$ because the revival signal and its statistical error are of the same order of magnitude. In this regime, barely any nuclear focusing takes place.

In the presence of the nuclear Zeeman effect (Sec. 5.3), we always find $\Delta\varphi \approx 0$ for both pulse models I and II, i.e., even resonances in accordance with the analysis of the weight $\Sigma_\mathrm{even} > 0.5$.

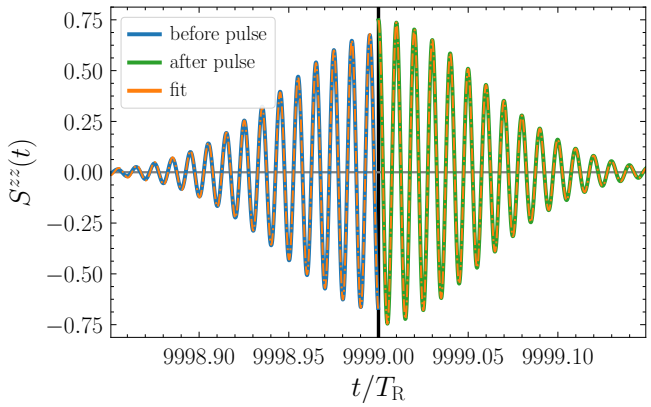

Figure B.1: Example of fitting Eq. (B.1) to the simulated autocorrelation $S^{zz}(t)$ before and after the pulse (fitted separately) to determine the phase shift $\Delta\varphi$ at the pulse boundary, which is highlighted by the black vertical line. The phase shift follows from Eq. (B.2), yielding $\Delta\varphi \approx 1.03\pi$. The data stems from a simulation using pulse model I without nuclear Zeeman effect and setting $h = 40A_\mathrm{Q}$ and $\gamma = 10^{-2}$.

Table B.1: Phase shifts $\Delta\varphi$ for various combinations of g and γ calculated after $n_\mathrm{p} = 10000$ pulses of type II without nuclear Zeeman effect (Sec. 5.2.2).

h	γ	$P = h\gamma^2$	$\Delta\varphi$
$40A_\mathrm{Q}$	10^{-2}	$4 \times 10^{-3} A_\mathrm{Q}$	0.005π
$40A_\mathrm{Q}$	3×10^{-3}	$3.6 \times 10^{-4} A_\mathrm{Q}$	0.077π
$40A_\mathrm{Q}$	10^{-3}	$4 \times 10^{-5} A_\mathrm{Q}$	0.832π
$40A_\mathrm{Q}$	3×10^{-4}	$3.6 \times 10^{-6} A_\mathrm{Q}$	1.024π
$40A_\mathrm{Q}$	10^{-4}	$4 \times 10^{-7} A_\mathrm{Q}$	1.028π
$80A_\mathrm{Q}$	$3/\sqrt{2} \times 10^{-3}$	$3.6 \times 10^{-4} A_\mathrm{Q}$	0.009π
$80A_\mathrm{Q}$	$1/\sqrt{2} \times 10^{-3}$	$4 \times 10^{-5} A_\mathrm{Q}$	1.237π
$80A_\mathrm{Q}$	$1/(3\sqrt{2}) \times 10^{-3}$	$4.\overline{4} \times 10^{-4} A_\mathrm{Q}$	1.027π
$160A_\mathrm{Q}$	10^{-2}	$1.6 \times 10^{-2} A_\mathrm{Q}$	0.005π
$240A_\mathrm{Q}$	10^{-2}	$2.4 \times 10^{-2} A_\mathrm{Q}$	0.011π

Appendix C

Alternative nondeterministic pulse descriptions

It is not straightforward to establish a nondeterministic semiclassical pulse description that *on average* retains the properties of the deterministic pulse (6.6). In this appendix, we discuss three alternatives to the nondeterministic pulse description (6.14) introduced in Sec. 6.2, which is based on the Gaussian TWA, and benchmark them against the deterministic pulse (6.6) and its quantum mechanical counterpart used by Kleinjohann *et al.* [117] in the SML regime without NIFF. We point out that the relations (6.6c) and (6.6d) for the trion pseudospin $\boldsymbol{J}_\mathrm{a}$ remain unchanged in all approaches.

C.1 Discrete truncated Wigner approximation

As a first alternative, the deterministic pulse (6.6) is extended by applying the *discrete* truncated Wigner approximation (DTWA) [232] instead of the Gaussian TWA whenever a pulse is applied. This method acts on a discrete phase space, which, in turn, comprises certain benefits but also disadvantages.

In this approach, each spin component S^α, $\alpha \in \{x, y, z\}$, is sampled from the discrete phase space $\{+1/2, -1/2\}$ so that *all* quantum mechanical moments of the spin of the same component are taken into account correctly. Moreover, the spin length after a pulse is always given by $|\boldsymbol{S}_\mathrm{a}| = \sqrt{3}/2$, not only on average. The

ensuring discrete probability distribution is defined by the probabilities

$$P\left(S_{\mathrm{a}}^{\alpha} = +\frac{1}{2}\right) = \frac{1}{2} + \mathrm{E}[S_{\mathrm{a}}^{\alpha}], \tag{C.1a}$$

$$P\left(S_{\mathrm{a}}^{\alpha} = -\frac{1}{2}\right) = \frac{1}{2} - \mathrm{E}[S_{\mathrm{a}}^{\alpha}], \tag{C.1b}$$

where $\mathrm{E}[S_{\mathrm{a}}^{\alpha}]$ is the mathematical expectation value of this probability distribution given by Eq. (6.14).

The approach works as long as $|S^{\alpha}| \leq 1/2$, e.g., for the first pulse. But since the spin with initial length $\sqrt{3}/2$ precesses according to the equation of motion (6.2a), this condition does not necessarily hold for every pulse, leading to the appearance of negative probabilities in Eq. (C.1). Our heuristic solution consists of effectively truncating the probability distribution, i.e., we set $P(S_{\mathrm{a}}^{z} = 1/2) = 1$ when $S_{\mathrm{b}}^{z} > 1/2$. However, this changes the resulting expectation value of the distribution and thereby, also the revival amplitude in SML steady state without NIFF. Another drawback of the DTWA is the broken rotational spin symmetry resulting from the fact that certain spin axes are treated in a special way.

C.2 Trion probability approach

In another approach, we use S_{b}^{z} to determine the probability to excite a trion. In this interpretation, the system realizes either the ground state electron spin $\boldsymbol{S}$ *or* the trion pseudospin $\boldsymbol{J}$ directly after the pulse.

The circularly polarized pump pulse σ^{-} excites a trion only if the electron spin is in the state $|{\downarrow}\rangle$. In the classical picture, this means that $S_{\mathrm{b}}^{z} = -1/2$ leads to the excitation of a trion and thus, $S_{\mathrm{a}}^{z} = 0$ and $J_{\mathrm{a}}^{z} = -1/2$. For $S_{\mathrm{b}}^{z} = +1/2$, no trion can be excited so that $S_{\mathrm{a}}^{z} = +1/2$ and $J_{\mathrm{a}}^{z} = 0$ follows. More generally, the probability to find the spin in the state $|{\downarrow}\rangle$ and therefore to excite a trion is given by

$$P_{\downarrow} = \frac{1}{2} - S_{\mathrm{b}}^{z}. \tag{C.2}$$

If no trion is excited, the z component of the electron spin simply takes the value $S_{\mathrm{a}}^{z} = +1/2$, whereas the x and y component are sampled from a normal distribution with mean value zero and variance $1/4$ to account for the uncertainty principle as

before in the approach based on the Gaussian TWA. Sampling from the discrete phase space introduced in Sec. C.1 is another option, but the results turn out to be worse.

Mathematically, this procedure leads to expectation values that are identical to the deterministic pulse relation (6.6), but the same issue as discussed in Sec. C.1 arises. Since negative probabilities can appear, the probability distribution needs to be truncated, i.e., we set $P_\downarrow = 1$ if $S_\mathrm{b}^z < -1/2$ and $P_\downarrow = 0$ if $S_\mathrm{b}^z > 1/2$. Eventually, this leads to a deviation of the expectation value from Eq. (6.6) and consequently also to a deviation from the correct revival amplitude in the SML steady state without NIFF.

A potential solution consists of scaling the spin $\boldsymbol{S}_\mathrm{b}$ to the Bloch sphere of spin length 1/2 before applying the pulse. We will see, however, that this procedure leads to the emergence of an unwanted phase shift.

C.3 Comparison to established pulse descriptions

Let us compare the various nondeterministic pulse descriptions to the established deterministic pulse relation (6.6) [113] and its quantum mechanical counterpart used by Kleinjohann *et al.* [117] in the SML regime without NIFF. Note that we do not include the trion pseudospin dynamics introduced in Sec. 6.3 because it has no relevant influence on revival amplitude in this regime.

Figure C.1 shows the revival amplitude $S^\perp$ (upper panel) and the corresponding z component S^z (lower panel) for the following pulse descriptions: quantum mechanical (black), deterministic [green, Eq. (6.6)], Gaussian TWA [orange, Eq. (6.14)], DTWA [blue, Eq. (C.1)], trion probability approach (TPA) [red, Eq. (C.2)], and TPA with scaling to the Bloch sphere (see end of Sec C.2, brown).

As expected, the quantum mechanical and the deterministic results are almost identical. Small deviations stem from the fact that the quantum mechanical results are obtained for only $N = 6$ nuclear spins, which requires the calculation of an additional ensemble average to reduce finite-size effects [117]. These results serve as our benchmark. They show the expected behavior of the revival amplitude, i.e., it approaches the SML steady-state value $S_\mathrm{SML} \approx 0.07735$ given by Eq. (6.9), and there is almost no difference between $S^\perp$ and S^z so that there is no phase shift.

The results for the nondeterministic pulse based on the Gaussian TWA, which is introduced in Sec. 6.2 for the EM I, are in perfect agreement with the benchmark results (quantum mechanical and deterministic). Small deviations stem from the statistical nature of the ensemble average in our approach. We average over $M = 10^6$ configurations here; the statistical deviations scale like $1/\sqrt{M}$.

For the remaining nondeterministic pulse descriptions, we find no satisfying agreement with the benchmark results. As expected, the DTWA and TPA yield a too small revival amplitude in the steady state. By scaling the spin vector $\boldsymbol{S}_\mathrm{b}$ to the Bloch sphere of spin length 1/2 before applying the TPA, the revival amplitude $S^\perp$ reaches the correct steady-state value. But it turns out that the revival amplitude is about two times larger than S^z, i.e., a significant phase shift is introduced by scaling to the Bloch sphere. Such a phase shift does not appear in the benchmark results. Since only the pulse based on the Gaussian TWA yields convincing results, it is the nondeterministic pulse description that we put to use in Chap. 6.

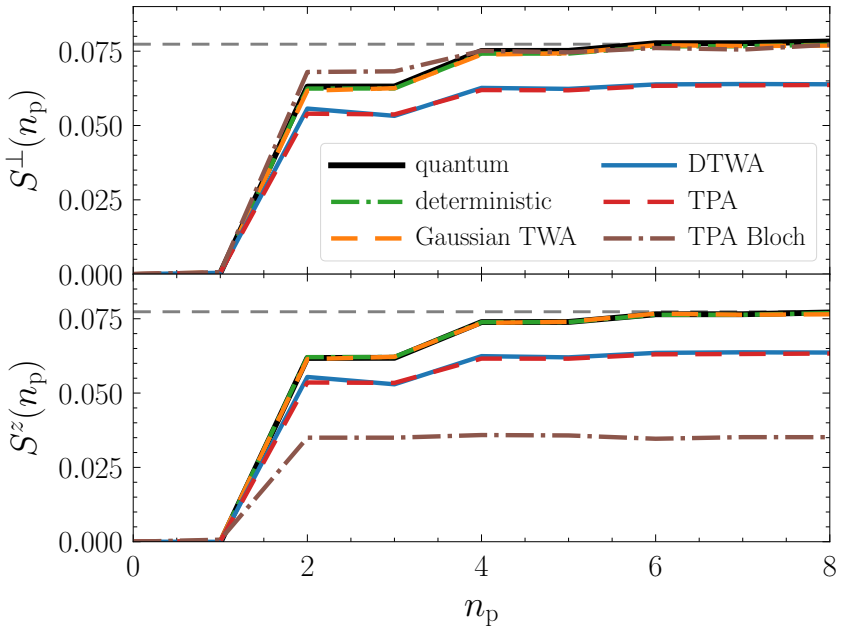

Figure C.1: Buildup of the revival amplitude $S^\perp$ (upper panel) and its z component (lower panel) to the SML steady state without NIFF for the different pulse descriptions discussed in Appendix C, combined with the equations of motion of the initial model used in Sec. 6.1. The gray horizontal dashed line represents the analytical SML steady state value $S_\mathrm{SML} \approx 0.07735$. Parameters: $B_\mathrm{ext} = 1\,\mathrm{T}$, $\gamma = 0.01$, averaged over $M = 10^6$ configurations. The quantum mechanical results are provided by I. Kleinjohann.

Appendix D

Role of the in-plane orientation of the quantum dot sample

The g factor g_h of the unpaired heavy-hole spin in the negatively-charged trion T^- strongly depends on the in-plane orientation of the QD sample, with values ranging from $g_\mathrm{h} = 0.05$ to 0.15 [96, 132]. In the extended models (EM) II and III studied in Chap. 6, the precession of this hole spin about the external magnetic field described by Eq. (6.19) acts as a perturbation to the recombination dynamics responsible for the appearance of the ORC (6.10b) in the results of the initial model and of the the EM I.

D.1 Magnetic field dependence of the revival amplitude

In Fig. D.1(a), we compare the revival amplitude $S^\perp_\mathrm{NESS}$ as a function of the external magnetic field B_ext resulting from the EM II for $g_\mathrm{h} = 0.15$ and $g_\mathrm{h} = 0.05$ at $\gamma = 0.004$. We also study the influence of a finite spread of the g factors existing in an inhomogeneous ensemble of QDs (EM III).[1] We use $\Delta g_\mathrm{e} = 0.005$ [24, 123] and $\Delta g_\mathrm{h} = 0.05$ [132] as in Sec. 6.4. The results for $g_\mathrm{h} = 0.15$ with (EM III, orange) and without (EM II, blue) the spread of the g factors are identical within the accuracy of the data. For $g_\mathrm{h} = 0.05$, the inclusion of the spread results in a larger revival amplitude (red versus green). The observation is very similar for the limit of an infinite bath size ($\gamma \to 0$, not shown). For $\gamma = 0.01$ at $B_\mathrm{ext} = 7.8\,\mathrm{T}$ while using $g_\mathrm{h} = 0.05$, we find $S^\perp_\mathrm{NESS} > S_\mathrm{SML}$ (not by much), hinting at the emergence of a weak ERC instead of the usual ORC at this particular magnetic field (or at no NIFF at all). In the limit $\gamma \to 0$ and also at $\gamma = 0.004$, the revival amplitude at

[1] For simplicity, the notation $\overline{g_\mathrm{e}} = g_\mathrm{e}$ and $\overline{g_\mathrm{h}} = g_\mathrm{h}$ is used here for the EM III.

$B_{\mathrm{ext}} = 7.8\,\mathrm{T}$ is larger than zero but smaller than S_{SML}, implying that the system chooses the ORC.

Comparing $g_{\mathrm{h}} = 0.05$ (red) to 0.15 (orange) for the EM III, the revival amplitude is slightly larger for $g_{\mathrm{h}} = 0.05$. Differences between two samples of QD ensembles were reported in Ref. [117]. In this context, it would be interesting to study the influence of the in-plane orientation of the samples experimentally.

D.2 Dynamic nuclear polarization

Complementary, we compare the results for the DNP B_{DNP} as a function of the magnetic field B_{ext} in Fig. D.1(b). Here, we plot the DNP reached after $S^{\perp}_{\mathrm{NESS}}$ is approximately in saturation, i.e., B_{DNP} is not in its steady state. For the broad range of magnetic fields, reaching the steady state of B_{DNP} is computationally out of reach because two orders of magnitude more pulses need to be simulated. Again, no significant differences are found between the EMs II and III for $g_{\mathrm{h}} = 0.15$. For $g_{\mathrm{h}} = 0.05$, the DNP for the majority of magnetic fields is slightly smaller than for $g_{\mathrm{h}} = 0.15$. This is also the case in the DNP saturation regime at $B_{\mathrm{ext}} = 0.5\,\mathrm{T}$ and 1 T (not shown).

Interestingly, for $g_{\mathrm{h}} = 0.05$ when using the EM III, there is a slight buckling around $B_{\mathrm{ext}} \approx 3.9\,\mathrm{T}$, where no DNP is found for the other cases. There is also a rather large DNP at $B_{\mathrm{ext}} = 7.8\,\mathrm{T}$, where again no DNP is found for the other cases. But note that this particular case needs to be treated cautiously because the spread $\Delta g_{\mathrm{h}} = 0.05$ was obtained for $g_{\mathrm{h}} = 0.15$ [132]. Probably, the behavior is related to the fact that we have combined $g_{\mathrm{h}} = 0.05$ with $\Delta g_{\mathrm{h}} = g_{\mathrm{h}} = 0.05$ so that the g factor can change its sign or be very close to zero in many cases. Especially when it is close to zero, there is no fast Larmor precession of the trion pseudospin about the external magnetic field that can act as a perturbation to the recombination dynamics, i.e., the qualitative behavior of the nonequilibrium spin dynamics can change.

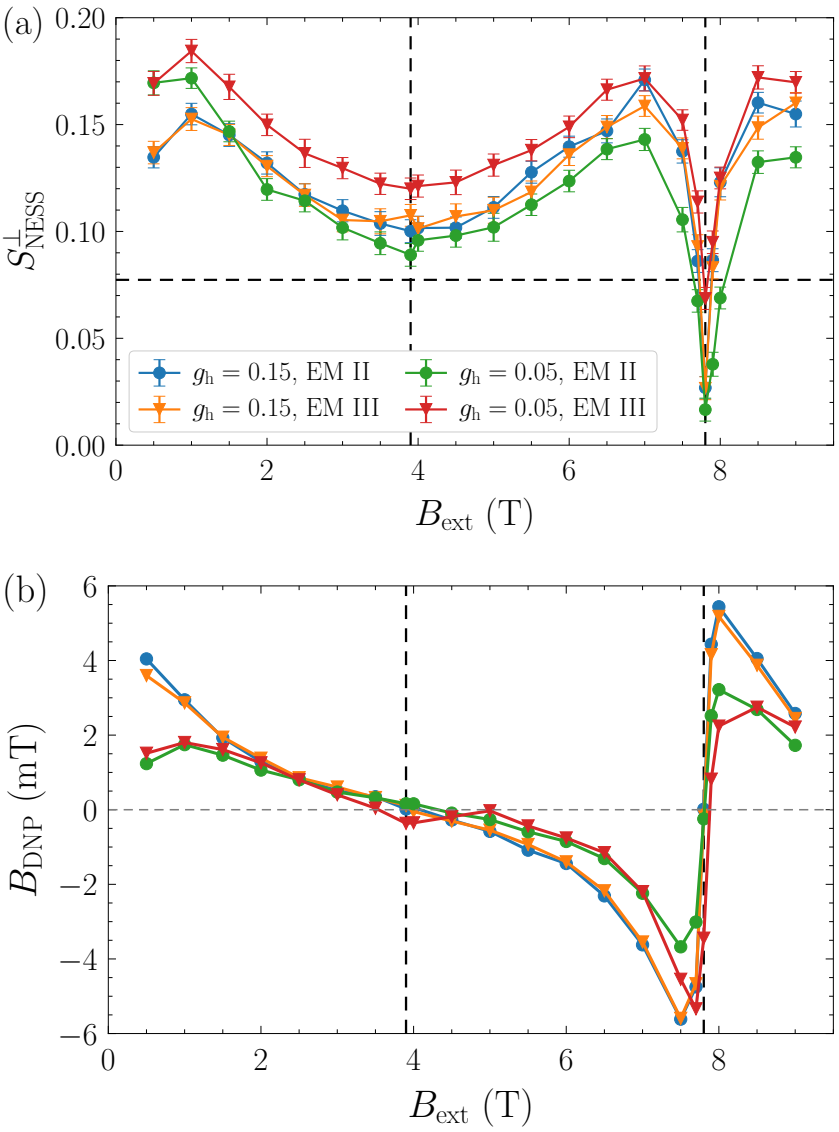

Figure D.1: Influence of the g factor of the trion pseudospin g_{h} on NIFF and DNP for the extended models (EM) II and III at $\gamma = 0.004$: **(a)** Limiting values $S^{\perp}_{\mathrm{NESS}}$ of the revival amplitude as a function of the magnetic field B_{ext}. The vertical dashed lines represent the NRC (6.13) for $k = 1$ and 2, the horizontal dashed line indicates the SML steady-statue value S_{SML}. **(b)** DNP B_{DNP} as a function of the external magnetic field B_{ext}. The number of pulses is chosen such that $S^{\perp}_{\mathrm{NESS}}$ is approximately in its NESS.

Appendix E

Algebraic solution of the equations of motion expanded in the magnetic field for a single nuclear species

When considering only a single nuclear species in the $\mathcal{O}(h^{-1})$ expansion of the classical equations of motion (7.8) introduced in Sec. 7.2, it is possible to describe the dynamics by a set of algebraic relations. For a single isotope, i.e., without any sums over different nuclear species and using the notation $A = A_j$, we have the algebraic relations

$$z_0(t) = \frac{1}{h} b_0 S_0^x \,, \tag{E.1a}$$

$$z_2(t) = -\frac{J^z(0)}{2\tau_0(h - h_\mathrm{h})} \, \mathrm{e}^{-t/\tau_0} \,, \tag{E.1b}$$

$$z_3(t) = -\frac{J^z(0)}{2\tau_0(h + h_\mathrm{h})} \, \mathrm{e}^{-t/\tau_0} \,, \tag{E.1c}$$

$$b_1(t) = -\frac{A}{h} z_1 B_0^x \,, \tag{E.1d}$$

$$S_1^x(t) = -\frac{1}{h} z_1 b_0^* \,, \tag{E.1e}$$

$$B_1^x(t) = \frac{A}{h} z_1 b_0^* \,, \tag{E.1f}$$

$$S_0^x(t) = S_0^x(0) \,, \tag{E.1g}$$

$$B_0^x(t) = B_0^x(0) \,, \tag{E.1h}$$

and the two ordinary differential equations

$$\frac{\mathrm{d}}{\mathrm{d}t} z_1 = \mathrm{i}\left(B_0^x + \frac{A}{h} B_0^x S_0^x + \frac{|b_0|^2}{2h}\right) z_1 \,, \tag{E.2a}$$

$$\frac{\mathrm{d}}{\mathrm{d}t} b_0 = \mathrm{i}\left[A S_0^x \left(1 - \frac{B_0^x}{h}\right) + h_\mathrm{n} - \frac{A^2}{2h}|z_1|^2\right] b_0 \,. \tag{E.2b}$$

The differential equations imply that z_1 and b_0 only change their phase but not their length. Hence, they can be solved by inserting the complex exponential functions

$$z_1(t) = z_1(0)\, \mathrm{e}^{\mathrm{i}\varphi_{z_1}(t)} \,, \tag{E.3a}$$

$$b_0(t) = b_0(0)\, \mathrm{e}^{\mathrm{i}\varphi_{b_0}(t)} \,, \tag{E.3b}$$

yielding the two new ordinary differential equations

$$\frac{\mathrm{d}}{\mathrm{d}t} \varphi_{z_1} = B_0^x + \frac{A}{h} S_0^x B_0^x + \frac{|b_0|^2}{2h} \,, \tag{E.4a}$$

$$\frac{\mathrm{d}}{\mathrm{d}t} \varphi_{b_0} = A S_0^x \left(1 - \frac{B_0^x}{h}\right) + h_\mathrm{n} - \frac{A^2}{2h}|z_1|^2 \,, \tag{E.4b}$$

with $|z_1(t)|^2 = |z_1(0)|^2$ and $|b_0(t)|^2 = |b_0(0)|^2$. Thanks to $S_0^x(t) = S_0^x(0)$ and $B_0^x(t) = B_0^x(0)$, the right-hand sides of the two differential equations are time-independent so that their integration simply yields the two linear equations

$$\varphi_{z_1}(t) = \left(B_0^x(0) + \frac{A}{h} S_0^x(0) B_0^x(0) + \frac{|b_0(0)|^2}{2h}\right) t \,, \tag{E.5a}$$

$$\varphi_{b_0}(t) = \left[A S_0^x(0) \left(1 - \frac{B_0^x(0)}{h}\right) + h_\mathrm{n} - \frac{A^2}{2h}|z_1(0)|^2\right] t \,, \tag{E.5b}$$

starting from the initial conditions $\varphi_{z_1}(0) = \varphi_{b_0}(0) = 0$.

Provided all initial conditions are known, the dynamics in $\mathcal{O}(h^{-1})$ is fully determined by the algebraic relations (E.1) and (E.5), i.e., no numerical integration of differential equations is required.

The procedure to determine the correct initial conditions is very similar to the one used in Sec. 7.2.2. We determine the initial values by inserting $t = 0$ into the algebraic relations (E.1). The time argument $t = 0$ is omitted for brevity in the following. The known initial conditions are z, b, S^x, B^x, and J^z, from which we

have to deduce the initial conditions of the expansion variables z_0, z_1, b_0, b_1, S_0^x, S_1^x, B_0^x, and B_1^x. First, we know that $z_1 = z - z_0 - z_2 - z_3$ and $b_0 = b - b_1$, with

$$z_0 = \frac{1}{h} b_0 S_0^x \,, \tag{E.6a}$$

$$z_2 = -\frac{J^z}{2\tau_0 (h - h_\mathrm{h})} \,, \tag{E.6b}$$

$$z_3 = -\frac{J^z}{2\tau_0 (h + h_\mathrm{h})} \,, \tag{E.6c}$$

$$b_1 = -\frac{A}{h} z_1 B_0^x \,. \tag{E.6d}$$

The initial conditions for z_2 and z_3 are known, but this is not the case for z_0 and b_1. They depend on b_0 and z_1, for which we have

$$z_1 = z - \frac{1}{h} b_0 S_0^x + \frac{J^z}{2\tau_0} \left(\frac{1}{h + h_\mathrm{h}} + \frac{1}{h - h_\mathrm{h}} \right) , \tag{E.7}$$

$$b_0 = b + \frac{A}{h} z_1 B_0^x \,. \tag{E.8}$$

Thus, we need to find either b_0 or z_1; we opt for b_0. To this end, we define

$$F := \mathrm{Re}(z_1 b_0^*) \tag{E.9a}$$

$$= \mathrm{Re} \left[z^* b_0 + \frac{J^z}{2\tau_0} b_0 \left(\frac{1}{h + h_\mathrm{h}} + \frac{1}{h - h_\mathrm{h}} \right) \right] - \frac{|b_0|^2}{h} \left(S^x + \frac{F}{h} \right) . \tag{E.9b}$$

and express the initial conditions for S_0^x and B_0^x as

$$S_0^x = S^x + \frac{1}{h} F \,, \tag{E.10a}$$

$$B_0^x = B^x - \frac{A}{h} F \,. \tag{E.10b}$$

Next, we can express Eq. (E.9b) solely via b_0 besides other known quantities. After a few algebraic transformations, we find

$$F = \frac{\mathrm{Re} \left[z^* b_0 + \frac{J^z}{2\tau_0} b_0 \left(\frac{1}{h + h_\mathrm{h}} + \frac{1}{h - h_\mathrm{h}} \right) \right] - \frac{|b_0|^2}{h} S^x}{1 + \frac{|b_0|^2}{h}} \,. \tag{E.11}$$

But we can also express b_0 via F, which results in

$$b_0 = b + \frac{A}{h}\left[z - \frac{1}{h}b_0\left(S^x + \frac{1}{h}F\right) + \frac{J^z}{2\tau_0}\left(\frac{1}{h+h_\mathrm{h}} + \frac{1}{h-h_\mathrm{h}}\right)\right]\left(B^x - \frac{A}{h}F\right). \quad \text{(E.12)}$$

Since F depends only on b_0, this expression also depends only on b_0, but in a nonlinear and nonpolynomial way. However, all corrections on the right-hand side are suppressed by at least a factor of h^{-1} so that the relevant zero for b_0 is quickly found by iteration starting from $b_0 = b$. Fast convergence is reached within approximately five iteration steps. Afterwards, F can be calculated by using Eq. (E.11). Thus, all initial conditions are now fully determined. The missing ones are given by

$$S_1^x = -\frac{1}{h}z_1 b_0^*\,, \quad \text{(E.13a)}$$

$$B_1^x = \frac{A}{h}z_1 b_0^*\,. \quad \text{(E.13b)}$$

Bibliography

[1] M. A. Nielsen and I. L. Chuang, *Quantum Computation and Quantum Information: 10th Anniversary Edition* (Cambridge University Press, Cambridge, 2010).

[2] P. W. Shor, "Algorithms for quantum computation: discrete logarithms and factoring", in *Proceedings 35th Annual Symposium on Foundations of Computer Science* (1994), pp. 124–134.

[3] P. W. Shor, *Polynomial-Time Algorithms for Prime Factorization and Discrete Logarithms on a Quantum Computer*, SIAM Rev. **41**, 303–332 (1997).

[4] L. K. Grover, *Quantum Mechanics Helps in Searching for a Needle in a Haystack*, Phys. Rev. Lett. **79**, 325–328 (1997).

[5] R. P. Feynman, *Simulating physics with computers*, Int. J. Theor. Phys. **21**, 467–488 (1982).

[6] I. M. Georgescu, S. Ashhab, and F. Nori, *Quantum simulation*, Rev. Mod. Phys. **86**, 153–185 (2014).

[7] F. Arute, K. Arya, R. Babbush, D. Bacon, J. C. Bardin, R. Barends, R. Biswas, S. Boixo, F. G. S. L. Brandao, D. A. Buell, B. Burkett, Y. Chen, Z. Chen, *et al.*, *Quantum supremacy using a programmable superconducting processor*, Nature **574**, 505–510 (2019).

[8] H.-S. Zhong, H. Wang, Y.-H. Deng, M.-C. Chen, L.-C. Peng, Y.-H. Luo, J. Qin, D. Wu, X. Ding, Y. Hu, P. Hu, X.-Y. Yang, W.-J. Zhang, *et al.*, *Quantum computational advantage using photons*, Science **370**, 1460–1463 (2020).

[9] E. Pednault, J. A. Gunnels, G. Nannicini, L. Horesh, and R. Wisnieff, *Leveraging Secondary Storage to Simulate Deep 54-qubit Sycamore Circuits*, arXiv:1910.09534 (2019).

[10] J. Koch, T. M. Yu, J. Gambetta, A. A. Houck, D. I. Schuster, J. Majer, A. Blais, M. H. Devoret, S. M. Girvin, and R. J. Schoelkopf, *Charge-insensitive qubit design derived from the Cooper pair box*, Phys. Rev. A **76**, 042319 (2007).

[11] T. D. Ladd, F. Jelezko, R. Laflamme, Y. Nakamura, C. Monroe, and J. L. O'Brien, *Quantum computers*, Nature **464**, 45–53 (2010).

[12] D. P. DiVincenzo, *The Physical Implementation of Quantum Computation*, Fortschr. Phys. **48**, 771–783 (2000).

[13] D. Loss and D. P. DiVincenzo, *Quantum computation with quantum dots*, Phys. Rev. A **57**, 120–126 (1998).

[14] R.-B. Liu, W. Yao, and L. Sham, *Quantum computing by optical control of electron spins*, Adv. Phys. **59**, 703–802 (2010).

[15] A. P. Alivisatos, *Semiconductor Clusters, Nanocrystals, and Quantum Dots*, Science **271**, 933–937 (1996).

[16] R. C. Ashoori, *Electrons in artificial atoms*, Nature **379**, 413–419 (1996).

[17] U. Banin, Y. Cao, D. Katz, and O. Millo, *Identification of atomic-like electronic states in indium arsenide nanocrystal quantum dots*, Nature **400**, 542–544 (1999).

[18] R. Hanson, L. P. Kouwenhoven, J. R. Petta, S. Tarucha, and L. M. K. Vandersypen, *Spins in few-electron quantum dots*, Rev. Mod. Phys. **79**, 1217–1265 (2007).

[19] B. Urbaszek, X. Marie, T. Amand, O. Krebs, P. Voisin, P. Maletinsky, A. Högele, and A. Imamoglu, *Nuclear spin physics in quantum dots: An optical investigation*, Rev. Mod. Phys. **85**, 79–133 (2013).

[20] N. H. Bonadeo, J. Erland, D. Gammon, D. Park, D. S. Katzer, and D. G. Steel, *Coherent Optical Control of the Quantum State of a Single Quantum Dot*, Science **282**, 1473–1476 (1998).

[21] J. R. Petta, A. C. Johnson, J. M. Taylor, E. A. Laird, A. Yacoby, M. D. Lukin, C. M. Marcus, M. P. Hanson, and A. C. Gossard, *Coherent Manipulation of Coupled Electron Spins in Semiconductor Quantum Dots*, Science **309**, 2180–2184 (2005).

[22] F. H. L. Koppens, C. Buizert, K. J. Tielrooij, I. T. Vink, K. C. Nowack, T. Meunier, L. P. Kouwenhoven, and L. M. K. Vandersypen, *Driven coherent oscillations of a single electron spin in a quantum dot*, Nature **442**, 766–771 (2006).

[23] A. Greilich, R. Oulton, E. A. Zhukov, I. A. Yugova, D. R. Yakovlev, M. Bayer, A. Shabaev, A. L. Efros, I. A. Merkulov, V. Stavarache, D. Reuter, and A. Wieck, *Optical Control of Spin Coherence in Singly Charged (In,Ga)As/GaAs Quantum Dots*, Phys. Rev. Lett. **96**, 227401 (2006).

[24] A. Greilich, D. R. Yakovlev, A. Shabaev, A. L. Efros, I. A. Yugova, R. Oulton, V. Stavarache, D. Reuter, A. Wieck, and M. Bayer, *Mode Locking of Electron Spin Coherences in Quantum Dots*, Science **313**, 341–345 (2006).

[25] A. Greilich, A. Shabaev, D. R. Yakovlev, A. L. Efros, I. A. Yugova, D. Reuter, A. D. Wieck, and M. Bayer, *Nuclei-Induced Frequency Focusing of Electron Spin Coherence*, Science **317**, 1896–1899 (2007).

[26] A. Greilich, M. Wiemann, F. G. G. Hernandez, D. R. Yakovlev, I. A. Yugova, M. Bayer, A. Shabaev, A. L. Efros, D. Reuter, and A. D. Wieck, *Robust manipulation of electron spin coherence in an ensemble of singly charged quantum dots*, Phys. Rev. B **75**, 233301 (2007).

[27] K. C. Nowack, F. H. L. Koppens, Y. V. Nazarov, and L. M. K. Vandersypen, *Coherent Control of a Single Electron Spin with Electric Fields*, Science **318**, 1430–1433 (2007).

[28] F. H. L. Koppens, K. C. Nowack, and L. M. K. Vandersypen, *Spin Echo of a Single Electron Spin in a Quantum Dot*, Phys. Rev. Lett. **100**, 236802 (2008).

[29] J. Berezovsky, M. H. Mikkelsen, N. G. Stoltz, L. A. Coldren, and D. D. Awschalom, *Picosecond Coherent Optical Manipulation of a Single Electron Spin in a Quantum Dot*, Science **320**, 349–352 (2008).

[30] A. Greilich, S. E. Economou, S. Spatzek, D. R. Yakovlev, D. Reuter, A. D. Wieck, T. L. Reinecke, and M. Bayer, *Ultrafast optical rotations of electron spins in quantum dots*, Nat. Phys. **5**, 262–266 (2009).

[31] A. Greilich, S. G. Carter, D. Kim, A. S. Bracker, and D. Gammon, *Optical control of one and two hole spins in interacting quantum dots*, Nat. Photonics **5**, 702–708 (2011).

[32] D. Kim, S. G. Carter, A. Greilich, A. S. Bracker, and D. Gammon, *Ultrafast optical control of entanglement between two quantum-dot spins*, Nat. Phys. **7**, 223–229 (2011).

[33] K. De Greve, P. L. McMahon, D. Press, T. D. Ladd, D. Bisping, C. Schneider, M. Kamp, L. Worschech, S. Höfling, A. Forchel, and Y. Yamamoto, *Ultrafast coherent control and suppressed nuclear feedback of a single quantum dot hole qubit*, Nat. Phys. **7**, 872–878 (2011).

[34] H. Bluhm, S. Foletti, I. Neder, M. Rudner, D. Mahalu, V. Umansky, and A. Yacoby, *Dephasing time of GaAs electron-spin qubits coupled to a nuclear bath exceeding 200 μs*, Nat. Phys. **7**, 109–113 (2011).

[35] T. M. Godden, J. H. Quilter, A. J. Ramsay, Y. Wu, P. Brereton, S. J. Boyle, I. J. Luxmoore, J. Puebla-Nunez, A. M. Fox, and M. S. Skolnick, *Coherent Optical Control of the Spin of a Single Hole in an* InAs/GaAs *Quantum Dot*, Phys. Rev. Lett. **108**, 017402 (2012).

[36] R. Hanson and D. D. Awschalom, *Coherent manipulation of single spins in semiconductors*, Nature **453**, 1043–1049 (2008).

[37] A. J. Ramsay, *A review of the coherent optical control of the exciton and spin states of semiconductor quantum dots*, Semicond. Sci. Technol. **25**, 103001 (2010).

[38] R. J. Warburton, *Single spins in self-assembled quantum dots*, Nat. Mater. **12**, 483–493 (2013).

[39] W. M. Witzel and S. D. Sarma, *Multiple-Pulse Coherence Enhancement of Solid State Spin Qubits*, Phys. Rev. Lett. **98**, 077601 (2007).

[40] P. Michler (ed.), *Quantum Dots for Quantum Information Technologies*, Nano-Optics and Nanophotonics (Springer, Cham, CH, 2017).

[41] D. Press, T. D. Ladd, B. Zhang, and Y. Yamamoto, *Complete quantum control of a single quantum dot spin using ultrafast optical pulses*, Nature **456**, 218–221 (2008).

[42] E. A. Chekhovich, M. N. Makhonin, A. I. Tartakovskii, A. Yacoby, H. Bluhm, K. C. Nowack, and L. M. K. Vandersypen, *Nuclear spin effects in semiconductor quantum dots*, Nat. Mater. **12**, 494–504 (2013).

[43] A. Imamoḡlu, E. Knill, L. Tian, and P. Zoller, *Optical Pumping of Quantum-Dot Nuclear Spins*, Phys. Rev. Lett. **91**, 017402 (2003).

[44] D. J. Reilly, J. M. Taylor, J. R. Petta, C. M. Marcus, M. P. Hanson, and A. C. Gossard, *Suppressing Spin Qubit Dephasing by Nuclear State Preparation*, Science **321**, 817–821 (2008).

[45] S. Meiboom and D. Gill, *Modified Spin-Echo Method for Measuring Nuclear Relaxation Times*, Rev. Sci. Instrum. **29**, 688–691 (1958).

[46] S. Varwig, E. Evers, A. Greilich, D. R. Yakovlev, D. Reuter, A. D. Wieck, and M. Bayer, *All-optical implementation of a dynamic decoupling protocol for hole spins in (In,Ga)As quantum dots*, Phys. Rev. B **90**, 121306(R) (2014).

[47] L. Huthmacher, R. Stockill, E. Clarke, M. Hugues, C. Le Gall, and M. Atatüre, *Coherence of a dynamically decoupled quantum-dot hole spin*, Phys. Rev. B **97**, 241413(R) (2018).

[48] G. S. Uhrig, *Keeping a Quantum Bit Alive by Optimized π-Pulse Sequences*, Phys. Rev. Lett. **98**, 100504 (2007).

[49] B. Lee, W. M. Witzel, and S. Das Sarma, *Universal Pulse Sequence to Minimize Spin Dephasing in the Central Spin Decoherence Problem*, Phys. Rev. Lett. **100**, 160505 (2008).

[50] M. J. Biercuk, H. Uys, A. P. VanDevender, N. Shiga, W. M. Itano, and J. J. Bollinger, *Optimized dynamical decoupling in a model quantum memory*, Nature **458**, 996–1000 (2009).

[51] M. J. Biercuk, H. Uys, A. P. VanDevender, N. Shiga, W. M. Itano, and J. J. Bollinger, *Experimental Uhrig dynamical decoupling using trapped ions*, Phys. Rev. A **79**, 062324 (2009).

[52] J. Du, X. Rong, N. Zhao, Y. Wang, J. Yang, and R. B. Liu, *Preserving electron spin coherence in solids by optimal dynamical decoupling*, Nature **461**, 1265–1268 (2009).

[53] L. Viola and S. Lloyd, *Dynamical suppression of decoherence in two-state quantum systems*, Phys. Rev. A **58**, 2733–2744 (1998).

[54] L. Viola, E. Knill, and S. Lloyd, *Dynamical Decoupling of Open Quantum Systems*, Phys. Rev. Lett. **82**, 2417–2421 (1999).

[55] K. Khodjasteh and D. A. Lidar, *Performance of deterministic dynamical decoupling schemes: Concatenated and periodic pulse sequences*, Phys. Rev. A **75**, 062310 (2007).

[56] G. S. Uhrig, *Exact results on dynamical decoupling by π pulses in quantum information processing*, New J. Phys. **10**, 083024 (2008).

[57] G. S. Uhrig, *Concatenated Control Sequences Based on Optimized Dynamic Decoupling*, Phys. Rev. Lett. **102**, 120502 (2009).

[58] S. Pasini and G. S. Uhrig, *Optimized dynamical decoupling for power-law noise spectra*, Phys. Rev. A **81**, 012309 (2010).

[59] K. Khodjasteh, D. A. Lidar, and L. Viola, *Arbitrarily Accurate Dynamical Control in Open Quantum Systems*, Phys. Rev. Lett. **104**, 090501 (2010).

[60] J. R. West, D. A. Lidar, B. H. Fong, and M. F. Gyure, *High Fidelity Quantum Gates via Dynamical Decoupling*, Phys. Rev. Lett. **105**, 230503 (2010).

[61] G. de Lange, Z. H. Wang, D. Ristè, V. V. Dobrovitski, and R. Hanson, *Universal Dynamical Decoupling of a Single Solid-State Spin from a Spin Bath*, Science **330**, 60–63 (2010).

[62] J. Medford, Ł. Cywiński, C. Barthel, C. M. Marcus, M. P. Hanson, and A. C. Gossard, *Scaling of Dynamical Decoupling for Spin Qubits*, Phys. Rev. Lett. **108**, 086802 (2012).

[63] D. A. Lidar, "Review of Decoherence-Free Subspaces, Noiseless Subsystems, and Dynamical Decoupling", in *Quantum Information and Computation for Chemistry*, edited by S. A. Rice, A. R. Dinner, and S. Kais (John Wiley & Sons, Inc., Hoboken, NJ, 2014), pp. 295–354.

[64] M. Issler, E. M. Kessler, G. Giedke, S. Yelin, I. Cirac, M. D. Lukin, and A. Imamoglu, *Nuclear Spin Cooling Using Overhauser-Field Selective Coherent Population Trapping*, Phys. Rev. Lett. **105**, 267202 (2010).

[65] J. H. Prechtel, A. V. Kuhlmann, J. Houel, A. Ludwig, S. R. Valentin, A. D. Wieck, and R. J. Warburton, *Decoupling a hole spin qubit from the nuclear spins*, Nat. Mater. **15**, 981–986 (2016).

[66] G. Éthier-Majcher, D. Gangloff, R. Stockill, E. Clarke, M. Hugues, C. Le Gall, and M. Atatüre, *Improving a Solid-State Qubit through an Engineered Mesoscopic Environment*, Phys. Rev. Lett. **119**, 130503 (2017).

[67] J. M. Taylor, C. M. Marcus, and M. D. Lukin, *Long-Lived Memory for Mesoscopic Quantum Bits*, Phys. Rev. Lett. **90**, 206803 (2003).

[68] P. Maletinsky, M. Kroner, and A. Imamoglu, *Breakdown of the nuclear-spin-temperature approach in quantum-dot demagnetization experiments*, Nat. Phys. **5**, 407–411 (2009).

[69] C. Latta, A. Srivastava, and A. Imamoglu, *Hyperfine Interaction-Dominated Dynamics of Nuclear Spins in Self-Assembled InGaAs Quantum Dots*, Phys. Rev. Lett. **107**, 167401 (2011).

[70] D. A. Gangloff, G. Éthier-Majcher, C. Lang, E. V. Denning, J. H. Bodey, D. M. Jackson, E. Clarke, M. Hugues, C. Le Gall, and M. Atatüre, *Quantum interface of an electron and a nuclear ensemble*, Science **364**, 62–66 (2019).

[71] E. V. Denning, D. A. Gangloff, M. Atatüre, J. Mørk, and C. Le Gall, *Collective Quantum Memory Activated by a Driven Central Spin*, Phys. Rev. Lett. **123**, 140502 (2019).

[72] E. A. Chekhovich and A. da Silva Saimon F. Covre and Rastelli, *Nuclear spin quantum register in an optically active semiconductor quantum dot*, Nat. Nanotechnol. **15**, 999–1004 (2020).

[73] D. M. Jackson, D. A. Gangloff, J. H. Bodey, L. Zaporski, C. Bachorz, E. Clarke, M. Hugues, C. Le Gall, and M. Atatüre, *Quantum sensing of a coherent single spin excitation in a nuclear ensemble*, Nat. Phys. **17**, 585–590 (2021).

[74] M. Bayer, *All for one and one for all*, Science **364**, 30–31 (2019).

[75] A. Greilich, S. Spatzek, I. A. Yugova, I. A. Akimov, D. R. Yakovlev, A. L. Efros, D. Reuter, A. D. Wieck, and M. Bayer, *Collective single-mode precession of electron spins in an ensemble of singly charged (In,Ga)As/GaAs quantum dots*, Phys. Rev. B **79**, 201305(R) (2009).

[76] E. Evers, N. E. Kopteva, I. A. Yugova, D. R. Yakovlev, D. Reuter, A. D. Wieck, M. Bayer, and A. Greilich, *Suppression of nuclear spin fluctuations in an InGaAs quantum dot ensemble by GHz-pulsed optical excitation*, npj Quantum Inf. **7**, 60 (2021).

[77] D. D. Awschalom, D. Loss, and N. Samarth (eds.), *Semiconductor Spintronics and Quantum Computation*, NanoScience and Technology (Springer, Berlin, 2002).

[78] A. Hirohata, K. Yamada, Y. Nakatani, I.-L. Prejbeanu, B. Diény, P. Pirro, and B. Hillebrands, *Review on spintronics: Principles and device applications*, J. Magn. Magn. Mater. **509**, 166711 (2020).

[79] L. Stranski I. N. and Krastanow, *Zur Theorie der orientierten Ausscheidung von Ionenkristallen aufeinander*, Monatsh. Chem. **71**, 351–364 (1937).

[80] L. Goldstein, F. Glas, J. Y. Marzin, M. N. Charasse, and G. Le Roux, *Growth by molecular beam epitaxy and characterization of InAs/GaAs strained-layer superlattices*, Appl. Phys. Lett. **47**, 1099–1101 (1985).

[81] D. Leonard, K. Pond, and P. M. Petroff, *Critical layer thickness for self-assembled InAs islands on GaAs*, Phys. Rev. B **50**, 11687–11692 (1994).

[82] X. Marie, B. Urbaszek, O. Krebs, and T. Amand, "Exciton Spin Dynamics in Semicondcutor Quantum Dots", in *Spin Physics in Semiconductors*, Vol. 157, edited by M. I. Dyakonov, 2nd ed., Springer Series in Solid-State Sciences (Springer, Cham, CH, 2017), pp. 105–129.

[83] H. Eisele, A. Lenz, R. Heitz, R. Timm, M. Dähne, Y. Temko, T. Suzuki, and K. Jacobi, *Change of InAs/GaAs quantum dot shape and composition during capping*, J. Appl. Phys. **104**, 124301 (2008).

[84] S. Malik, C. Roberts, R. Murray, and M. Pate, *Tuning self-assembled InAs quantum dots by rapid thermal annealing*, Appl. Phys. Lett. **71**, 1987–1989 (1997).

[85] R. Leon, S. Fafard, P. G. Piva, S. Ruvimov, and Z. Liliental-Weber, *Tunable intersublevel transitions in self-forming semiconductor quantum dots*, Phys. Rev. B **58**, R4262(R) (1998).

[86] S. Fafard and C. N. Allen, *Intermixing in quantum-dot ensembles with sharp adjustable shells*, Appl. Phys. Lett. **75**, 2374–2376 (1999).

[87] O. Gunawan, H. S. Djie, and B. S. Ooi, *Electronics states of interdiffused quantum dots*, Phys. Rev. B **71**, 205319 (2005).

[88] M. Y. Petrov, I. V. Ignatiev, S. V. Poltavtsev, A. Greilich, A. Bauschulte, D. R. Yakovlev, and M. Bayer, *Effect of thermal annealing on the hyperfine interaction in InAs/GaAs quantum dots*, Phys. Rev. B **78**, 045315 (2008).

[89] A. O. Kosogov, P. Werner, U. Gösele, N. N. Ledentsov, D. Bimberg, V. M. Ustinov, A. Y. Egorov, A. E. Zhukov, P. S. Kop'ev, N. A. Bert, and Z. I. Alferov, *Structural and optical properties of InAs–GaAs quantum dots subjected to high temperature annealing*, Appl. Phys. Lett. **69**, 3072–3074 (1996).

[90] S. Bietti, L. Esposito, A. Fedorov, A. Ballabio, A. Martinelli, and S. Sanguinetti, *Characterization and Effect of Thermal Annealing on InAs Quantum Dots Grown by Droplet Epitaxy on GaAs(111)A Substrates*, Nanoscale Res. Lett. **10**, 247 (2015).

[91] S. Cortez, O. Krebs, S. Laurent, M. Senes, X. Marie, P. Voisin, R. Ferreira, G. Bastard, J.-M. Gérard, and T. Amand, *Optically Driven Spin Memory in n-Doped InAs-GaAs Quantum Dots*, Phys. Rev. Lett. **89**, 207401 (2002).

[92] S. Laurent, M. Senes, O. Krebs, V. K. Kalevich, B. Urbaszek, X. Marie, T. Amand, and P. Voisin, *Negative circular polarization as a general property of n-doped self-assembled* InAs/GaAs *quantum dots under nonresonant optical excitation*, Phys. Rev. B **73**, 235302 (2006).

[93] E. A. Zhukov, E. Kirstein, D. S. Smirnov, D. R. Yakovlev, M. M. Glazov, D. Reuter, A. D. Wieck, M. Bayer, and A. Greilich, *Spin inertia of resident and photoexcited carriers in singly charged quantum dots*, Phys. Rev. B **98**, 121304(R) (2018).

[94] P. Schering, E. Evers, V. Nedelea, D. S. Smirnov, E. A. Zhukov, D. R. Yakovlev, M. Bayer, G. S. Uhrig, and A. Greilich, *Resonant spin amplification in Faraday geometry*, Phys. Rev. B **103**, L201301 (2021).

[95] S. Varwig, A. Greilich, D. R. Yakovlev, and M. Bayer, *Spin mode locking in quantum dots revisited*, Phys. Status Solidi B **251**, 1892–1911 (2014).

[96] S. A. Crooker, J. Brandt, C. Sandfort, A. Greilich, D. R. Yakovlev, D. Reuter, A. D. Wieck, and M. Bayer, *Spin Noise of Electrons and Holes in Self-Assembled Quantum Dots*, Phys. Rev. Lett. **104**, 036601 (2010).

[97] P. Glasenapp, D. S. Smirnov, A. Greilich, J. Hackmann, M. M. Glazov, F. B. Anders, and M. Bayer, *Spin noise of electrons and holes in (In,Ga)As quantum dots: Experiment and theory*, Phys. Rev. B **93**, 205429 (2016).

[98] E. A. Zhukov, E. Kirstein, N. E. Kopteva, F. Heisterkamp, V. L. Yugova I. A. and Korenev, D. R. Yakovlev, A. Pawlis, M. Bayer, and A. Greilich, *Discretization of the total magnetic field by the nuclear spin bath in fluorine-doped ZnSe*, Nat. Commun. **9**, 1941 (2018).

[99] L. E. Brus, *Electron–electron and electron-hole interactions in small semiconductor crystallites: The size dependence of the lowest excited electronic state*, J. Chem. Phys. **80**, 4403–4409 (1984).

[100] J.-Y. Marzin, J.-M. Gérard, A. Izraël, D. Barrier, and G. Bastard, *Photoluminescence of Single InAs Quantum Dots Obtained by Self-Organized Growth on GaAs*, Phys. Rev. Lett. **73**, 716–719 (1994).

[101] P. Michler, A. Kiraz, C. Becher, W. V. Schoenfeld, P. M. Petroff, L. Zhang, E. Hu, and A. Imamoglu, *A Quantum Dot Single-Photon Turnstile Device*, Science **290**, 2282–2285 (2000).

[102] A. Högele, S. Seidl, M. Kroner, K. Karrai, R. J. Warburton, B. D. Gerardot, and P. M. Petroff, *Voltage-Controlled Optics of a Quantum Dot*, Phys. Rev. Lett. **93**, 217401 (2004).

[103] D. Gammon, S. W. Brown, E. S. Snow, T. A. Kennedy, D. S. Katzer, and D. Park, *Nuclear Spectroscopy in Single Quantum Dots: Nanoscopic Raman Scattering and Nuclear Magnetic Resonance*, Science **277**, 85–88 (1997).

[104] I. A. Merkulov, A. L. Efros, and M. Rosen, *Electron spin relaxation by nuclei in semiconductor quantum dots*, Phys. Rev. B **65**, 205309 (2002).

[105] A. V. Khaetskii, D. Loss, and L. Glazman, *Electron Spin Decoherence in Quantum Dots due to Interaction with Nuclei*, Phys. Rev. Lett. **88**, 186802 (2002).

[106] J. Schliemann, A. Khaetskii, and D. Loss, *Electron spin dynamics in quantum dots and related nanostructures due to hyperfine interaction with nuclei*, J. Phys. Condens. Matter **15**, R1809–R1833 (2003).

[107] S. Lee, P. von Allmen, F. Oyafuso, G. Klimeck, and K. B. Whaley, *Effect of electron-nuclear spin interactions for electron-spin qubits localized in InGaAs self-assembled quantum dots*, J. Appl. Phys. **97**, 043706 (2005).

[108] F. Meier and B. P. Zakharchenya (eds.), *Optical Orientation*, Vol. 8, Modern Problems in Condensed Matter Sciences (North Holland, Amsterdam, 1984).

[109] M. I. Dyakonov, "Basics of Semiconductor and Spin Physics", in *Spin Physics in Semiconductors*, Vol. 157, edited by M. I. Dyakonov, 2nd ed., Springer Series in Solid-State Sciences (Springer, Cham, CH, 2017), pp. 1–37.

[110] S. E. Economou and T. L. Reinecke, "Optical induced spin rotations in quantum dots", in *Optical Generation and Control of Quantum Coherence in Semiconductor Nanostructures*, edited by G. Slavcheva and P. Roussignol, NanoScience and Technology (Springer-Verlag, Berlin, Heidelberg, 2010), pp. 63–84.

[111] A. Greilich, M. Schwab, T. Berstermann, T. Auer, R. Oulton, D. R. Yakovlev, M. Bayer, V. Stavarache, D. Reuter, and A. Wieck, *Tailored quantum dots for entangled photon pair creation*, Phys. Rev. B **73**, 045323 (2006).

[112] A. Shabaev, A. L. Efros, D. Gammon, and I. A. Merkulov, *Optical readout and initialization of an electron spin in a single quantum dot*, Phys. Rev. B **68**, 201305(R) (2003).

[113] I. A. Yugova, M. M. Glazov, E. L. Ivchenko, and A. L. Efros, *Pump-probe Faraday rotation and ellipticity in an ensemble of singly charged quantum dots*, Phys. Rev. B **80**, 104436 (2009).

[114] M. M. Glazov, *Coherent spin dynamics of electrons and excitons in nanostructures (a review)*, Phys. Solid State **54**, 1–27 (2012).

[115] M. M. Glazov, *Electron & Nuclear Spin Dynamics in Semiconductor Nanostructures*, Vol. 23, Series on Semiconductor Science and Technology (Oxford University Press, Oxford, 2018).

[116] D. S. Smirnov and M. M. Glazov, *Spin coherence generation and detection in spherical nanocrystals*, J. Phys. Condens. Matter **24**, 345302 (2012).

[117] I. Kleinjohann, E. Evers, P. Schering, A. Greilich, G. S. Uhrig, M. Bayer, and F. B. Anders, *Magnetic field dependence of the electron spin revival amplitude in periodically pulsed quantum dots*, Phys. Rev. B **98**, 155318 (2018).

[118] I. I. Ryzhov, G. G. Kozlov, D. S. Smirnov, M. M. Glazov, Y. P. Efimov, S. A. Eliseev, V. A. Lovtcius, V. V. Petrov, K. V. Kavokin, A. V. Kavokin, and V. S. Zapasskii, *Spin noise explores local magnetic fields in a semiconductor*, Sci. Rep. **6**, 21062 (2016).

[119] S. E. Economou, L. J. Sham, Y. Wu, and D. G. Steel, *Proposal for optical U(1) rotations of electron spin trapped in a quantum dot*, Phys. Rev. B **74**, 205415 (2006).

[120] S. G. Carter, A. Shabaev, S. E. Economou, T. A. Kennedy, A. S. Bracker, and T. L. Reinecke, *Directing Nuclear Spin Flips in InAs Quantum Dots Using Detuned Optical Pulse Trains*, Phys. Rev. Lett. **102**, 167403 (2009).

[121] H.-P. Breuer and F. Petruccione, *The Theory of Open Quantum Systems* (Oxford University Press, New York, 2007).

[122] N. Jäschke, A. Fischer, E. Evers, V. V. Belykh, A. Greilich, M. Bayer, and F. B. Anders, *Nonequilibrium nuclear spin distribution function in quantum dots subject to periodic pulses*, Phys. Rev. B **96**, 205419 (2017).

[123] A. Fischer, E. Evers, S. Varwig, A. Greilich, M. Bayer, and F. B. Anders, *Signatures of long-range spin-spin interactions in an (In,Ga)As quantum dot ensemble*, Phys. Rev. B **98**, 205308 (2018).

[124] E. A. Zhukov, D. R. Yakovlev, M. Bayer, M. M. Glazov, E. L. Ivchenko, G. Karczewski, T. Wojtowicz, and J. Kossut, *Spin coherence of a two-dimensional electron gas induced by resonant excitation of trions and excitons in CdTe/(Cd,Mg)Te quantum wells*, Phys. Rev. B **76**, 205310 (2007).

[125] D. S. Smirnov, E. A. Zhukov, E. Kirstein, D. R. Yakovlev, D. Reuter, A. D. Wieck, M. Bayer, A. Greilich, and M. M. Glazov, *Theory of spin inertia in singly charged quantum dots*, Phys. Rev. B **98**, 125306 (2018).

[126] D. S. Smirnov, E. A. Zhukov, D. R. Yakovlev, E. Kirstein, M. Bayer, and A. Greilich, *Spin polarization recovery and Hanle effect for charge carriers interacting with nuclear spins in semiconductors*, Phys. Rev. B **102**, 235413 (2020).

[127] G. Slavcheva and P. Roussignol (eds.), *Optical Generation and Control of Quantum Coherence in Semiconductor Nanostructures*, NanoScience and Technology (Springer-Verlag, Berlin, Heidelberg, 2010).

[128] M. I. Dyakonov (ed.), *Spin Physics in Semiconductors*, 2nd ed., Vol. 157, Springer Series in Solid-State Sciences (Springer, Cham, CH, 2017).

[129] V. V. Belykh, E. Evers, D. R. Yakovlev, F. Fobbe, A. Greilich, and M. Bayer, *Extended pump-probe Faraday rotation spectroscopy of the submicrosecond electron spin dynamics in n-type GaAs*, Phys. Rev. B **94**, 241202(R) (2016).

[130] E. Evers, N. E. Kopteva, I. A. Yugova, D. R. Yakovlev, M. Bayer, and A. Greilich, *Shielding of external magnetic field by dynamic nuclear polarization in (In,Ga)As quantum dots*, Phys. Rev. B **104**, 075302 (2021).

[131] M. M. Glazov, I. A. Yugova, and A. L. Efros, *Electron spin synchronization induced by optical nuclear magnetic resonance feedback*, Phys. Rev. B **85**, 041303(R) (2012).

[132] I. A. Yugova, A. Greilich, E. A. Zhukov, D. R. Yakovlev, M. Bayer, D. Reuter, and A. D. Wieck, *Exciton fine structure in InGaAs/GaAs quantum dots revisited by pump-probe Faraday rotation*, Phys. Rev. B **75**, 195325 (2007).

[133] S. Varwig, A. Schwan, D. Barmscheid, C. Müller, A. Greilich, I. A. Yugova, D. R. Yakovlev, D. Reuter, A. D. Wieck, and M. Bayer, *Hole spin precession in a (In,Ga)As quantum dot ensemble: From resonant spin amplification to spin mode locking*, Phys. Rev. B **86**, 075321 (2012).

[134] S. Varwig, A. René, A. Greilich, D. R. Yakovlev, D. Reuter, A. D. Wieck, and M. Bayer, *Temperature dependence of hole spin coherence in (In,Ga)As quantum dots measured by mode-locking and echo techniques*, Phys. Rev. B **87**, 115307 (2013).

[135] I. A. Yugova, M. M. Glazov, D. R. Yakovlev, A. A. Sokolova, and M. Bayer, *Coherent spin dynamics of electrons and holes in semiconductor quantum wells and quantum dots under periodical optical excitation: Resonant spin amplification versus spin mode locking*, Phys. Rev. B **85**, 125304 (2012).

[136] J. M. Kikkawa and D. D. Awschalom, *Resonant Spin Amplification in n-Type GaAs*, Phys. Rev. Lett. **80**, 4313–4316 (1998).

[137] E. A. Zhukov, O. A. Yugov, I. A. Yugova, D. R. Yakovlev, G. Karczewski, T. Wojtowicz, J. Kossut, and M. Bayer, *Resonant spin amplification of resident electrons in CdTe/(Cd,Mg)Te quantum wells subject to tilted magnetic fields*, Phys. Rev. B **86**, 245314 (2012).

[138] E. Barnes and S. E. Economou, *Electron-Nuclear Dynamics in a Quantum Dot under Nonunitary Electron Control*, Phys. Rev. Lett. **107**, 047601 (2011).

[139] M. Y. Petrov and S. V. Yakovlev, *Comparison of quantum-mechanical and semiclassical approaches for an analysis of spin dynamics in quantum dots*, JETP **115**, 326–336 (2012).

[140] S. E. Economou and E. Barnes, *Theory of dynamic nuclear polarization and feedback in quantum dots*, Phys. Rev. B **89**, 165301 (2014).

[141] W. Beugeling, G. S. Uhrig, and F. B. Anders, *Quantum model for mode locking in pulsed semiconductor quantum dots*, Phys. Rev. B **94**, 245308 (2016).

[142] W. Beugeling, G. S. Uhrig, and F. B. Anders, *Influence of the nuclear Zeeman effect on mode locking in pulsed semiconductor quantum dots*, Phys. Rev. B **96**, 115303 (2017).

[143] A. Vezvaee, G. Sharma, S. E. Economou, and E. Barnes, *Driven dynamics of a quantum dot electron spin coupled to a bath of higher-spin nuclei*, Phys. Rev. B **103**, 235301 (2021).

[144] V. L. Korenev, *Multiple stable states of a periodically driven electron spin in a quantum dot using circularly polarized light*, Phys. Rev. B **83**, 235429 (2011).

[145] N. E. Kopteva, I. A. Yugova, E. A. Zhukov, E. Kirstein, E. Evers, V. V. Belykh, V. L. Korenev, D. R. Yakovlev, M. Bayer, and A. Greilich, *Theoretical Modeling of the Nuclear-Field Induced Tuning of the Electron Spin Precession for Localized Spins*, Phys. Status Solidi B **256**, 1800534 (2019).

[146] M. M. Glazov, I. A. Yugova, S. Spatzek, A. Schwan, S. Varwig, D. R. Yakovlev, D. Reuter, A. D. Wieck, and M. Bayer, *Effect of pump-probe detuning on the Faraday rotation and ellipticity signals of mode-locked spins in (In,Ga)As/GaAs quantum dots*, Phys. Rev. B **82**, 155325 (2010).

[147] S. Spatzek, S. Varwig, M. M. Glazov, I. A. Yugova, A. Schwan, D. R. Yakovlev, D. Reuter, A. D. Wieck, and M. Bayer, *Generation and detection of mode-locked spin coherence in (In,Ga)As/GaAs quantum dots by laser pulses of long duration*, Phys. Rev. B **84**, 115309 (2011).

[148] E. Evers, V. V. Belykh, N. E. Kopteva, I. A. Yugova, A. Greilich, D. R. Yakovlev, D. Reuter, A. D. Wieck, and M. Bayer, *Decay and revival of electron spin polarization in an ensemble of (In,Ga)As quantum dots*, Phys. Rev. B **98**, 075309 (2018).

[149] S. Markmann, C. Reichl, W. Wegscheider, and G. Salis, *Universal nuclear focusing of confined electron spins*, Nat. Commun. **10**, 1097 (2019).

[150] A. M. Ross, A. S. Bracker, M. K. Yakes, D. Gammon, L. J. Sham, and D. G. Steel, *Direct high-resolution resonant Raman scattering measurements of dynamic nuclear spin polarization states of an InAs quantum dot*, Phys. Rev. B **102**, 235425 (2020).

[151] X. Xu, W. Yao, B. Sun, D. G. Steel, A. S. Bracker, D. Gammon, and L. J. Sham, *Optically controlled locking of the nuclear field via coherent dark-state spectroscopy*, Nature **459**, 1105–1109 (2009).

[152] C. Latta, A. Högele, Y. Zhao, A. N. Vamivakas, P. Maletinsky, M. Kroner, J. Dreiser, I. Carusotto, A. Badolato, D. Schuh, W. Wegscheider, M. Atature, and A. Imamoglu, *Confluence of resonant laser excitation and bidirectional quantum-dot nuclear-spin polarization*, Nat. Phys. **5**, 758–763 (2009).

[153] A. Högele, M. Kroner, C. Latta, M. Claassen, I. Carusotto, C. Bulutay, and A. Imamoglu, *Dynamic Nuclear Spin Polarization in the Resonant Laser Excitation of an InGaAs Quantum Dot*, Phys. Rev. Lett. **108**, 197403 (2012).

[154] W. Yang and L. J. Sham, *Collective nuclear stabilization in single quantum dots by noncollinear hyperfine interaction*, Phys. Rev. B **85**, 235319 (2012).

[155] T. Nutz, E. Barnes, and S. E. Economou, *Solvable quantum model of dynamic nuclear polarization in optically driven quantum dots*, Phys. Rev. B **99**, 035439 (2019).

[156] J. Fischer, W. A. Coish, D. V. Bulaev, and D. Loss, *Spin decoherence of a heavy hole coupled to nuclear spins in a quantum dot*, Phys. Rev. B **78**, 155329 (2008).

[157] C. Testelin, F. Bernardot, B. Eble, and M. Chamarro, *Hole–spin dephasing time associated with hyperfine interaction in quantum dots*, Phys. Rev. B **79**, 195440 (2009).

[158] P. Philippopoulos, S. Chesi, and W. A. Coish, *First-principles hyperfine tensors for electrons and holes in GaAs and silicon*, Phys. Rev. B **101**, 115302 (2020).

[159] F. Heisterkamp, E. A. Zhukov, A. Greilich, D. R. Yakovlev, V. L. Korenev, A. Pawlis, and M. Bayer, *Longitudinal and transverse spin dynamics of donor-bound electrons in fluorine-doped ZnSe: Spin inertia versus Hanle effect*, Phys. Rev. B **91**, 235432 (2015).

[160] G. Burkard, D. Loss, and D. P. DiVincenzo, *Coupled quantum dots as quantum gates*, Phys. Rev. B **59**, 2070–2078 (1999).

[161] A. V. Khaetskii and Y. V. Nazarov, *Spin relaxation in semiconductor quantum dots*, Phys. Rev. B **61**, 12639–12642 (2000).

[162] D. Gammon, A. L. Efros, T. A. Kennedy, M. Rosen, D. S. Katzer, D. Park, S. W. Brown, V. L. Korenev, and I. A. Merkulov, *Electron and Nuclear Spin Interactions in the Optical Spectra of Single GaAs Quantum Dots*, Phys. Rev. Lett. **86**, 5176–5179 (2001).

[163] A. Khaetskii, D. Loss, and L. Glazman, *Electron spin evolution induced by interaction with nuclei in a quantum dot*, Phys. Rev. B **67**, 195329 (2003).

[164] E. Fermi, *Über die magnetischen Momente der Atomkerne*, Z. Phys. **60**, 320–333 (1930).

[165] A. Abragam, *The Principles of Nuclear Magnetism*, International Series of Monographs on Physics (Oxford University Press, Oxford, 1961).

[166] M. I. Dyakonov and V. I. Perel, "Theory of optical spin orientation", in *Optical Orientation*, Vol. 8, edited by F. Meier and B. P. Zakharchenya, Modern Problems in Condensed Matter Sciences (North Holland, Amsterdam, 1984), pp. 11–71.

[167] W. A. Coish and J. Baugh, *Nuclear spins in nanostructures*, Phys. Status Solidi B **246**, 2203–2215 (2009).

[168] W. D. Knight, *Nuclear Magnetic Resonance Shift in Metals*, Phys. Rev. **76**, 1259–1260 (1949).

[169] N. J. Stone, *Table of Nuclear Magnetic Dipole and Electric Quadrupole Moments*, Technical Report No. INDC(NDS)–0658 (International Atomic Energy Agency, Vienna, 2014).

[170] J. Meija, T. B. Coplen, M. Berglund, W. A. Brand, P. D. Bièvre, M. Gröning, N. E. Holden, J. Irrgeher, R. D. Loss, T. Walczyk, and T. Prohaska, *Isotopic compositions of the elements 2013 (IUPAC Technical Report)*, Pure Appl. Chem **88**, 293–306 (2016).

[171] A. W. Overhauser, *Polarization of Nuclei in Metals*, Phys. Rev. **92**, 411–415 (1953).

[172] M. Gaudin, *Diagonalisation d'une classe d'hamiltoniens de spin*, J. Phys. France **37**, 1087–1098 (1976).

[173] M. Gaudin, *La Fonction d'Onde de Bethe*, Série Scientifique (Masson, Paris, 1983).

[174] M. Bortz and J. Stolze, *Exact dynamics in the inhomogeneous central-spin model*, Phys. Rev. B **76**, 014304 (2007).

[175] M. Bortz and J. Stolze, *Spin and entanglement dynamics in the central-spin model with homogeneous couplings*, J. Stat. Mech. **2007**, P06018 (2007).

[176] M. Bortz, S. Eggert, C. Schneider, R. Stübner, and J. Stolze, *Dynamics and decoherence in the central spin model using exact methods*, Phys. Rev. B **82**, 161308(R) (2010).

[177] A. Faribault and D. Schuricht, *Integrability-Based Analysis of the Hyperfine-Interaction-Induced Decoherence in Quantum Dots*, Phys. Rev. Lett. **110**, 040405 (2013).

[178] W. A. Coish and D. Loss, *Hyperfine interaction in a quantum dot: Non-Markovian electron spin dynamics*, Phys. Rev. B **70**, 195340 (2004).

[179] A. Faribault and D. Schuricht, *Spin decoherence due to a randomly fluctuating spin bath*, Phys. Rev. B **88**, 085323 (2013).

[180] U. Seifert, P. Bleicker, P. Schering, A. Faribault, and G. S. Uhrig, *Persisting correlations of a central spin coupled to large spin baths*, Phys. Rev. B **94**, 094308 (2016).

[181] L. B. Gravert, P. Lorenz, C. Nase, J. Stolze, and G. S. Uhrig, *Increased coherence time in narrowed bath states in quantum dots*, Phys. Rev. B **94**, 094416 (2016).

[182] R. Röhrig, P. Schering, L. B. Gravert, B. Fauseweh, and G. S. Uhrig, *Quantum mechanical treatment of large spin baths*, Phys. Rev. B **97**, 165431 (2018).

[183] D. Stanek, C. Raas, and G. S. Uhrig, *Dynamics and decoherence in the central spin model in the low-field limit*, Phys. Rev. B **88**, 155305 (2013).

[184] J. Hackmann and F. B. Anders, *Spin noise in the anisotropic central spin model*, Phys. Rev. B **89**, 045317 (2014).

[185] D. Bechtold Alexander and Rauch, F. Li, T. Simmet, P.-L. Ardelt, A. Regler, K. Müller, N. A. Sinitsyn, and J. J. Finley, *Three-stage decoherence dynamics of an electron spin qubit in an optically active quantum dot*, Nat. Phys. **11**, 1005–1008 (2015).

[186] N. A. Sinitsyn, Y. Li, S. A. Crooker, A. Saxena, and D. L. Smith, *Role of Nuclear Quadrupole Coupling on Decoherence and Relaxation of Central Spins in Quantum Dots*, Phys. Rev. Lett. **109**, 166605 (2012).

[187] J. Hackmann, P. Glasenapp, A. Greilich, M. Bayer, and F. B. Anders, *Influence of the Nuclear Electric Quadrupolar Interaction on the Coherence Time of Hole and Electron Spins Confined in Semiconductor Quantum Dots*, Phys. Rev. Lett. **115**, 207401 (2015).

[188] A. Bechtold, F. Li, K. Müller, T. Simmet, P.-L. Ardelt, J. J. Finley, and N. A. Sinitsyn, *Quantum Effects in Higher-Order Correlators of a Quantum-Dot Spin Qubit*, Phys. Rev. Lett. **117**, 027402 (2016).

[189] N. Fröhling and F. B. Anders, *Long-time coherence in fourth-order spin correlation functions*, Phys. Rev. B **96**, 045441 (2017).

[190] N. Fröhling, N. Jäschke, and F. B. Anders, *Fourth-order spin correlation function in the extended central spin model*, Phys. Rev. B **99**, 155305 (2019).

[191] S. M. Ryabchenko and Y. G. Semenov, *Spin-correlation effects for a large-radius electron center in a magnetically mixed semiconductor*, JETP **57**, 825 (1983).

[192] Y. G. Semenov and K. W. Kim, *Effect of an external magnetic field on electron-spin dephasing induced by hyperfine interaction in quantum dots*, Phys. Rev. B **67**, 073301 (2003).

[193] G. G. Kozlov, *Exactly solvable spin dynamics of an electron coupled to a large number of nuclei; the electron-nuclear spin echo in a quantum dot*, J. Exp. Theor. Phys. **105**, 803–815 (2007).

[194] E. Barnes, Ł. Cywiński, and S. Das Sarma, *Master equation approach to the central spin decoherence problem: Uniform coupling model and role of projection operators*, Phys. Rev. B **84**, 155315 (2011).

[195] A. V. Shumilin and D. S. Smirnov, *Nuclear Spin Dynamics, Noise, Squeezing, and Entanglement in Box Model*, Phys. Rev. Lett. **126**, 216804 (2021).

[196] M. Y. Petrov, G. G. Kozlov, I. V. Ignatiev, R. V. Cherbunin, D. R. Yakovlev, and M. Bayer, *Coupled electron-nuclear spin dynamics in quantum dots: A graded box model approach*, Phys. Rev. B **80**, 125318 (2009).

[197] J. Schliemann, A. V. Khaetskii, and D. Loss, *Spin decay and quantum parallelism*, Phys. Rev. B **66**, 245303 (2002).

[198] V. V. Dobrovitski, H. A. De Raedt, M. I. Katsnelson, and B. N. Harmon, *Quantum Oscillations without Quantum Coherence*, Phys. Rev. Lett. **90**, 210401 (2003).

[199] V. V. Dobrovitski and H. A. De Raedt, *Efficient scheme for numerical simulations of the spin-bath decoherence*, Phys. Rev. E **67**, 056702 (2003).

[200] D. Stanek, C. Raas, and G. S. Uhrig, *From quantum-mechanical to classical dynamics in the central-spin model*, Phys. Rev. B **90**, 064301 (2014).

[201] G. S. Uhrig, J. Hackmann, D. Stanek, J. Stolze, and F. B. Anders, *Conservation laws protect dynamic spin correlations from decay: Limited role of integrability in the central spin model*, Phys. Rev. B **90**, 060301(R) (2014).

[202] H.-P. Breuer, D. Burgarth, and F. Petruccione, *Non-Markovian dynamics in a spin star system: Exact solution and approximation techniques*, Phys. Rev. B **70**, 045323 (2004).

[203] J. Fischer and H.-P. Breuer, *Correlated projection operator approach to non-Markovian dynamics in spin baths*, Phys. Rev. A **76**, 052119 (2007).

[204] E. Ferraro, H.-P. Breuer, A. Napoli, M. A. Jivulescu, and A. Messina, *Non-Markovian dynamics of a single electron spin coupled to a nuclear spin bath*, Phys. Rev. B **78**, 064309 (2008).

[205] W. A. Coish, J. Fischer, and D. Loss, *Free-induction decay and envelope modulations in a narrowed nuclear spin bath*, Phys. Rev. B **81**, 165315 (2010).

[206] E. Barnes, Ł. Cywiński, and S. Das Sarma, *Nonperturbative Master Equation Solution of Central Spin Dephasing Dynamics*, Phys. Rev. Lett. **109**, 140403 (2012).

[207] C. Deng and X. Hu, *Analytical solution of electron spin decoherence through hyperfine interaction in a quantum dot*, Phys. Rev. B **73**, 241303(R) (2006).

[208] C. Deng and X. Hu, *Electron-spin dephasing via hyperfine interaction in a quantum dot: An equation-of-motion calculation of electron-spin correlation functions*, Phys. Rev. B **78**, 245301 (2008).

[209] W. M. Witzel, R. de Sousa, and S. Das Sarma, *Quantum theory of spectral-diffusion-induced electron spin decoherence*, Phys. Rev. B **72**, 161306(R) (2005).

[210] W. M. Witzel and S. Das Sarma, *Quantum theory for electron spin decoherence induced by nuclear spin dynamics in semiconductor quantum computer architectures: Spectral diffusion of localized electron spins in the nuclear solid-state environment*, Phys. Rev. B **74**, 035322 (2006).

[211] J. R. Maze, J. M. Taylor, and M. D. Lukin, *Electron spin decoherence of single nitrogen-vacancy defects in diamond*, Phys. Rev. B **78**, 094303 (2008).

[212] W. Yang and R.-B. Liu, *Quantum many-body theory of qubit decoherence in a finite-size spin bath*, Phys. Rev. B **78**, 085315 (2008).

[213] W. Yang and R.-B. Liu, *Quantum many-body theory of qubit decoherence in a finite-size spin bath. II. Ensemble dynamics*, Phys. Rev. B **79**, 115320 (2009).

[214] Ł. Cywiński, W. M. Witzel, and S. Das Sarma, *Electron Spin Dephasing due to Hyperfine Interactions with a Nuclear Spin Bath*, Phys. Rev. Lett. **102**, 057601 (2009).

[215] Ł. Cywiński, W. M. Witzel, and S. Das Sarma, *Pure quantum dephasing of a solid-state electron spin qubit in a large nuclear spin bath coupled by long-range hyperfine-mediated interactions*, Phys. Rev. B **79**, 245314 (2009).

[216] W. M. Witzel, M. S. Carroll, Ł. Cywiński, and S. Das Sarma, *Quantum decoherence of the central spin in a sparse system of dipolar coupled spins*, Phys. Rev. B **86**, 035452 (2012).

[217] R. Röhrig, *Quantenmechanische Berechnung von Autokorrelationsfunktionen im Zentralspinmodell für unendlich große Spinbäder*, Master's thesis (TU Dortmund University, 2017).

[218] L. P. Lindoy and D. E. Manolopoulos, *Simple and Accurate Method for Central Spin Problems*, Phys. Rev. Lett. **120**, 220604 (2018).

[219] K. Schulten and P. G. Wolynes, *Semiclassical description of electron spin motion in radicals including the effect of electron hopping*, J. Chem. Phys **68**, 3292–3297 (1978).

[220] D. E. Manolopoulos and P. J. Hore, *An improved semiclassical theory of radical pair recombination reactions*, J. Chem. Phys. **139**, 124106 (2013).

[221] L. P. Lindoy, T. P. Fay, and D. E. Manolopoulos, *Quantum mechanical spin dynamics of a molecular magnetoreceptor*, J. Chem. Phys. **152**, 164107 (2020).

[222] S. I. Erlingsson and Y. V. Nazarov, *Hyperfine-mediated transitions between a Zeeman split doublet in GaAs quantum dots: The role of the internal field*, Phys. Rev. B **66**, 155327 (2002).

[223] S. I. Erlingsson and Y. V. Nazarov, *Evolution of localized electron spin in a nuclear spin environment*, Phys. Rev. B **70**, 205327 (2004).

[224] M. M. Glazov and E. L. Ivchenko, *Spin noise in quantum dot ensembles*, Phys. Rev. B **86**, 115308 (2012).

[225] V. K. Kalevich, K. V. Kavokin, I. Merkulov, and M. R. Vladimirova, "Dynamic Nuclear Polarization and Nuclear Fields", in *Spin Physics in Semiconductors*, Vol. 157, edited by M. I. Dyakonov, 2nd ed., Springer Series in Solid-State Sciences (Springer, Cham, CH, 2017), pp. 387–430.

[226] G. Chen, D. L. Bergman, and L. Balents, *Semiclassical dynamics and long-time asymptotics of the central-spin problem in a quantum dot*, Phys. Rev. B **76**, 045312 (2007).

[227] K. A. Al-Hassanieh, V. V. Dobrovitski, E. Dagotto, and B. N. Harmon, *Numerical Modeling of the Central Spin Problem Using the Spin-Coherent-State P Representation*, Phys. Rev. Lett. **97**, 037204 (2006).

[228] W. Zhang, V. V. Dobrovitski, K. A. Al-Hassanieh, E. Dagotto, and B. N. Harmon, *Hyperfine interaction induced decoherence of electron spins in quantum dots*, Phys. Rev. B **74**, 205313 (2006).

[229] D. Stanek, *Dynamics and Decoherence in the Central Spin Model: From a Quantum Mechanical to a Classical Description*, PhD thesis (TU Dortmund University, 2014).

[230] A. Polkovnikov, *Phase space representation of quantum dynamics*, Ann. Phys. **325**, 1790–1852 (2010).

[231] S. M. Davidson and A. Polkovnikov, *SU*(3) *Semiclassical Representation of Quantum Dynamics of Interacting Spins*, Phys. Rev. Lett. **114**, 045701 (2015).

[232] J. Schachenmayer, A. Pikovski, and A. M. Rey, *Many-Body Quantum Spin Dynamics with Monte Carlo Trajectories on a Discrete Phase Space*, Phys. Rev. X **5**, 011022 (2015).

[233] U. Fano, *Description of States in Quantum Mechanics by Density Matrix and Operator Techniques*, Rev. Mod. Phys. **29**, 74–93 (1957).

[234] W. K. Wootters, *A Wigner-function formulation of finite-state quantum mechanics*, Ann. Phys. (N.Y.) **176**, 1–21 (1987).

[235] M. Hillery, R. F. O'Connell, M. O. Scully, and E. P. Wigner, *Distribution functions in physics: Fundamentals*, Phys. Rep. **106**, 121–167 (1984).

[236] Y. Takahashi and F. Shibata, *Spin Coherent State Representation in Non-Equilibrium Statistical Mechanics*, J. Phys. Soc. Jpn. **38**, 656–668 (1975).

[237] A. Altland, V. Gurarie, T. Kriecherbauer, and A. Polkovnikov, *Nonadiabaticity and large fluctuations in a many-particle Landau-Zener problem*, Phys. Rev. A **79**, 042703 (2009).

[238] A. Auerbach, *Interacting Electrons and Quantum Magnetism*, Graduate Texts in Contemporary Physics (Springer, New York, 1994).

[239] B. Zhu, A. M. Rey, and J. Schachenmayer, *A generalized phase space approach for solving quantum spin dynamics*, New J. Phys. **21**, 082001 (2019).

[240] W. A. Coish, D. Loss, E. A. Yuzbashyan, and B. L. Altshuler, *Quantum versus classical hyperfine-induced dynamics in a quantum dot*, J. Appl. Phys. **101**, 081715 (2007).

[241] J. Dormand and P. Prince, *A family of embedded Runge-Kutta formulae*, J. Comput. Appl. Math. **6**, 19–26 (1980).

[242] K. Ahnert and M. Mulansky, *Odeint – Solving Ordinary Differential Equations in C++*, AIP Conf. Proc. **1389**, 1586–1589 (2011).

[243] W. H. Press, S. A. Teukolsky, W. T. Vetterling, and B. P. Flannery, *Numerical Recipes: The Art of Scientific Computing*, 3rd ed. (Cambridge University Press, New York, 2007).

[244] M. Matsumoto and T. Nishimura, *Mersenne Twister: A 623-Dimensionally Equidistributed Uniform Pseudo-Random Number Generator*, ACM Trans. Model. Comput. Simul. **8**, 3–30 (1998).

[245] Message Passing Interface Forum, *MPI: A Message-Passing Interface Standard, Version 3.1* (High Performance Computing Center Stuttgart (HLRS), 2015).

[246] P. Schering, P. W. Scherer, and G. S. Uhrig, "Simulation of nonequilibrium spin dynamics in quantum dots subjected to periodic laser pulses", in *High Performance Computing in Science and Engineering '20, Transactions of the High Performance Computing Center, Stuttgart (HLRS) 2020*, edited by W. E. Nagel, D. H. Kröner, and M. M. Resch (Springer International Publishing, in press).

[247] B. Fauseweh, P. Schering, J. Hüdepohl, and G. S. Uhrig, *Efficient algorithms for the dynamics of large and infinite classical central spin models*, Phys. Rev. B **96**, 054415 (2017).

[248] J. Hüdepohl, *Effiziente Algorithmen zur Berechnung von Autokorrelationsfunktionen im klassischen Zentralspinmodell mit unendlich vielen Badspins*, Master's thesis (TU Dortmund University, 2016).

[249] C. Lanczos, *An Iteration Method for the Solution of the Eigenvalue Problem of Linear Differential and Integral Operators*, J. Res. Natl. Bur. Stand. **45**, 255–282 (1950).

[250] M. Abramowitz and I. A. Stegun, *Handbook of Mathematical Functions* (Dover Publications, New York, 1964).

[251] D. G. Pettifor and D. L. Weaire (eds.), *The Recursion Method and its Applications*, Vol. 58, Springer Series in Solid State Sciences (Springer-Verlag, Berlin, Heidelberg, 1987).

[252] P. Schering, J. Hüdepohl, G. S. Uhrig, and B. Fauseweh, *Nuclear frequency focusing in periodically pulsed semiconductor quantum dots described by infinite classical central spin models*, Phys. Rev. B **98**, 024305 (2018).

[253] G. S. Uhrig, *Quantum Coherence from Commensurate Driving with Laser Pulses and Decay*, SciPost Phys. **8**, 40 (2020).

[254] P. Schering, P. W. Scherer, and G. S. Uhrig, *Interplay of spin mode locking and nuclei-induced frequency focusing in quantum dots*, Phys. Rev. B **102**, 115301 (2020).

[255] P. Schering, G. S. Uhrig, and D. S. Smirnov, *Spin inertia and polarization recovery in quantum dots: Role of pumping strength and resonant spin amplification*, Phys. Rev. Research **1**, 033189 (2019).

[256] N. Jäschke, F. B. Anders, and M. M. Glazov, *Electron spin noise under the conditions of nuclei-induced frequency focusing*, Phys. Rev. B **98**, 045307 (2018).

[257] N. Jäschke, *A semiclassical approach to the spin dynamics in a singly charged semiconductor quantum dot*, PhD thesis (TU Dortmund University, 2019).

[258] P. Schering and G. S. Uhrig, *Nuclear magnetic resonance spectroscopy of nonequilibrium steady states in quantum dots*, EPL (Europhys. Lett.) **133**, 57003 (2021).

[259] P. Scherer, *Getriebene Spindynamik in Quantenpunkten mit mehreren Isotopen*, Master's thesis (TU Dortmund University, 2019).

[260] P. S. Sokolov, M. Y. Petrov, T. Mehrtens, K. Müller-Caspary, A. Rosenauer, D. Reuter, and A. D. Wieck, *Reconstruction of nuclear quadrupole interaction in (In,Ga)As/GaAs quantum dots observed by transmission electron microscopy*, Phys. Rev. B **93**, 045301 (2016).

[261] W. Hanle, *Über magnetische Beeinflussung der Polarisation der Resonanzfluoreszenz*, Z. Phys. **30**, 93–105 (1924).

[262] V. S. Zapasskii, *Spin-noise spectroscopy: from proof of principle to applications*, Adv. Opt. Photon. **5**, 131–168 (2013).

[263] N. A. Sinitsyn and Y. V. Pershin, *The theory of spin noise spectroscopy: a review*, Rep. Prog. Phys. **79**, 106501 (2016).

[264] D. S. Smirnov, V. N. Mantsevich, and M. M. Glazov, *Theory of optically detected spin noise in nanosystems*, Phys. Usp., accepted, 10.3367/UFNe.2020.10.038861 (2021).

[265] A. Greilich, A. Pawlis, F. Liu, O. A. Yugov, D. R. Yakovlev, K. Lischka, Y. Yamamoto, and M. Bayer, *Spin dephasing of fluorine-bound electrons in ZnSe*, Phys. Rev. B **85**, 121303(R) (2012).

[266] A. Esser, E. Runge, R. Zimmermann, and W. Langbein, *Photoluminescence and radiative lifetime of trions in GaAs quantum wells*, Phys. Rev. B **62**, 8232–8239 (2000).

[267] M. M. Glazov and E. L. Ivchenko, *Resonant spin amplification in nanostructures with anisotropic spin relaxation and spread of the electronic g factor*, Semiconductors **42**, 951–957 (2008).

[268] I. A. Yugova, A. A. Sokolova, D. R. Yakovlev, A. Greilich, D. Reuter, A. D. Wieck, and M. Bayer, *Long-Term Hole Spin Memory in the Resonantly Amplified Spin Coherence of InGaAs/GaAs Quantum Well Electrons*, Phys. Rev. Lett. **102**, 167402 (2009).

[269] P. L. Jeune, D. Robart, X. Marie, T. Amand, M. Brousseau, J. Barrau, V. Kalevich, and D. Rodichev, *Anisotropy of the electron Landé g factor in quantum wells*, Semicond. Sci. Technol. **12**, 380–383 (1997).

[270] J.-C. Diels and W. Rudolph, *Ultrashort Laser Pulse Phenomena*, 2nd ed. (Academic Press, San Diego, 2006).

[271] V. G. Fleisher and I. A. Merkulov, "Optical orientation of coupled electron-nuclear spin system", in *Optical Orientation*, Vol. 8, edited by F. Meier and B. P. Zakharchenya, Modern Problems in Condensed Matter Sciences (North Holland, Amsterdam, 1984), pp. 173–258.

[272] A. Schwan, B.-M. Meiners, A. Greilich, D. R. Yakovlev, M. Bayer, A. D. B. Maia, A. A. Quivy, and A. B. Henriques, *Anisotropy of electron and hole g-factors in (In,Ga)As quantum dots*, Appl. Phys. Lett. **99**, 221914 (2011).

List of figures

List of tables

Acknowledgments

Many people contribute to a successful doctorate, completing such a tremendous project is hardly possible otherwise. But at first, I want to express my gratitude to my supervisor Prof. Dr. Götz S. Uhrig for the continuous support and all the words of advice over the past years. It was a pleasure!

I thank Prof. Dr. Frithjof B. Anders and Prof. Dr. Mikhail M. Glazov for taking on the role of the second and third assessor, respectively.

Many people have contributed to the different projects of the thesis. In particular, I want to mention Eiko Evers, Dr. Benedikt Fauseweh, Dr. Alex Greilich, Philipp W. Scherer, and Dr. Dmitry S. Smirnov. Thanks a lot for the fruitful collaborations!

Many thanks go to the members of the group Theoretische Physik Ia for the nice working atmosphere over the past years and for the fun lunch and coffee breaks.

A special thanks goes to my office colleague Mohsen Yarmohammadi for the numerous discussions and the fun time!

I am very grateful to Philip Bleicker for proof-reading the whole thesis. Thanks a lot, also for the long phone calls during the pandemic and for the fun workshops that we attended together!

I thank Dr. Carsten Nase for the technical support and also for all the IT related stuff that I have learned from him. Thanks also to Dr. Daniel May and Andreas Fischer for the good teamwork as co-admins.

I am grateful to Prof. Dr. Mikhail M. Glazov and Dr. Dmitry S. Smirnov for their hospitality during my research stay at the Ioffe Institute in St. Petersburg, which took place in the frame of the International Collaborative Research Centre TRR 160.

I gratefully acknowledge the resources provided by the Gauss Centre for Supercomputing e.V. on the supercomputers Hawk and Hazel Hen at High-Performance Computing Center Stuttgart in the frame of the federal project NFFinQDs.

I thank Iris Kleinjohann for the provision of the quantum mechanical data shown in Appendix C.

Last but not least, there is one special person – my wife Jacqueline Schering – to whom I owe so much. I can hardly imagine how hard it must have been to endure my lengthy monologues about physics and my recent findings. Dear Jacqueline, it is impossible to express in words how grateful I am for your daily support and encouragement. Thank you so much!